

3-24-2016

Conceptual Design, Structural Analysis, and Design Space Exploration of a Vacuum Lighter than Air Vehicle

Brian C. Cranston

Follow this and additional works at: <https://scholar.afit.edu/etd>



Part of the [Aerospace Engineering Commons](#)

Recommended Citation

Cranston, Brian C., "Conceptual Design, Structural Analysis, and Design Space Exploration of a Vacuum Lighter than Air Vehicle" (2016). *Theses and Dissertations*. 424.
<https://scholar.afit.edu/etd/424>

This Dissertation is brought to you for free and open access by the Student Graduate Works at AFIT Scholar. It has been accepted for inclusion in Theses and Dissertations by an authorized administrator of AFIT Scholar. For more information, please contact richard.mansfield@afit.edu.



**CONCEPTUAL DESIGN, STRUCTURAL ANALYSIS, AND DESIGN SPACE
EXPLORATION OF A VACUUM LIGHTER THAN AIR VEHICLE**

DISSERTATION

Brian C. Cranston, Civ

AFIT-ENY-DS-16-M-202

**DEPARTMENT OF THE AIR FORCE
AIR UNIVERSITY**

AIR FORCE INSTITUTE OF TECHNOLOGY

Wright-Patterson Air Force Base, Ohio

DISTRIBUTION STATEMENT A.
APPROVED FOR PUBLIC RELEASE; DISTRIBUTION UNLIMITED.

The views expressed in this thesis are those of the author and do not reflect the official policy or position of the United States Air Force, Department of Defense, or the United States Government. This material is declared a work of the U.S. Government and is not subject to copyright protection in the United States.

AFIT-ENY-DS-16-M-202

**CONCEPTUAL DESIGN, STRUCTURAL ANALYSIS, AND DESIGN SPACE
EXPLORATION OF A VACUUM LIGHTER THAN AIR VEHICLE**

DISSERTATION

Presented to the Faculty

Department of Aeronautics and Astronautics

Graduate School of Engineering and Management

Air Force Institute of Technology

Air University

Air Education and Training Command

In Partial Fulfillment of the Requirements for the

Degree of Doctor of Philosophy

Brian C. Cranston, M.S.

Civ

March 2016

DISTRIBUTION STATEMENT A.
APPROVED FOR PUBLIC RELEASE; DISTRIBUTION UNLIMITED.

AFIT-ENY-DS-16-M-202

CONCEPTUAL DESIGN, STRUCTURAL ANALYSIS, AND DESIGN SPACE
EXPLORATION OF A VACUUM LIGHTER THAN AIR VEHICLE

Brian C. Cranston, MS
PhD Candidate

Committee Membership:

Dr. Anthony Palazotto
Chair

Dr. William Baker
Member

Lt. Col. Jeremy Agte, PhD
Member

ADEDJI B. BADIRU, PhD
Dean, Graduate School of Engineering
and Management

ABSTRACT

The research detailed in this study investigates an internal vacuum as well as its optimal structural design, utilizing currently available materials, as an alternative to traditional gases to create and sustain buoyancy in lighter than air vehicles. To date, the consideration of a vacuum lighter than air vehicle has been limited to three sources of literature, the earliest of which dates back to 1663. This study will initially summarize and review this literature. We will then combine finite element analysis, dimensional analysis, design of experiments, and response surface methodology studies to explore the feasibility, and the functional design of a vacuum lighter than air vehicle constrained by modern technology and materials. The process developed herein allows a designer to perform a broad scope initial structural response design space investigation based on user defined constraints to determine if and where structurally feasible regions or points lie. This research then specifically analyzes two cylindrical pultruded rod geometric frame designs with membrane skins stretched over the top vacuum lighter than air vehicle designs. The first being an icosahedron frame and skin structure proposed by Metlen at the Air Force Institute of Technology. The second is a similar frame and skin concept, a hexakis icosahedron, designed by the author. The major findings resulting from the two case studies analyzed are: 1) The structural design space exploration methodology is a viable and cost effective way to perform an early-stage structural feasibility analysis on a vehicle design that relies heavily on its structural performance, 2) For the frame and skin vacuum lighter than air vehicle concepts analyzed, the beam thickness/beam radius ratio, as well as the frame specific modulus had the most significant effect on the max frame and skin stress responses, 3) The experimental test conducted to validate the frame modeling technique agreed with the finite element results, therefore validating the frame modeling technique, 4) Performing a dimensional analysis on a finite element system before performing a design of experiments resulted in a significant reduction in the number of terms to evaluate in order to represent the entire system, 5) Within the limits analyzed for both case studies, the icosahedron did not have a structurally feasible design region while the hexakis design had a significantly large region within the design space that was structurally feasible.

Acknowledgements

Firstly, I would like to express my sincere gratitude to my advisor Dr. Anthony Palazotto for the continuous support of my Ph.D study and related research, for his patience, motivation, and immense knowledge. His guidance helped me in all the time of research and writing of this thesis. I could not have imagined having a better advisor and mentor for my Ph.D study. Besides my advisor, I would like to thank the rest of my thesis committee: Dr. William Baker and Lt. Col. Jeremy Agte for their insightful comments and encouragement, but also for their hard questions which inspired me to widen my research from various perspectives. I would like to thank my family: my parents and to my twin brother (now we have a professional athlete and Dr. in the family) and my sister for supporting me throughout writing this thesis and my life in general. Last but not the least, I would like to thank my fiancé for all of her love and support and help with editing this dissertation.

This work was performed at the Air Force Institute of Technology, where it was supported by Dr. David Stargel and Mr. James Fillerup of AFOSR for their financial support and interest.

Brian C. Cranston

Table of Contents

ABSTRACT.....	IV
LIST OF FIGURES	VIII
LIST OF TABLES	XI
LIST OF ACRONYMS	XIII
I. INTRODUCTION	1
Motivation	2
Document Outline	6
II. BACKGROUND AND PREVIOUS WORK	9
Lighter than Air Vehicles	9
Previous Work on Vacuum LTAVs	12
Chapter II Summary	26
III. STRUCTURAL DESIGN SPACE EXPLORATION AND FEASIBILITY ANALYSIS	
METHODOLOGY	26
Structural Design Space Creation.....	28
Structural Feasibility Analysis	56
Chapter III Summary.....	59
IV. GEOMETRIC FRAME CONSIDERATIONS AND MODELING AND ANALYSIS TECHNIQUE	
VALIDATION	61
Cylindrical Beam Buckling Development and Thickness/Radius Ratio Analysis	62
Frame Finite Element Analysis Modeling Technique Validation	70
Chapter IV Summary	92
V. METLEN ICOSAHEDRON VLTAV DSE AND FEASIBILITY ASSESSMENT CASE STUDY	
94	
Icosahedron Finite Element Models Development.....	94
Icosahedron VLTAV FEM Dimensional Analysis.....	106
DOE Analysis Results and Discussion for the Icosahedron Vacuum Vehicle	112
Icosahedron Response Surfaces	147
Icosahedron VLTAV Structural Feasibility Assessment and Response Discussion	150
Icosahedron Design Trades and Vehicle Sizing	158
Chapter V Summary	161
VI. HEXAKIS ICOSAHEDRON DSE AND FEASIBILITY ASSESSMENT CASE STUDY	162
Hexakis Icosahedron Selection.....	162
Hexakis Icosahedron Finite Element Model Development	165
Hexakis Icosahedron VLTAV FEA Dimensional Analysis	173
DOE Analysis Results and Discussion for the Hexakis Icosahedron Vacuum Vehicle	174
Hexakis Icosahedron Response Surfaces	190
Hexakis Icosahedron VLTAV Structural Feasibility Assessment and Response Discussion	194
Hexakis Icosahedron Vehicle Sizing	201

Chapter VI Summary	205
VII. SUMMARY AND CONCLUSIONS	207
Major Contributions	210
REFERENCES.....	215
A. APPENDIX A	236
B. APPENDIX B.....	236

LIST OF FIGURES

PAGE

Figure 1: Metlen Icosahedron Design.....	5
Figure 2: Buoyancy Illustration.....	10
Figure 3: Francesco Lana de Terzi’s LTAV concept [3].....	13
Figure 4: Optimization contours for beryllium face sheets and an aluminum honeycomb core [4].	17
Figure 5: Increasing Geodesic Frequencies starting with 1, an icosahedron	19
Figure 6: Icosahedron Frame	20
Figure 7: Full skin-frame icosahedral model.....	22
Figure 8: Singularities in the skin due to tie constraints.....	25
Figure 9: Newton Raphson technique for a single iteration	33
Figure 10: True underlying curved relationship between low and high factor level	41
Figure 11: DOE Evaluation Process Diagram	43
Figure 12: 2 ² Factorial Design Treatment Representation.....	46
Figure 13: Illustration of plotted DOE data points and the generated Response Surface.	55
Figure 14: Triangular frame section with reference point and coupling constraint. The reference point is where the arrow points to and the coupling constraint is denoted by the blue lines.	58
Figure 15: First two mode shapes for a simply supported column.	63
Figure 16: First buckling mode for various boundary conditions and its corresponding c value.	64
Figure 17: Load displacement curve for a buckled column.....	65
Figure 18: Solid vs. Hollow Beam Profile Study [5] (the top left plot is beam bending moment of inertia (I_n) versus (tb/rb), the top right plot is maximum beam stress (S_{max}) versus (tb/rb), the bottom left plot is maximum beam displacement (U_{max}) versus (tb/rb), and the bottom right plot is critical buckling load (P_{crit}) versus (tb/rb)).....	68
Figure 19: Critical buckling Load of a hollow beam with varying thickness/radius ratio.	69
Figure 20. AFIT MTS with compression plates	73
Figure 21. MTS with Icosahedron frame.....	74
Figure 22. Boundary Conditions and Loading for MTS FE model.	76
Figure 23. First failure mode of icosahedron under MTS loading conditions.	78
Figure 24. Load vs. Displacement for various moduli icosahedron modeled with Abaqus	80
Figure 25. Load vs. Displacement of Abaqus MTS and Experiment	82
Figure 26: Superimposed before and after deformation images. Abaqus images-Left, High speed camera experimental images-Right. (Green color is deformed image)	82
Figure 27: 3D printed Icosahedron hanging with a free-free boundary condition. The red dot indicated where the laser vibrometer was focused and the blue dot indicates where the structure was excited. ...	85
Figure 28: Polytec PSV-500 Laser Vibrometer Frequency Analysis System.....	85
Figure 29: 3D printed icosahedron frequency analysis experimental set-up.	86
Figure 30: FE Icosahedron model for frequency analysis. (Red dot indicates the traced beam for experiment comparison.)	87
Figure 31: Impulse Hammer Input Signal	88
Figure 32: Coherence of Input Signal to Laser Response.....	88
Figure 33: 1 st and 2 nd modes computed from the frequency analysis of the experimental Icosahedron by the Polytec software.....	90
Figure 34: Eigenvalues and Eigenvectors of the first two modes in Abaqus associated with the beam scanned from the laser vibrometer experiment (the red dot indicates the point observed in the model, matching the laser vibrometer).	92

Figure 35: Icosahedron top view (The green dot indicates the top and bottom vertices, the blue dots indicate the top group of five vertices, and the blue dots indicate the bottom group of five vertices).	96
Figure 36: Icosahedron Frame with vertex labels (The green dot indicates the top and bottom vertices, the blue dots indicate the top group of five vertices, and the blue dots indicate the bottom group of five vertices).	96
Figure 37. Boundary Conditions and Loads for the Icosahedron FE model.	101
Figure 38: Icosahedron Frame with Reference Point Loading	102
Figure 39: Icosahedron Vacuum FE model mesh convergence study.	105
Figure 40: Cubic Tech CT155HB UHMWPE material properties [29].	121
Figure 41: (a) Illustration of straightening the CNT fibers then combining them with the polymer matrix and layering them in a composite fashion. (b) Illustration of the stretch-winding process [27].	123
Figure 42: Comparison of the CNT composite (red dots) material properties with other high performance engineering composites. (a) Tensile Strength vs. Young’s Modulus. (b) Specific Strength vs. Specific Modulus [27].	124
Figure 44: Laminate Composites [29].	126
Figure 45: Lighter than Air Membrane Manufacturing thicknesses [30].	127
Figure 46: Half Normal Plot and Pareto Chart of the Effects with respect to Max Frame Stress (pseudo standard error term).	133
Figure 47: Cube Interaction Plot for the Max Frame Stress – Icosahedron.....	138
Figure 48: Example Representation of a 2 ³ Factorial Main Effect and Interactions Contrasts.....	138
Figure 49: Main effects and 2 nd degree interactions effects for Max Frame Stress – Icosahedron.....	139
Figure 50: Least squares regression general equation for the icosahedron model.....	143
Figure 51: Least Squares Regression Fit for the Icosahedron Model Outputs	145
Figure 52: Icosahedron Max Frame Stress Response Surface	147
Figure 53: Icosahedron Max Skin Stress Response Surface.....	148
Figure 54: Icosahedron Final W/B Response Surface	148
Figure 55: Icosahedron Frame SF Response Surface	149
Figure 56: Icosahedron Skin SF Response Surface	150
Figure 57: Icosahedron Contour Plot of Frame and Skin Safety Factor with respect to the input variables or factors.	152
Figure 58: Icosahedron Skin Instance only FEA results for the optimum point.....	153
Figure 59: Icosahedron Frame Instance FEA results for the optimum point	154
Figure 60: Icosahedron Displacement contour and resulting Final W/B.	154
Figure 61: Icosahedron Critical Buckling Pressure at Optimal Design Point.....	157
Figure 62: Icosahedron Contour Plot of Frame and Skin Safety Factor with expanded factor levels.	159
Figure 63: Possible Feasible Icosahedron Structure Dimensions for Frame SF = 1	160
Figure 64: Icosahedral Symmetry.....	164
Figure 65: Full icosahedral symmetry isohedron shapes	164
Figure 66: Hexakis Icosahedron	165
Figure 67. Boundary Conditions and Loads for the Hexakis Icosahedron VLTAV FE model.	170
Figure 68: Hexakis Icosahedron Frame with Reference Point Loading	170
Figure 69: Hexakis Icosahedron Vacuum FE model mesh convergence study.	172
Figure 70: Initial Pareto chart and half normal plot for the frame safety factor of the hexakis icosahedron structure.	178
Figure 71: Cube Interaction Plot for the Max Frame Stress - Hexakis Icosahedron	183
Figure 72: Main effects and 2 nd degree interactions effects for Max Frame Stress - Hexakis Icosahedron	184
Figure 73: Least squares regression general equation for the hexakis icosahedron model.....	187

Figure 74: Least Squares Regression Fit for the Hexakis Icosahedron Model Outputs	189
Figure 75: Hexakis Icosahedron Max Frame Stress Response Surface	191
Figure 76: Hexakis Icosahedron Max Skin Stress Response Surface.....	191
Figure 77: Hexakis Icosahedron Final W/B Response Surface	192
Figure 78: Hexakis Icosahedron Frame SF Response Surface	193
Figure 79: Hexakis Icosahedron Skin SF Response Surface	193
Figure 80: Hexakis Icosahedron Contour Plot of Frame and Skin Safety Factor with high level material properties.	196
Figure 81: Hexakis Icosahedron Contour Plot of Frame and Skin Safety Factor low level material properties.	196
Figure 82: Hexakis Icosahedron Optimal Design Point Skin Stress Contour with SF	197
Figure 83: Hexakis Icosahedron Optimal Design Point Frame Stress Contour with SF	197
Figure 84: Hexakis Icosahedron Optimal Design Point Displacement Contour with Final W/B	198
Figure 85: Hexakis Icosahedron Critical Buckling Pressure at the most Sub-Optimal Point.....	201
Figure 86: Feasible Hexakis Icosahedron Structure Dimensions for High Material Level	203
Figure 87: Feasible Hexakis Icosahedron Structure Dimensions for Low Material Level	204
Figure 87: Manufacturable Hexakis designs with W/B < 1 and low material properties.	205
Figure 88: Half Normal Plot and Pareto Chart of the Effects with respect to Max Skin Stress (pseudo standard error term).	236
Figure 89: Half Normal Plot and Pareto Chart of the Effects with respect to Final W/B (pseudo standard error term).....	236
Figure 90: Cube Interaction Plot for Max Skin Stress – Icosahedron	236
Figure 91: Cube Interaction Plot for Final W/B – Icosahedron.....	236
Figure 92: Main effects and 2 nd degree interactions effects for Max Skin Stress – Icosahedron.....	236
Figure 93: Main effects and 2 nd degree interactions effects for Final W/B – Icosahedron.....	236
Figure 94: Half Normal Plot and Pareto Chart of the Effects with respect to Max Skin Stress (Hexakis). ..	236
Figure 95: Half Normal Plot and Pareto Chart of the Effects with respect to Final W/B (Hexakis).	236
Figure 96: Cube Interaction Plot for Max Skin Stress – Hexakis.....	236
Figure 97: Cube Interaction Plot for Final W/B – Hexakis	236
Figure 98: Main effects and 2 nd degree interactions effects for Max Skin Stress – Hexakis	236
Figure 99: Main effects and 2 nd degree interactions effects for Final W/B – Hexakis	236

LIST OF TABLES

PAGE

Table 1: Material properties for possible materials	23
Table 2: Model Configurations for Rodriguez	23
Table 3: Feasible Models for Rodriguez.	26
Table 4: 2 ² Unreplicated Full Factorial Design Test Matrix and Response.....	45
Table 5: 2 ² Example ANOVA Table with Equations	48
Table 6: MTS 661.19E-03 Force Transducer Error Data [20].....	71
Table 7: VeroBlue Material Property Range.	75
Table 8. Critical buckling load of 3D print icosahedron estimated by buckling analysis for various modulus.	77
Table 9: Estimated Material Strength and Stress at 2mm vertical displacement of VeroBlue FE Models....	80
Table 10: Icosahedron vertex locations.	95
Table 11: Icosahedron Convergence Study Parameters.....	104
Table 12: Icosahedron FEM Independent Variables.	107
Table 13: Icosahedron FEM Independent and Dependent Variable Dimensions.	108
Table 14: Icosahedron Invariants for scaling example	112
Table 15: Icosahedron Scale vs. FE Model Outputs and % Difference.....	112
Table 16: Factors for the DOE created from the Invariants of the Dimensional Analysis	115
Table 17: DOE Experimental Test Matrix.....	117
Table 18: Icosahedron Factors and Levels for a 2 ⁵ Factorial Design	118
Table 19: Icosahedron DOE Observations	119
Table 20: List of Materials for Vacuum Models Development	121
Table 21: Icosahedron DOE Inputs and Results	129
Table 22: 2 ⁵ Full Factorial Terms	131
Table 23: Summary of Icosahedron Initial Significant Effect Terms	134
Table 24: ANOVA Results for Icosahedron Max Frame Stress.....	135
Table 25: Model ANOVA values (SS _T and SS _E values) - Icosahedron	136
Table 26: Summary of Icosahedron Final Significant Effect Terms	137
Table 27: Icosahedron Curvature Analysis.....	141
Table 28: Least Squares Regression Estimates – Icosahedron Model Outputs	144
Table 29: Summary of Regression Fit Information – Icosahedron Model	146
Table 30: Icosahedron Input Parameters for Optimal Point	153
Table 31: Hexakis Icosahedron Vertex Locations	166
Table 32: Hexakis Icosahedron coordinate equations.	167
Table 33: Hexakis Convergence Study Parameters	171
Table 34: Hexakis Icosahedron Scale vs. FE Model Outputs and % Difference.....	174
Table 35: Hexakis Icosahedron Factors.....	175
Table 36: Hexakis Icosahedron DOE Inputs and Results	176
Table 37: Initial Significant Factor Terms for the outputs of the hexakis icosahedron DOE.....	179
Table 38: ANOVA Results for Hexakis Icosahedron Frame Safety Factor	181
Table 39: Model ANOVA values (SS _T and SS _E values) - Hexakis Icosahedron	182
Table 40: Hexakis Icosahedron Significant Terms estimated using standard error	182
Table 41: Hexakis Icosahedron Curvature Analysis.....	186
Table 42: Least Squares Regression Estimates – Hexakis Icosahedron Model Outputs	188
Table 43: Summary of Regression Fit Information – Hexakis Icosahedron Model	190
Table 44: ANOVA Results for Max Skin Stress - Icosahedron	236

Table 45: ANOVA Results for Final W/B - Icosahedron.....	236
Table 46: ANOVA Results for Max Skin Stress - Hexakis.....	236
Table 47: ANOVA Results for Final W/B - Hexakis	236

LIST OF ACRONYMS

LTAV	Lighter than air vehicle
VLTA V	Vacuum lighter than air vehicle
FEA	Finite element analysis
DA	Dimensional analysis
DOE	Design of experiments
RSM	Response surface methodology
LTA	Lighter than air
DLC	Diamond-like carbon
AFIT	Air Force Institute of Technology
FEM	Finite element model
FE	Finite element
CNT	Carbon nanotubes
DA	Dimensional analysis
ANOVA	Analysis of variance
SS	Sum of squares
DOF	Degrees of freedom
PSE	Lenth's pseudo-standard error
SME	Simultaneous margin of error
RSM	Response surface methodology
SF	Safety factor
LVDT	Linear variable differential transformer
VT	Virginia Tech
FRF	Frequency response function
CPU	Computer processing unit
MWNT	Multi-walled nano-tubes
BMI	bismaleimide
BC	Boundary Condition

LIST OF VARIABLES

$\frac{E}{\rho}$	Specific modulus
w/b	Weight to buoyancy
W	Weight
B	Buoyant force
E	Modulus of elasticity
ρ_s	Material density
ρ_a	Sea level air density (kg/m ³)
μ	Poisson's ratio
P_{cr}	Sea level atmospheric pressure (Pa)
h	Altitude
R	radius
F	starting (or previous) load
U	starting (or previous) displacement value
K	stiffness matrix
P^N	preloads
Q^N	load increments
λ	eigenvalues
v_i^M	eigenvectors
L	length
M	mass
t	time
l_n	Dimensionless length indicator
m_n	Dimensionless mass indicator
t_n	Dimensionless time indicator
Π	Buckingham pie invariant
SS	sum of squares
SS _T	total sum of squares
SS _E	sum of squares error
y	response variable
β_i	regression coefficient
K^{MN}	stiffness matrix
c	boundary condition of beam or column
D	wall flexural stiffness per unit width
ν	Poisson's ratio
N_x	axial load
$\frac{t_b}{r_b}$	beam thickness/radius ratio
F_{crit}	critical buckling load
λ_{crit}	lowest eigenvalue from buckling analysis
F_{ref}	magnitude of reference load applied for the buckling analysis
M^{MN}	mass matrix

U^N	displacements or eigenvectors that produce eigenvalues
ω^2	natural frequency
ϕ^N	eigenvector
r_{icos}	radius of a sphere circumscribing the icosahedron
ψ	golden ratio
A_I ,	surface area
V_I	volume
V_f	frame volume
V_s	skin volume
ρ_f	frame density
ρ_s	skin density
$\rho_{air,i}$	internal air density
$\rho_{air,o}$	external air density
V_i	initial internal volume
IQ	Isoperimetric quotient

CONCEPTUAL DESIGN, STRUCTURAL ANALYSIS, AND DESIGN SPACE

EXPLORATION OF A VACUUM LIGHTER THAN AIR VEHICLE

I. Introduction

To date, lighter than air vehicles (LTAV) achieve “lift” through the use of lighter than air gases. These gases produce the buoyant force necessary to float or lift the vehicles in air, where the force is equal to the weight of the fluid displaced by the volume. If the mass of the displaced fluid is greater than the mass of the volume, the volume will float or be positively buoyant. If the displaced mass is less than the volume’s mass, the volume will sink or be negatively buoyant. If the masses are equal then the volume will neither float nor sink, or be neutrally buoyant. With this concept in mind, a theoretical alternative to creating buoyancy in a vehicle is a vacuum. A vehicle could theoretically be made positively buoyant with a vacuum instead of a gas as long as the volume is maintained. However, a vacuum presents a unique set of challenges and requirements, namely that the vehicle’s structure would need to be rigid or semi-rigid, so that its volume is maintained, and the structure will need to be stiff enough to resist the compressive loads due to an internal vacuum and be light enough to float. A vacuum lighter than air vehicle (VLTAV) satisfying these requirements can certainly be designed, but can a design constrained by current technology and materials be feasibly manufactured that satisfies these requirements? This research addresses this question in two parts. First, the research combines finite element analysis (FEA), dimensional analysis (DA), design of experiments (DOE), and response surface methodology (RSM) to explore the structural response design space of a vacuum LTAV constrained by modern technology and materials. Second, the bounded design space will be analyzed to

evaluate if any structurally feasible regions exist within the design space. This process will include the analysis of the VLTAV design proposed by Metlen in 2012 [1], and then will be extended to a similar frame and skin design, hexakis icosahedron, developed by the author.

This introduction begins with the motivation for the work as well as a review of previous relevant research, and ends with a list detailing the flow of the research work performed.

Motivation

To date, the only way to achieve lighter than air flight is with a lifting gas. Some of these gases are heated air, hydrogen, and helium. Helium is the primary lifting gas for all LTAVs. However, in the near future it is expected that the cost and availability of helium are going to change considerably. Due to a US law passed in 1996, all of the helium stored in the US National Helium Reserve must all be sold off by 2015 [2]. This gas field is by far the biggest store of helium in the world. It is estimated that the world could run out of helium in 25 to 30 years. This is true because helium is a non-renewable resource. It is estimated that after 2016 the price of helium will increase 20-50 fold. Therefore, the need for a replacement will become necessary in the near future. The one proposed by this research is a vacuum. The lightest internal gas would be nothing, i.e. a vacuum. This concept is not a novel concept, however to date a vacuum “filled” vehicle does not exist.

Since the conception of the idea of a vacuum lighter than air vehicle, proposed by Lana de Terzi in 1663 [3], a vacuum lighter than air vehicle has yet to be manufactured or

heavily investigated. Lana's idea utilized a thin spherical shell consisting of a single material, copper. Lana, certainly had the right idea in choosing a sphere, but with shell buckling having not yet been developed, his design was destined for failure as further explained below. His spherical shell of copper with an internal vacuum would have failed due to shell buckling. Shell buckling occurs in this instance because of the geometric instability of the sphere under circumferential external pressure. The only way a sphere of this type would not fail due to shell buckling would be if the material chosen had a specific modulus, $\frac{E}{\rho}$, of approximately 4.9×10^8 , which did not exist in 1663 [4]. Now if we fast forward 353 years to today, the material with the highest specific stiffness found in literature, a carbon nanotube composite, has a specific stiffness value that is half of what is necessary to create a thin shelled vacuum lighter than air sphere without shell buckling occurring.

The weight-to-buoyancy ratio is a way to state the buoyancy strength of a lighter than air vehicle. A value less than 1 yields a positively buoyant structure, equal to 1 yields neutrally buoyant, and greater than 1 yields negatively buoyant. A sphere is the most ideal geometry because it has the largest volume for the smallest surface area out of any geometric shape, and therefore the best weight-to-buoyancy potential if you ratio the surface area over the volume. The concept will be further discusses and developed in chapter II.

Since a material to create a thin shelled vacuum sphere does not exist presently, we look to other design alternatives to see if this vacuum vehicle is feasible. In 2005, Andrey M. Akhmeteli and Andrey V. Gavrilin [4] developed a patent for a layered shell

vacuum balloon. This design utilized sandwich layering of materials to create a layered sphere to combat the shell buckling limit of de Terzi's design. Within their patent, they theoretically showed that a vacuum vehicle of this design is feasible utilizing modern technology. However, the manufacturing difficulty of a layered balloon has prohibited this vehicle from being manufactured and tested to date. Again, the current state of technology appears to be the limiting factor for a vacuum lighter than air vehicle.

In 2012, a design for a vacuum lighter than air vehicle (VLTAV) was proposed by Metlen that utilized a geodesic frame, an icosahedron, of cylindrical pultruded rods with a membrane skin stretched over the frame [1]. His design is shown in Figure 1 as a split view to show the frame and skin, where the black is empty space. Now, this design appears quite different from those proposed previously which utilize a spherical geometry. The icosahedron shape, which is formed by the skin, does attempt to approximate a sphere where each vertex of the icosahedron lies on a circumscribing sphere. The internal frame with membrane skin design, allows for and in fact encourages the skin to buckle so that it can acquire stiffness and apply the pressure load developed by the vacuum to the internal supporting frame. As long as the skin deflection is minimal and the internal volume loss is insignificant, the "empty" internal volume will produce a buoyant force. This vehicle was structurally analyzed using finite elements in 2012 and 2014 by Metlen and Rodriguez at the Air Force Institute of Technology [1] [5]. When this vehicle was analyzed, the design was fairly constrained to fit a niche category of a small unmanned air vehicle, and the material properties utilized for the analyses were geared to the future and unattainable with any material found presently in the literature [6]- [7]. When Metlen and Rodriguez analyzed the icosahedron structure, they either

chose specific design points to analyze or only allowed some of the model input parameters of the vehicle to vary. The above analysis on the icosahedron VLTAV sets the foundation for the research work to be performed.

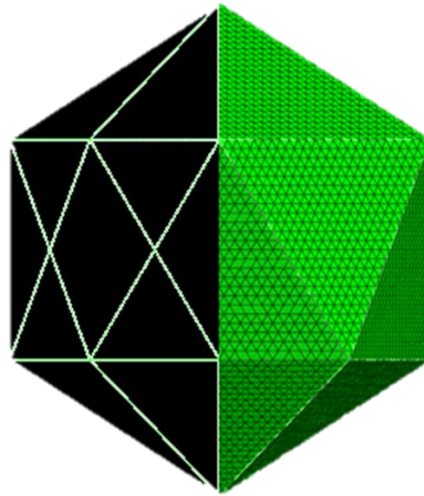


Figure 1: Metlen Icosahedron Design

Now, consider the icosahedron vehicle design or rather any design, they all have what is known as an input and output design spaces. An input design space is a multidimensional space that contains all combinations of the input variables for the design. An output design space is a multidimensional space that contains the observed responses of the design at all combinations of the input variables within the input design space. Theoretically, these spaces are infinite. However, they can be viewed in finite regions where the design parameter are defined within a set of bounds. Looking back at the structural results obtained by Metlen and Rodriguez for the icosahedron design, their results along with their respective input parameters would fill portions of the theoretically infinite structural design space associated with the design. The design space regions

defined by their results, do however, contribute toward the regions that are infeasible to manufacture in the present day because of their materials selection [5] [1].

This is where the research work proposed in the introduction develops significant merit. The research work will state the inputs of a VLTAV design finite element structural analysis into its defining parameters with a dimensional analysis. Then it will apply material and manufacturing constraints where applicable to the defining parameters and conduct a broad scope set of finite element analyses. A design of experiments (DOE) will then be developed as a first order approximation of the structural response design space (RSM) (within the input parameter limits established), and evaluate if feasible regions or points exist. These regions will be the answer to the question of “what makes this design work?” and “where do I start?”

Document Outline

The research presented in this dissertation begins with a literature review of lighter than air vehicles and previous research of vacuum lighter than air vehicles. Next, the methodology for constructing a finite element structural response design space and evaluating it for feasibility is developed. Before the proposed methodology is applied to the Metlen Icosahedron and subsequently the hexakis icosahedron designs, a baseline series of experiments were performed to validate the frame finite element modeling and analysis technique utilized in modeling both case study designs. The validation experiments were conducted on only the icosahedron frame, because the desire was to validate the modeling and analysis technique of a geometric frame composed of cylindrical rods, not necessarily the response of the icosahedron itself. Therefore, the results obtained by the validation experiment of the Metlen icosahedron were extended to

the hexakis icosahedron design. With the modeling technique validated, the proposed structural DSE and analysis methodology was applied to the Metlen Icosahedron and the similar hexakis icosahedron designs.

The process that was taken to conduct the proposed research and accomplish the goals of mapping the feasible design space associated with both vacuum lighter than air vehicle case studies are shown in the following steps:

1. Develop the methodology to create and evaluate a structural response design space of a VLTAV structure to determine if a structurally feasible region or points exist with modern material and manufacturing limitations.
2. Validate the finite element modeling and analysis technique of a geometric frame composed of cylindrical rods by designing and conducting a compression and modal analysis experiment on a 3D printed icosahedron frame.
3. Analyze the Metlen Icosahedron and hexakis icosahedron case study for feasibility, utilizing the proposed methodology.
 - a. Design and create mesh converged finite element models of the icosahedron and hexakis icosahedron frame and skin structures loaded with an internal vacuum.
 - b. Determine the materials to be investigated for the analysis and the manufacturing limits for the proposed frame and skin structures.
 - c. Characterize the inputs of the finite element analysis (FEA) system by utilizing a dimensional analysis or Buckingham Pi to determine how or if the input parameters are related to each other and create non-dimensional pi parameters that are composed of the original inputs to the system. These

π parameters are valuable because they condense the original system of many inputs to a new system of relationships, where these relationships show how the system is driven.

- d. Utilize the non-dimensional quantities acquired from the dimensional analysis to conduct a design of experiments on both case studies to determine which input parameters significantly affect the structural responses of the structures.
 - e. Use the DOE data and the resulting significant terms to create structural response surfaces for each of the case studies, and phrase the stress results into safety factor for feasibility assessment.
4. Observe the structural response surfaces to determine where and if a feasible design region or points with respect to the input parameters and manufacturing constraints exist.
 5. Lastly, perform a general buckling analysis on the frames of the two case studies to indicate whether or not global buckling is a concern for the case studies evaluated within the input limits.

II. Background and Previous Work

This chapter will discuss background information relating to lighter than air vehicles and previous work on designs for vacuum lighter than air vehicles.

Lighter than Air Vehicles

The working force behind all lighter than air vehicles is buoyancy. A buoyant force is an upward force felt on an object that is equal to the weight of the fluid displaced by the object, also known as the Archimedes principle, as shown in Figure 2. This principle is the foundation of lighter than air vehicles. All bodies have a buoyant force except when the body is in a vacuum. These forces range from negative, neutral, and positive buoyancy [8]. Negative buoyancy is created when the weight of the object is greater than the weight of the fluid displaced by the object, causing the object to sink. Neutral buoyancy is where the weight of the object is equal to the weight of the displaced fluid; the vessel will neither rise nor fall. Lastly, positive buoyancy is where the weight of the object is less than the weight of the displaced fluid, causing the object to float. Thus, for any vehicle to be considered a lighter than air vehicle, its weight needs to be less than the weight of the displaced fluid [8]. The buoyancy of a vehicle can be characterized by a ratio known as weight/buoyancy (W/B). Where a W/B less than one results in a floating vehicle, a W/B greater than one results in a sinking vehicle, and a W/B equal to one results a neutrally buoyancy vehicle. The optimal shape for a lighter than air vehicle is a sphere, which has the highest surface area/volume ratio of any shape. The surface area/volume ratio directly correlates to W/B , where surface area can be thought of as the weight (W) and volume can be thought of as the buoyant force (B). Current lighter than air vehicles are designed with a W/B less than one so that they will float, but they will not

increase in altitude forever. As altitude increases the air density decreases which decreases the buoyant force on the vehicle. Eventually, the altitude rise will decrease the buoyancy to equal the weight, and the vehicle will become neutrally buoyant.

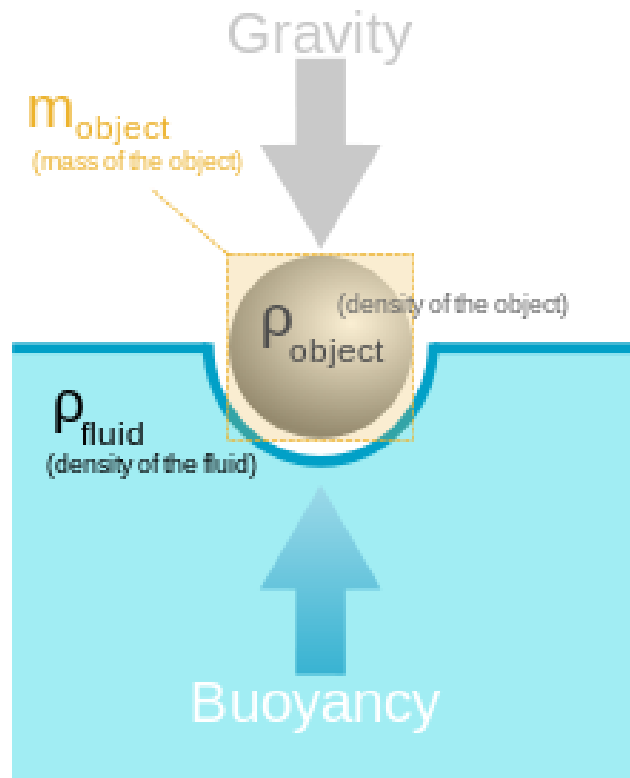


Figure 2: Buoyancy Illustration

Traditional LTA have existed since 1783, where the first flight of the hot air balloon occurred on June 4th by the Montgolfier brothers [9]. Since then, there have been a few modern advancements with LTA vehicles. Lighter than air vehicles are structures that attain positive buoyancy through the use of an internal gas. Historically these internal gases have been helium, heated air, and hydrogen, with helium and heated air being the two currently used today. These LTA vehicles can be broken down into three different categories: non-rigid, rigid, and semi-rigid.

Non-rigid LTAVs are vehicles that utilize a membrane or skin to enclose internal gas and take a non-rigid shape in order to achieve buoyancy. The gases typically used are hot air and helium. A non-rigid structure was the first lighter than air vehicle, specifically a hot air balloon, accomplished by Jacques-Étienne Montgolfier in 1783 [9]. These vehicles were originally utilized for transportation, however, as airships evolved the non-rigid structures became less useful as passenger vehicles and are now commonly used for atmospheric experimentation, advertisements, and decoration. These vehicles can be more resilient over other LTAVs because the internal gas acts as the only structural support, so the skin can fold and not be damaged unlike a rigid airship [10]. These vehicles also tend to be cheaper and easier to manufacture over any other LTAV.

Semi-rigid LTAVs are airships that have an inflated skin that maintains the vehicle's shape and have an internal frame. The internal frame helps to distribute loads throughout the vehicle and it allows for control surface and engine mounting anywhere on the vehicle. With a gas bag to maintain the exterior shape, the internal frame does not have to be as robust and therefore the vehicle has less weight when compared to a rigid airship. The gas bag carries the majority of the aerodynamic loading and allows for the exterior of the airship to be more durable because the gas bag can deflate significantly before failure.

Rigid airships consist of a rigid internal frame with a membrane covering the outside. Inside of the frame are separate bags that contain the lighter than air gas. The exterior membrane keeps the ship enclosed as well as helps distribute the air loads across the frame. The rigid frame has the same benefits as the semi-rigid design however, it allows for more significant payload and higher air load endurance [11]. These vehicles

have the worst weight to buoyancy ratio out of the three LTA categories. This construction allows for the expansion of designs that focus on the body shape to act as a lifting body, therefore, producing a hybrid lift vehicle. Hybrid lift is accomplished by utilizing both aerodynamic lift as well as lift attributed to buoyancy. The aerodynamic lift is produced through the vehicle's body shape. This, in conjunction with varying the buoyancy of the vehicle, transforms a hybrid lift vehicle from a heavier than air vehicle to a lighter than air vehicle. However, these vehicles are subject to increased weight, and poor exterior damage tolerance [11].

Previous Work on Vacuum LTAVs

1670's Spherical Shell

In 1663, Francesco Lana de Terzi proposed an idea for a lighter than air vehicle. This vehicle was composed of four 7.5 m diameter thin foil copper spheres. The concept is shown below in Figure 3. While Francesco's buoyancy calculations were correct for his proposed design, his vehicle would never float. This is because the spheres would have failed, due to collapse, during the evacuation process. It was later proved by Gottfried William Leibniz in 1710 that no material exists to date to construct a vacuum vehicle as de Terzi proposed [3].

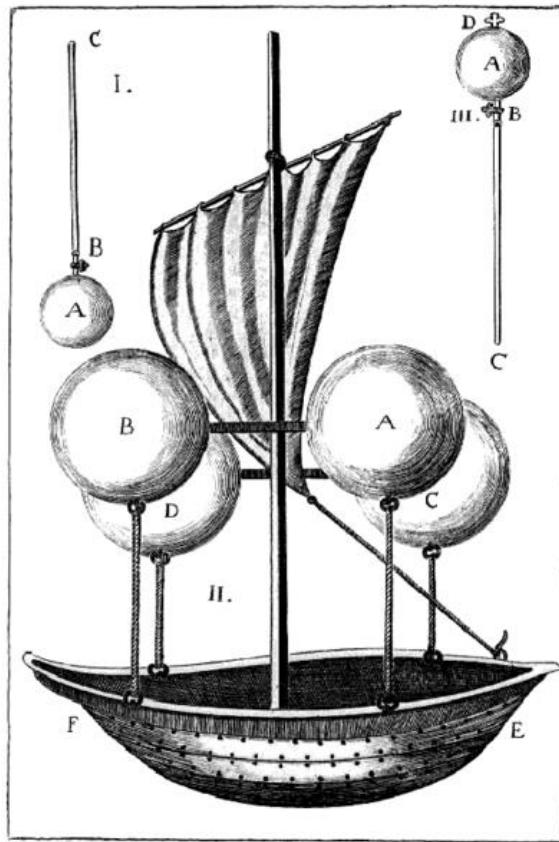


Figure 3: Francesco Lana de Terzi's LTAV concept [3].

Layered Shell Vacuum Balloons

In 2005, Andrey M. Akhmeteli and Andrey V. Gavrilin devised a design for a vacuum lighter than air vehicle. This vehicle is based off the same design as de Terzi in 1663, but with a modern upgrade. Akhmeteli and Gavrilin go as far as to perform a complete analysis of a vacuum sphere composed of a single material, proving that this design still to this day cannot be achieved. The limiting factor for a single material is the collapse of that material due to buckling. Utilizing equation (1), where h is equal to $(\rho_a R)/(3\rho_s)$, a relationship can be formed that determines the material properties that will yield a neutrally buoyant vehicle composed of a single material [4]. This equation is

shown below in equation (2), where E is equal to the modulus of elasticity (the materials resistance to being deformed elastically or linear stiffness) and ρ_s is equal to the materials density. If you let ρ_a be sea level air density (1.225 kg/m^3), μ be the Poisson's ratio (0.3), and P_{cr} be sea level atmospheric pressure ($101,325 \text{ Pa}$), the right side yields approximately $4.5 * 10^5 \text{ kg}^{-1}\text{m}^5\text{s}^{-2}$. In other words, a very stiff and light weight material would be necessary. With this constraint, no material is known to exist to create a vacuum LTAV out of a homogeneous shell.

$$P_{cr} = \frac{2Eh^2}{\sqrt{3(1-\mu^2)}} \frac{1}{R^2} \quad (1)$$

$$\frac{E}{\rho_s^2} = \frac{9P_{cr}\sqrt{3(1-\mu^2)}}{2\rho_a^2} \quad (2)$$

With this known, Akhmeteli and Gavrilin propose to construct a skin or “shell” out of multiple layers in a sandwich configuration. Their structure will be composed of three layers, two thin (top and bottom) layers and a relatively thick cellular core layer. The core's material properties were low density, high compressive strength in the transverse direction, high out-of-plane shear strength, high compressive modulus in the transverse direction, and high out-of-plane shear modulus [4]. An example is a material called Plascore PAMG-XR 1 1.0-3/8-0007-5056. The inner and outer layers' properties are high modulus of elasticity, low density, and high ultimate strength. Some of the materials considered were I220H beryllium, 546-3E boron carbide ceramic, and diamond-like carbon (DLC). The team performed a buckling analysis as well as a critical load analysis on their three-layer shell. With known equations for three layer buckling

and critical load, they were able to propose several possible floating configurations with the materials mentioned above. They also performed a finite element buckling analysis on their sphere to confirm their theoretical results.

Akhmeteli and Gavrilin were able to determine, in general for their vehicle, if the mass of the core was equal to the mass of the top and bottom sheet layers, they would have a floating vehicle at any desired altitude. They next were able to develop a set of optimization constraints that would in turn determine the critical design region for specific materials that satisfy buckling as well as positive buoyancy. These equations and criteria are stated below where E_1 and E_2 are the inner and outer shell material moduli, respectively. h_1 , h_2 , and h_3 are the thicknesses of each layer with h_1 and h_2 being the inner and outer shell thicknesses and h_3 being the core thickness. E_c is the core modulus, μ_1 and μ_2 are the Poisson's ratio of the inner and outer shells, and R is the radius of the sphere. The entire development of these criteria equations can be found in Akhmeteli and Gavrilin's patent application. They developed the following criteria based off their observed results from the evaluation of many layer and material vehicle configurations [4].

1. "Compressive strength values in the transverse direction of at least the same order of magnitude as the atmospheric pressure"
2. "Out-of-plane shear strength values of at least the same order of magnitude as the atmospheric pressure."
3. "The value for the expressions $2E_1 \frac{h_1 h_3}{R^2}$ and $2E_2 \frac{h_2 h_3}{R^2}$ must be of the same order of magnitude as the atmospheric pressure."

4. “The value for the expressions $\left[16E_c^2 \frac{E_1}{1-\mu_1^2}\right]^{1/3} \frac{h_1}{R}$ and $\left[16E_c^2 \frac{E_2}{1-\mu_2^2}\right]^{1/3} \frac{h_2}{R}$

must likewise be at least of the same order of magnitude as the atmospheric pressure.”

5. $4\pi R^2(h_1\rho_1 + h_2\rho_2 + h_3\rho_c) < \frac{4}{3}\pi R^3\rho_a$

The last equation deals with the buoyancy constraint, where the left side must be less than the right side for positive buoyancy. The first four constraints fight against the last constraint to define a narrow range of critical values that allow for a floating vehicle. An example, where beryllium face sheets and an aluminum honeycomb core are being considered is shown in Figure 4 where the z axis is safety factor, the x axis, h_1 , is weight/buoyancy, and the y axis, h_3 , is the thickness of the core [4].

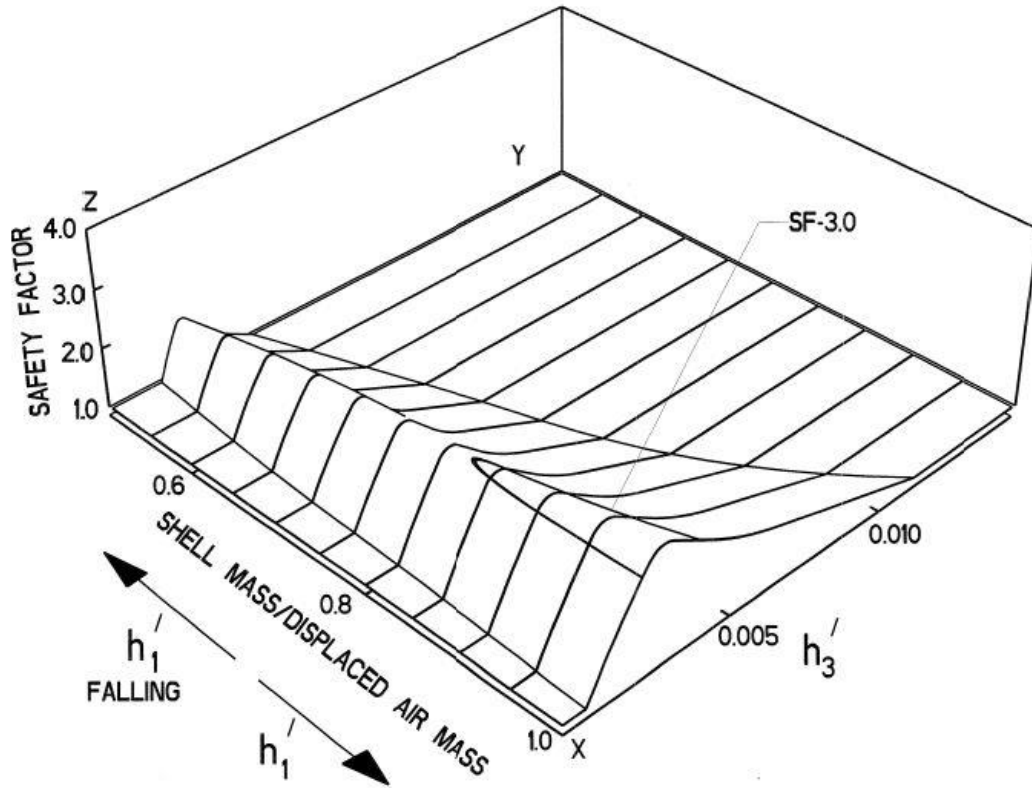


Figure 4: Optimization contours for beryllium face sheets and an aluminum honeycomb core [4].

Figure 4 demonstrates for a safety factor of one, there are a wide range of core thicknesses and weight/buoyancies that would lead to a viable floating vehicle. As the safety factor increases, the solution range gets significantly smaller with a maximum weight/buoyancy of approximately 0.82. These results show, quite convincingly, that a vehicle composed of layered spherical shells could certainly work if the manufacturing challenges associated with the design could be overcome. To date, this research work continues at Florida State University and the vehicle has yet to be constructed [4].

Icosahedron Vacuum Lighter than Air Vehicle

In 2012, at the Air Force Institute of Technology (AFIT), Trent Metlen developed the idea of a vacuum lighter than air vehicle utilizing a geometric frame and membrane skin. The design that Metlen considered was a geodesic stiffened sphere. Metlen analyzed geodesic spheres ranging from a frequency of one, an icosahedron, to ten in order to determine trends in weight to buoyancy.

To define frequency, we have to define what an icosahedron is first. An icosahedron is a 20 sided polyhedron, with 12 vertices where each vertex lies on circumscribing sphere. Frequency denotes the number of times the beams of the icosahedron are divided, where at the points of divisions, new vertices, are created and those vertices are then placed on the original circumscribing sphere. As the frequency number increases, the new geodesic frame grows in a similar way to the sphere its vertices lie on. This is shown in Figure 5, where the top frame (all red) is an icosahedron and the subsequent frames are incremented frequency divisions of the original icosahedron. To clarify, in Figure 5, the higher frequency frames appear larger than the original icosahedron. Figure 5 is presented this way to visualize the increased number of vertices and beams making up the higher frequency structures.

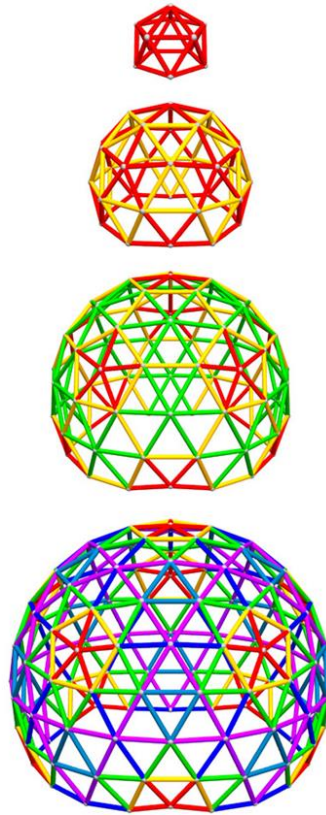


Figure 5: Increasing Geodesic Frequencies starting with 1, an icosahedron

Metlen wrote a finite element analysis (FEA) code in Matlab that analyzed geodesic frames, of frequency one through ten, for material failure and buckling. The frame, making up the geodesic configuration, was a series of hollow cylindrical tubes joined at each vertex of the geodesic. An illustration of an icosahedron built in this manner is shown in Figure 6. Metlen was able to optimize each frequency for W/B with failure mode constraints. Metlen determined that the simplest and best configuration was an icosahedron, or a geodesic sphere of frequency one. The icosahedron proved to be the best, because of its symmetric nature in that all of the triangle leg lengths are identical. This proves to be valuable because, as the geodesic frequency increases, some of the legs of the triangle experience more stress due to the dissimilar leg lengths amongst the higher frequency frames. A frequency of one also results in the lowest amount of surface area

and weight in the frame itself. The optimal design for the frame proposed by Metlen used a UHM carbon epoxy frame, which yielded a W/B of 0.57. It is noted that this is for the frame only, and it does not include any skin that would enclose the frame to contain the internal vacuum [1].

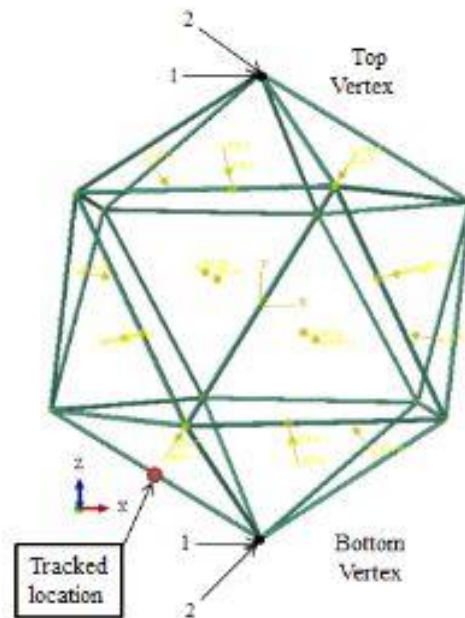


Figure 6: Icosahedron Frame

For the skin, Metlen considered using Zylon fibers as the material. In reality, the fibers would need to be integrated into a laminate so that a skin could be manufactured. When this occurs, the material properties of the laminate will be less than that of the Zylon fibers alone. He performed a FEA on a membrane segment, considering a single triangular face, to estimate the stresses and displacements in the skin face segment. The approximated skin stress and Zylon's material yield strength were then used to optimize the skin thickness, such that the stress in the skin did not exceed the materials yield strength. The thickness of the skin was computed to be 0.0259 mm thick, and the W/B of

the skin alone was 0.37. This results in a total W/B of 0.94. Metlen's proposed geodesic sphere just barely achieves theoretical floating with a W/B less than one [1].

Continuing with Metlen's icosahedron development, Ruben Rodriguez in 2012-2014 [5] at AFIT constructed a, icosahedron frame with covering skin within a finite element model. Rodriguez's focus was modeling the skin's interaction with the frame. The full icosahedron model developed by Rodriguez is shown in Figure 7. In order to model the icosahedron and its skin, the dimensions of the frame (structure radius, beam radius, beam thickness, and skin thickness) needed to be determined. The approach taken by Rodriguez to determine the dimensions of the skin and the beams of the icosahedron, was to select a W/B value for the vehicle with a specified set of material properties and compute the skin thickness, beam radius, and beam thickness that satisfy the selected W/B. The author completed a full stress analyses for a wide range of materials and W/B with an icosahedron frame and covering skin [5]. The materials and their material properties that Rodriguez considered to model the frame and skin with are shown in Table 1. Table 2 then shows seven model configurations with the materials for the frame and skin indicated as well as the W/B, dimensions, and total number of finite elements for the skin and frame respectively. The total W/B for each configuration is determined by adding the W/B for the frame and skin together.

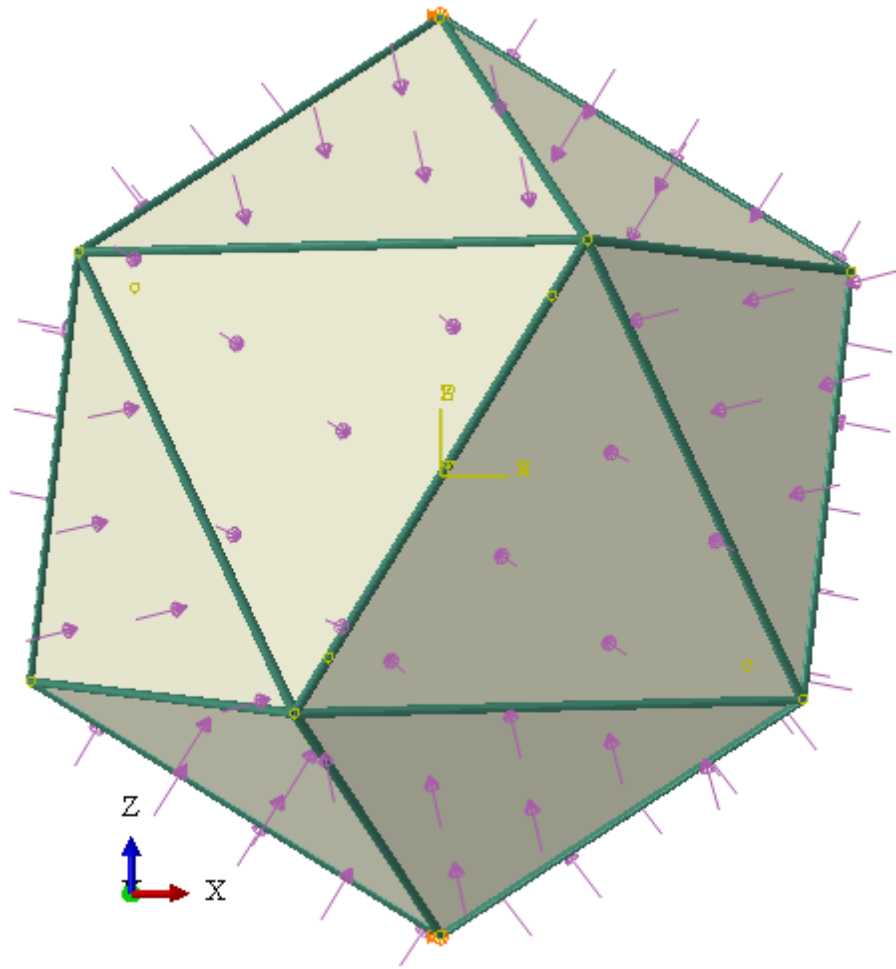


Figure 7: Full skin-frame icosahedral model

Table 1: Material properties for possible materials

Table 1: Material Selection

#	Name	ρ (kg/m ³)	ν	E (GPa)	S_y (GPa)	S_u (GPa)	$E(\text{Pa})^{1/2}/\rho$	$S_y(\text{Pa})^{2/3}/\rho$	$S_u(\text{Pa})^{2/3}/\rho$
1	UHM Unidirectional Carbon Epoxy tubes	1870	0.3	440.00	-	3.73	355	-	1286
2	Zylon	1560	0.37	303.00	5.80	-	352	2069	-
3	Diamond like Carbon, or Diamond thin film [43]	2700	0.12	757.00	75.70	-	322	6627	-
4	Boron Monofilament	2570	0.33	400.00	-	3.60	246	-	914
5	Nanocyl NC7000 Thin Multi-Wall CNT [56]	1650	0.2	1000.00	10.00	30.00	606	2813	5851
6	Beryllium S-200, Tubing	1844	0.18	303.00	0.40	0.8	299	294	467
7	CoorsTek Boron Carbide Reaction-Bonded	2650	0.18	379.00	1.70	-	232	538	-
8	Duramold-2 Cast Aluminum Mold Plate	2800	0.33	738.00	0.14	-	307	96	-
9	BALTEK SB.150 Structural End-Grain Balsa	247	0.33	5.76	0.02	-	307	337	-
10	Honeywell Spectra 1000 Fiber	970	0.33	172.00	-	3.00	428	-	2144

ρ = density, ν = Poison's ratio, E = modulus of elasticity, S_y = yield strength, S_u = ultimate strength

Table 2: Model Configurations for Rodriguez

<i>Model</i>	Material		Desired W/B					<i># Ele.</i>
	<i>Frame</i>	<i>Skin</i>	<i>Frame</i>	<i>Skin</i>	r_{beam}	t_{skin}		
1	6 (Beryllium)	6 (Beryllium)	0.5	0.4	1.41E-03	1.05E-05	7020	
2	10 (Spectra)	10 (Spectra)	0.5	0.4	1.95E-03	2.00E-05	8600	
3	5 (CNT)	5 (CNT)	0.5	0.4	1.49E-03	1.18E-05	7020	
4	6 (Beryllium)	5 (CNT)	0.5	0.4	1.41E-03	1.18E-05	7020	
5	10 (Spectra)	5 (CNT)	0.5	0.4	1.95E-03	1.18E-05	8600	
6	10 (Spectra)	10 (Spectra)	0.4	0.4	1.74E-03	2.00E-05	7020	
7	5 (CNT)	5 (CNT)	0.4	0.4	1.33E-03	1.18E-05	8600	

Rodriguez utilized his finite element model (FEM) to analyze five different material configurations with a W/B of 0.9 and two configurations with a W/B of 0.8 as

shown in Table 2. A configuration was determined valid, if the maximum frame and skin stress in the configuration predicted by the FEM, was less than the material yield strength of the frame and skin materials in the configuration respectively. The comparison of max predicted stress and the material yield strength is known as the material safety factor. The safety factor is equal to material yield strength/max predicted stress. If the safety factor ratio is greater than or equal to 1, then the material is predicted to not fail. If the safety factor ratio is less than 1, then the material is predicted to fail. The results from his tests indicated that the only configurations that did not fail due to material failure were configurations 3 and 7 with finite element (FE) stress singularities in the skin removed. A singularity in FEA occurs when a corner is modeled with a single point. This occurs in Rodriguez's model, because he models the beams as 2D wires instead of 3D hollow rods. The intersection of the beams are modeled with a single points because the beams are modeled as 2D wires. This is shown in Figure 8, where the skin folds over the 2D wire beams, making a crease and creating the sharp corners on the skin at the vertices. The sharp corners in the frame create a large stress concentration to occur in the skin because the skin only has a single point to interact or contact the frame. This drives the stress solution at the corners to not converge and create stress singularities resulting in overly large stress values. If the singularities are removed, the maximum stress is greatly reduced in the skin and the safety factors for the frame and skin of configurations 3 and 7 are 1.47 and 1.16 and 1.94 and 1.72, respectively [5]. A summary of these two designs, detailing the model dimensions, material properties, frame and skin stress values, and

displacement values, is shown in Table 3. It should be pointed out that the singularities are by-products of the elastic constitutive relationships.

In summary, an icosahedron frame and skin constructed completely of carbon nanotubes (CNT) (configuration 3 and 7) is shown to have W/B less than one frame and skin safety factors greater than one with an internal vacuum. The cause of failure in all of the other models was material failure or frame and skin safety factors less than one. The maximum stress in the skin for all models could be significantly reduced if the stress singularities were removed [5].

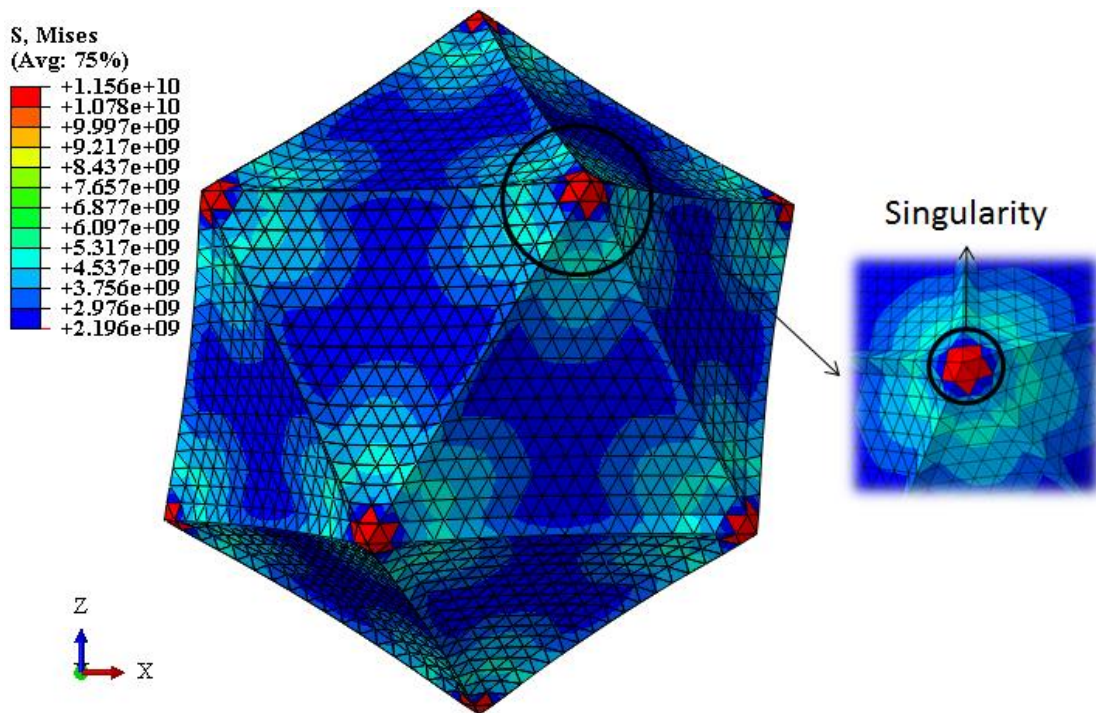


Figure 8: Singularities in the skin due to tie constraints.

Table 3: Feasible Models for Rodriguez.

Model:	3	7
r_{beam} (mm)	1.49	1.33
t_{skin} (mm)	0.0118	0.0118
W/B	0.91	0.81
Maximum Altitude - with Ultra High Vacuum (m : ft)	512 : 1680	676 : 2219
<i>Material Properties</i>		
Density (kg/m^3)	1650	1650
Poisson's ratio	0.2	0.2
Modulus of Elasticity (GPa)	1000	1000
<i>Frame</i>		
Maximum Displacement (mm)	3.05	3.97
Maximum von Mises Stress (Pa)	6.79E+09	8.64E+09
Safety Factor	1.47	1.16
<i>Skin</i>		
Maximum Displacement (mm)	8.64	9.53
Maximum von Mises Stress (Pa)	9.62E+09	1.33E+10
Safety Factor (w.r.t the yielding point)	1.04	0.75
Maximum von Mises Stress - No Singularities (Pa)	5.15E+09	5.83E+09
Safety Factor - No Singularities (w.r.t the yielding point)	1.94	1.72

Chapter II Summary

The objective of this chapter was to outline the background information detailing general LTAV and previous work detailing VLTAV designs. The previous work shows that very little work has been performed on the investigation of a modern day vacuum lighter than air vehicle. In reviewing the three structure concepts that have been investigated to date: a thin shelled sphere, a sandwich sphere, and a geodesic oriented frame with a membrane skin, the limiting factor for all of the proposed designs are manufacturing limitations and non-existent materials.

III. Structural Design Space Exploration and Feasibility Analysis Methodology

This chapter develops the general methodology that will be used to conduct the structural feasibility analysis of the Metlen icosahedron and the hexakis icosahedron

VLTA V structure. This chapter details two main sections. The first section details the tools and techniques utilized to develop the structural response design space for exploration. The second section focuses on utilizing the created structural design space to determine if and where feasible regions or points exist within the input boundaries. A structural response design space or any design space for that matter can be thought of as a multi-dimensional space or region with dimensions of the independent variables defining the region of the space. The points that define the space are the dependent variables, or in this case the FE stress and displacement solutions with respect to the independent variables (FE model geometry, material properties, loadings, and boundary conditions). The process to construct the design space will be to first define what the independent and dependent variables are and how they relate to each other for the FE model. This will be performed utilizing a technique known as dimensional analysis. Let it be noted, that the strategy described subsequently to construct a design space, a dimensional analysis is not an integral step. It was the decision of the author to perform this analysis to gain the benefits of performing a dimensional analysis. Specifically, the ability to reduce the number of independent variables defining the FEMs so that the number of individual FEA's required by the DOE to be performed is minimized. Dimensional analysis is used to analyze the dimensions that make up the independent and dependent variables that define a system, in this case the FEM is the system. The dimensions of the variables are used to deduce any possible relationship between the independent variables themselves and the dependent variables. These relationships simplify the original complex set of independent and dependent variables with relationships. This is explained in further detail in the following Dimensional Analysis section. With the independent (FE model

geometry, material properties, loadings, and boundary conditions) and dependent (FE stress and displacement) variables characterizing the FE system, the structural response design space for the system can be constructed. Now, a design space for any design or system is theoretically infinite. This is because the independent variables defining the system could take on an infinite number of values and combinations. Thus an infinite number of solutions or dependent variables are produced. To remedy this, the independent variables need to be bounded. Once the independent variables are bounded, the design space becomes finite. The next objective is to populate the design space. However, even with the independent variables bounded there are now an infinite number of combinations of the independent variables within the bounds to be evaluated to populate the entire bounded design space. To avoid performing an infinite number of experiments or FEA to populate the structural response design space a technique known as design of experiments (DOE) is utilized to perform a systematic number of experiments to give a representation of the infinite number of solutions within the bounded structural response design space. The results from the systematic number of experiments can then be used to construct what is known as response surfaces which approximate the design space based on the response data gathered from the experiments conducted. Once constructed, the structural response design spaces for the FE stress and displacements of the models can be observed for feasibility.

Structural Design Space Creation

The structural design space creation will occur in four steps, each building off of the results from the previous step. The first step will be to define and construct the vacuum LTAV FEMs to be analyzed for stresses and displacements to determine

feasibility. The second step will be to phrase the FEM systems in terms of their independent and dependent variables so that a dimensional analysis can be performed on system to simplify the original set of variables into relationships of each other. With the system simplified by the dimensional analysis, the third step will bound and use the relationships produced by the dimensional analysis to conduct a design of experiments to map the structural responses of the FEM experiments with an internal vacuum. The last step will be to take the structural response data obtained by the DOE to construct response surfaces that approximate the bounded design space.

Step 1: Finite Element Modeling and Analysis

To approximate the stress and displacement values to be evaluated for feasibility, a FEM needs to be created and analyzed. To create a FEM for analysis, the structure's geometry, material properties, boundary conditions, loading conditions, element definitions, and mesh discretization all need to be provided. The two case studies to be analyzed are both frame and skin structures. Both case studies will share the same material properties, boundary conditions, loading conditions, and element definitions due to their likeness in design. The only difference between the two VLTAV case studies is their structure's geometry, and therefore their mesh discretization will be different as well. The structure geometries, material properties, boundary conditions, loading conditions, and mesh discretization for each FEM will be detailed in their respective case studies developed in chapters V and VI.

Once the model is developed, a solver needs to be chosen to compute the estimated stresses and displacements of the modeled structure for feasibility. The feasibility of the models will be assessed in terms of material and geometric instability.

The material feasibility will be determined in the same way as Rodriguez had for his models in chapter II, by computing a frame and skin safety factor. The geometric instability will be assessed by analyzing the frame's critical buckling pressure. The material instability will be analyzed using the non-linear solver in Abaqus, and the geometric instability will be analyzed using the linear buckling solver. The following sub-sections will discuss the beam and membrane elements used to develop the FEMs, and the solvers used to estimate the structural responses of the models related to material and geometric instability.

Beam and Membrane Elements

The finite element analyses performed in chapters V, and VI, use membrane and beams elements to model the VLTAV structures. The beam elements are used to model the frame structure. The membrane elements are used to model the membrane skin. Beam elements were chosen because they approximate the behavior of structural components that undergo both axial and transverse loads. The important factor to note is when selecting which type of beam element to use. Abaqus offers two main types of beams, those being Euler-Bernoulli and Timoshenko beams. Both beams can be used to model slender beams in 2D or 3D space. The benefits to using a beam element instead of pure three-dimensional elements is that they are geometrically easier to model, and they require a significantly smaller amount of computing time to solve. Beam elements can be used to resemble beams with solid, thin-walled closed, and thin-walled open cross sections. This approximation relies on the assumption that the deformation of the beam along the beam's axis only is sufficient to estimate the displacements of a comparable three-dimensional beam. The main difference between Euler-Bernoulli and Timoshenko

beam theories is that in the Euler-Bernoulli beam, the plane sections initially normal to the beam's axis remain normal to the beam axis. The transverse shear deformation is not allowed. The Timoshenko beam allows for rotation between the cross section and the bending line, which yields the transverse shear deformation [12].

Membrane elements are used to represent thin surfaces that transmit in-plane forces only, no moments, and have no bending stiffness. These elements are considered surface elements and can be used for planar and curved surfaces in three dimensions. An example of where to use a membrane element would be for the skin that makes up a latex balloon. One issue to consider when dealing with membrane elements is that initially flat and stress free membranes have no stiffness. This lack of stiffness when out-of-plane loading is applied, such as a pressure load, causes numerical singularities and convergence complications. Two options are available to mitigate this problem. These are to pre-stress the membrane before the analysis is conducted such that the membrane has an initial stiffness or to use a feature called adaptive stabilization within Abaqus. The stabilization technique adds viscous forces to the model to overcome local instabilities such as an out-of-plane loaded membrane with no initial stiffness. The adaptive portion of the stabilization technique varies the damping factor of the added viscous forces to minimize the effect of the forces in order to achieve a converged solution. Once the membrane has developed some out-of-plane deformation with the assistance of the stabilization, the membrane acquires some stiffness which is then used to resist the out-of-plane loading instead of the added viscous forces for the remainder of the analysis [12].

Finite Element Nonlinear Solver

The non-linear solver was used to compute the stresses and displacements of the vacuum FEMs because of the non-linear displacements expected in the membrane skin. Typically, when studying the behavior of a body under load, linear analysis tools are used. When considering small displacements and solid structures, these linear modeling tools provide an acceptable approximation to the real model. The nonlinear analysis is needed for the vacuum FEMs because the membrane undergoes large displacement compared to its thickness. In addition, the pressure loading must be applied normal to the membrane displacement. This is referred to as a follower force. These tools require iterative numerical techniques to solve load and displacement equilibrium equations to capture the actual structural behavior. A structure's nonlinear behavior can arise from geometric and material nonlinearities. The geometric nonlinearities come from large displacements within the structure, where the structures stiffness changes due to deformation. The nonlinear solver used for the finite element analysis in this research is the Newton Raphson Technique, which is an iterative technique that solves the nonlinear static equilibrium equations at small steps. The technique increments the load and determines the residual between the load and solution path, and this residual is used to update the displacement associated with the load. This process is incremented until the residual becomes small and converges where the equilibrium equations are satisfied. A brief description of the theory for a one-dimensional case is given below.

As stated above the technique begins by selecting a load increment $R_{t+\Delta t}$, followed by determining the initial slope $K_t = \frac{\partial F_t}{\partial U_t}$ where F is the starting or previous load value and U is the starting or previous displacement value. A displacement step is then

chosen, $U_{t+\Delta t} = U_t + U$ and the residual is solved for by using equation (3). From here, a new displacement is determined using equation (4) and the iterative process continues until $R_{t+\Delta t} - F_{t+\Delta t}^{(i-1)}$ becomes sufficiently small and that iteration is determined converged. This process is continued until the final load value is reached. An illustration of this technique for one iteration is shown in Figure 9.

$$K_{t+\Delta t}^{(i-1)} \Delta U^i = R_{t+\Delta t} - F_{t+\Delta t}^{(i-1)} \quad (3)$$

$$U_{t+\Delta t}^i = U_{t+\Delta t}^{(i-1)} + \Delta U^i \quad (4)$$

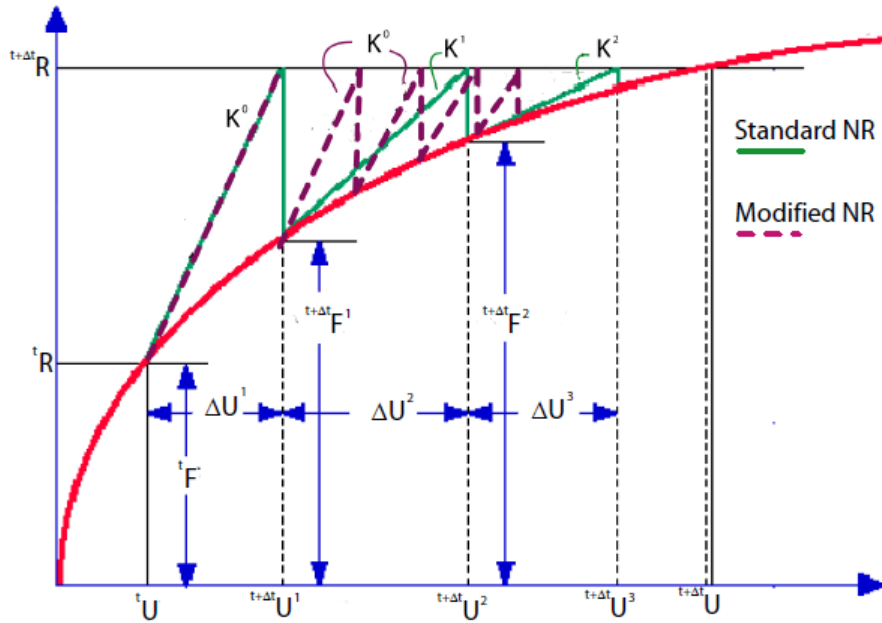


Figure 9: Newton Raphson technique for a single iteration

Finite Element Linear Buckling Solver

The finite element linear solver was used to estimate the case study frames' critical buckling load through an eigenvalue/eigenvector analysis. The eigenvalue buckling problem within Abaqus applies incremented load magnitudes in the direction prescribed by the user until the model stiffness matrix becomes singular. The load values that cause the stiffness matrix to become singular are estimated critical buckling loads for the structure. The eigenvalue problem is shown in equation (5).

$$(K_0^{NM} + \lambda_i K_{\Delta}^{NM})v_i^M = 0 \quad (5)$$

Where K_0^{NM} is the initial stiffness matrix with any preloads, P^N , included. K_{Δ}^{NM} is the differential stress matrix from the initial matrix due to the incremental loading pattern, Q^N . λ_i and v_i^M are the eigenvalues and the eigenvectors that correspond to the stiffness matrix singularities with respect to the load increments Q^N . The M and N indicate the degrees of freedom for the entire model and i indicates the i^{th} buckling mode. Where the first buckling mode is the only mode and eigenvalue of interest, because if the frame will buckle it will happen at the first mode and eigenvalue first. The critical buckling loads are denoted by equation 6 where P^N is the preload pattern and Q^N is the applied load pattern on the structure [12].

$$P_{crit,i} = P^N + \lambda_i Q^N \quad (6)$$

Step 2: Dimensional Analysis

Dimensional analysis (DA) is a method of analyzing a system in terms of the dimensions of its independent and dependent variables. Where, independent and

dependent variables are the input and outputs of a system, respectively. Bridgman in 1969 states, “The principal use of dimensional analysis is to deduce from a study of the dimensions of the variables in any physical system certain limitations on the form of any possible relationship between those variables. The method is of great generality and mathematical simplicity”. By doing this, the number of independent variables that define the dependent variables are reduced. Dimensional analysis is rooted in the concept of similarity. Mathematical similarity is where the independent and dependent variables can be transformed such that the number of independent variables are reduced. The transformation creates relationships (ratios) known as invariants that are non-dimensional. If two different models have the same invariants and the invariants are equal, then there exists equivalence between the two models even though they are different. For example, if the variables defining the forces acting on a small scale wind tunnel aircraft model, and a full scale aircraft are identical, then relationships between the variables and the forces can be created (invariants). Under special circumstances these relationships can be equal, and if so a direct relationship between their forces can be formed. This idea is known as scale-invariance.

The ultimate purpose of the dimensional analysis to be performed on the FEMs, is to provide valuable relationships between the independent and dependent variables that define the system and to reduce the complexity of the model. Since the intent is to conduct a design of experiments (DOE) on the FEMs, the number of independent variables should be minimized if possible. Minimization of the independent variables is ideal in this case because the number of independent variables has a direct effect on the number of experiments required for a DOE. For example, if a two level full factorial

design were chosen for the DOE, the number of minimum experiments required is 2^k , where k is the number of independent variables. If there were originally four independent variables defining a system, the minimum number of experiments required to perform the DOE would be 2^4 or 16. Now, if the number of independent variables were reduced to one by performing a DA, the new DOE would be a 2^1 or 2 experiments which results in a reduction of 93.75% experiments. Due to the transformation performed by the DA, the original four variables can be represented by one variable. The 2 experiments with the one variable yield the same amount of information about the dependent variable as the 16 experiments varying all four of the original independent variables.

The dimensional analysis technique that will be detailed for this research is Buckingham's Pi theorem. This theorem can be thought to have four steps as indicated in [13].

The first step is to define the complete set of independent quantities $x_2 \dots x_k$ that define the dependent variable x_1 .

$$x_1 = f(x_2, x_3, \dots, x_k) \quad (7)$$

The set $x_2 \dots x_k$ is considered complete only if no other variable can affect the dependent variable x_1 . Additionally, the independent set is only considered independent if changing the value of any variable in the set has no effect on any of the other variables in the set. It is important to make sure the set of independent variables is correct with respect to the dependent variable because once $x_2 \dots x_k$ are specified, the equality in equation (7) is maintained regardless of the base units used to measure the x quantities.

The second step is to define the dimensions that make up the dependent and independent variables x_1 and $(x_2 \dots x_k)$. This process can be performed by inspection of the variables themselves. If the variables are part of a mechanical system, for instance where all of the variables are made up of mass, length, and time then $[x_k]$ quantities are represented by equation (8). It is noted that if an independent variable is dimensionless, its dimensions are denoted by $[x_k] = [1]$ and that variable is inherently already a Π parameter.

$$[x_k] = L^{l_k} M^{m_k} t^{\tau_k} \quad (8)$$

In equation (8), the exponents l_k, m_k, τ_k are dimensionless numbers that indicate the units for each quantity. For example, if x_2 were modulus of elasticity, having units $\frac{M}{LT^2}$, it can be written using equation (8) as $[x_2] = L^{-1} M^1 t^{-2}$. Now, let's call a variable r the number of the basic units needed to characterize the independent and dependent variables. In this case $r=3$ for length (L), mass (M) and time (t). The number of Π parameters that will be created is $(k-r)$.

The third step is to pick r independent variables within $(x_2 \dots x_k)$ that will be used to generate the Π parameters. These variables can be thought of as a dimensionally independent subset of the independent variables. The selection of these variables is somewhat arbitrary, but there are some "rules": Each dimension should be represented by the subset chosen, variables with the same dimension or exponent of that dimension should never be chosen (i.e. length and area), the dependent variable should never be chosen, and the dimensions of each one cannot be created by combining the dimensions

of the others. The main thing to note is that the variables selected could appear in each Π parameter and therefore define them. For this example where r is equal to three, three independent variables out of the independent variables need to be chosen. Let's suppose that the subset chosen is x_2, x_3, x_4 .

The fourth step is to now compute the Π_i parameters using the subset chosen above and the remaining dependent and independent variables. As stated above, there will be $(k-r)$ Π parameters. The procedure for computing the Π_i parameters is as follows, and will be conducted $(k-r)$ times:

First select one of the independent or dependent variables that are not within the subset chosen (x_2, x_3, x_4) . This will be called x_j , where typically it begins with $j=1$ continuing to k ignoring the x_n 's that are part of the independent subset, in this case x_2, x_3 , and, x_4 .

$$\Pi_i = x_j x_2^a x_3^b x_4^c \quad (9)$$

Where a, b , and c are dimensionless coefficients and x_2, x_3 , and x_4 are the dimensionally independent subset. Now, recalling equation (8), taking into account each x 's dimensions, and assuming that Π_i is dimensionless, we can write equation (9) as:

$$L^0 M^0 t^0 = L^j M^m t^{\tau_j} (L^{l_2} M^{m_2} t^{\tau_2})^a (L^{l_3} M^{m_3} t^{\tau_3})^b (L^{l_4} M^{m_4} t^{\tau_4})^c \quad (10)$$

Now, we write the following r equations (in this case 3) to solve for a, b , and c . (Note, the left side must be set equal to zero)

$$\begin{aligned}
0 &= l_j + al_2 + bl_3 + cl_4 \\
0 &= m_j + am_2 + bm_3 + cm_4 \\
0 &= t_j + at_2 + bt_3 + ct_4
\end{aligned}
\tag{11}$$

With a, b, and c solved, the coefficients can be plugged back into equation (9), where now one of the (k-r) Π terms is determined. Once all the Π terms have been solved for, they can be written as a function of the dependent Π term, in this case Π_1 .

$$\Pi_1 = f(\Pi_2, \Pi_3, \dots, \Pi_{k-r})
\tag{12}$$

Once the Π parameters or now invariants are determined, the boundaries for the each invariant needs to be assigned so that each invariant has an upper and lower bound. These boundaries form the limits of the inputs to the DOE, and therefore constrain the structural response design space to be constructed.

Step 3: Design of Experiments

A great way to learn about the operation of a system or process is to observe it. However, it is not as simple as just watching. Every system or process has an input factor or factors that govern a response. In order to understand how the input(s) affect the response, the input(s) need to be changed deliberately. This idea is known as conducting an experiment on the system. When a series of experiments are performed, the response is observed such that we may identify the reasons for its change. The response data obtained can be used to determine which input variables produce the most significant effect on the response with the use of an analysis of variance (ANOVA).

Unreplicated 2^k Factorial Design

The design of experiments “design” that will be utilized for this research is an unreplicated 2^k full factorial design. This factorial design is typically chosen to perform a “screening” analysis on a system when the effects and interactions of the input parameters are generally unknown and a relatively quick analysis is desired. This avoids performing unnecessary and potentially costly experiments to investigate the response.

This is a design with only one observation, or experiment at each test case. These types of designs are used where k is very large or the expense (time and/or money) is significant for a single experiment. This design evaluates each factor at two levels, a high and low value, to quantify the effect of the factor on the response. The k in the 2^k represents the number of factors or independent variables. The number of experiments required to perform the DOE is equal to 2^k , referred to as N . For instance if $k=3$ then the minimum number of experiments required is 2^3 [14].

There are of course risks to running a DOE with no replicates, where a replicate is a repeated experiment. The first risk is that the response captured at a given test point could be unusual and therefore not indicative of the average response of that test case. The next risk is determining the spacing of the factor levels, since there are only two levels at each factor. One needs to make sure that the levels are sufficiently far apart so that the estimated response is outside of potential “noise”. However, there is a chance that the relationship between the low and high case is curved and two points will not be able to represent the curvature, therefore incorrect conclusions could be drawn. This is shown in Figure 10, where the line connecting the L and H points is curved and not linear.

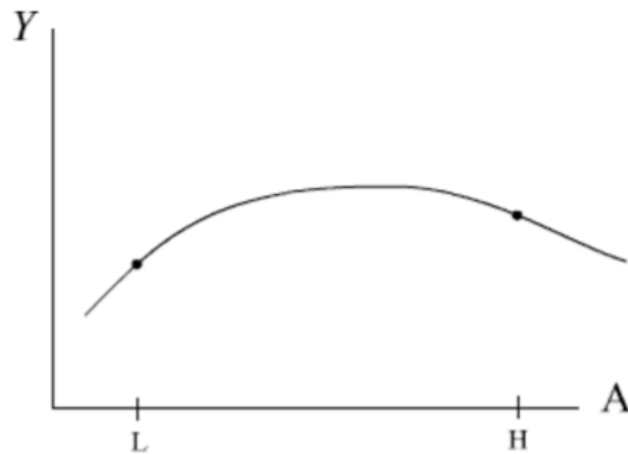


Figure 10: True underlying curved relationship between low and high factor level

The researcher should have some understanding of the factors in order to make good judgements on what the levels should be, in order to avoid misinterpreting the response of the system. In the case for this research the results presented by [1], [5] were used. However, if there is not enough information about the system, a common way to check for curvature is to add a center point to a 2^k full factorial DOE. A center point is a test case where all of the factors are evaluated at a level that is mid-way in-between the high and low level values. The curvature or lack thereof is investigated by comparing the center point test results with the averaged results from all the other test points. If the center point test results are approximately equal to the response averages, it is concluded that there is no curvature and the data obtained is sufficient to create a regression fit for response surface modeling and design space investigation. If the center point results are significantly different, greater or less than, the averaged response(s), it is concluded that curvature is present. If there is curvature, then a new DOE would need to be conducted with a test matrix designed to capture the nonlinearities present in the design space [14].

The next issue, which is described in detail in the ANOVA section, is how to analyze the factor and interaction effects when replicates are typically needed to do so. Without replicates, analyzing the effect strength of all the factors and interactions is impossible. Typically, in order to analyze some of the factors and interactions, higher order interactions are ignored. This is known as the sparsity of effects principle; that is, most systems are dominated by the main effects and low order interactions, and most high order interactions are negligible. This effect has been studied by Li, Sudarsanam, and Frey in 2006 as well as Bergquist, Vanhatalo, and Nordenvaad in 2011. Both of their results largely agree with each other in that about 40% of the experiments studied main effects were significant, 11% two-factor interactions were significant, and higher order interactions were rare making up 5% of the experiments [14].

Structural Analysis Process Flow

A continuous multi-step process was developed to perform the finite element analyses on either the Metlen icosahedron or the hexakis icosahedron structures. The strategy laid out in this section provides the process used in order to collect the structural response data to be used in an ANOVA to characterize the model being analyzed. This process was developed using a combination of Matlab programming, Python scripting, and Abaqus for the finite element evaluation. A flow chart of the process is shown in Figure 11. The input design parameters for the structures are the invariants determined by the dimensional analysis for the respective finite element system.

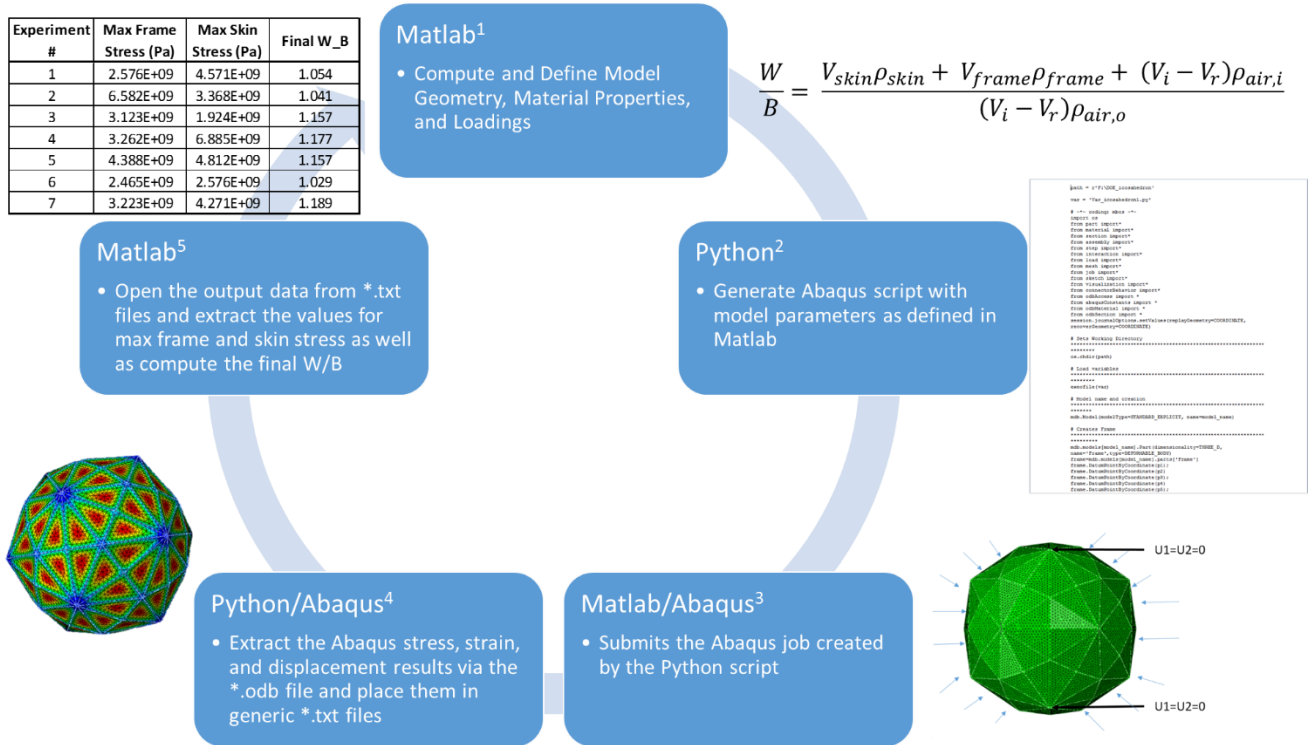


Figure 11: DOE Evaluation Process Diagram

The first step in the evaluation process is that a Matlab routine imports the DOE test matrix and scans in the parameter values for the factors and their levels. The continuous process in Figure 11 starts with the factor levels specified for experiment 1. The Matlab routine would then write in the values for the input parameters or invariants determined by the dimensional analysis. An Abaqus python input script is created, which details how the model's geometry is to be created, the parameters that define it, such as material properties or skin thickness, and the loads and boundary conditions. Once the script is created with the Matlab values the python input script is submitted to the Abaqus standard solver for structural analysis. While the finite element analysis is being conducted, the Matlab routine waits until a solved or unsolved feedback response is sent through Abaqus to Matlab. If solved, a separate prewritten python script is executed to

read in the Abaqus results and write them to text files which Matlab can import and operate on. Specifically, the Abaqus outputs of stress and displacements are read into Matlab so that the maximum value of stress in the frame and skin can be recorded. The displacement results are used to compute the final internal volume of the structure due to deformation. This volume is then used to compute the final weight-to-buoyancy ratio. The evaluation of the internal volume is necessary because it is initially assumed that the weight-to-buoyancy ratio is equal to one for vehicle sizing. Yet, when the pressure is applied, the skin and frame deform inward thus reducing the assumed initial volume. This entire process is executed for every experiment number in the DOE test matrix. Each test point has different inputs for each factor and therefore a different model is analyzed at each point. The responses observed by this process, stress and final W/B, and the corresponding input values are next analyzed using an analysis of variance.

Analysis of Variance (ANOVA) – Fixed Effects Model

The analysis of variance is a way to determine whether or not a factor and its possible interactions has a significant effect on the response. The term factor is the same as independent variable. When performing an ANOVA, there are three different types of models that can be used. These are fixed effects, random effects and mixed effects. A fixed effects model is when all of the factors and their levels are controlled and non-random. A random effects model is when the factors are treated as if they come from random occurrences. A mixed model is when some of the factors are random and some are fixed. For this research, a fixed effects model will be outlined because all of the factors and their levels are controlled and non-random.

For the ease of explanation, a simple unreplicated 2^2 full factorial analysis of the fixed effects model will be explained in which it can be expanded readily for more involved models. In this case, there exists two factors with two levels as shown in Table 4. The two factors are denoted by ‘A’ and ‘B’ and their interaction is ‘AB’. The interaction of ‘A’ and ‘B’, making up ‘AB’, represents the response, y . The interaction is defined as an attempt to evaluate whether ‘A’ and ‘B’ are coupled. A ‘1’ indicates the factor is at its low level and a ‘2’ indicates the factor is at its high level. The response column y_{ijk} denotes the response corresponding to the levels of ‘A’ (i), ‘B’ (j), and the replicate number (k). (An example of a response that is observed for the FEA is the stresses within the model once analyzed.) For instance, in the first row of Table 4, both ‘A’ and ‘B’ are low, and it is the first time this experiment at this level combination is run, therefore $y_{ijk} = y_{111}$. An example of ‘A’ and ‘B’ that could be used in the subsequent analysis performed in chapter V could be frame material properties and design altitude, respectively.

Table 4: 2^2 Unreplicated Full Factorial Design Test Matrix and Response

2^2 Unreplicated Full Factorial Design		
Factor		Response
A	B	y_{ijk}
1	1	y_{111}
2	1	y_{211}
1	2	y_{121}
2	2	y_{221}

A geometric representation of the design is shown in Figure 12, where \bar{y}_{ij} is equal to the average of the responses y at the specific level combination. The “dot” in \bar{y}_{ij} in place where k used to be indicates a summation over the subscript it has replaced. In

our example, since no replicates are present, k is constant and a summation over it is not possible. If we observe the top right corner of Figure 12, \bar{y}_{22} could very well be replaced with y_{221} since no replicates are present. The notation of a 's, b 's, and (1) is just a way of indicating which factor is at its high level, so for instance looking back at the top right corner, if both A and B are at their high level it is written that $\bar{y}_{22} = ab$. Additionally, a and b indicate the number of levels (low and high) each factor has. In this example, a and b are both equal to 2, which is utilized throughout the ANOVA process.

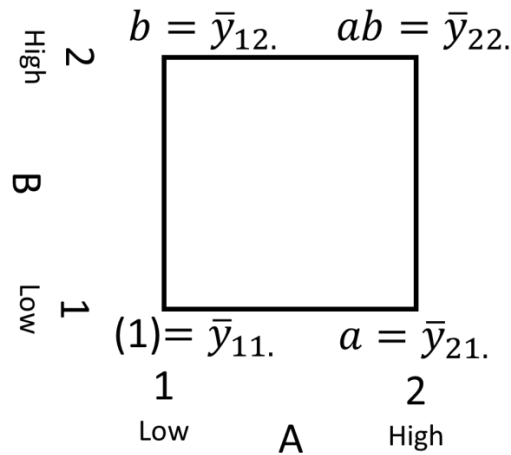


Figure 12: 2² Factorial Design Treatment Representation

With the data collected and labeled as shown in Table 4, and represented in Figure 12, the next step in the process to determine which factors have significance. This is performed by first computing each factor and their interactions sum of squares (SS). The sum of square term is the way to determine the variation of the individual factor and interaction from the total average of all the experiments. The equations for computing the sum of squares for the factors and interactions in a 2² unreplicated full factorial analysis with a single output is shown below, using the same notation as defined above.

$$SS_A = \frac{1}{bn} \sum_{i=1}^a y_{i..}^2 - \frac{y_{...}^2}{abn} \quad (13)$$

$$SS_B = \frac{1}{an} \sum_{j=1}^b y_{.j.}^2 - \frac{y_{...}^2}{abn} \quad (14)$$

$$SS_{AB} = SS_{Subtotal(AB)} - SS_A - SS_B \quad (15)$$

$$SS_{Subtotals(AB)} = \frac{1}{n} \sum_{i=1}^a \sum_{j=1}^b y_{ij.}^2 - \frac{y_{...}^2}{abn} \quad (16)$$

Where, for example $SS_A = \frac{1}{(2)(1)} [(y_{111} + y_{121})^2 + (y_{211} + y_{221})^2] - [(y_{111} + y_{121} + y_{211} + y_{221})^2 / (2)(2)(1)]$ referencing Table 4.

The next step is to compute the total sum of squares (SS_T) and the sum of squares error (SS_E), which are used to compute the mean square values shown in Table 5.

$$SS_T = \sum_{i=1}^a \sum_{j=1}^b \sum_{k=1}^n y_{ijk}^2 - \frac{y_{...}^2}{abn} \quad (17)$$

$$SS_E = SS_T - SS_{AB} - SS_A - SS_B \quad (18)$$

Table 5: 2² Example ANOVA Table with Equations

Source of Variation	Sum of Squares	Degrees of Freedom	Mean Square	F₀
A	SS_A	$a - 1$	$MS_A = \frac{SS_A}{a - 1}$	$F_0 = \frac{MS_A}{MS_E}$
B	SS_B	$b - 1$	$MS_B = \frac{SS_B}{b - 1}$	$F_0 = \frac{MS_B}{MS_E}$
AB	SS_{AB}	$(a - 1)(b - 1)$	$MS_{AB} = \frac{SS_{AB}}{(a - 1)(b - 1)}$	$F_0 = \frac{MS_{AB}}{MS_E}$
Error	SS_E	$ab(n - 1)$	$MS_E = \frac{SS_E}{ab(n - 1)}$	
Total	SS_T	$abn - 1$		

It is now desired to determine whether or not the factor that produced these observations is significant. This is performed by testing whether the null hypothesis that the factor has no effect is true. The way we evaluate this is by computing a ratio known as F_0 . This is shown in equation 19 for the treatment of A.

$$F_{0,A} = \frac{SS_A/(a - 1)}{SS_E/ab(n - 1)} = \frac{MS_A}{MS_E} \quad (19)$$

If $F_{0,A} > F_{\alpha,a-1,N-a}$, where $F_{\alpha,a-1,N-a}$ is the critical value with significance level, α , typically taken to be 0.05 the null hypothesis can be rejected and the factor determined to be significant. This critical value is obtained by using a critical F_0 lookup table [14]. This procedure can be expanded to any number of factors and levels to determine whether or not the factors have a significant effect on the observations. Additionally, this process can be expanded to consider if an observation is effected by changing a main factor alone or by changing the factor with others at the same time, this is known as cross effects or interactions. Sometimes the interaction effect could be more significant than the main effects themselves.

Now that the process for computing an ANOVA and determining significance has been detailed, a pitfall with respect to the unreplicated 2^k factorial design will be discussed. Typically, in a DOE analysis replicate tests are performed so that when computing the error term it does not equate to zero when all of the treatments are being analyzed. In other words, if 8 tests were completed for a 2^2 full factorial, that would mean that 4 of the 8 tests were replicated or extra. When computing the sum of squares error, SS_E in equation (18), considering the 2 factors and their interaction, 7 ($abn - 1$, where $a,b,n = 2$) degrees of freedom (DOF) are available for the sum of squares total (SS_T). Knowing that the SS for each treatment or effect and interaction takes up 1 DOF as shown in the first 3 rows of Table 5, where a and $b = 2$ that leave $7-3 = 4$ DOF left over to compute error $ab(n-1) = 4$ where $n = 2$. Now, if the replicates were not performed then the total DOF would equal $abn-1=3$ where $a, b=2$ and $n=1$, and if all the treatments were analyzed just as before, the treatments would take up the 3 total DOF $3-3=0$ and no DOF would be left over for the error term. This is a problem when conducting a 2^k

unreplicated designs and all of the treatments want to be initially observed for significance because there is no error term, and with no error term the mean square cannot be computed and thus the F_0 cannot be computed as well to test for significance [14].

Fortunately, there are ways around this obstacle for unreplicated designs. The simplest remedy to this problem is to initially ignore some of the factors or interactions to gain DOF for the error term. The problem is, what factors or interactions should you ignore if you know nothing about the significance of the factors or interactions in the model? Therefore, another technique known as Lenth's pseudo-standard error (PSE) is used. Lenth's PSE is utilized to approximate an initial pseudo error value when the SS_E value is equal to zero. To obtain this error value, first compute each factor and interaction's estimated effect. Continuing with the example above, the estimated effect or contrast of A is computed by taking the difference in the averaged response when A is at its high value and when A is at its low value or the difference in the average response of the system on the right hand side and left hand side of Figure 12. The equation for this is shown in equation (20). The same representation can be performed for B and AB [14].

$$c_A = \bar{y}_{A+} - \bar{y}_{A-} = \frac{ab + a}{2n} - \frac{b + (1)}{2n} \quad (20)$$

Once the treatment contrasts have been computed, Lenth's PSE can be calculated. The equation for the PSE is shown in equation 22. After the PSE is obtained the individual contrast is compared to a value known as the simultaneous margin of error (SME) to determine initial significance. The equation for SME is shown in equation (23).

$$s_0 = 1.5 * \text{median}(|c_j|) \quad (21)$$

Where for a 2^2 factorial design $c = [c_A, c_B, c_{AB}]$

$$PSE = 1.5 * \text{median}(|c_j|: |c_j| < 2.5s_0) \quad (22)$$

$$SME = t_{\gamma,d} - PSE \quad (23)$$

Where, $\gamma = 1 - \frac{1+0.95^{\frac{1}{m}}}{2}$, $= m/3$, $m = \text{size of } c$, and $t_{\gamma,d}$ is determined from a lookup table.

Each contrast c_j that is greater than the SME value is said to be significant using Lenth's method [14]. After this process is completed, the terms that are determined insignificant can be excluded from the model and their DOF will be included in the error term so that the ANOVA for the model can be computed with a nonzero error term.

Regression Model

A useful model that can be developed from the response of a DOE is a regression model. Regression models are used to fit a set of sample data to a function where the response(s) is a function of the independent or regressor variables. The effects results from a DOE and ANOVA can be used to establish a function or multiple functions ϕ to approximate a response variable(s). The focus of this description will be on linear regression models. As stated above a response variable, y , is fit to β_i parameters which are known as the regression coefficients multiplied by its corresponding regressor variable x_i . A general form of the first-order fit is shown in equation (24). This general form can be extended to second, third, fourth, etc. order fits. As an example a first-order

response surface model with interactions for two factors is shown in equation (25). This equation can be equated to equation (26) if we let $x_3 = x_1^2, x_4 = x_2^2, x_5 = x_1x_2, \beta_3 = \beta_{11}, \beta_4 = \beta_{22},$ and $\beta_5 = \beta_{12}.$

$$y = \beta_0 + \beta_1x_1 + \beta_2x_2 + \dots + \beta_kx_k + \epsilon \quad (24)$$

$$y = \beta_0 + \beta_1x_1 + \beta_2x_2 + \beta_{11}x_1^2 + \beta_{22}x_2^2 + \beta_{12}x_1x_2 + \epsilon \quad (25)$$

$$y = \beta_0 + \beta_1x_1 + \beta_2x_2 + \beta_3x_3 + \beta_4x_4 + \beta_5x_5 + \epsilon \quad (26)$$

Reformulating equation (25) to equation (26), creates a linear regression model since the β parameters are linearized. A regression model that has linear regression coefficients is considered to be linear even if the shape of the response surface is not.

The next step in the regression model is to estimate the β parameters, and this is typically done using the method of least squares. A complete derivation of this method will not be shown here but can be acquired in [14], however simplified matrix representation is shown below.

$$\mathbf{y} = \mathbf{X}\boldsymbol{\beta} + \boldsymbol{\epsilon} \quad (27)$$

Where:

$$\mathbf{y} = \begin{bmatrix} y_1 \\ y_2 \\ \vdots \\ y_n \end{bmatrix}, \mathbf{X} = \begin{bmatrix} 1 & x_{11} & x_{12} & \dots & x_{1k} \\ 1 & x_{21} & x_{22} & \dots & x_{2k} \\ \vdots & \vdots & \vdots & & \vdots \\ 1 & x_{n1} & x_{n2} & \dots & x_{nk} \end{bmatrix}, \boldsymbol{\beta} = \begin{bmatrix} \beta_1 \\ \beta_2 \\ \vdots \\ \beta_n \end{bmatrix}, \text{ and } \boldsymbol{\epsilon} = \begin{bmatrix} \epsilon_1 \\ \epsilon_2 \\ \vdots \\ \epsilon_n \end{bmatrix} \quad (28)$$

Using this setup, the next step is to determine a set of least squares estimators, $\hat{\boldsymbol{\beta}}$ that minimizes the least squares function:

$$L = \sum_{i=1}^n \epsilon_i^2 = \boldsymbol{\epsilon}'\boldsymbol{\epsilon} = (\mathbf{y} - \mathbf{X}\boldsymbol{\beta})'(\mathbf{y} - \mathbf{X}\boldsymbol{\beta}) \quad (29)$$

Through rearrangement and evaluation, this function simplifies to equation (30), where the fitted regression model is represented by equation (31) and the residual is shown in equation (32).

$$\mathbf{X}'\mathbf{X}\hat{\boldsymbol{\beta}} = \mathbf{X}'\mathbf{y} \text{ or } \hat{\boldsymbol{\beta}} = (\mathbf{X}'\mathbf{X})^{-1}\mathbf{X}'\mathbf{y} \quad (30)$$

$$\hat{\mathbf{y}} = \mathbf{X}\hat{\boldsymbol{\beta}} \quad (31)$$

$$\mathbf{e} = \mathbf{y} - \hat{\mathbf{y}} \quad (32)$$

The residual is then used to determine the residual sum of squares, shown in equation 33. Which is an important term because it can be used to determine the how well the model fits the data [14].

$$SS_E = \mathbf{y}'\mathbf{y} - \widehat{\boldsymbol{\beta}}'\mathbf{X}'\mathbf{y} \quad (33)$$

Step 4: Response Surface Methodology

Response surface methodology or RSM is a technique used to model a system or process with respect to any number of control variables or inputs. In order to model the system, a system model needs to be generated. Two of the main models are a first order model, which is discussed in the above section, and a second order model. These models can be used to predict response values within the range of the model inputs not previously tested, as well as determine optimal settings for the inputs to maximize or minimize the observed response. An illustration of data points obtained by a DOE and the generated response surface are shown in Figure 13. The graph on the left side of Figure 13 shows the response data points obtained by a DOE plotted with respect to its independent variables. Likewise, the graph on the right side shows the response surface generated by a second order model to approximate the response data points shown on the left chart.

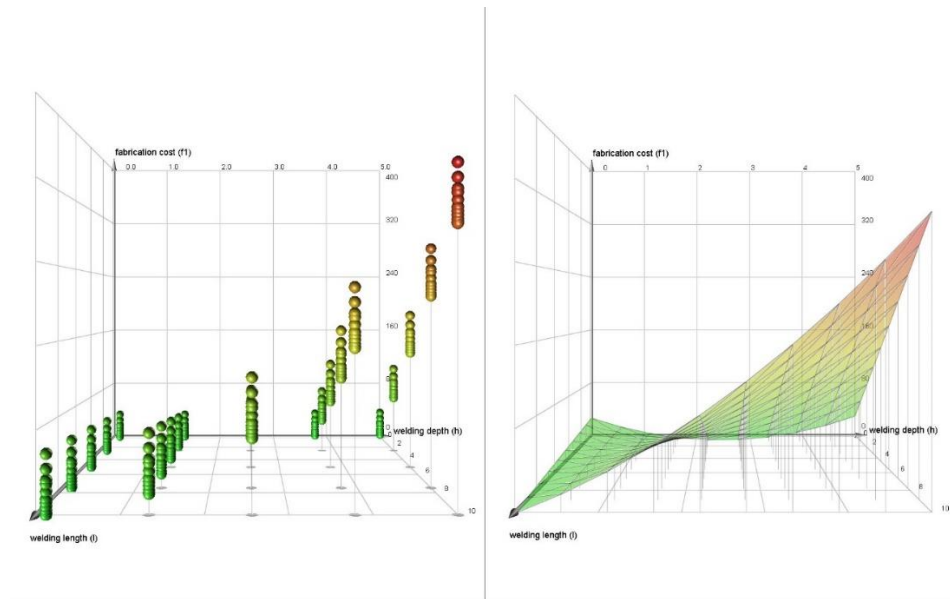


Figure 13: Illustration of plotted DOE data points and the generated Response Surface.

The response surface shown on the right of Figure 13 uses a model generated from the data on the left to predict the response of the system at the points where data was not explicitly obtained by the DOE to create a continuous surface. More data points obtained by the DOE creates a more accurate prediction that the model makes to create the continuous surface. Linear or first order models only need data points at the corners of the design space, and typically have at least one data point at the center to check for curvature to create a response surface. Non-linear or second order models need data points spread throughout the design space as shown in Figure 13, to capture the non-linearities occurring within the design space. Typically, if the true response of a system has curvature or non-linearity, a first order model with interactions cannot appropriately capture the curvature, which is when a second degree model is necessary. However, when a first order or second order model is desired, the DOE has to be specially designed to produce data points that allow for the respective models to be created [15] [16].

Structural Feasibility Analysis

The structural feasibility analysis will be conducted in two parts. The first is a material safety factor analysis and the second is a geometric instability analysis.

The material safety factor analysis will be conducted by converting the max frame and skin stress values from the regression models into safety factors. This will be performed by dividing the max stresses from the regression fits obtained above by their materials yield strength values. This will produce what is known as a safety factor value for the frame and skin stress responses obtained from the finite element analyses. This computation is shown in equation (34). If the safety factor is above or equal to 1 for both the skin and frame at a design point, then the design parameters associated with that design are said to have produced a structurally feasible design with respect to material failure.

$$SF_{s,f} = \frac{\sigma_{y_{s,f}}}{\sigma_{max_{s,f}}} \quad (34)$$

The geometric instability of the vacuum frame-skin structures for the two case study designs will be analyzed using the linear buckling solver described in Step 1. This is known as solving the linear elastic buckling eigenvalue problem. The eigenvalue problem is shown again for conscience in equation (35).

$$(K_0^{NM} + \lambda_i K_{\Delta}^{NM})v_i^M = 0 \quad (35)$$

Where K_0^{NM} is the initial stiffness matrix with any preloads, P^N , included. K_{Δ}^{NM} is the differential stress matrix from the initial matrix due to the incremental loading pattern, Q^N . λ_i and v_i^M are the eigenvalues and the eigenvectors that correspond to the stiffness

matrix singularities with respect to the load increments Q^N . The M and N indicate the degrees of freedom for the entire model and i indicates the ith buckling mode. As developed in Step 1 above, the linear buckling solver searches for loads in the applied direction where the model stiffness matrix, K, becomes singular. The model stiffness matrix is composed of two parts, the material stiffness matrix (K_0^{NM}), which is a function of the material properties, and the geometric stiffness matrix (K_{Δ}^{NM}), which is a function of the component forces produced by the boundary conditions and applied loads.

In order to estimate the pressure required to produce geometric instability in the two VLTAV case studies, the frame of the designs were analyzed without the skin. The skin is excluded because Rodriguez shows in his research, [5] that a large quantity of the critical loads predicted for the icosahedron frame-skin model are skin dominated and significantly smaller than when the frame is considered by itself. Therefore, one would need to extract a large number of critical loads (eigenvalues) to attempt to capture any frame dominated states (modes), which are the modes (eigenvectors) of interest. In order to avoid extracting potentially thousands of modes to view frame dominated features, a buckling analysis of the frame alone will be conducted. This was performed by constructing reference points at the center of each planar face and coupling those reference points to its triangles beams with coupling constraints. A point load equal to the external pressure times the area of each triangle was applied to the reference point to be distributed by the coupling constraints to each triangle as if the skin were present. An example of this is shown in Figure 14 for a triangular section. Both case studies, the Metlen icosahedron and the hexakis icosahedron have, frame structures with planar triangular faces that make up the geometry and therefore the frame buckling analysis

technique will be performed using that same reference point technique developed by Rodriguez [5].

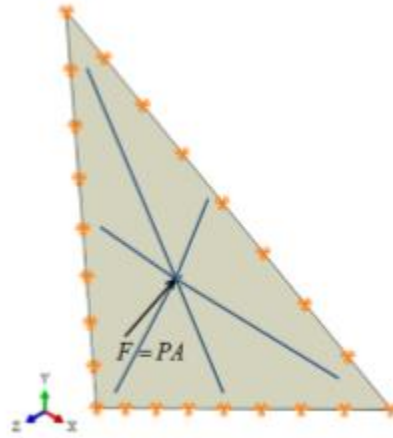


Figure 14: Triangular frame section with reference point and coupling constraint. The reference point is where the arrow points to and the coupling constraint is denoted by the blue lines.

The critical loads predicted this way will be an indication of the pressure necessary to produce global buckling in the frame. The evaluation will not be a perfect representation of the frame-skin model because the loads applied to the frame in the buckling analysis, were applied without the skin. The skin adds additional boundary conditions and stiffness not represented when the frame is alone [5].

The goal of the frame buckling analysis is to determine an indication if geometric instability within the frame could cause the structures in either case study to fail before material failure. It is important to note that the critical buckling load predicted by the buckling solver will be conservative because the skin is not present in the analysis. To determine if geometric instability in the frame could cause failure, a frame buckling analysis will be performed at a design point in the SF design space where SF is equal to

one, if that point exists. The reason why the analysis would be performed at this design point is that the only reason to investigate geometric instability is if the structure does not fail first due to material failure. If the estimated critical buckling pressure, at the design point of SF equal to one, is greater than the pressure (101,325 Pa) applied, then geometric instability will be determined to be a non-factor in terms of structural feasibility. The reason why additional analyses at other points would not be necessary is because any design that has a SF greater than one would have a higher frame stiffness and therefore a larger estimated critical buckling pressure.

Chapter III Summary

This chapter discussed the methodology to be applied to the two case studies in chapters V and VI. The methodology highlighted the four step process which begins with the development of finite element models to produce the structural response outputs to be used to determine the potential feasible design space. The next step involved parameterizing the finite element system in terms of its inputs and outputs with a dimensional analysis to non-dimensionalize the inputs into relational ratios or invariants, to condense the number of inputs. So that the numbers of DOE factors to be analyzed for the system were minimized. The next step detailed the process to establish, perform, and analyze the design of experiments for the two case studies. This research focused on creating a broad scope first order DOE design so that the numerous inputs/invariants/factors could be tested while minimizing the number of initial experiments to gain a feel of what the design space looks like. The final step in the process detailed the response surface methodology for constructing first order surfaces based on the DOE data obtained. The last section of this chapter detailed the process that

will be used to evaluate the structural feasibility of the design space in terms of material and geometric instability.

IV. Geometric Frame Considerations and Modeling and Analysis Technique

Validation

A model is only as good as the reality it predicts. With this in mind, it was desirable to develop a physical experiment that could be used to validate the finite element models. When developing the ideal experiment, one would want to create an experiment that matches the loading scenario being modeled. A test specimen frame covered by a membrane skin with an internal vacuum would be quite difficult to develop and execute that would be equivalent to the finite element model without an excess of cost and time. Since experimentation is desired and sensors and data collection are a function of that, an experiment needs to be developed such that accurate and reliable data can be obtained in order to compare against a finite element model. Therefore, a simplified yet similar loading scenario to the vacuum cause was developed. The scenario was to consider the frame alone and to load the frame in compression in a single direction with an MTS device. This experiment allows us to characterize the deformation of a geometric structure, in this case the icosahedron, under compression. As long as the experiment results are adequately captured with a corresponding model, confidence in the predicted results of the more complex vacuum model could be established and justified.

In order to conduct the proposed experiment, a frame needed to be manufactured. The manufacturing process used to construct the frame specimen was additive manufacturing, in the form of plastic resin stereolithographic 3D printing. The specific printer was an Objet Eden 500V 3D printer [17]. When utilizing this style of additive manufacturing, there are printing constraints to be considered. These constraints are overall scale of the object, minimum thicknesses, and geometry (hollow or solid). The

Objet Eden 500V has an approximate 7 inch z-axis or object height limit, able only to print solid parts if closed contours exist in the model. Additionally, a 3D printed specimen used in an experimental loading scenario needs to be sufficiently strong enough to provide usable data. Therefore, the dimensionality of the object needs to be carefully considered such that the specimen is not too fragile, nor too stiff for the loading device.

This chapter begins with a development of cylindrical beam global and local buckling, and the effect that the wall thickness/beam radius has on the design. The global and local cylindrical beam buckling is developed because the frame in the Metlen icosahedron and the hexakis icosahedron are both composed of cylindrical beams. The second section details the experimental tests performed to validate the frame finite element modeling and analysis technique.

Cylindrical Beam Buckling Development and Thickness/Radius Ratio Analysis

The first section will describe global column/beam buckling and collapse. It is important to understand this phenomenon because the frames being considered for the construction of a vacuum LTAV would be built using column/beam like profiles. The second section describes the local buckling that can occur when dealing with thin walled cylindrical columns. The last section combines both the global and local buckling equations to perform an analysis on the predicted buckling loads for a cylindrical column with respect to its wall thickness/ radius ratio.

Global Cylindrical Beam/Column Instability

Bifurcation buckling is a mathematical explanation for collapse within a column. The bifurcation is a function of compressive energy. When the compressive potential

energy of the external load exceeds the internal ability to resist this energy, the form of movement is required to maintain equilibrium. That movement is a curved shape of the column leading to bending. The bifurcation is an attempt at nonlinearity using linear relationships. When a real column buckles it takes the physical shape of one of its mode shapes. This is shown in Figure 15, where the 1st mode is indicated when the beam bends upward as indicated by the lower illustration in Figure 15.

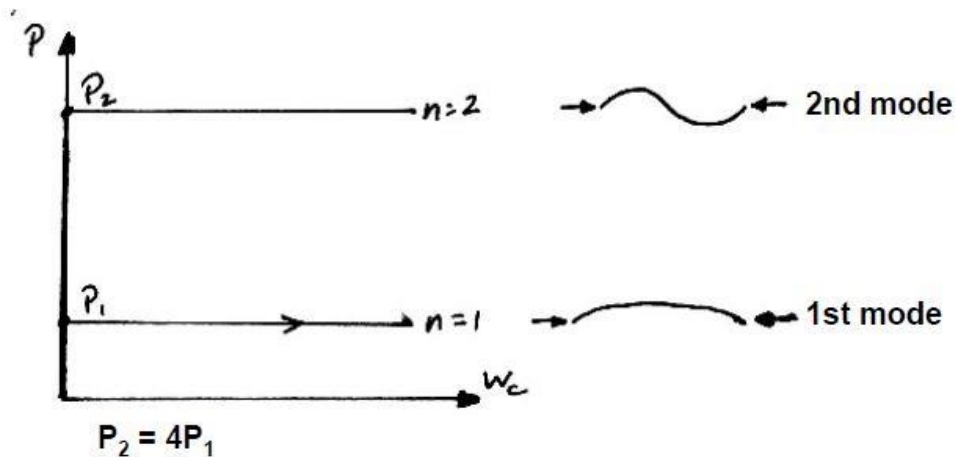


Figure 15: First two mode shapes for a simply supported column.

The mode shape is dependent on the load applied as well as boundary conditions. The critical load at which the column will buckle can be determined by solving an eigenvalue problem with respect to the governing equation and boundary conditions. The solution, for a simply supported column is shown in equation (3636363636363636) [18], where n is the mode shape of interest. Typically, one is used, and l is the effective length. A more general form of this equation can be produced for the first mode specifically to represent multiple boundary conditions. This equation is shown in equation (373737), where c is the coefficient of defining the boundary condition of the column. An illustration depicting the various boundary conditions and the corresponding

value of c is shown in Figure 16, where for instance a $c = 0.25$ indicates a clamped-free condition, shown as the third scenario from the left.

$$P_{crit} = \frac{n^2 \pi^2 EI}{l^2} \quad (36)$$

$$P_{crit} = \frac{c^2 \pi^2 EI}{l^2} \quad (37)$$

Where, E is the modulus of elasticity, I is the bending moment of inertia, l is the beam or column length, and c is the parameter between 1 and 4 denoting the boundary condition of the beam or column.

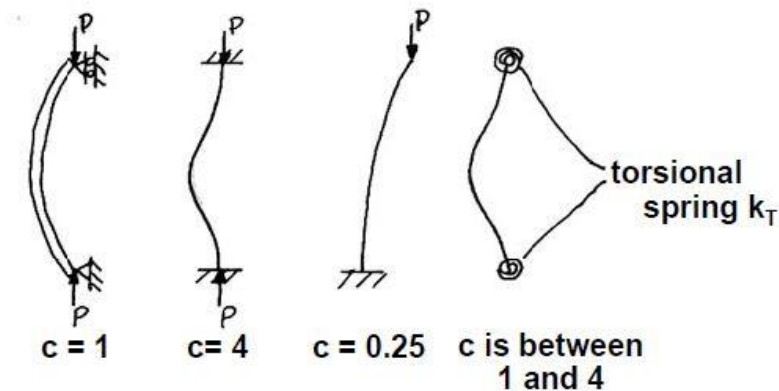


Figure 16: First buckling mode for various boundary conditions and its corresponding c value.

It is noted that for a real life scenario one cannot truly produce a perfectly clamped end, therefore a c value of 2 is typically used for clamped ends. A typical load displacement curve for a buckled column is shown in Figure 17. The structure reaches the

critical load B and produces large displacement for little increased load. Note, that the critical load B is below the failure load of the material indicated by C in Figure 17 [19].

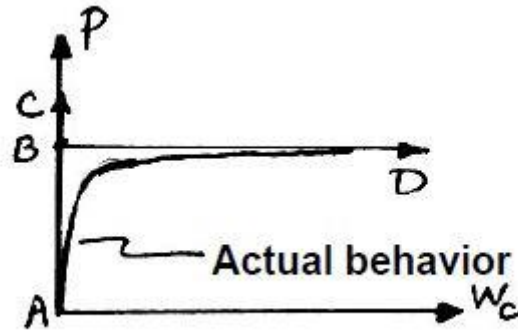


Figure 17: Load displacement curve for a buckled column.

Local Thin-Walled Circular Cylinder Instability

The following section will describe beam buckling, considering isotropic thin-walled circular cylinders under axial compression and bending. The concept behind determining the buckling load of a circular cylindrical shell is similar to that of a beam-column or plate.. The buckling load for a circular cylindrical shell under axial compression is shown in equation (38) [20].

$$N_x = -D \left[\frac{n^2 \pi^2}{L^2} + \frac{EhL^2}{DR^2 n^2 \pi^2} \right] \quad (38)$$

$$D = \frac{Eh^3}{12(1 - \nu^2)} \quad (39)$$

Where, D is the wall flexural stiffness per unit width, E is the modulus of elasticity, h is the wall thickness, L is the beam length, R is the beam radius, and ν is the materials Poisson's ratio.

This equation states that any axial load N_x will cause a lateral displacement which is known as buckling. The variable n , just as when considering the column scenario, denotes the unique buckling mode shape and buckling load. Since it is desired to know what the critical or minimum buckling load is for the shell, the lowest mode and respectively the lowest buckling load is desired. Therefore when we let $n = 1$ in equation (38), it reduces to equation (40).

$$N_{x_{crit}} = -D \left[\frac{\pi^2}{L^2} + \frac{EhL^2}{DR^2\pi^2} \right] \quad (40)$$

This equation can be reduced further if we take the derivative of N_x with respect to L equal to 0, this would then represent the length at which minimum buckling occurs. Substituting equation (41) into equation (40), one obtains the minimum buckling load. The resulting reduced equation is valid when the length of the cylinder is greater than or equal to the length obtained in equation (41). In order to obtain the critical axial buckling stress, equation (42) is divided by the thickness of the cylinder, shown in equation (43) [20].

$$L = \pi \left[\frac{R^2 h^2}{12(1 - \nu^2)} \right]^{1/4} \quad (41)$$

$$N_{x_{min}} = - \frac{Eh^2}{R\sqrt{3(1 - \nu^2)}} \quad (42)$$

$$\sigma_{x_{cr}} = \frac{N_{x_{min}}}{h} = - \frac{Eh}{R\sqrt{3(1-\nu^2)}} \quad (43)$$

The same development is used when considering a thin cylindrical shell column under pure bending. In practice however, it has been experimentally found that on average a cylindrical column in bending, has a 30% higher buckling load, than the same column in axial compression [20].

Cylindrical Beam Thickness/Radius Ratio Buckling Analysis

A beam profile study was conducted by Rodriguez, where he found for a hollow beam the more you reduce the beam thickness to radius ratio the better the beam “performs”. This statement is true for the range of beam thickness/radius ratio that Rodriguez performed. The method that was used to evaluate the performance of the beam profile is Euler buckling as described in the global column buckling section above. This is illustrated in Figure 18, where the beam moment bending moment of inertia and critical buckling load increase as the beams max stress and displacement decrease as the beams thickness/radius ratio $\left(\frac{t_b}{r_b}\right)$ decreases. This increasing trends occur because as the ratio decreases the beams radius gets larger which directly increase the bending moment of inertia and critical buckling load since I is in the numerator of the column buckling equation (37). The decreasing trends in max stress and displacement occur because the increase in bending moment of inertia increases the beams stiffness.

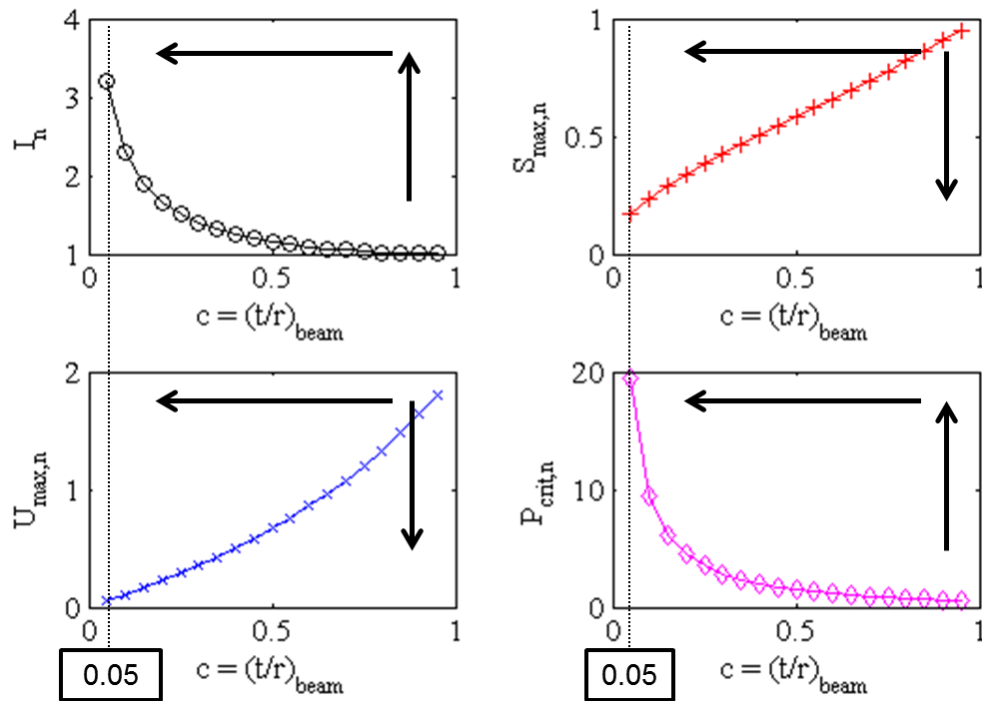


Figure 18: Solid vs. Hollow Beam Profile Study [5] (the top left plot is beam bending moment of inertia (I_n) versus (t_b/r_b) , the top right plot is maximum beam stress (S_{max}) versus (t_b/r_b) , the bottom left plot is maximum beam displacement (U_{max}) versus (t_b/r_b) , and the bottom right plot is critical buckling load (P_{crit}) versus (t_b/r_b)).

If a hollow beams “performance” did in fact get infinitely better as $(\frac{t_b}{r_b})$ decreased, then one would assume that all beams would be hollow beams and their radii would be large and thicknesses very small. This however is not the case due to local shell buckling and a beams $(\frac{t_b}{r_b})$ does have a limit. Equation (43) illustrates the buckling of a thin-walled circular cylinder as a function of the beams thickness to radius. As the walls of the beam continually get thinner, it is expected that the beam will buckle due to local skin buckling, as opposed to global Euler buckling occurring first. A study was conducted on the beam profile in the same manner as was done in Rodriguez’s study, with the addition of the buckling load, due to local skin buckling as a function of beam thickness to radius ratio. This is shown in Figure 19, where the shaded regions are the critical regions. The

transparent black region denotes that the beam will fail due to local buckling and the blue region denotes that the beam will fail due to Euler buckling.

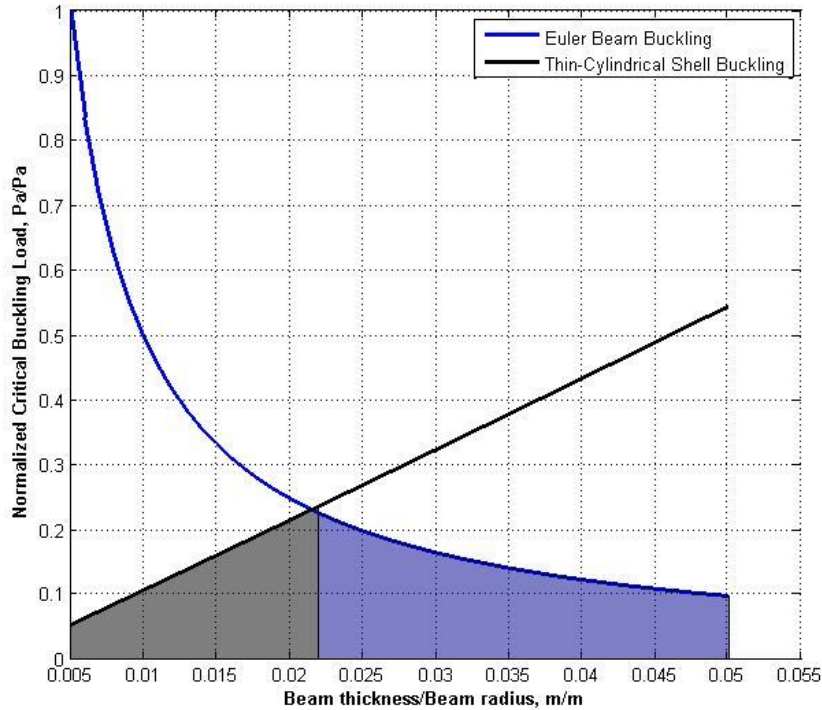


Figure 19: Critical buckling Load of a hollow beam with varying thickness/radius ratio.

Observations from , show that beam thickness/radius ratios below 0.02 have a significant increase in Euler buckling, but are predicted to fail in local buckling first. This local failure can be prevented by building in ring stiffeners within the hollow beam, or by internally pressurizing the hollow beams [20]. If local buckling can be prevented then there would be a significant growth in the beams buckling performance below a beam thickness/radius ratio of 0.02. This would follow the Euler buckling theory instead of the thin cylindrical shell buckling theory. It is important to note that the buckling FEA performed on the structures frames in the chapters V and VI cannot capture the local

buckling phenomena. The beams are modeled using 2D wires with a circular hollow profile, not 3D elements where the stress through the thickness of the beam can be properly modeled. As a result, the buckling analysis that Abaqus performs cannot account for the thinness of the beam when computing the critical buckling load of the structure. The analysis will tend to show increased structure performance as the beam thickness/radius ratio decreases. In the analyses performed in chapters V and VI, where beam thickness/radius ratio is less than the limit of approximately 0.02, local buckling could become a dominating factor. Thus, creating the potential for localized failures before material failure or global buckling can occur. This study in effect sets the manufacturing limit for the thickness/radius ratio of an unsupported hollow beam without considering local buckling.

Frame Finite Element Analysis Modeling Technique Validation

An icosahedron model was developed in Solidworks to be printed. The dimensions of the model are as follows: 17.78 cm frame diameter and 0.47625 cm solid beam diameter. The specimen was modeled as one continuous part and therefore solid beams had to be used so that they would comply with the printer's constraints. A single piece model was developed to eliminate any user error or unintended failure points from assembly. The 17.78 cm frame diameter was chosen because it maximized the limits of the printer and a "large" frame produced more slender beams, $r_b \ll L_b$ than if the frame diameter were smaller. Slender beams were desired because they are used in the vacuum models. The beam's diameter was chosen such that the frame would be stiff enough to handle the minimum load required to collect usable data on the MTS device and slender enough to be within the printer's thickness tolerances. The usable data range is

considered to be the range of force measurements greater than the tolerance of the load cell. This is required such that the data recorded is not primarily near the tolerance of the load cell where the response is subject to significant error. The error tolerance is shown in Table 6 for MTS force transducer 661.19E-03 [21]. The beams minimum dimension was limited on the manufacturing process because during manufacturing, a secondary support material is printed which encompasses the part and needs to be removed after printing. During removal of the secondary material, if the interior part is too fragile it is likely to break. Therefore, a beam diameter dimension of 0.47625 cm was chosen because it was thought to be large enough to remain intact during cleaning. A buckling analysis, which is detailed below, was performed to indicate that a 17.78 cm icosahedron with 0.47625 cm beam diameter would be stiff enough to properly load the MTS device above its error tolerance. Therefore, it was deemed that a 0.47625 cm beam diameter was satisfactory and no other beam dimensions for experimentation were investigated.

Table 6: MTS 661.19E-03 Force Transducer Error Data [21]

MTS 661.19E-03 Force Transducer		
Force Range (N)	Max Measurement Error (%)	Max Measurement Error (N)
± 15000	0.16	± 24

MTS Setup

With the icosahedron specimen’s dimensions determined and printed, the experiment can be set up. The experiment utilized an MTS 810 Material Test System servo-hydraulic load frame (661.19E-03), shown in Figure 20. The MTS was fitted with T-shaped plates that were inserted into the tension grips so that a flat top and bottom

surface could be created for compression testing. The MTS has its own load cell to measure both tension and compression loads and displacement sensor to measure the displacement of the loading hydraulic cylinder. The load cell was within calibration, but the displacement sensor was unknown. Therefore, a validation test of the displacement feedback from the MTS was performed to ensure that the data collected was reliable throughout the desired range. The validation for the MTS displacement feedback was performed using a Linear Variable Differential Transformer (LVDT). The specific model was a LBB-315-PA-100-1 and was calibrated. The test was performed by clamping the LVDT above the lower actuated cylinder and commanding the cylinder to move upward, and comparing the LVDT results to the MTS displacement results. The results of this test were that the maximum error between the two was approximately 5% and the average error was 1.7%. With the average error being small, the MTS displacement feedback was determined to be adequate for experimentation.

The specimen was placed in the center of the bottom plate, where the vertical position of the plate was controlled by a servo-hydraulic piston. To compress the frame, the bottom plate was driven upward into the top plate, which was fixed. The load response data was recorded by a load cell connected in line above the top plate, shown in Figure 21. The data collection was performed using the MTS FlexTest 40 digital controller and data logger. The software used was the FlexTest 40 station manager and MultiPurpose TestWare application. The loading of the icosahedron was performed using displacement control. The model was manually moved up into the top plate until there was no gap between the top of the icosahedron and top plate. The load cell and displacement were tared to 0 at this point. The model displaced at a constant rate of 0.02

mm/s (0.047 in/min) into the top plate until a displacement of 2 mm was reached, then the model was unloaded at the same rate.

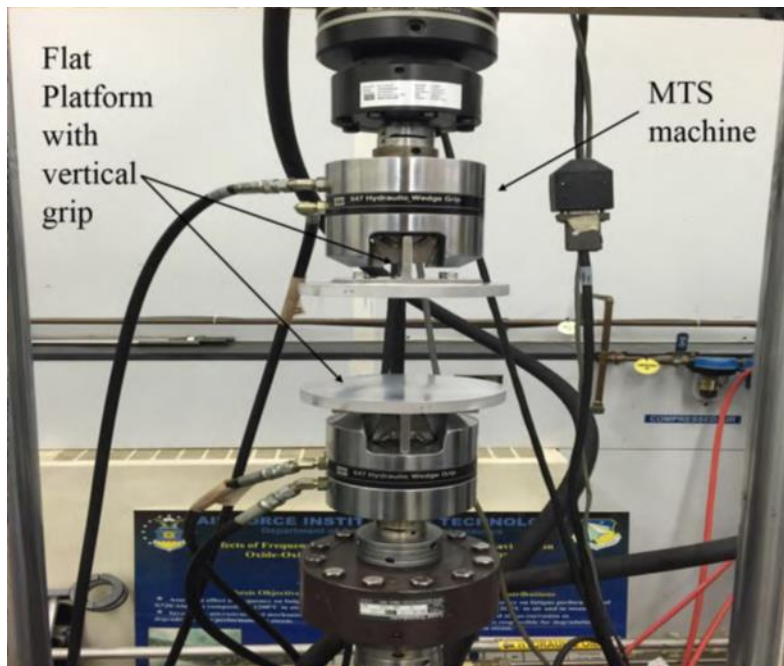


Figure 20. AFIT MTS with compression plates

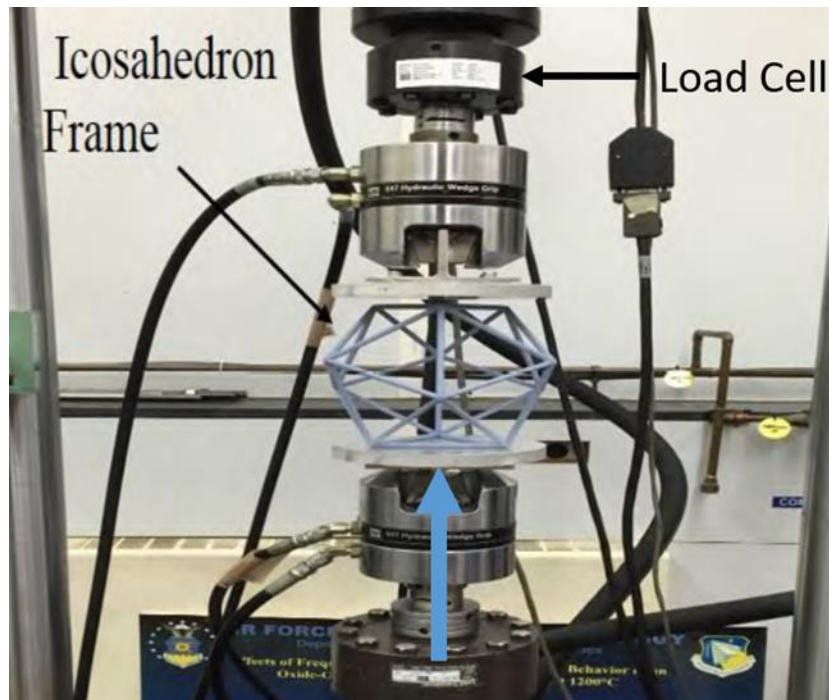


Figure 21. MTS with Icosahedron frame

MTS FE Setup

Since, the beams in the fabricated model are solid instead of hollow, as in the vacuum model, a solid beam model was generated in Abaqus to match the model that was printed. The material properties, modulus, density, and Poisson's ratio, used for the model were chosen via the material datasheet for VeroBlue RGD840 from Stratasys [17]. The values are 2.295 GPa, 1190 kg/m³, and 0.35 respectively. A literature search showed that the material properties of the printed materials could be far removed from the quoted values. The materials investigation indicated that the material properties of a printed object can vary significantly based on the geometry and placement of the specimen within the machine. Research work from Virginia Tech shows this issue occurring, therefore it is difficult to know what the material properties of the printed object are [22]. Since the properties could not be exactly determined, a range was chosen based on data

from VT and in house material testing at AFIT. The range for the material properties used in the analysis is shown in Table 7.

Table 7. VeroBlue Material Property Range.

	VeroBlue-VPI	VeroBlue-Stratasys	
Density	1190	1190	kg/m ³
Poisson's Ratio	0.35	0.35	
Modulus of Elasticity	1.874-1.000	2.295	Mpa

The next step in the model development is establishing the boundary conditions. The boundary conditions were placed on two opposing triangular faces vertices, where the top vertices' displacements were restricted only in the x and y direction. The bottom vertices were pinned restricting all displacements and allowing rotations. The "load" was applied using displacement control at the top vertices in the downward z-direction. The boundary conditions and loading are depicted in Figure 22. The boundary and loading conditions were chosen to create the same scenario as the physical experiment. The elements and seeding for this model are the same, 20 B32 beam elements per edge, used for the model developed by Rodriguez. The analyses performed on the model were both a buckling and non-linear static analysis.

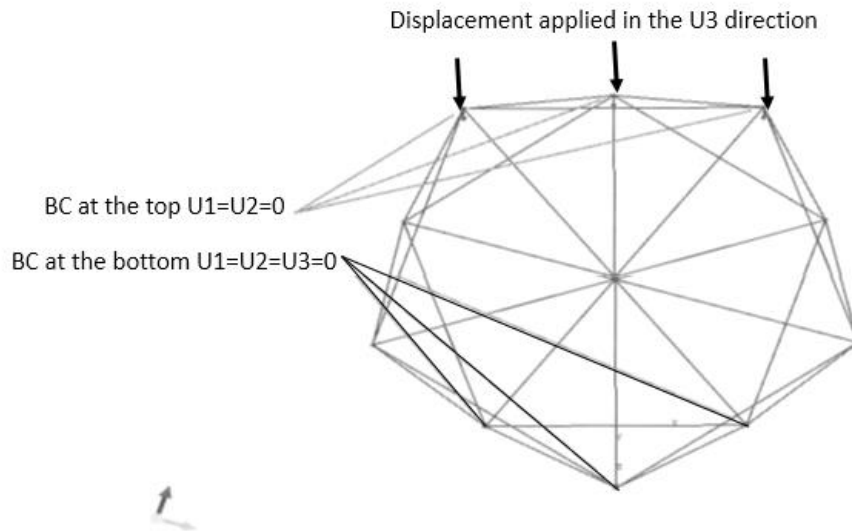


Figure 22. Boundary Conditions and Loading for MTS FE model.

Icosahedron MTS FE Results

The analysis was conducted in two parts: linear buckling analysis and non-linear static standard analysis. The linear buckling analysis approximated the buckling load and mode shape for the icosahedron frame under the loading and boundary conditions shown in Figure 22. The material properties used for this analysis used a range of modulus values defined in Table 8, because the modulus properties are unknown for the printed frame. The first mode shape and corresponding eigenvalue that did not detail rigid body motion was the mode of interest. This mode is the first failure mode and is what is expected that the frame will exhibit when loaded by the MTS. The higher modes are not significant because the frame will have already collapsed at the first mode. The result of the 2.295 GPa modulus buckling analysis depicting the first mode and eigenvalue is shown in Figure 23. The same analysis was performed four additional times with each having a degraded modulus value. The eigenvalues obtained from the analysis can readily

be converted to the critical load value using equation (44). The corresponding critical loads for the various moduli analyses are shown in Table 8 [23].

$$F_{crit} = \lambda_{crit} F_{ref} \quad (44)$$

Where: F_{crit} = Critical buckling load

λ_{crit} = lowest eigenvalue from buckling analysis

F_{ref} = magnitude of reference load applied for the buckling analysis

(usually a unit load)

Table 8. Critical buckling load of 3D print icosahedron estimated by buckling analysis for various modulus.

Test #	Modulus of Elasticity (MPa)	Fcrit (N)
1	2.295	650.09
2	1.874	481.98
3	1.577	405.59
4	1.176	302.46
5	1	257.2

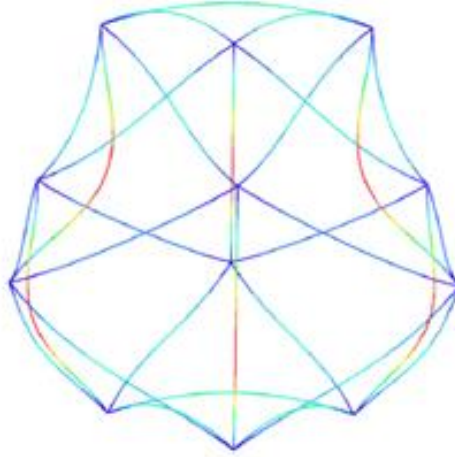


Figure 23. First failure mode of icosahedron under MTS loading conditions.

After the linear buckling analysis, a non-linear static analysis was performed to map the nonlinear displacements and stresses of the frame as it undergoes deformation in order to compare the buckling load predicted by the linear buckling analysis. The same frame and boundary conditions were used for the non-linear analysis as well as the linear buckling. The load applied to the frame was performed using displacement control at the top of the frame. The forced displacement was 0.002 m applied in the downward direction at the three top vertices as shown in Figure 22. As the displacement occurs, the frame can fail in two ways, collapse or material failure. The non-linear analysis can be used to estimate which will occur first. The load versus displacement curves of the frame tracing the displacement at the top and reaction at the bottom for the various modulus values are shown in Figure 24. These curves all show that the structure reaches a limit

where linear displacement no longer occurs, and after this limit the structure continues to carry load but at a reduced stiffness. In the models produced, the structures will infinitely be able to carry an increasing amount of load no matter the displacement because there is no material plasticity definition in the model. Realistically when a structure begins to deform non-linearly, it can either continue to carry load at a reduced stiffness until material failure or lose its ability to carry further load and displace until local instability, either geometric or material. A model without plasticity relationships cannot accurately predict post buckling behavior. It can show whether structural yielding occurs first, as long as the calculated stress values are lower than the materials yield strength and deformations are relatively small. Looking at Table 8 and Figure 24, all of the load points where the onset of non-linear behavior occurs coincide closely to the critical load values estimated by the linear buckling analysis. If the material strength is estimated to be approximately 2% of the modulus as indicated by the data collected by VT, it can be estimated whether or not material failure or structural yielding will occur first. The estimated material strengths and max stress values at 2mm vertical compression with their corresponding moduli are shown in Table 9. As shown in the table, the stress values at 2mm displacement are below the estimated material strengths. Thus, it is estimated that structural yield would occur before material failure at the point where the load vs. displacement curve goes non-linear.

Table 9: Estimated Material Strength and Stress at 2mm vertical displacement of VeroBlue FE Models

VeroBlue Material Model		
Modulus of Elasticity (Gpa)	Estimated Material Strength (Mpa)	Estimated Max Stress at 2mm Displacement (Abaqus) (Mpa)
2.295	45.9	39.85
1.874	37.48	32.55
1.577	31.54	27.39
1.176	23.52	20.43
1	20	17.37

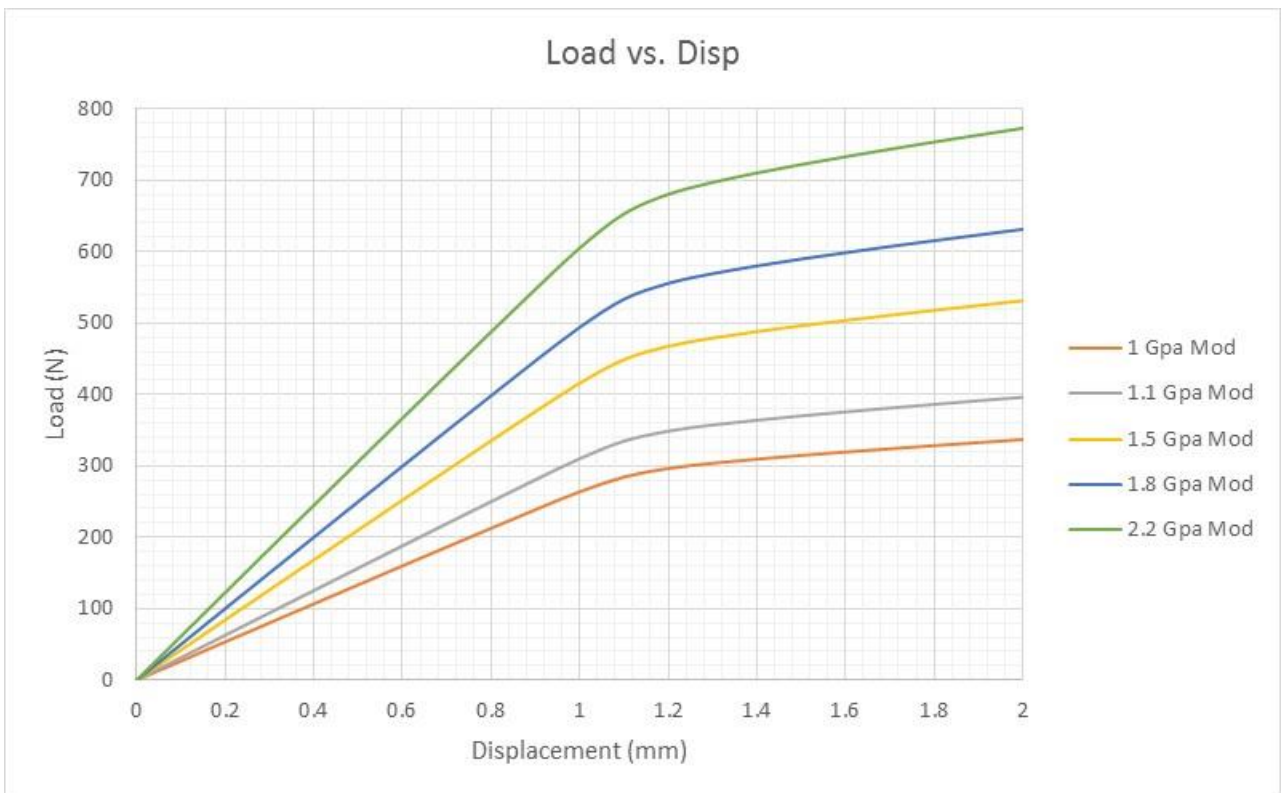


Figure 24. Load vs. Displacement for various moduli icosahedron modeled with Abaqus

Icosahedron MTS Results

With the response of the experimental specimen generally unknown for this loading case, all we had was an estimate from the FE model. Therefore, initial very small

displacement test cases, approximately 0.5-1mm compression, were performed on the printed frame. These test cases allowed us to see whether the frames response measured by the MTS system was repeatable and allowed us to determine which orientation of the icosahedron gave consistent results. Loading of up to 1mm was chosen because that was the limit where non-linear displacement began to occur in the FE models, and permanent deformation of the frame was not desired at this point. With consistent and repeatable test runs, it was determined that the behavior of the frame was sufficiently captured to load the frame to failure. Figure 25, shows the failure test run load vs. displacement along with the 1 GPa modulus FE model analysis. The experiment indicates that structural yielding occurs first at approximately 1 mm because the frame continues to carry the load. The material failure occurs due to the large deformations brought about by the structural yielding at approximately 2 mm. The deformations produce necking, which increases the stress, causing material failure. The results obtained lie almost exactly with the 1 GPa Abaqus model, up until material failure in the experiment around 2 mm. A side by side of the FEM and experimental model frame in their deformed and un-deformed states are superimposed on themselves and are shown in Figure 26. The important thing to note in Figure 26 is the similarities of the displacement magnitude and direction of the beams between the FEM and the test specimen. The green image is the deformed state for both of the models. The black on the left and the orange on the right are the unreformed states of the FEM and test specimen. The images to produce the right image in Figure 26 were captured using a high speed camera recording at 40 frames per second.

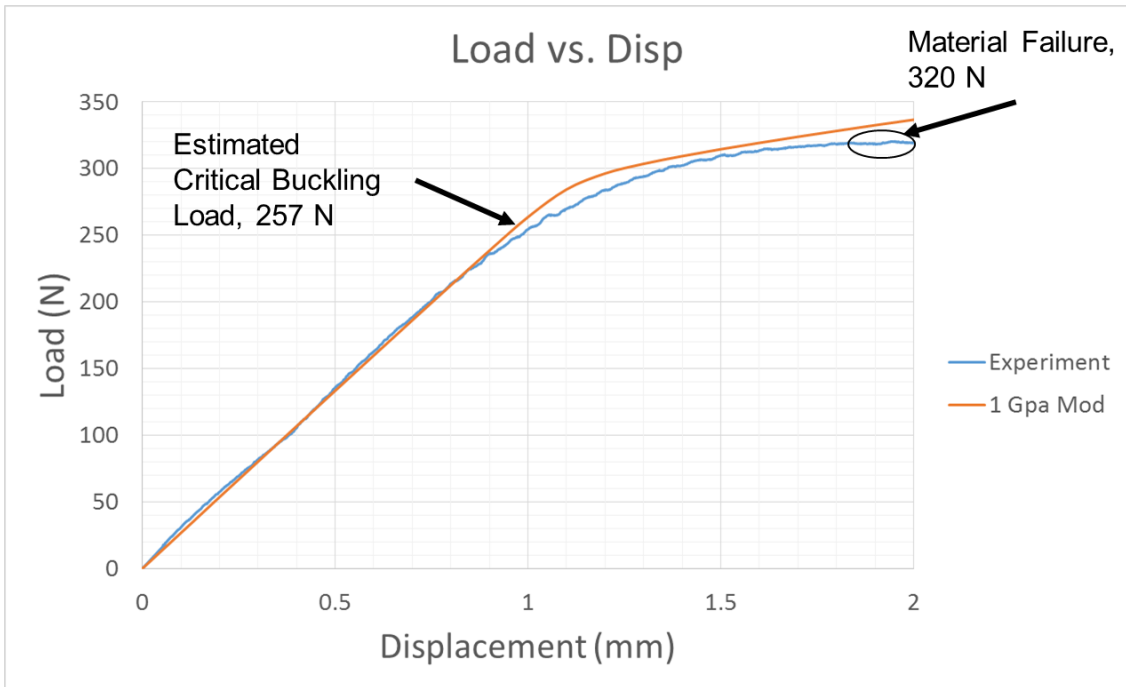


Figure 25. Load vs. Displacement of Abaqus MTS and Experiment

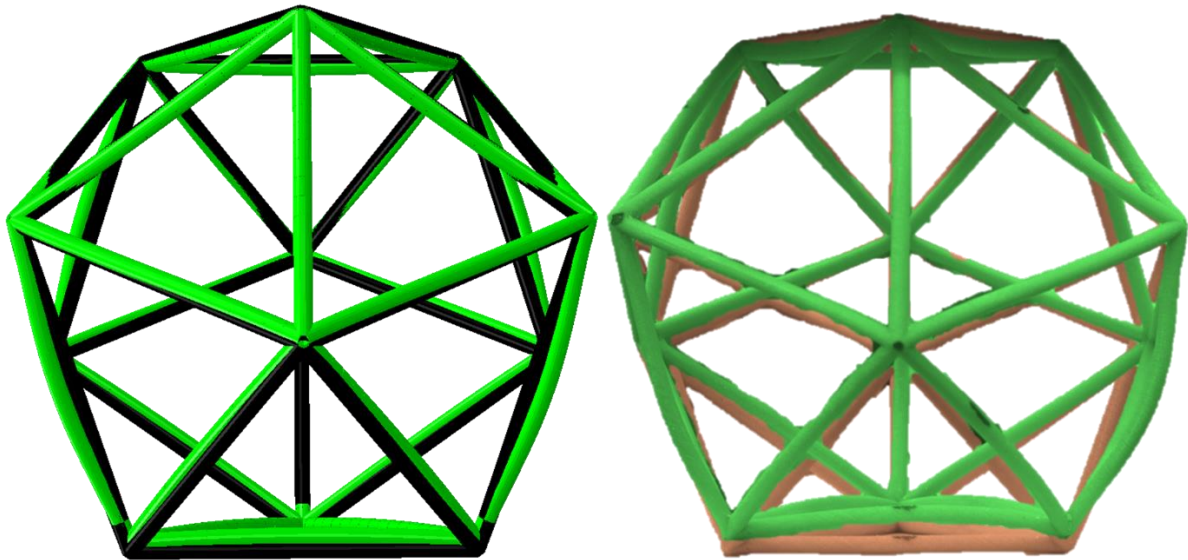


Figure 26: Superimposed before and after deformation images. Abaqus images-Left, High speed camera experimental images-Right. (Green color is deformed image)

3D printed Icosahedron Frequency Analysis Setup

Due to the fact that the material properties of the printed icosahedron frame are somewhat ambiguous as pointed out by VT, further testing was desired to see if the material properties determined from the MTS experiment could be confirmed. Therefore, a non-destructive test was developed to investigate the material properties of the printed icosahedron. This test was to conduct an experimental and FE frequency modal analysis on the icosahedron frame in order to compare them. The modal analysis in Abaqus reports the eigenvalues and eigenvectors that satisfy the general eigenvalue problem for an undamped FE model. This general expression is shown in equation (45). Where M^{MN} is the mass matrix, K^{MN} is the stiffness matrix, λ are the eigenvalues, and U^N are the displacements or eigenvectors that produce the eigenvalues. This equation can be rewritten in terms of natural frequencies, shown in equation (46). Where ω^2 is the natural frequency and ϕ^N is the corresponding eigenvector. Equation (46) can estimate (MN) number of eigenvalues and eigenvectors for the FEM within Abaqus. For this analysis, the eigenvalues or frequencies that are of interest are the low modes which are typically referred to as first bending and first torsion modes, disregarding rigid body modes. These are the smallest eigenvalues that produce a bending or torsion eigenvector shape.

$$M^{MN}U^N\lambda + K^{MN}U^N = 0 \quad (45)$$

$$(-\omega^2M^{MN} + K^{MN})\phi^N = 0 \quad (46)$$

When conducting a frequency analysis, the only parameters that have an effect of the eigenvalues are the stiffness, mass, damping, and boundary conditions of the system. It is assumed that the system is undamped or there is no additional damping other than the structures natural damping associated with its mass and stiffness. With the mass and

stiffness of the system determined by the structures geometry and material properties, it leaves only the boundary conditions to be defined. It was desired for this experiment to use what is known as a free-free boundary condition or “no” boundary condition. This is simple to execute within Abaqus, where the user just applies no boundary conditions to the model and runs the frequency analysis. However, in an experimental setting, it is not as simple as just not applying a boundary condition. Simply floating the object in the air and having it remain in relatively the same position is not an option unless the experiment were conducted in space. The experimental specimen needs to have some sort of boundary condition. Fortunately, creating the environment of effectively no boundary condition, or free-free condition, is not overly difficult. The free-free boundary condition for the icosahedron model was conducted by selecting one of the vertices, with no particular importance, and looping a string around it and hang the icosahedron in air. This free-free experimental boundary condition is shown in Figure 27. The experimental data was obtained and analyzed using a Polytec PSV-500 laser vibrometer system, shown in Figure 28. In addition to the Polytec system, an impulse hammer was used to excite the system so that the natural frequencies could be extracted. The impulse hammer, PCB product model number 086C01, is shown in Figure 29. The hammer was fitted with the soft tip and the extended mass so that low frequency values would be excited and therefore measured by the Polytec system. With sufficient practice, the hammer was used to strike the icosahedron on the blue point in Figure 27, a series of three times to obtain the modal response.

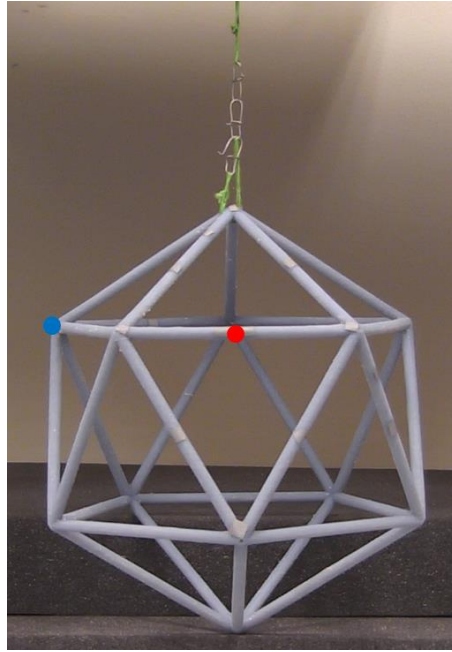


Figure 27: 3D printed Icosahedron hanging with a free-free boundary condition. The red dot indicated where the laser vibrometer was focused and the blue dot indicates where the structure was excited.



Figure 28: Polytec PSV-500 Laser Vibrometer Frequency Analysis System.

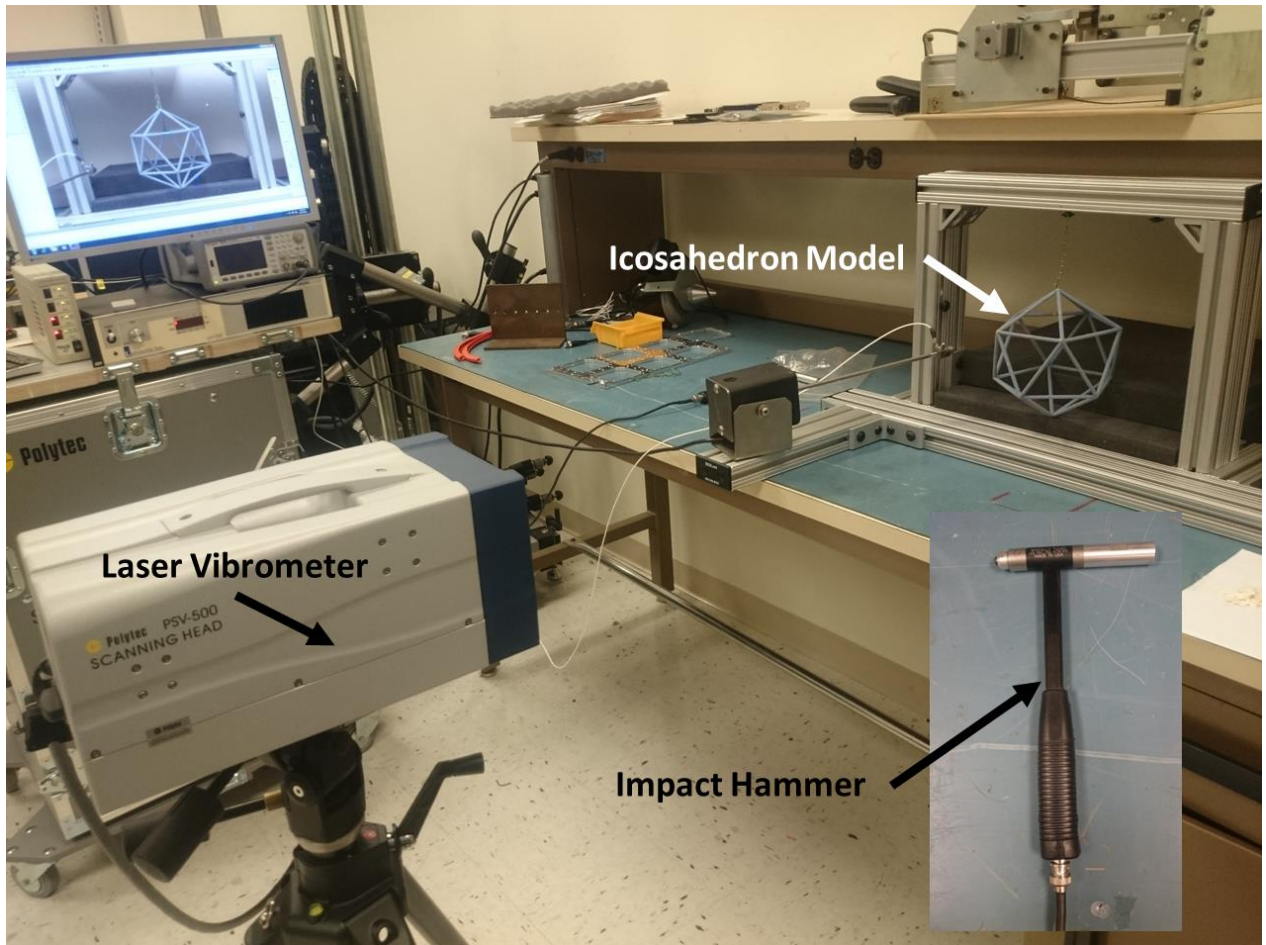


Figure 29: 3D printed icosahedron frequency analysis experimental set-up.

With the experiment set up, a corresponding FE model was developed to estimate the eigenvalues associated with the 3D printed icosahedron with 1 GPa modulus of elasticity. The geometry and mesh of the model is the same as the MTS model, shown in Figure 30. The difference here is that there are no loads or boundary conditions applied and a frequency step is used to extract the eigenvalues and eigenvectors of the icosahedron.

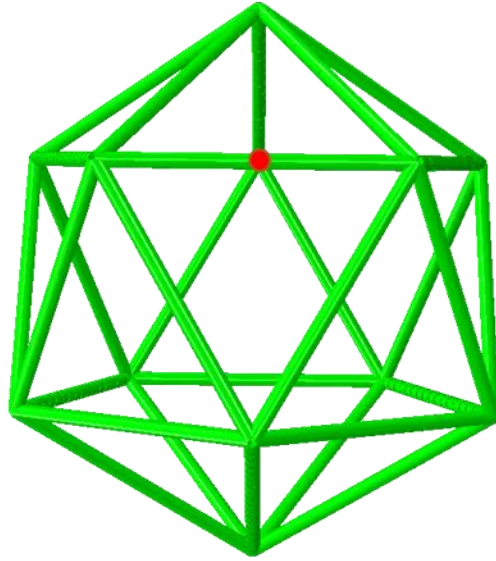


Figure 30: FE Icosahedron model for frequency analysis. (Red dot indicates the traced beam for experiment comparison.)

3D printed Icosahedron Frequency Analysis Results

In order to extract experimental natural frequencies from the icosahedron, the laser of the laser vibrometer needs to be focused on a particular point or series of points along the structure. Focusing on more than one point of the structure would allow the user to view quasi mode shapes. They would not be the full shape of the structure only because a single laser is being used and the displacement magnitudes and directions can only be tracked in a single plane. If the complete picture were desired then a three dimensional array of lasers would need to be set up. Extracting and viewing the mode shapes were not the priority of this experiment, therefore a single laser is sufficient enough to capture the natural frequencies of interest. An important consideration, when using a laser vibrometer to scan a point for a frequency analysis, is that the frequency results will be specific to the point scanned, not the global structure. With that in mind,

the frequency response computed by the vibrometer software will only capture the frequencies with the largest harmonic response at the point scanned. This is important to note when looking to compare the experimental results to FE frequency results, which is discussed below. The input signal, coherence, and frequency response of the point scanned in Figure 27, with three averaged impulse hammer excitations are shown in Figure 31, Figure 32, and Figure 33.

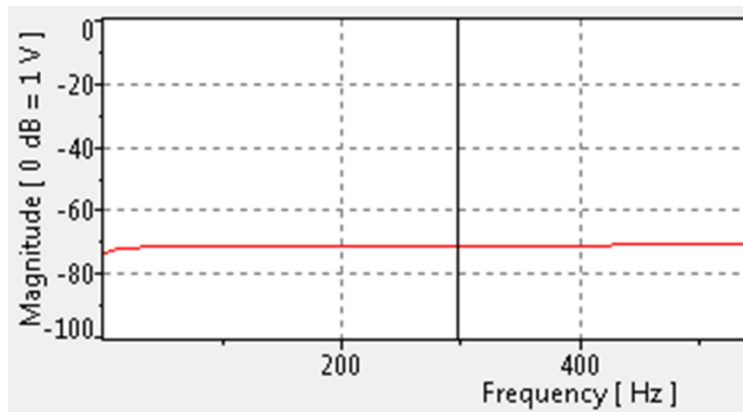


Figure 31: Impulse Hammer Input Signal

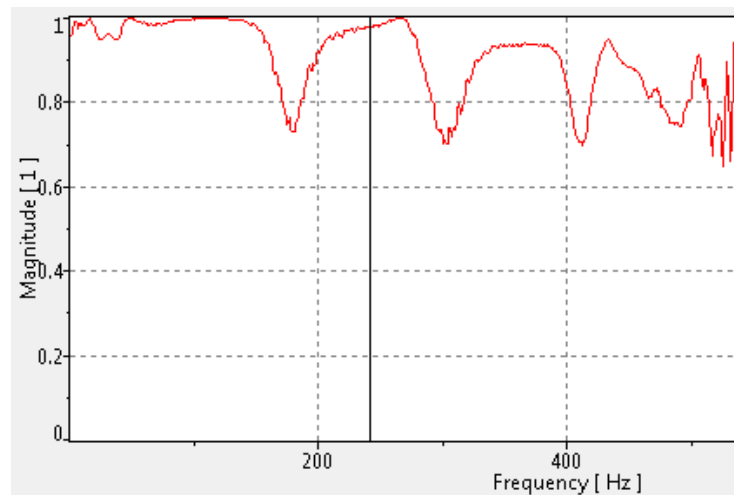


Figure 32: Coherence of Input Signal to Laser Response

It is important to excite the structure more than once and average the data. Without doing this, a coherence value cannot be obtained and the data obtained could be

heavily subject to noise. The averaging of the power spectrums associated with the input and output signals allows for the noise values to be approximated. A coherence value close to 1 indicates that the signal-to-noise ratio is high, or good. This means that the power input to the system by the hammer is reflected strongly in the power measured by the vibrometer. This evaluation is performed across the power spectrum which is why the coherence magnitude changes with respect to frequency. The averaged input signal in Figure 31, shows that all of the strikes were single impacts and not multiple impacts, which would show up as an oscillatory component on the input signal. Additionally, the input signal was flat across the frequency spectrum which ensures that differing amounts of energy were not input at differing frequencies. In other words, the same amount of energy or power was provided across all of the frequencies. This is important when analyzing the frequency response function (FRF), because it ensures that a constant amount of power is provided across the entire frequency band analyzed. If the power input were not constant, then the FRF would reflect those inconsistencies, which produce error in determining which frequencies are resonant.

In analyzing the FRF in Figure 33, and confirming that good coherence is achieved in Figure 32, at the peaks, the frequencies of 229 Hz and 439 Hz were determined to be the first two natural frequencies of the scanned beam. From here it was necessary to determine whether the experimental boundary condition provided was indeed a free-free condition. According to McConnell [24], an experimental free-free condition is met when the measured rigid body frequency is 10 times less than the first measured natural frequency. In this case this rigid body frequency measured was 13 Hz

and the first natural frequency was 229 Hz, which is 17 times greater than the rigid body frequency, ensuring that the assumption of a free-free boundary condition is met.

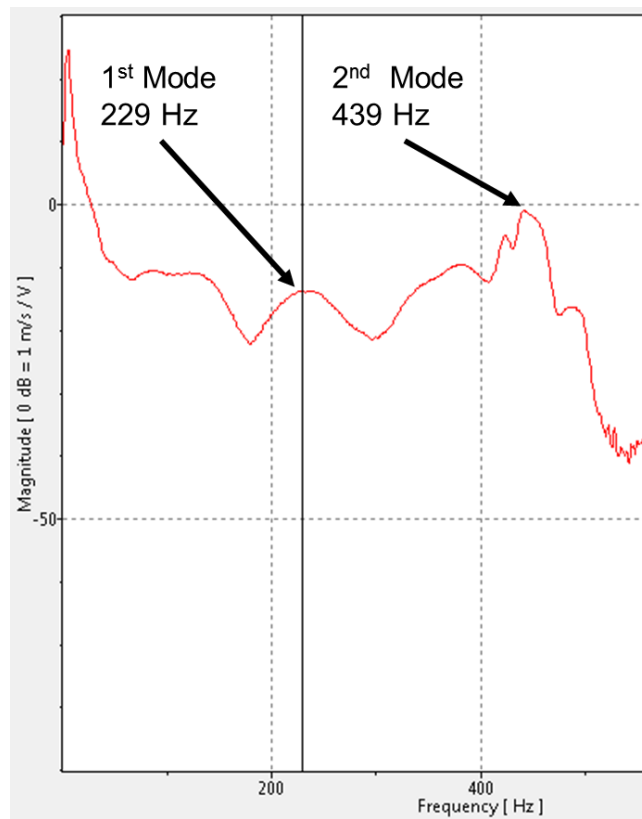


Figure 33: 1st and 2nd modes computed from the frequency analysis of the experimental Icosahedron by the Polytec software.

With the free-free boundary condition confirmed, the natural frequencies extracted from the Polytec system can be compared to the eigenvalues estimated by Abaqus. Comparing the two evaluations is not completely straightforward as comparing the experimental values to the first two eigenvalues estimated by Abaqus. When Abaqus estimates the eigenvalues, it is looking at the entire discretized structure and not just one point as in the experimental set-up. Therefore, Abaqus lists the eigenvalues from low to high of the entire structure, and the results need to be “filtered” to specially focus on the response of the beam scanned in the experiment. A point, having the same position as the

one scanned by the laser vibrometer was identified in the FEM, and its eigenvalues and eigenvectors were observed. Since the laser vibrometer scans for velocity values of the point it is scanning the frequencies that produce the largest change in displacement with the specimen are associated with the points natural frequencies. A single scanning laser vibrometer can only measure the velocity component in the direction normal to the laser head. Since this is true the eigenvalues and eigenvectors of the point observed within the Abaqus model needs to be observed from the perspective of the laser vibrometer to be able to compare the their respective natural frequencies or eigenvalues. Therefore, the only eigenvalues that were considered natural frequencies of the point observed in the FEM were those whose eigenvector directions matched the direction the laser vibrometer was scanning in. These eigenvectors were singled out and their respective eigenvalues were 240.58 Hz and 430.10 Hz within Abaqus. This is shown in Figure 34. The error between the experimental values and Abaqus values are 4% and 2% respectively for the two modes from lowest to highest with the modulus of elasticity equal to one GPa in the Abaqus model. This serves as another point of confirmation alongside the MTS results that that modulus of the printed icosahedron is approximately one GPa.

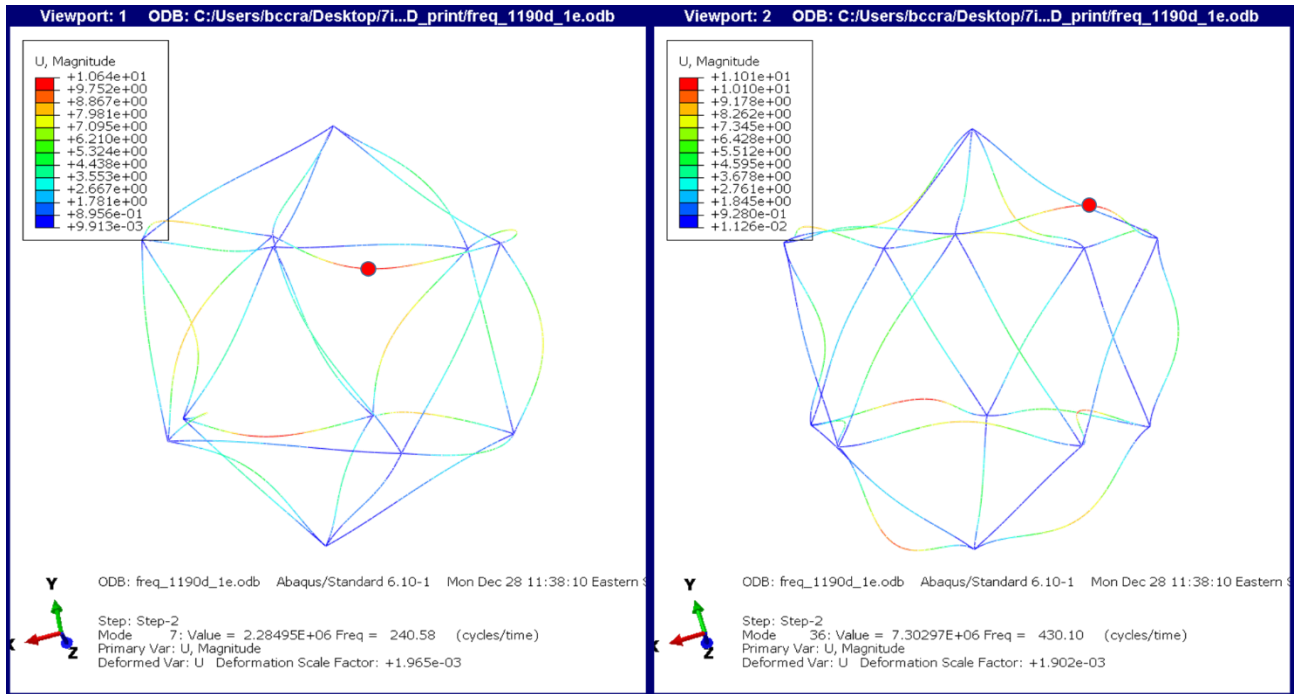


Figure 34: Eigenvalues and Eigenvectors of the first two modes in Abaqus associated with the beam scanned from the laser vibrometer experiment (the red dot indicates the point observed in the model, matching the laser vibrometer).

Chapter IV Summary

The objective of this chapter was to first describe the buckling theory related to cylindrical beams and the effect that the wall thickness/beam radius has on the estimated critical buckling loads. Next, the chapter describes the two experimental tests conducted, MTS and modal analysis, on a 3D printed icosahedron. The experiments were to validate the icosahedron FEMs, as well as the technique of modeling them. It was shown that the load versus displacement response of the frame in the MTS and the modal analysis frequencies were approximated almost exactly by their respective Abaqus models. However, there were problems that arose with the 3D printed material, where it is highly subject to variability in its material properties. This required further experimental testing to approximate with good confidence what the exact material properties were. The

experiments proved the validity of the modeling technique, and it proved that a robust model has been developed which will be used in the next two case study analyses.

V. Metlen Icosahedron VLTAV DSE and Feasibility Assessment Case Study

This chapter applies the methodology developed in chapter III on the icosahedron design proposed by Metlen in 2012 with modern material and manufacturing constraints. The chapter begins with a discussion on the development of the icosahedron finite element models (FEM) to be analyzed for stresses, displacements, and critical buckling loads. Once, the FEMs are developed a model convergence study is performed to determine what mesh settings are necessary to produce converged responses (stresses, displacements, and critical buckling loads). With a converged model mesh criteria, the DSE methodology developed in chapter III is performed, beginning with the dimensional analysis and ending with a structural response design space. The space will then be evaluated to determine if any feasible icosahedron designs exist within the boundaries applied.

Icosahedron Finite Element Models Development

Icosahedron Geometry Development

An icosahedron is a platonic solid that has 20 faces, 30 edges, and 12 vertices. Each face of the icosahedron is composed of the same unit equilateral triangle, making it a regular polyhedron. In order to model the structure, the geometry has to be established. The parameters defining the geometry of the icosahedron are vertex locations, surface area, and volume. Considering the vertex locations, it is noted that the vertices of the icosahedron all lie on sphere circumscribing the polyhedron. Therefore, the only parameter needed to determine the vertex locations is the radius of the circle that inscribes the icosahedron. In spherical coordinates (ϕ, θ, r) , we will identify the 12 vertices. The first and last will be top and bottom vertices, followed by two groups of five

vertices in between the top and bottom points. The vertex points in spherical coordinates are shown in Table 10, where r_{icos} is equal to the radius of the sphere circumscribing the icosahedron. In addition, two illustrations of the vertex locations are shown in Figure 35 (a top down view) and Figure 36 (an isometric view). It is also shown in Figure 36 how the vertices lie on a circumscribing sphere, by noticing the vertices that lie on the dotted circle.

Table 10: Icosahedron vertex locations.

Icosaedron vertex locations			
Point	ϕ (degrees)	θ (degrees)	r (meters)
1	90	0	r_{icos}
2	$\tan^{-1}(1/2)$	0	r_{icos}
3	$\tan^{-1}(1/2)$	72	r_{icos}
4	$\tan^{-1}(1/2)$	144	r_{icos}
5	$\tan^{-1}(1/2)$	216	r_{icos}
6	$\tan^{-1}(1/2)$	288	r_{icos}
7	$-\tan^{-1}(1/2)$	36	r_{icos}
8	$-\tan^{-1}(1/2)$	108	r_{icos}
9	$-\tan^{-1}(1/2)$	180	r_{icos}
10	$-\tan^{-1}(1/2)$	252	r_{icos}
11	$-\tan^{-1}(1/2)$	324	r_{icos}
12	-90	0	r_{icos}

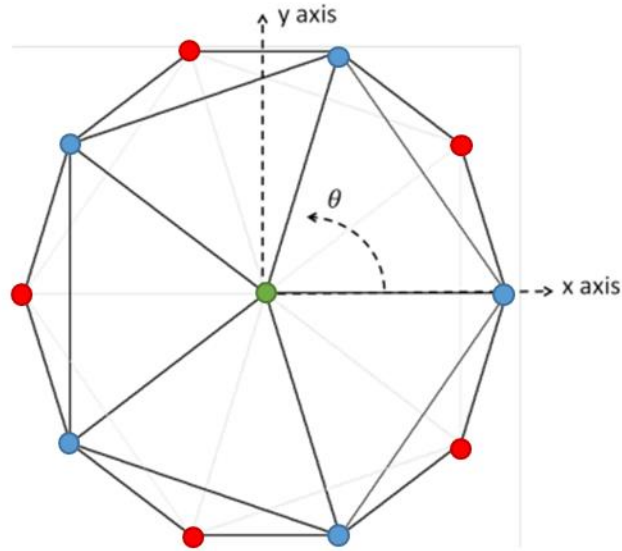


Figure 35: Icosahedron top view (The green dot indicates the top and bottom vertices, the blue dots indicate the top group of five vertices, and the blue dots indicate the bottom group of five vertices).

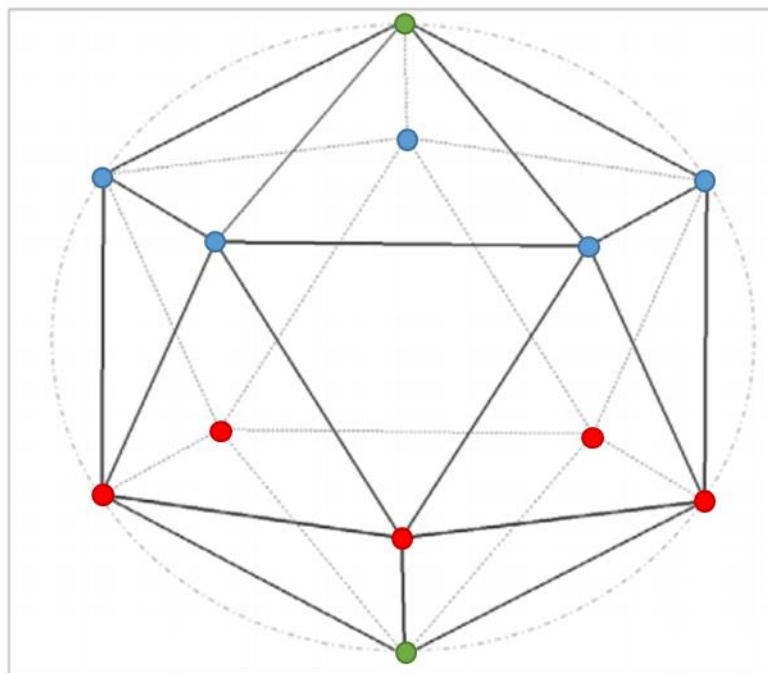


Figure 36: Icosahedron Frame with vertex labels (The green dot indicates the top and bottom vertices, the blue dots indicate the top group of five vertices, and the blue dots indicate the bottom group of five vertices).

The importance of using spherical coordinates is that the scale or radius of the vehicle can be altered by adjusting only the r_{icos} parameter. With the vertex locations known, and the fact that every edge is the same length, the length of one of the edges can be determined by computing the distance between any two adjacent vertices with equation (47) in Cartesian coordinates. Additionally, the edge length can also be computed using equation (48), where ψ is equal to the golden ratio $\left(\frac{1+\sqrt{5}}{2}\right)$. With the edge length known, the surface area, A_I , and volume, V_I , can be readily computed using equations (49) and (50) [1], [5].

$$a = \sqrt{(x_1 - x_2)^2 + (y_1 - y_2)^2 + (z_1 - z_2)^2} \quad (47)$$

$$a = \frac{2r_{icos}}{\sqrt{\psi\sqrt{5}}} = \frac{4r_{icos}}{\sqrt{10 + 2\sqrt{5}}} \quad (48)$$

$$A_I = 5\sqrt{3}a^2 \quad (49)$$

$$V_I = \frac{5}{12}(3 + \sqrt{5})a^3 \quad (50)$$

Icosahedron Sizing Equations

In order to model the Metlen icosahedron in Abaqus for analysis, the independent variables that define the geometry need to be computed. These variables are beam radius and thickness for the frame (hollow rods) and skin thickness for the skin. To determine

these parameters, the sizing equation, (51), developed by Rodriguez [5] will be utilized. Equation (51) is a general formula to compute the W/B for any frame-skin structure with an internal vacuum.

$$\frac{W}{B} = \frac{V_s \rho_s + V_f \rho_f + (V_i - V_r) \rho_{air,i}}{(V_i - V_r) \rho_{air,o}} \quad (51)$$

Where, V_f and V_s are the frame and skin volume respectively; ρ_f , ρ_s , $\rho_{air,i}$, and $\rho_{air,o}$ are the frame, skin, internal air, and external air density respectively; V_i and V_r are the initial internal volume and the volume lost or reduced due to the structure deforming when an internal vacuum is present. The W and B are the weight and buoyant force of the vehicle respectively. In order to compute the frame and skin dimensions for the icosahedron VLTA V, the first step is to set the left hand side (W/B) of equation (51) to an initial value. For instance, if an icosahedron design was desired to float or carry a payload the initial value of W/B in equation (51) would be set to a number less than one (indicating a positively buoyant design). Now, for this example, just because a positively buoyant vehicle can be geometrically sized does not mean the design would actually float or carry any payload in reality. The proposed design not only has satisfy the W/B constraint of being less than one, it has to not fail due to material and geometric instability as well. It is noted, that the W/B value can only be less than one when the weight of the vehicle is less than the buoyant force produced. Therefore, when this is performed, any amount of weight given up for buoyancy, directly reduces the design's resistance to material and geometric instability. For this research, since the objective is to determine if structurally feasible designs exist within a bounded design space the W/B value for all designs will be set to one. This value was chosen because it is desired to give every design considered its

best chance for structural feasibility and technically produce a floating design. A W/B equal to one does not produce a VLTA V that can rise, however, it does produce a VLTA V that can float (neutrally buoyant). It is noted that the initial W/B value selected is only an initial value so that the vehicle can be sized. After an FEA is conducted, the final W/B is determined by calculating the internal volume based on the displacements within the frame and skin.

The next step, is to specify what percentage of the designs weight (W) is to be dedicated to the frame and skin. To do this, Rodriguez introduced two variables,

$\frac{W}{B_f}$ and $\frac{W}{B_s}$, frame W/B and skin W/B where the total of these W/B's is equal to the W/B on the left hand side of equation (51). Utilizing equation (51) and the introduction of $\frac{W}{B_f}$ and $\frac{W}{B_s}$ Rodriguez developed equations (52-54) to compute an icosahedron VLTA V

design's frame and skin dimensions.

$$r_{b_{icos}} = r_{icos} \sqrt{\frac{\frac{W}{B_f} \rho_a}{39.0742(2c - c^2)\rho_f}} \quad (52)$$

$$c = \frac{t_{b_{icos}}}{r_{b_{icos}}} \quad (53)$$

$$t_{s_{icos}} = \frac{r_{icos} \rho_a \frac{W}{B_s}}{3.77523 \rho_s} \quad (54)$$

Where, $r_{b_{icos}}$ is equal to the icosahedron frame beam radius, $t_{b_{icos}}$ is equal to the frame beam thickness, and $t_{s_{icos}}$ is equal to the icosahedron skin thickness.

Icosahedron Finite Element Models

Now that the dimensions of any icosahedron VLTAV design can be determined, utilizing equations (52-54) with $\frac{W}{B}$, $\frac{W}{B_f}$ and $\frac{W}{B_s}$ specified ($\frac{W}{B} = 1$ in this research), FEMs can be constructed to analyze the stresses, displacements, and critical buckling pressure of the design. Before any analysis can be conducted, three additional independent variables are required to perform the structural analysis. These are, the frame and skin's material modulus of elasticity (E_b , and E_s), Poisson's ratio (ν), and pressure applied to the membrane (P). For this research, the Poisson's ratio (ν) will be a constant 0.33 for all materials. This value is based on the Poisson's ratio that Rodriguez used in his analyses. Rodriguez showed in his research, that altering Poisson's ratio had very little effect on the overall structural response [5]. As stated in chapter III, two Abaqus solvers (linear and non-linear) will be utilized to approximate the icosahedron design's stresses, displacements, and critical buckling pressure. The solver used to approximate the stresses and displacements will be the non-linear solver. The FEM for this analysis will include both the frame and skin coupled together, shown in Figure 37. Remember, the membrane stresses and displacements can only be analyzed with a non-linear solver because of the pressure load and expected large displacements compared to its thickness. The FEM in utilizes numerical tie constraints to tie the membrane to the mid-section of the wire beams at the points where the membrane and beams overlap. This allows the external pressure applied to the membrane to evenly distribute the pressure load to the frame. The

boundary conditions are applied to the frame at any two opposite vertices where vertical movement and rotations are allowed. These constraints are consistent with those developed by Rodriguez [5].

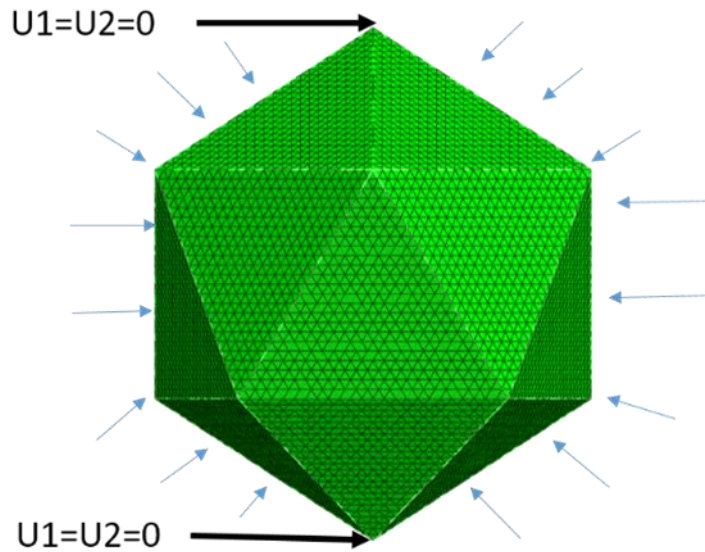


Figure 37. Boundary Conditions and Loads for the Icosahedron FE model.

The solver used to approximate the critical buckling load of a design, will be the linear buckling solver. As stated in the structural feasibility analysis section of chapter III, the only viable way to perform a buckling analysis on the icosahedron VLTAV is to consider the frame alone, as Rodriguez did [5]. The FEM for this analysis will include the frame alone with reference points added. So that the “pressure” load can be distributed to the frames beams as if the membrane were there. This is shown in Figure 38. The boundary conditions for the linear FEM are the same as described for the non-linear model.



Figure 38: Icosahedron Frame with Reference Point Loading

The finite element models developed for this research were analyzed using Abaqus. The beams of the frame were modeled using 2D wire-beam elements in 3D space. The beam elements were given a hollow circular profile based on the beam radius and thickness specified in the sizing equations. The beam element chosen in Abaqus was the B32 element, which is a quadratic element with three nodes and six degrees of freedom (DOF) at each node and is based on Timoshenko's beam theory. This element's DOF, translation and rotation, allow it to capture both axial and transverse loads. The Timoshenko beam theory was chosen because it allows for a wide variety of beam cross sections and length to be chosen without sacrificing accuracy of the solution, as well as the ability to capture in-plane deformation. The skin of the structure was modeled using membrane elements for the static non-linear analysis. The membrane elements chosen

were M3D3. The M3D3 element is a triangular element with three nodes and three displacement DOF at each node.

Icosahedron FE Mesh Convergence Study

To ensure that the stresses, displacements, and critical buckling loads approximated by the non-linear and linear solvers are accurate, the FEM's need to have a converged mesh. The mesh in finite elements, is the discretization of the model into what are called elements. Hence, the beam and membrane elements discussed above. For example, let's consider one of the legs of one of the triangles that make up the icosahedron. During the FEA, displacements and stresses are computed along the length of the beam. If the leg is represented by a single element, the stresses computed for that analysis would be far lower than what they would be in reality. This is because when only a single element is used, the leg in the model has only 6 DOF on each end and cannot accurately predict the displacements and stresses. Therefore model convergence tests are carried out on FEMs to determine what discretization of the model is necessary to produce converged displacement and stress results.

The convergence study performed on the icosahedron model, was performed using the non-linear solver with the frame-skin FEM. The model was analyzed at a single design point repeatedly, with only the number of elements varying, to determine what minimum element discretization produces a converged stress and displacement response. The design point chosen for the repeated analysis is shown in Table 11, where the values chosen are based on the bounds decided in the following DOE section.

Table 11: Icosahedron Convergence Study Parameters.

Icosahedron Convergence Study Parameters		
Parameter		Units
W/Bf	0.9	
W/Bs	0.1	
ρ_a	1.225	kg/m ³
ρ_b	1250	kg/m ³
ρ_s	970	kg/m ³
c	0.005	
r_{icos}	0.1524	m
Eb	2.93E+11	Pa
Es	1.72E+11	Pa
P	101325	Pa

The number of elements per edge or seed number per edge that were tested were: [5, 10, 15, 20, 25, 30, and 35]. The results of the convergence study are shown in Figure 39, where max frame stress, max skin stress, final W/B, and Abaqus CPU solver time are plotted versus seed number per edge.

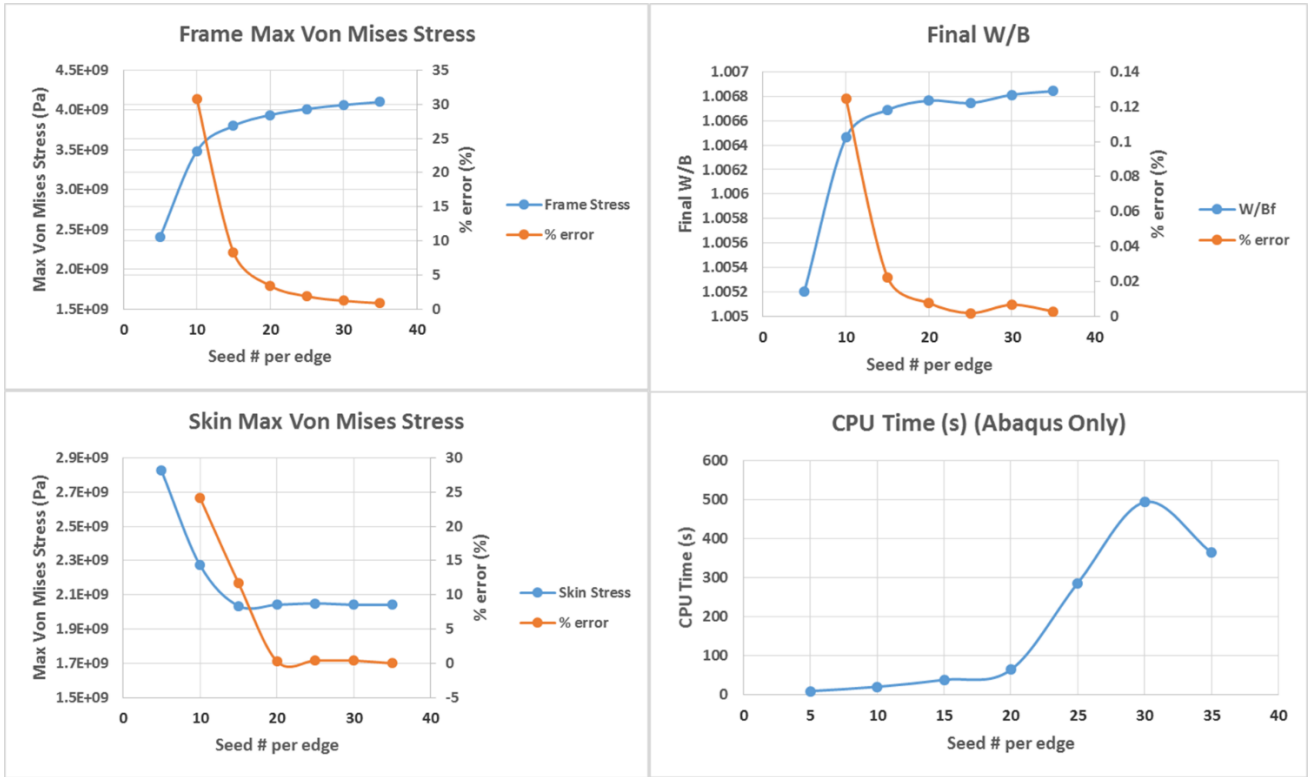


Figure 39: Icosahedron Vacuum FE model mesh convergence study.

The percent error term in all of the plots was computed by using equation (55).

Where p represents the output values, stress and final W/B, and i denotes the current iteration. The error term was the percent difference between each seeding iteration.

$$\left(\frac{p_i - p_{i-1}}{p_i} \right) 100 = \text{Percent Difference} \quad (55)$$

The number of elements per edge that was determined to yield a converged solution was 20 elements per edge. This seeding produced a frame stress, skin stress, and final W/B solution that was 4%, 0.3%, and 0.007% different than the solution with 35 elements per edge. This seeding also produced a CPU computation time of approximately 1 minute, 82% less time than it took to solve the 35 elements per edge model.

Icosahedron VLTAV FEM Dimensional Analysis

As stated in chapter III, “The ultimate purpose of the dimensional analysis to be performed on the FEMs, is to provide valuable relationships between the independent and dependent variables that define the system and to reduce the complexity of the model.”

The dimensional analysis will be conducted on only the icosahedron frame-skin model and not the frame alone model. This is because, the frame-skin model is the FEM that the stresses and displacements will be extracted from during the DOE. The dimensional analysis on the frame-skin FEM will follow the steps indicated in chapter III.

Step 1: Determine independent and dependent variables

The icosahedron model is defined in terms of its sizing and FE inputs. Recall equations (52-54), where the dimensions of the frame and skin are determined. These equations can be expressed in terms of their inputs, as shown in Table 12 in the first column. Now, recall the necessary FE inputs to define the FEM for analysis, as shown in Table 12 in the second column. With all of the variables that define the FEM system listed, we can select which variables that are independent and define the FEM completely. Beginning with the first column of Table 12 we select the first instance of the variables on the right hand side of the equations. These variables are listed in red. Note, that air density (ρ_a) does appear on the right hand side but is not selected to be an independent variable. This is because air density depends on another variable, altitude (h). Continuing to the second column of independent variables, we have frame and skin modulus of elasticity, pressure, and Poisson’s ratio. The variables that are selected as independent are listed in red (moduli and pressure). Note, that pressure (P) is also a function of altitude. Therefore we must choose to include either air density (ρ_a) or

pressure (P) as an independent variable but not both. When one is specified the other is as well and therefore both are dependent on each other. The last column of Table 12 indicates the dependent variables or FEM responses that are desired to be observed. They are max frame stress ($\sigma_{f_{max}}$), max skin stress ($\sigma_{s_{max}}$), and displacement (u). With the independent and dependent variables determined, their relationship can be written as equation (56).

Table 12: Icosahedron FEM Independent Variables.

Icosahedron Sizing Independent Variables	Finite Element Model Independent Variables	Finite Element Model Dependent Variables
$r_b = r_b \left(\frac{W}{B_f}, c, \rho_a, \rho_b, r_{icos} \right)$	E_b	$\sigma_{f_{max}}$
$t_b = t_b(c, r_b)$	E_s	$\sigma_{s_{max}}$
$t_s = t_s \left(\rho_a, \frac{W}{B_s}, \rho_s, r_{icos} \right)$	$P = P(h)$	u
$\rho_a = \rho_a(h)$	ν_b, ν_s	

$$\sigma_{f_{max}}, \sigma_{s_{max}}, u = f \left(\frac{W}{B_f}, c, \rho_b, r_{icos}, \frac{W}{B_s}, \rho_s, E_b, E_s, P \right) \quad (56)$$

For this model there are three dependent variables and nine independent variables, making the constant $k = 12$. Additionally, equation (56) can be rewritten as equation (57).

$$x_k = \left(\sigma_{f_{max}}, \sigma_{s_{max}}, u, \frac{W}{B_f}, c, \rho_b, r_{icos}, \frac{W}{B_s}, \rho_s, E_b, E_s, P \right) \quad (57)$$

Step 2: Define Dimensions

The independent variables are known as the dimensioned quantities that make up the physical law for the model (dependent variables), which in this case is the FEA of

either the icosahedron. The fundamental dimensions that make up the dimensioned quantities are $M = \text{mass}$, $L = \text{length}$, and $T = \text{time}$. With the fundamental dimensions known, the independent and dependent variables can be represented by their dimensions, shown in Table 13.

Table 13: Icosahedron FEM Independent and Dependent Variable Dimensions.

Icosahedron FEM Independent and Dependent Variable Dimensions		
Symbol	Units	Dimensions
$\frac{W}{B_f}$ (Frame W/B)	Non-dimensional	[1]
$\frac{W}{B_s}$ (Skin W/B)	Non-dimensional	[1]
$c \left(\frac{t_{b_{icos}}}{r_{b_{icos}}} \right)$	Non-dimensional	[1]
r_{icos} (Icosahedron radius)	m	$L^1 M^0 T^0$
ρ_s (Skin density)	kg/m^3	$L^{-3} M^1 T^0$
ρ_b (Beam density)	kg/m^3	$L^{-3} M^1 T^0$
E_s (Skin modulus)	Pa	$L^{-1} M^1 T^{-2}$
E_b (Beam modulus)	Pa	$L^{-1} M^1 T^{-2}$
P (Applied pressure)	Pa	$L^{-1} M^1 T^{-2}$
$\sigma_{f_{max}}$ (Max frame stress)	Pa	$L^{-1} M^1 T^{-2}$
$\sigma_{s_{max}}$ (Max skin stress)	Pa	$L^{-1} M^1 T^{-2}$
u (Model displacements)	m	$L^1 M^0 T^0$

Step 3: Select the Dimensionally Independent Subset

Since we have three dimensions making up the model (L , M , and T) we can select up to three independent variables to be in the dimensionally independent subset. Following the rules laid out in chapter III for selecting the subset, the variables r_{icos} , ρ_b , and E_b are chosen. These three variable are chosen because they are not any of the dependent variables, they are not dimensionless, and their dimensions cannot be created by combining the other two in the subset. Note, that the FEM has two terms with dimensions

of density (ρ_b, ρ_s) and three terms with dimensions Pa (E_s, E_b, P). When selecting the subset, ρ_s could have been selected instead of ρ_b , and either of the other terms with units Pa could have been selected instead of E_b . r_{icos} had to be selected because it was the only independent variable with units of only length (L).

Step 4: Compute Pi Parameters

Now that a subset has been chosen the Π terms can be solved for. Since this model has 12 terms and three parameters in the subset, there are nine Π terms to be solved for. Conveniently, three of the independent variables are non-dimensional ($\frac{W}{B_f}, \frac{W}{B_s}$, and $\frac{t_{b_{icos}}}{r_{b_{icos}}}$) and therefore are inherently Π parameters. The remaining independent and dependent variables that are not in the dimensionally independent subset are plugged into equation (58) to create the remaining Π parameters as shown in chapter III. An example of how to compute Π_1 will be shown, and the same procedure will be used to compute the remaining Π terms, but will not be shown.

$$\Pi_i = x_j x_6^a x_7^b x_{10}^c \quad (58)$$

$$\Pi_1 = x_1 x_6^a x_7^b x_{10}^c:$$

$$L^0 M^0 t^0 = L^{-1} M^1 t^{-2} (L^{-3} M^1 t^0)^a (L^1 M^0 t^0)^b (L^{-1} M^1 t^{-2})^c$$

$$0 = -1 - a3 + b1 - c1$$

$$0 = 1 + a1 + b0 + c1$$

$$0 = -2 + a0 + b0 - c2$$

Solve for a , b , and c :

$$\begin{aligned}
a &= 0 \\
b &= 0 \\
c &= -1
\end{aligned}$$

Plug a , b , and c into $\Pi_1 = x_1 x_6^a x_7^b x_{10}^c$:

$$\Pi_1 = \frac{x_1}{x_{10}} = \frac{\sigma_{fmax}}{E_b}$$

Repeating for the remaining independent and dependent variables that are not in the dimensionally independent subset and placing in the initial non-dimensional values

$(\frac{W}{B_f}, \frac{W}{B_s}, \text{ and } \frac{t_{bicos}}{r_{bicos}})$ yields:

$$\Pi_i = \left(\frac{\sigma_{fmax}}{E_b} \right), \left(\frac{\sigma_{smax}}{E_b} \right), \left(\frac{u}{r_{bicos}} \right), \left(\frac{W}{B_f} \right), \left(\frac{t_{bicos}}{r_{bicos}} \right), \left(\frac{W}{B_s} \right), \left(\frac{\rho_s}{\rho_b} \right), \left(\frac{E_s}{E_b} \right), \left(\frac{P}{E_b} \right) \quad (59)$$

Where, the dependent Π parameters with a dependent variable in it can be written as a function of the remaining Π 's. This is shown in equation (60).

$$\begin{aligned}
\Pi_1 &= f(\Pi_4, \Pi_5, \Pi_6, \Pi_7, \Pi_8, \Pi_9) \\
\Pi_2 &= f(\Pi_4, \Pi_5, \Pi_6, \Pi_7, \Pi_8, \Pi_9) \\
\Pi_3 &= f(\Pi_4, \Pi_5, \Pi_6, \Pi_7, \Pi_8, \Pi_9)
\end{aligned} \quad (60)$$

The dimensional analysis provides us with unique benefits after determining all of the Π parameters or invariant quantities. These benefits are similarity and out-of-scale modeling. Similarity states that if all of the independent invariants between two different designs are the same then their dependent invariants are actually equal as well. Out-of-scale modeling states that the performance of a full-scale system can be realized by

testing a geometrically similar smaller scale model. For the icosahedron FEM invariants, the independent Π parameters address this. If all of the independent Π parameters remain equal then scale of the vehicle can be increased or decreased and the stresses would remain constant (Π_1 and Π_2). However, as the vehicle scales the displacements will scale proportionally with the vehicle size, as indicated by $\Pi_3 = \left(\frac{u}{r_{icos}}\right)$. Therefore, if the stresses of a larger radii vehicle were desired, a test on a smaller scale model would yield the stress results for the larger vehicle as long as all the independent Π parameters remain constant. This scaling concept is powerful because the FEA results obtained for one model are the results for infinitely many radii models as long as the invariant parameters remain constant.

In order to test the concept of structural scaling and if the stress and relative displacement solution, remain constant, as long as the invariant quantities remained constant, the icosahedron model was analyzed at 6 different radii from 3-96 inches keeping all other inputs constant. The results are shown in Table 15. The constant invariant ratios are shown in Table 14. The analysis proved that if only changing the vehicle radii, no effect in the stress and relative displacement resulted, as indicated by the near zero percent difference between all models when comparing them to the 3 inch model.

Table 14: Icosahedron Invariants for scaling example

Icosahedron Invariants for scaling example	
Independent Invariants	Dependent Invariants
$\Pi_4 = \frac{W}{B_f} = 0.9$	$\Pi_1 = \frac{\sigma_f}{E_b} = \frac{\sigma_{f,max}}{293E9}$
$\Pi_5 = c = \frac{t_b}{r_b} = 0.005$	$\Pi_2 = \frac{\sigma_s}{E_b} = \frac{\sigma_{s,max}}{293E9}$
$\Pi_6 = \frac{W}{B_s} = 0.1$	$\Pi_3 = \frac{u}{r_{icos}} = \frac{u}{r_{icos}}$
$\Pi_7 = \frac{\rho_s}{\rho_b} = \frac{970}{1250}$	
$\Pi_8 = \frac{E_s}{E_b} = \frac{172E9}{293E9}$	
$\Pi_9 = \frac{P}{E_b} = \frac{101325}{293E9}$	

Table 15: Icosahedron Scale vs. FE Model Outputs and % Difference

Icosahedron Radius (in)	Frame Stress (Pa)	% Difference (%)	Skin Stress (Pa)	% Difference (%)	Final W/B	% Difference (%)
3	3.938E+09	0.0000	2.042E+09	0.0000	1.0069	0.0000
6	3.938E+09	0.0013	2.042E+09	0.0000	1.0068	0.0094
12	3.938E+09	0.0008	2.042E+09	0.0001	1.0067	0.0153
24	3.938E+09	0.0012	2.042E+09	0.0001	1.0066	0.0209
48	3.938E+09	0.0013	2.042E+09	0.0002	1.0066	0.0217
96	3.938E+09	0.0016	2.042E+09	0.0002	1.0066	0.0230

DOE Analysis Results and Discussion for the Icosahedron Vacuum Vehicle

This section will detail the setup and execution of the DOE to collect stress and displacement data of many icosahedron designs, so that the bounded structural design space can be created. The DOE analysis is broken down into five steps. The first step is to determine the factors and levels that will be used to perform the DOE. The factors for this analysis will be invariants (Π 's) developed in the dimensional analysis. Note, the DOE could have very well been performed without conducting the dimensional analysis first. (The factors would have been the nine independent variables on the right side of

equation (56).) The high and low levels or input ranges on the factors were developed with material and manufacturing constraints applied, where applicable. The second step was to perform a set of experiments prescribed by an unreplicated 2^k full factorial design. The third step will apply an ANOVA on the input and response data obtained from the DOE, to determine which factors and interactions had significant effects on the stress and displacement responses of the icosahedron frame and skin designs. The last step will create regression fits of the response data from the DOE using only the significant factors and interactions, where the fit and curvature of the DOE response data will be evaluated.

Determine Factors and Levels

With a converged FE model and the input parameters characterized by the dimensional analysis, the design of experiments can be setup. The DOE will be conducted using a full factorial 2^k unreplicated design. An unreplicated design is being used because the solver or simulator is a deterministic process where performing replicates will not yield different solutions from the original test case. Typically in a DOE, replicates are necessary to reduce the risk of outliers or bad tests in the test data. The input parameters or factors chosen for the factorial analysis are taken from the invariant quantities produced by the Buckingham Pi analysis.

Typically, when a dimensional analysis is performed before a DOE, the invariants are used outright as the factors for the DOE. This, in general, simplifies the analysis of the system being investigated. For the icosahedron FEM some of the invariants had to be manipulated so that their parameters could be integrated into the model generation process. When this was performed some of the factors developed for the DOE will

become dimensional again. Note, when this is performed the end user must use SI units when utilizing approximation models generated by the ANOVA, in the following section. This is not an ideal scenario, but the benefits of similarly, out-of-scale modeling, and independent variable reduction are still maintained from the dimensional analysis. The six invariants produced by the dimensional analysis, as shown in equation (59), will be manipulated to produce five factors, to be used for the FEM DOE.

The two invariants $\left(\frac{W}{B_s}\right)$ and $\left(\frac{W}{B_f}\right)$ will be reduced to a single invariant by forcing the total of their ratios to equal 1 for the factorial analysis. This is shown in equation (61).

$\frac{W}{B_s}$ will be the first factor for the DOE.

$$\frac{W}{B_f} = \frac{W}{B_{Tot}} - \frac{W}{B_s} \quad (61)$$

Where, $\frac{W}{B_{Tot}} = 1$

The next two factors are produced by combining the $\left(\frac{\rho_s}{\rho_b}\right)^{-1}$ and $\left(\frac{E_s}{E_b}\right)$ invariant quantities.

This is performed, because a materials density and modulus are coupled with each other.

When combined, these invariants equal $\frac{\rho_b E_s}{\rho_s E_b}$. Where, this ratio contains the material

property, specific stiffness $\left(\frac{E}{\rho}\right)$, for both the frame and skin. Now, the combined ratio can

be separated into two quantities, frame and skin specific modulus $\frac{E_b}{\rho_b}$ and $\frac{E_s}{\rho_s}$, so that their

coupling can be accounted for. At any time these parameters be recombined to form the

original invariant if desired. The fourth factor is the c-ratio $\frac{t_b}{r_b}$ or beam thickness-to-radius ratio. The last factor will be produced from the $\left(\frac{P}{E_b}\right)$ invariant where the pressure term P will be represented as altitude (h), in which P is a function of $(P(h))$. The denominator E_b will be ignored. Again, the original invariant $\left(\frac{P}{E_b}\right)$ can be reconstructed for any design considered. Thus, the factor to represent this invariant will be h or altitude. These five factors account for all six of the invariants determined from the dimensional analysis. The five invariant factors to model the FEA outputs are shown in Table 16.

Table 16: Factors for the DOE created from the Invariants of the Dimensional Analysis

Invariant From Dimensional Analysis	Factor for Factorial Analysis
$\frac{\rho_b E_s}{E_b \rho_s}$	$\frac{E_s}{\rho_s}$
$\frac{\rho_b E_s}{E_b \rho_s}$	$\frac{E_b}{\rho_b}$
$\frac{P}{E_b}$	$P = f(h)$
$\frac{t_b}{r_b}$	$\frac{t_b}{r_b}$
$\frac{W}{B_s}$	$\frac{W}{B_s}$

Performing the dimensional analysis before setting up the DOE reduced the number of factors or invariants to represent the model from the original nine independent variables to the five factors shown in Table 16. The five factors will be evaluated at a high and low level, producing a 2^5 un-replicated full factorial analysis. This analysis requires a minimum of 32 experiments to conduct an ANOVA and determine which factors and interactions significantly affect the response parameters. If the dimensional

analysis had not been conducted initially, a minimum of 2^9 or 512 experiments would have been required to determine which parameters were significant. That is approximately a 93.75% reduction in the number of tests required to characterize the model.

The 2^5 full factorial DOE analysis will be conducted in a multi-step process with the assistance of a statistical analysis software package JMP. The first step will be to construct the DOE test matrix. Within JMP, the user specifies the DOE design (2^k), number of factors (5), levels (2), replicates (0), and center points (1). A randomized or structured design matrix is then constructed containing at least the minimum number of experiments required (33) to perform an ANOVA on the data collected. The test matrix constructed, details the experiment number (FEA) and the corresponding levels for the frame specific modulus, skin specific modulus, altitude, c-ratio, and $\frac{W}{B_s}$ for each of the 33 experiments (FEA) to be performed. The tests within the matrix were assigned randomly and are shown in Table 17, where 1 indicates low factor level, 2 indicates high factor level, and 0 indicates a mid-level (center point).

Table 17: DOE Experimental Test Matrix

Test #	Frame Specific Modulus	Skin Specific Modulus	Altitude	C-ratio	Skin W/B
1	1	2	1	2	2
2	2	1	1	2	1
3	1	1	2	1	2
4	1	2	2	2	1
5	1	2	1	1	1
6	1	1	2	2	2
7	2	2	1	1	2
8	2	2	2	2	2
9	1	2	2	1	2
10	2	1	2	1	1
11	1	1	2	2	1
12	2	2	1	1	1
13	2	1	1	1	2
14	1	2	2	1	1
15	2	1	1	1	1
16	1	1	1	2	2
17	2	1	2	2	1
18	2	1	1	2	2
19	2	1	2	1	2
20	1	2	1	2	1
21	2	2	2	1	1
22	2	2	2	1	2
23	1	1	1	1	1
24	1	2	1	1	2
25	2	2	2	2	1
26	1	2	2	2	2
27	2	2	1	2	1
28	2	1	2	2	2
29	1	1	1	1	2
30	1	1	1	2	1
31	2	2	1	2	2
32	1	1	2	1	1
33	0	0	0	0	0

The factors and levels for the DOE of the icosahedron are shown in Table 18. Additionally, Table 19 shows the vector of outputs that were observed for the factorial analysis. The development of the level values chosen for the frame and skin specific

modulus are detailed in the Materials and Manufacturing Constraints Study section below. The levels for altitude, c-ratio, and skin W/B were not constrained by material or manufacturing limitations, and therefore some freedom existed when determining what range of values to choose for the levels. In order to gain a broad view of the structural design space for the icosahedron and produce finite element models that converged to a solution, the factors not driven by material properties were chosen so that their range was large. The actual magnitude of the ranges were determined by performing initial spot check structural analyses to determine if the set of inputs would allow for the finite element solver to converge to a solution with a reasonable amount of time. The definition of reasonable amount of time was setting a maximum of six hours for an analysis to be performed. To put into perspective, an icosahedron model with “good” design parameters took approximately 20-30 minutes to solve. Therefore the levels for altitude, c-ratio, and skin W/B were selectively arbitrarily chosen so that their range was large enough to provide a broad scope view of the structural design space to evaluate potential feasibility.

Table 18: Icosahedron Factors and Levels for a 2⁵ Factorial Design

Icosahedron Factorial Design Factors and Levels		
Factor	Level 1 (Low)	Level 2 (High)
<i>Frame Specific Modulus:</i> $\frac{E_b}{\rho_b}$ (m^2/s^2)	1.29E8	2.34E8
<i>Skin Specific Modulus:</i> $\frac{E_s}{\rho_s}$ (m^2/s^2)	9.52E7	1.77E8
<i>Altitude:</i> h (m)	0	4572
<i>Cratio:</i> $\frac{t_b}{r_b}$	0.005	0.05
<i>Skin Weight/Buoyancy:</i> $\frac{W}{B_s}$	0.1	0.4

Table 19: Icosahedron DOE Observations

Icosahedron DOE Response Variables	
Response	Units
Max Frame Stress (σ_{fmax})	Pa
Max Skin Stress (σ_{smax})	Pa
Final W/B	

Materials and Manufacturing Constraints Study

In order for a vacuum LTAV to be constructed, very specific material properties are necessary. Within the discussions authored by Akhmeteli, Gavrilin, Metlen, and Rodriguez, there is a common theme with regard to the materials considered to construct a vacuum LTAV. These materials need to have high ultimate strength, high modulus of elasticity, and low density. The following variables, high specific strength and high specific modulus were combined. As was pointed out by Akhmeteli, there exists no individual material that can resist buckling when built as a thin shell sphere with an internal vacuum [4]. Therefore, the need to develop some type of reinforcement is necessary. Rodriguez showed that with an icosahedron stiffened structure, buckling was indeed not the limiting factor; material failure was [5]. This is known as the materials ultimate strength. Metlen showed that utilizing a carbon fiber composite showed promise in constructing the frame of the structure. Metlen only investigated a unidirectional fiber epoxy combination for the frame that yielded a modulus of 538 GPa, which rivals that of the materials in Table 1 that could theoretically be used for the construction of a vacuum LTAV [1]. Let it be noted, that some of the materials quoted by Rodriguez cannot be used in their pure form to manufacture the components of a stiffened frame. These materials are CNT, Spectra, and Zylon. The materials presented by Rodriguez exhibited

properties that would produce a vacuum LTAV if constructed with an icosahedron frame and skin numerically. CNT, until recently, could not be constructed on a macro scale and therefore is approaching a functional material. Specifically, research is being performed where carbon nanotubes (CNT) are being utilized to make CNT fabrics. They have very low density and thicknesses [25] [26] [27]. Work is being performed where these fabrics are being stretched so that the CNT's are aligned and high unidirectional composite properties are generated and even exceeding that of Spectra fiber alone [6] [28]. Spectra and Zylon fibers can be formed into a composite where the bulk modulus and ultimate strength will decrease because of the bonding epoxy. Larger fill percentages of the fiber can be used to attempt to stay as close to the natural fiber properties. Studies recently have been performed that combine carbon nanotubes with epoxy resin to increase the modulus and strength of the epoxy by as much as 36-42% and 25%, respectively [29]. These types of epoxies could be utilized in the construction of composites with UHM, Spectra, and Zylon fibers. The models in this research will focus on utilizing current and near future materials for the investigation of a vacuum LTAV, such as, CNT, Spectra, Zylon, and UHM composites.

The materials used for the models in this research are materials that currently exist and can be purchased from a supplier. They have been created and tested in a lab setting but are not currently available for purchase, or have not been created with properties estimated from literature. The material properties derived from the "materials" that have not been created serve as a future material benchmarks that are not far removed from reality. The materials selected are shown in Table 20.

Table 20: List of Materials for Vacuum Models Development

Frame/Skin	Material	Level	Density, ρ (kg/m ³)	Poissons Ratio	E (Gpa)	σ_y (Gpa)	E/ ρ	E/ σ_y
Skin	CT155 UHMWPE	Low	1050	0.33	100	1.5	9.52E+07	1.43E+06
	Spectra 1000 Fiber	High	970	0.33	172	3	1.77E+08	3.09E+06
Frame	IM10 (Hexply 8552)	Low	970	0.33	125	1.75	1.29E+08	1.80E+06
	CNT Composite (NCSU)	High	1250	0.33	293	3.8	2.34E+08	3.04E+06

The properties for skin material 1 are the material properties of a membrane laminate constructed by Cubic Tech using CT155HB UHMWPE [30]. These properties are shown in Figure 40.

Product	CT155 UHMWPE Composite	CT135 PBO Composite
Weight (oz/yd ²)	13.0	10.3
Thickness (in)	0.016	0.011
Bollard Grip Method		
Tensile Strength @ 23°C / -60°C (lbf/in)	1813 / 2122	1618 / 1924
Theoretical Strength @ 23°C (lbf/in)	2402	2250
Conversion Efficiency @ 23°C (%)	75	72
Modulus @ 23°C / -60°C ((lbf/in)/(in/in))	85820 / 109965	72794 / 81682
Strain to Failure @ 23°C / -60°C (%)	2.1 / 1.9	2.0 / 2.4
Tabbed Specimen Method (ASTM D3039)		
Tensile Strength @ 23°C (lbf/in)	2167	1934
Theoretical Strength @ 23°C (lbf/in)	2402	2250
Conversion Efficiency @ 23°C (%)	90	86
Slit Tear Strength @ 23°C / -60°C (lbf)	313 / 504	250 / 423
Helium Gas Permeability (L/m ² /24hrs)	<0.2	<0.2

Figure 40: Cubic Tech CT155HB UHMWPE material properties [30].

Skin material 2's properties are that of Spectra alone and denote what material properties would be desired for a future membrane laminate [31] [30]. Currently, Spectra fibers with these material properties do exist, and therefore constructing a laminate membrane with the material properties of the bulk material is currently not available. It certainly is not far removed from reality in the near future. Frame material 1's properties are estimated from

what a unidirectional spectra composite with CNT epoxy would yield and is equivalent to IM10 in terms of specific modulus and strength according to Figure 42 [28] [6]. On average, when looking at unidirectional composites, the modulus and yield strength of the composite are approximately 50% and 60% less than the fiber alone [1]. Yet, with a CNT epoxy included, this reduction can be estimated to be 30% and 40% for the modulus and yield strength respectively [32] [29] [33]. Additionally, the properties estimated for the Spectra composite align very well with existing high strength composites, such as IM10 in Figure 42. Frame material 2's material properties are the most aggressive of all the material stated yet this material has been manufactured and tested in a lab setting. This material is a CNT fiber composite manufactured on the macro scale. The manufacturing technique is a novel technique developed by X. Wang et al at North Carolina State University [28]. The technique uses a novel stretch winding process where high volume fractions of long CNTs can be incorporated into a polymer matrix while simultaneously stretching and aligning the CNTs. This process is shown in Figure 41. The process allows for CNT composites or prepregs to be directly manufactured in a "one-step" process. The CNT type used for the composite are multi-walled nano-tubes (MWNT) and the matrix is bismaleimide (BMI) [28]. A comparison of this composites material properties to other high performance engineering composites is shown in Figure 42. Figure 42 (a) plots tensile strength versus modulus of elasticity, where the work performed at NCSU in red along with high performance carbon fiber composites. The material properties that are desired for the icosahedron VLTAV design are high tensile strength and high modulus of elasticity (the top right corner of Figure 42 (a)). Figure 42 (b) plots specific strength versus specific modulus, where the desirable region is again the top right corner for the icosahedron

VLTAV. Since material density plays such an important role in the vehicles buoyancy, any material that has high specific strength and modulus is desirable.

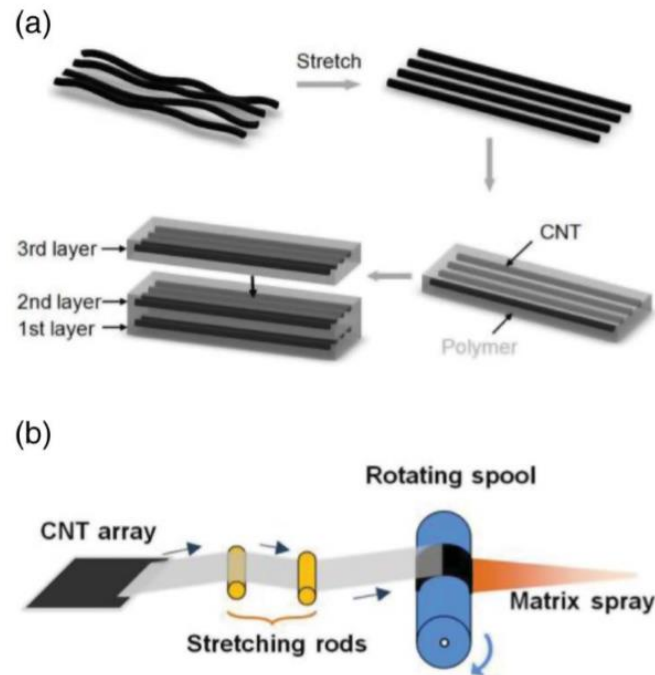


Figure 41: (a) Illustration of straightening the CNT fibers then combining them with the polymer matrix and layering them in a composite fashion. (b) Illustration of the stretch-winding process [28].

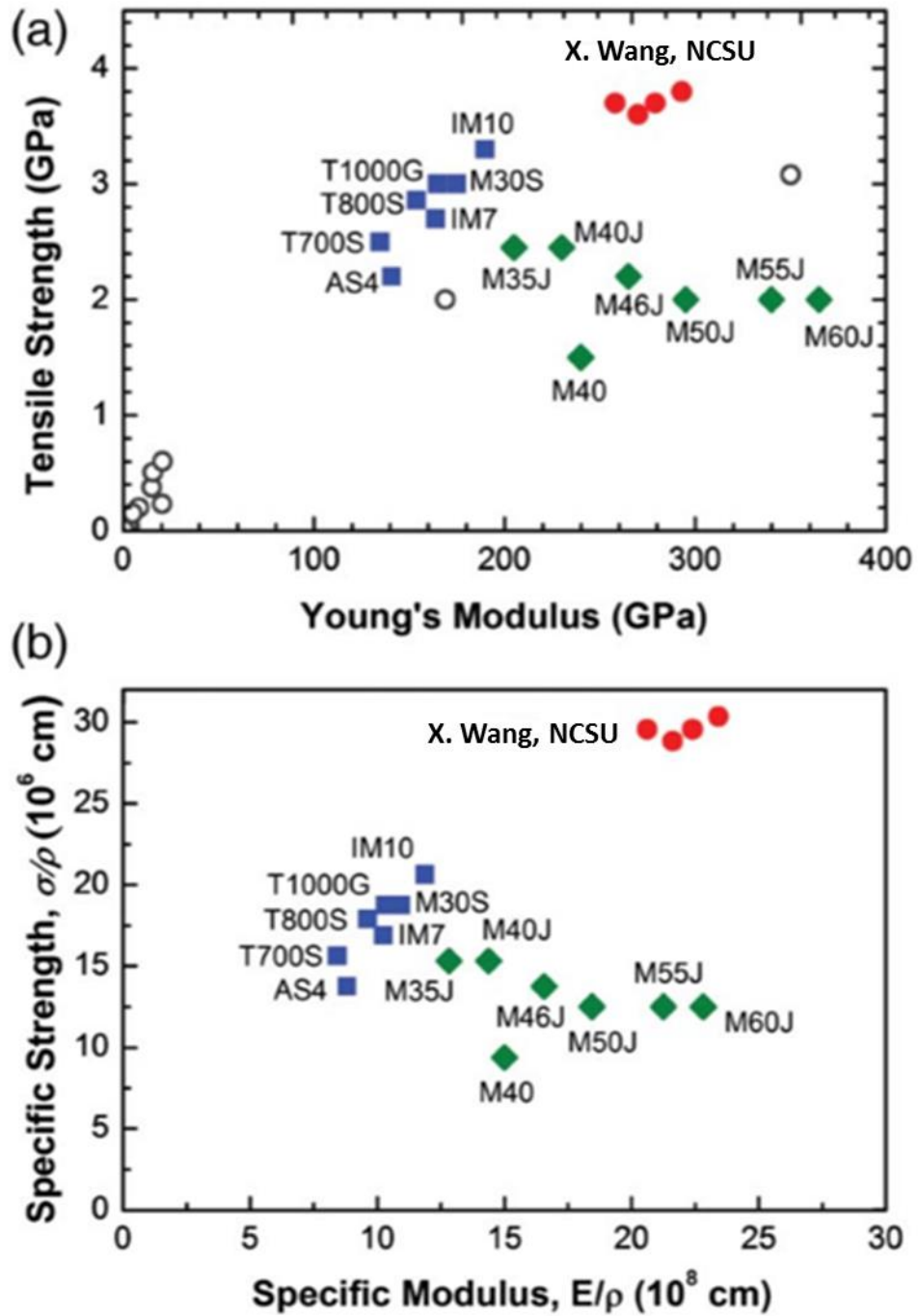


Figure 42: Comparison of the CNT composite (red dots) material properties with other high performance engineering composites. (a) Tensile Strength vs. Young's Modulus. (b) Specific Strength vs. Specific Modulus [28].

Skin Manufacturing

The manufacturing technique that is recommended to be utilized for setting the manufacturing limits for a membrane skin is a laminate technique. The laminate technique uses oriented laminates to allow for “the ability to optimize weight, thickness, and strength at particular locations or along predetermined load paths”. Laminate composites tend to have linear properties that can be used in the design of the membrane. In addition to the high strength of laminate fabrics, they have the ability to incorporate seams that can even be stronger than the base material itself, where typically seams are the limiting point in a material. Possible ways to fabricate the seams are sewing, adhesive bonding, heat welding, ultrasonic welding, and laser enhanced bonding [30]. Examples of some fabricated laminates are shown in Figure 43.

The manufacturing membrane thickness limit that will be used for this research will be taken from the data published by Cubic Tech and Khoury in *Airship Technology* [30] [31]. The medium and heavy weight laminate membranes produced by Cubic Tech [30] had an approximate average of 0.2mm in their study. Work by Khoury, in *Airship Technology*, illustrates the material layers utilized for LTAV membranes and their thicknesses. The average membrane thickness for his work was approximately 0.23mm for manufactured membranes, shown in Figure 44. The manufacturing skin thickness limit that will be used for this research will be 0.2mm. Note, that the skin thickness limit does not affect the structural feasibility of the icosahedron designs, it only dictates how thin a membrane could be manufactured. However, the skin thickness limit does dictate size or scale of a manufacturable icosahedron design. The effect of this limit is shown in the vehicle sizing section of this chapter.

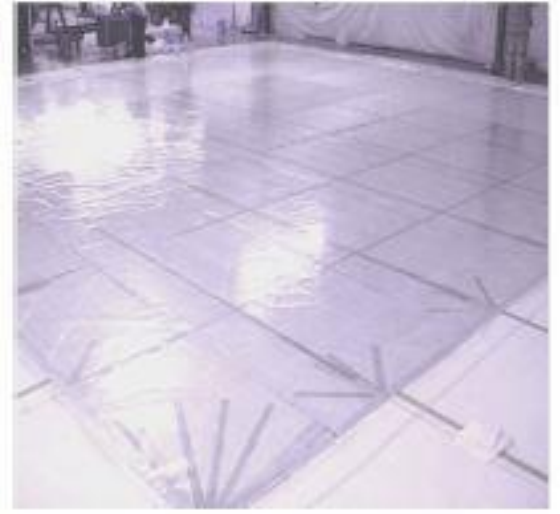


Figure 43: Laminate Composites [30].

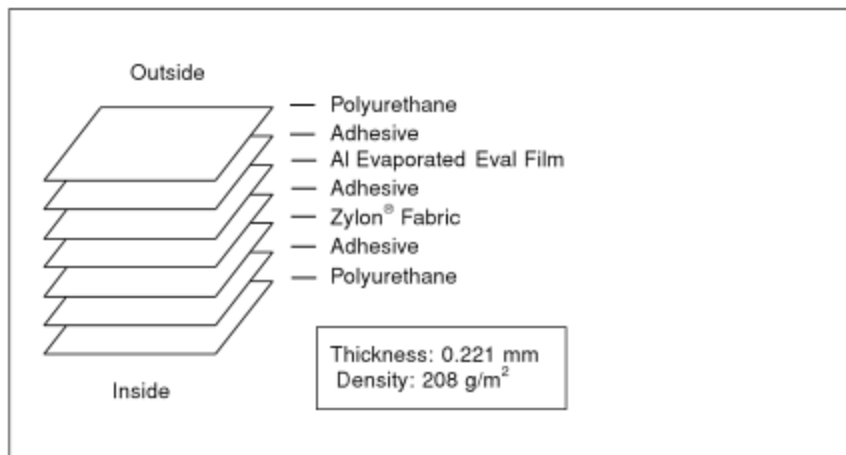
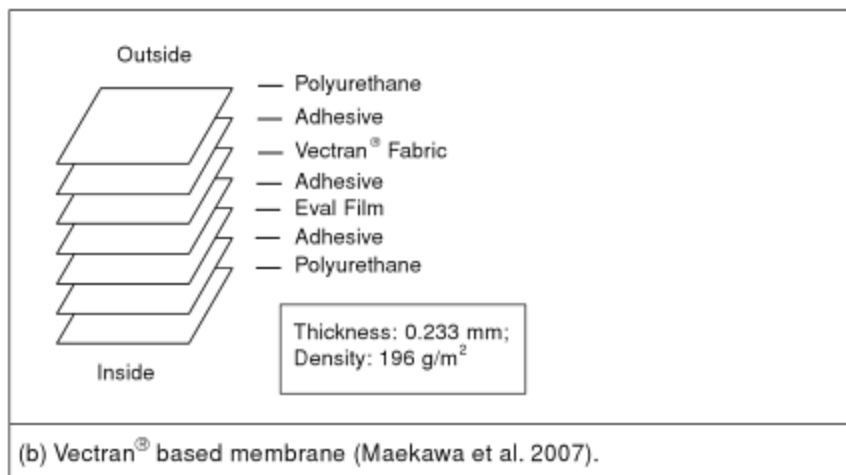
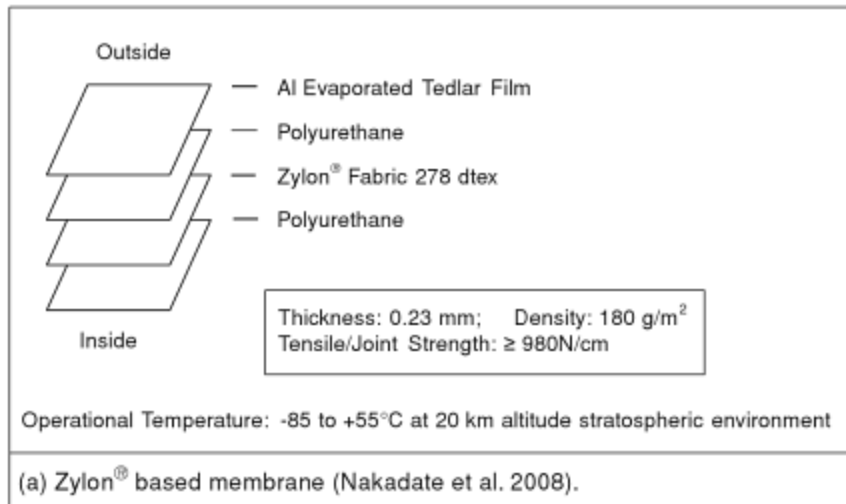


Figure 44: Lighter than Air Membrane Manufacturing thicknesses [31].

Experiments and Results

The FEAs prescribed by the DOE test matrix in Table 17 were automatically conducted utilizing the cyclic process identified in Figure 11, where it took approximately 11 hours to run the 33 experiments. The results of the DOE are shown in Table 21, where the inputs with engineering units instead of level indicator (0, 1, or 2) are shown to the left of the red line, and the FEA responses are shown to the right of the red line. For example, referencing the test matrix constructed in Table 17, the first experiment had factors [1, 2, 1, 2, and 2] for $\left[\frac{E_b}{\rho_b}, \frac{E_s}{\rho_s}, h, \frac{t_{bicos}}{r_{bicos}}, \text{ and } \frac{W}{B_s} \right]$. Now, referencing the levels determined in Table 18, the factors, in engineering units for the first test were [1.289E⁸ m²/s², 1.773E⁸ m²/s², 0 m, 0.05, and 0.4], respectively. The max frame stress, max skin stress, and final W/B responses for the first FEA were extracted from the stress and displacement data acquired, and were [2.576E⁹ Pa, 4.571E⁹ Pa, and 1.0536], respectively. Once all of the FEA's were complete, the input and output data in engineering units was input into the software package JMP to perform an ANOVA on the data. (as indicated in chapter III) To analyze the factor and interaction effects on the three responses (max frame stress, max skin stress, and final W/B) for the entire data set in Table 21.

Table 21: Icosahedron DOE Inputs and Results

Icosahedron DOE Inputs and Results							
Frame specific stiffness	Skin specific stiffness	Altitude	C-ratio	%skin	Max Frame Stress	Max Skin Stress	Final W_B
1.289E+08	1.773E+08	0	0.05	0.4	2.576E+09	4.571E+09	1.0536
2.340E+08	9.524E+07	0	0.05	0.1	6.582E+09	3.368E+09	1.0413
1.289E+08	9.524E+07	15000	0.005	0.4	3.123E+09	1.924E+09	1.1573
1.289E+08	1.773E+08	15000	0.05	0.1	3.262E+09	6.885E+09	1.1772
1.289E+08	1.773E+08	0	0.005	0.1	2.465E+09	2.576E+09	1.0294
1.289E+08	9.524E+07	15000	0.05	0.4	2.834E+09	3.878E+09	1.1912
2.340E+08	1.773E+08	0	0.005	0.4	4.927E+09	2.127E+09	1.0296
2.340E+08	1.773E+08	15000	0.05	0.4	3.680E+09	4.295E+09	1.1594
1.289E+08	1.773E+08	15000	0.005	0.4	2.725E+09	2.688E+09	1.1566
2.340E+08	9.524E+07	15000	0.005	0.1	4.066E+09	1.725E+09	1.1418
1.289E+08	9.524E+07	15000	0.05	0.1	3.899E+09	4.813E+09	1.1964
2.340E+08	1.773E+08	0	0.005	0.1	3.894E+09	2.039E+09	1.0242
2.340E+08	9.524E+07	0	0.005	0.4	5.420E+09	1.414E+09	1.0295
1.289E+08	1.773E+08	15000	0.005	0.1	2.525E+09	2.654E+09	1.1480
2.340E+08	9.524E+07	0	0.005	0.1	3.839E+09	1.850E+09	1.0238
1.289E+08	9.524E+07	0	0.05	0.4	3.202E+09	3.747E+09	1.0648
2.340E+08	9.524E+07	15000	0.05	0.1	6.385E+09	3.775E+09	1.1701
2.340E+08	9.524E+07	0	0.05	0.4	5.737E+09	3.266E+09	1.0458
2.340E+08	9.524E+07	15000	0.005	0.4	5.287E+09	1.494E+09	1.1483
1.289E+08	1.773E+08	0	0.05	0.1	3.489E+09	6.055E+09	1.0485
2.340E+08	1.773E+08	15000	0.005	0.1	4.042E+09	1.963E+09	1.1422
2.340E+08	1.773E+08	15000	0.005	0.4	4.703E+09	2.205E+09	1.1483
1.289E+08	9.524E+07	0	0.005	0.1	2.493E+09	1.804E+09	1.0289
1.289E+08	1.773E+08	0	0.005	0.4	2.877E+09	2.666E+09	1.0369
2.340E+08	1.773E+08	15000	0.05	0.1	5.539E+09	5.594E+09	1.1607
1.289E+08	1.773E+08	15000	0.05	0.4	2.283E+09	4.528E+09	1.1743
2.340E+08	1.773E+08	0	0.05	0.1	5.879E+09	4.824E+09	1.0367
2.340E+08	9.524E+07	15000	0.05	0.4	4.840E+09	3.480E+09	1.1684
1.289E+08	9.524E+07	0	0.005	0.4	3.233E+09	1.879E+09	1.0375
1.289E+08	9.524E+07	0	0.05	0.1	3.988E+09	4.069E+09	1.0562
2.340E+08	1.773E+08	0	0.05	0.4	4.355E+09	4.211E+09	1.0400
1.289E+08	9.524E+07	15000	0.005	0.1	2.605E+09	1.732E+09	1.1476
1.883E+08	1.347E+08	7500	0.025	0.25	4.177E+09	3.439E+09	1.0199

Analysis of Variance

For a 2^5 full factorial analysis there are five degrees of effects and interactions. If we let the five factors described above $\left(\frac{E_b}{\rho_b}, \frac{E_s}{\rho_s}, h, \frac{t_{bicos}}{r_{bicos}} \text{ and } \frac{W}{B_s}\right)$ be labeled as A, B, C, D, and E, their combinations will produce interactions up to a 5th degree or a five way interaction. Table 22 shows the main factor terms and all their possible combinations or interactions. With a full factorial DOE, all of these terms can be analyzed for significance in the ANOVA. Recall, in chapter III that for an unreplicated full factorial design, as performed for the icosahedron analysis, there is no way to naturally determine the significance of all of the terms for the ANOVA. This occurs because there exists no DOF (extra experiments or ignored interaction terms) to compute the sum of squares error (SS_E) necessary to calculate significance. However, the initial work-around is to use Lenth's PSE, detailed in chapter III, to compute an estimation of error, to conduct initial significance analysis. Lenth's PSE will be used to estimate the insignificant factors or interactions, which will be discarded so that a natural ANOVA can be conducted, where the discarded factors or interactions will allow for SS_E to be computed.

Table 22: 2⁵ Full Factorial Terms

Linear	
A	Frame Specific Modulus
B	Skin Specific Modulus
C	Altitude
D	C-ratio
E	% Skin/Frame
2-Way Interactions	
AB	Frame Specific Modulus*Skin Specific Modulus
AC	Frame Specific Modulus*Altitude
AD	Frame Specific Modulus*C-ratio
AE	Frame Specific Modulus*% Skin/Frame
BC	Skin Specific Modulus*Altitude
BD	Skin Specific Modulus*C-ratio
BE	Skin Specific Modulus*% Skin/Frame
CD	Altitude*C-ratio
CE	Altitude*% Skin/Frame
DE	C-ratio*% Skin/Frame
3-Way Interactions	
ABC	Frame Specific Modulus*Skin Specific Modulus*Altitude
ABD	Frame Specific Modulus*Skin Specific Modulus*C-ratio
ABE	Frame Specific Modulus*Skin Specific Modulus*% Skin/Frame
ACD	Frame Specific Modulus*Altitude*C-ratio
ACE	Frame Specific Modulus*Altitude*%Skin/Frame
ADE	Frame Specific Modulus*C-ratio*%Skin/Frame
BCD	Skin Specific Modulus*Altitude*%Skin/Frame
BCE	Skin Specific Modulus*Altitude*C-ratio
BDE	Skin Specific Modulus*C-ratio*%Skin/Frame
CDE	Altitude*C-ratio*%Skin/Frame
4-Way Interactions	
ABCD	Frame Specific Modulus*Skin Specific Modulus*Altitude*C-ratio
ABCE	Frame Specific Modulus*Skin Specific Modulus*Altitude*%Skin/Frame
ABDE	Frame Specific Modulus*Skin Specific Modulus*C-ratio*%Skin/Frame
ACDE	Frame Specific Modulus*Altitude*C-ratio*%Skin/Frame
BCDE	Skin Specific Modulus*Altitude*%Skin/Frame*%Skin/Frame
5-Way Interactions	
ABCDE	Frame Specific Modulus*Skin Specific Modulus*Altitude*C-ratio*%Skin/Frame

The initial significance data was obtained using Lenth's PSE method and is represented with both a half normal plot and Pareto chart. The half normal plot plots the absolute value of the estimated effect values or contrasts along with a fitted line which indicates where the effect would fall if the effect value was zero. The terms that deviate significantly from the fitted line are deemed significant terms and all the others are deemed not significant. The Pareto chart depicts similar information where the bar values are the absolute value of the effect and the vertical red line is the SME value calculated by Lenth's PSE value. Any term with an estimated effect greater than the critical value is deemed to be significant and anything less is not significant. These plots for the output of max frame stress is shown in Figure 45. Charts showing the same information for the remaining outputs are shown in Appendix A. Table 23 shows a summary of the effects that were determined to be significant for all of the outputs utilizing Lenth's PSE.

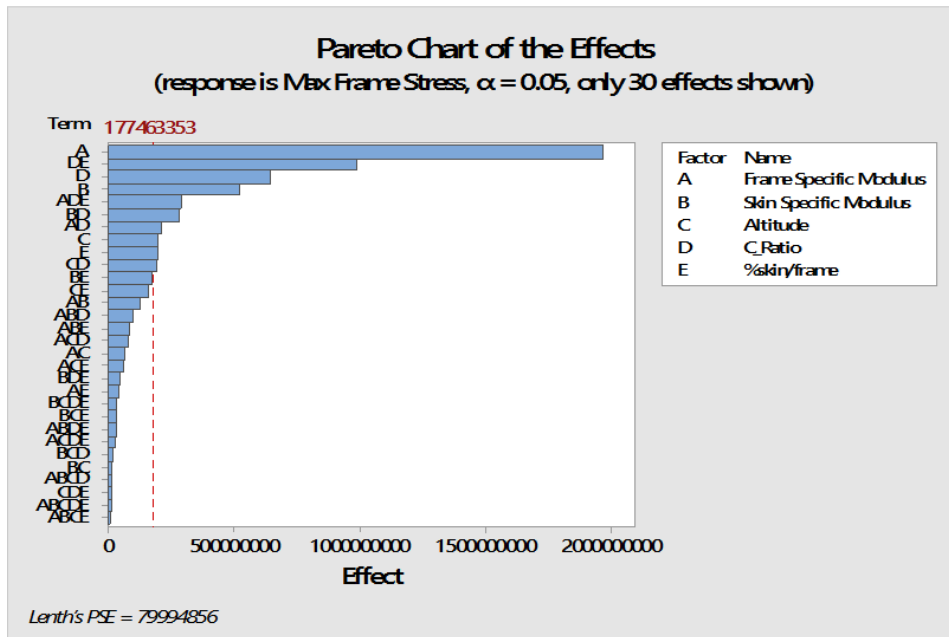
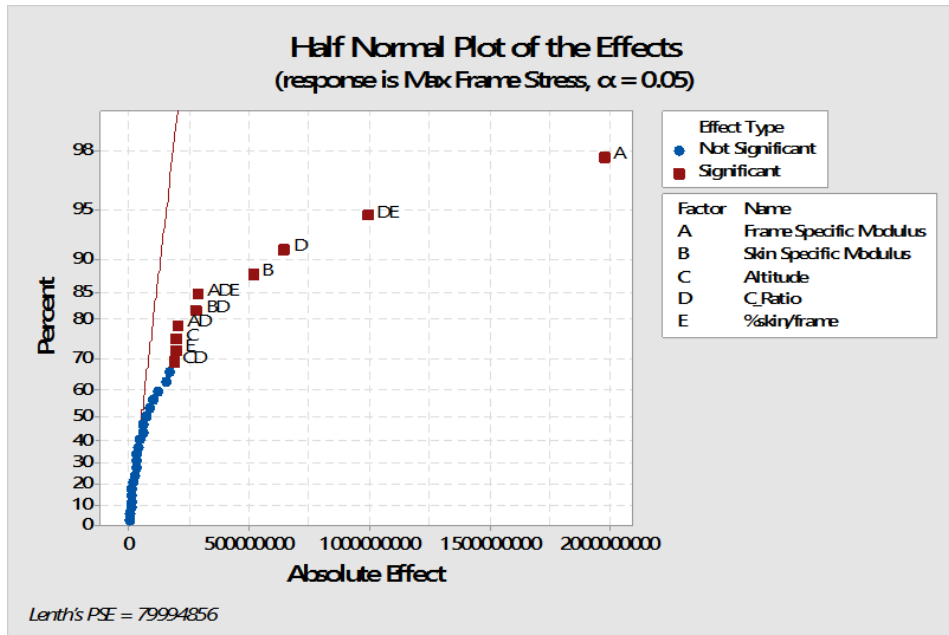


Figure 45: Half Normal Plot and Pareto Chart of the Effects with respect to Max Frame Stress (pseudo standard error term).

Table 23: Summary of Icosahedron Initial Significant Effect Terms

Icosahedron Significant Effects			
Max Frame Stress	Max Skin Stress	Final W/B	Combined
A	A	A	A
B	B	B	B
C	C	C	C
D	D	D	D
E	E	E	E
AD		AD	AD
AE	AE		AE
BD	BD	BD	BD
	BE		BE
CD		CD	CD
DE	DE	DE	DE
ADE	ADE		ADE
	BDE		BDE

The initial use of Lenth’s PSE allowed for 18 interactions indicated in Table 22 to be discarded. Table 23 shows the factors and interactions that were indicated to be significant for each respective response by inspecting their half normal and Pareto charts. Now that 18 interactions have been discarded, a natural ANOVA can be proceed with where the 18 discarded interactions make up the error term necessary to compute the ANOVA.

The ANOVA was computed using the combined significant terms between the 3 responses (max frame stress, max skin stress and final W/B), which are shown in the combined effects column of Table 23. The combined column was chosen so that all of the responses could be analyzed simultaneously as well as to see if any new terms out of the initially estimated significant terms using Lenth’s PSE became significant. Utilizing the JMP software, the 18 insignificant interactions were removed from the analysis and the ANOVA was computed for the max frame stress, max skin stress, and final W/B with

respect to the remaining 13 factors and interactions listed in the combined column of Table 23. The ANOVA data computed for the max frame stress response considering all 33 FEAs is shown in Table 24. Table 24 details the sum of squares (SS) values, the computed F ratio, and whether or not the effect is significant for each of the 13 factors and interactions included in the ANOVA. The individual sum of squares and F ratios were computed using the theory detailed in the ANOVA section of chapter III. Table 25 shows additional ANOVA information for each of the three responses, specifically SS_{Model} (SS_{Total}) and SS_E , which are used to compute the F ratios in Table 24.

Table 24: ANOVA Results for Icosahedron Max Frame Stress

Y	Source	DF	Sum of Squares	F Ratio	Prob > F	Significant
Frame Stress	Frame Specific Modulus (A)	1	3.12E+19	951.4134	<.0001	TRUE
Frame Stress	Skin Specific Modulus (B)	1	2.16E+18	65.8228	<.0001	TRUE
Frame Stress	Altitude [C]	1	3.11E+17	9.4866	0.0062	TRUE
Frame Stress	C-ratio (D)	1	3.33E+18	101.4179	<.0001	TRUE
Frame Stress	%skin [E]	1	3.09E+17	9.3999	0.0064	TRUE
Frame Stress	Frame Specific Modulus*C-ratio (AD)	1	3.47E+17	10.5606	0.0042	TRUE
Frame Stress	Frame Specific Modulus*%skin (AE)	1	1.11E+16	0.3377	0.568	FALSE
Frame Stress	Skin Specific Modulus*C-ratio (BD)	1	6.32E+17	19.2458	0.0003	TRUE
Frame Stress	Skin Specific Modulus*%skin (BE)	1	2.43E+17	7.3982	0.0136	TRUE
Frame Stress	Altitude*C-ratio (CD)	1	2.84E+17	8.642	0.0084	TRUE
Frame Stress	C-ratio*%skin (DE)	1	7.90E+18	240.679	<.0001	TRUE
Frame Stress	Frame Specific Modulus*C-ratio*%skin (ADE)	1	6.77E+17	20.6147	0.0002	TRUE
Frame Stress	Skin Specific Modulus*C-ratio*%skin (BDE)	1	1.61E+16	0.4901	0.4924	FALSE
(^ a higher order term containing this term is significant)						

Table 25: Model ANOVA values (SS_T and SS_E values) - Icosahedron

Max Frame Stress Model ANOVA					
Source	DF	Sum of Squares	Mean Square	F Ratio	Prob > F
Model	13	4.74E+19	3.65E+18	111.1311	<.0001
Error	19	6.24E+17	3.28E+16		
C. Total	32	4.80E+19			
Max Skin Stress Model ANOVA					
Source	DF	Sum of Squares	Mean Square	F Ratio	Prob > F
Model	13	6.35E+19	4.88E+18	117.4046	<.0001
Error	19	7.91E+17	4.16E+16		
C. Total	32	6.43E+19			
Final W/B Model ANOVA					
Source	DF	Sum of Squares	Mean Square	F Ratio	Prob > F
Model	13	0.007048305	0.000542177	38.9669	<.0001
Error	19	0.000264362	1.39138E-05		
C. Total	32	0.007312667			

With the F -ratios computed, the next step is to determine if the factors and interactions are significant with respect to their F values. As outlined in the ANOVA section of chapter III, the factor and interaction F ratio will be compared to a critical F value obtained from an F statistic table. The critical F ratio, $F_{\alpha,a-1,N-a}$, for this analysis was determined to be 4.17 by taking α to be 0.05, which is commonly chosen [14], $a = 2$ (2 levels), and $N = 33$ (total number of experiments). Equation (62) is then used to determine if the factor or interaction (Treatment) F -ratio is greater than the critical ratio. If the treatment F -ratio is greater than the critical ratio the factor or interaction (treatment) is determined to be significant. This same analysis was conducted for the remaining outputs and can be seen in Appendix A.

$$F_{Treatment} > F_{\alpha,a-1,N-a} \quad (62)$$

It is noted, that when the ANOVA was computed additional significant terms were acquired for the max frame stress output as well as all the other outputs compared to the

ones estimate by Lenth's PSE. A new final significant effects summary for all the responses based on the computed ANOVA and F ratios are shown in Table 26.

Table 26: Summary of Icosahedron Final Significant Effect Terms

Icosahedron Significant Effects			
Max Frame Stress	Max Skin Stress	Final W/B	Combined
A	A	A	A
B	B	B	B
C	C	C	C
D	D	D	D
E	E	E	E
AD		AD	AD
AE	AE		AE
BD	BD	BD	BD
BE	BE		BE
CD		CD	CD
DE	DE	DE	DE
ADE	ADE		ADE
	BDE		BDE

Interaction plots can be created to visually observe the main effect and interaction effects, using the ANOVA data. A cube interaction plot and main effects with 2nd degree interactions chart for the max frame stress are shown in Figure 46 and Figure 48. The interaction plots for the other two outputs are shown in Appendix A.

The cube plot shows the discrete effect on the output at the boundaries or corner points of each input and their combinations. These corner points are the values where each input is at either its high or low value or combination thereof. Since, the model was constructed using five factors, the only way to visualize all 32 experimental test, excluding the center point, results on a single chart is to use four cubes. Where, on a single cube three of the factors and their levels can be represented and the other two factors levels are represented by the additional cubes where each cube constitutes a high,

low, or combination thereof level. Since, the factorial design has only two levels for each factor all 32 test results can be viewed utilizing four cubes.

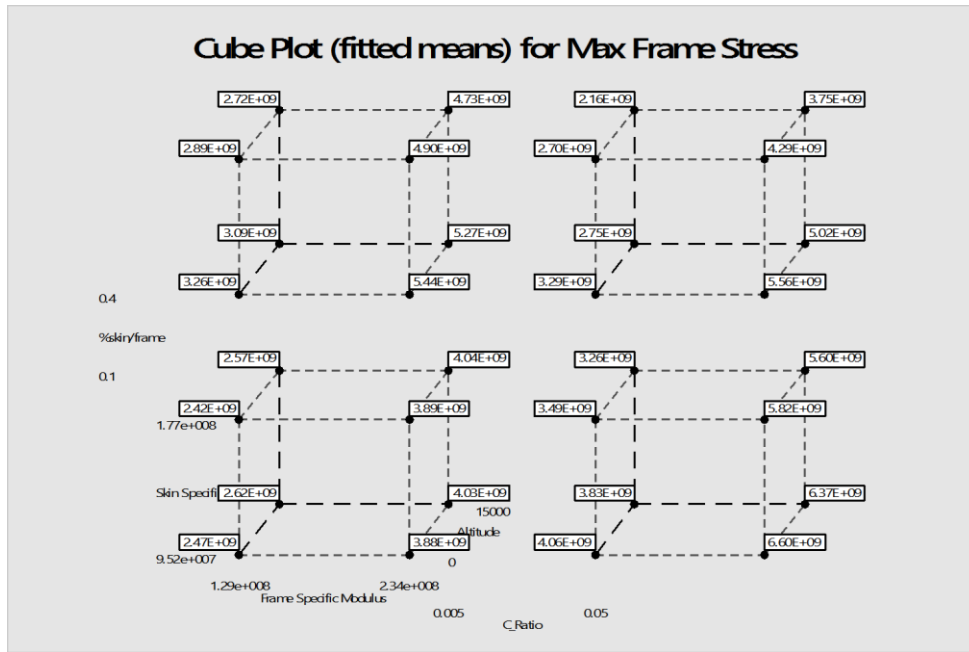


Figure 46: Cube Interaction Plot for the Max Frame Stress – Icosahedron

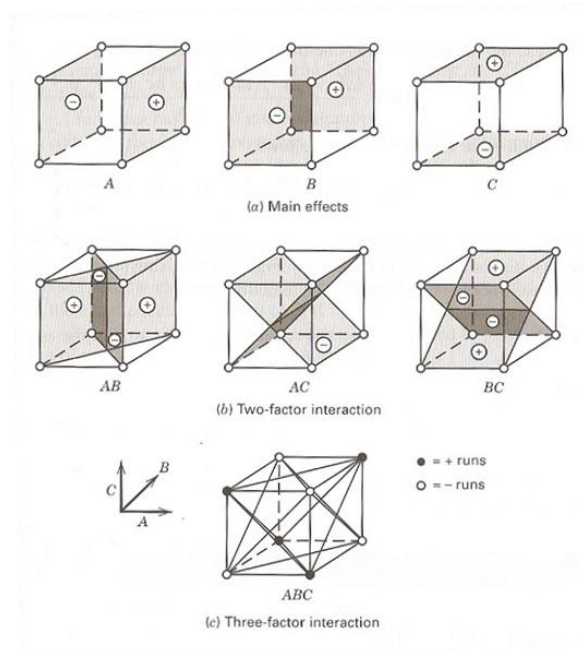


Figure 47: Example Representation of a 2^3 Factorial Main Effect and Interactions Contrasts

The data within the cube plot is used to determine the main effect and interaction strength values as well as develop the data for Figure 48. For instance, the slope of the main effect, frame specific modulus, shown in Figure 48 on the top left plot can be computed using the data represented in Figure 46. The way this is performed is to average all of the points where the frame specific modulus was high and low separately to obtain two values. The high level data points are on the right faces of the four cubes and the low level data points are on the left faces of the four cubes. A graphic of this is shown in Figure 47 for a single cube. The two averaged number can then be used to create the line shown in the top left plot of Figure 48. All of the other plots on Figure 48 are performed in a similar fashion referencing Figure 47.

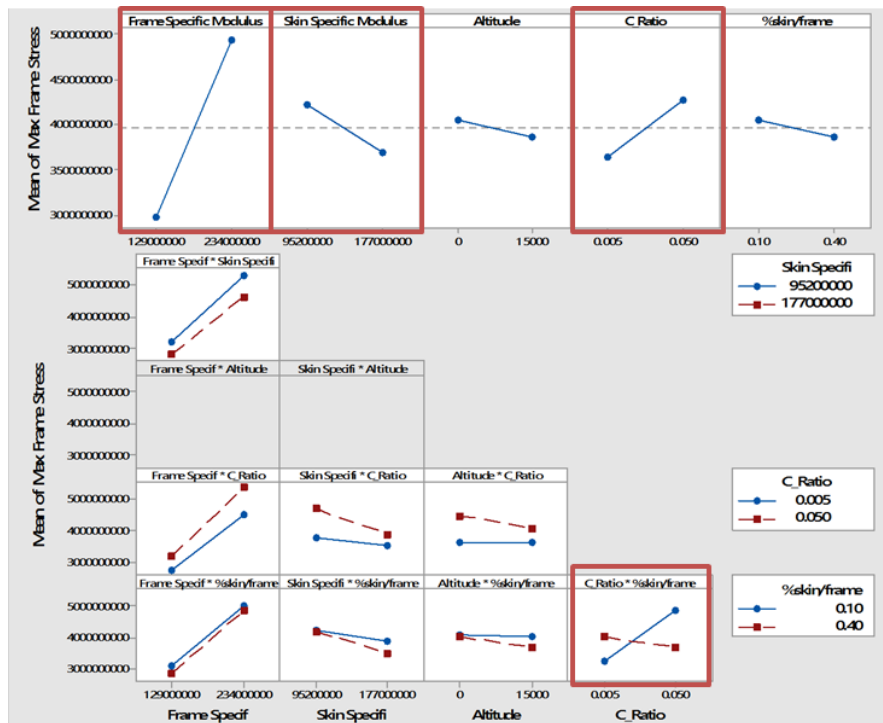


Figure 48: Main effects and 2nd degree interactions effects for Max Frame Stress – Icosahedron

The main effects and 2 way interactions plot in Figure 48 shows the effects of the factors and their interactions on max frame stress at the factors high and low levels. Observing the effects chart, it is shown that there are specific main effects and interactions that have a dominating effect on the response when compared to all the other factors and interactions. The main effects that are considerably dominate are the graphs that have steep slopes connecting the averaged response value when the factor was low to when the factor was high. The interactions that are considerable are the ones that have slopes that are significantly different from each other in the graph. The dominate main effects and interactions for the max frame stress are the frames material properties, $\frac{E_b}{\rho_b}$, the frames geometry, $\frac{t_b}{r_b}$, the combination of the frames geometry and the weighting of skin to frame, $\frac{t_b W}{r_b B_s}$, and the skins material properties, $\frac{E_s}{\rho_s}$. These effects and interactions are highlighted by the red boxes in Figure 48. The same observations were made for the max skin stress and the terms that are dominate are the frames geometry, $\frac{t_b}{r_b}$, the skins material properties, $\frac{E_s}{\rho_s}$, the frames material properties, $\frac{E_b}{\rho_b}$, the combination of frame geometry and the weighting of skin to frame, $\frac{t_b W}{r_b B_s}$, and the combination of skin material properties and frame geometry, $\frac{E_s t_b}{\rho_s r_b}$. The final weight-to-buoyancy, had the frames geometry, $\frac{t_b}{r_b}$, altitude, h , and the skin material property, $\frac{E_s}{\rho_s}$, terms to be considerably dominate.

Curvature Assessment

In order to continue to the regression fitting, the curvature of the responses needs to be investigated. Curvature of a response is determined if the center point data is

significantly difference from the mean of the response. Table 27 shows the mean of the response of the center point data in the first two rows. A percent difference between these rows was taken and the results are shown in the 3rd row of the table. It is shown that the error for the frame stress, skin stress, and final W/B is approximately 5%, 5%, and 1% respectively. Since the percent difference is fairly small and comparatively equal to the percent root mean square error (RSME) of the mean response, it indicated that the center point has no more error than any other point in the data set. It is therefore concluded that curvature does not exist for the three observed outputs, and the existing DOE data can be used to perform the regression fits.

Table 27: Icosahedron Curvature Analysis

Icosahedron Curvature Study			
	Frame Stress	Skin Stress	Final_W_B
Mean of Response	3.968E+09	3.259E+09	1.031
Center Point Response	4.177E+09	3.439E+09	1.020
% Center Point Error	5.266	5.530	1.111
% RSME of Mean Response	4.566	6.259	0.362

Regression Fits and Fit Assessment

With the factorial design reduced to primarily only significant terms, a linear regression fit on the outputs can be performed. This regression model that will be computed is a least squares linear regression model. This is performed by calculating the estimators, $\hat{\beta}$ in equation (63), where X are the set of inputs or factors and y are the outputs corresponding to the inputs. An estimator is computed for each significant term in the model per output considered. Therefore, three least squares regression fits are

constructed to model all three of the responses considered for the icosahedron model (max frame stress, max skin stress, and final W/B). The fitted regression model is constructed to look like equation (64), where \hat{y} is the fitted model, $\hat{\beta}_k$ are the estimators, x_k are the significant terms and ϵ is the error [14].

$$\hat{\beta} = (X'X)^{-1}X'y \quad (63)$$

$$\hat{y} = \hat{\beta}_0 + \hat{\beta}_1x_1 + \hat{\beta}_2x_2 + \cdots + \hat{\beta}_kx_k + \epsilon \quad (64)$$

The least squares regression equation for the icosahedron model is shown in Figure 49, where the β terms for each output parameter are defined in Table 28. The β terms are computed using the response data, y , and the corresponding inputs, X , provided by the DOE data, using equation (63) where only the 13 significant effects determined previously are considered. Figure 49 was generated through the use of JMP, where the β parameters are scaled dimensionally with the subtracting constants. With the model now defined from the DOE data the fit of the model to the real data can be tested by evaluating the model at the DOE data points and comparing the results. The plots of the regression fits of the three responses are shown in Figure 50 with 95% confidence intervals.

$$\begin{aligned}
y_{icos} = & \beta_0 + \beta_A \left(\frac{E_b}{\rho_b} \right) + \beta_B \left(\frac{E_s}{\rho_s} \right) + \beta_C(h) + \beta_D \left(\frac{t_b}{r_b} \right) + \beta_E \left(\frac{W}{B_s} \right) \\
& + \left(\frac{E_b}{\rho_b} - 1.82E^6 \right) \left(\left(\frac{t_b}{r_b} - 0.0275 \right) \beta_{AD} \right) \\
& + \left(\frac{E_b}{\rho_b} - 1.82E^6 \right) \left(\left(\frac{W}{B_s} - 0.25 \right) \beta_{AE} \right) \\
& + \left(\frac{E_s}{\rho_s} - 1.36E^6 \right) \left(\left(\frac{t_b}{r_b} - 0.0275 \right) \beta_{BD} \right) \\
& + \left(\frac{E_s}{\rho_s} - 1.36E^6 \right) \left(\left(\frac{W}{B_s} - 0.25 \right) \beta_{BE} \right) + (h - 7500) \left(\left(\frac{t_b}{r_b} - 0.0275 \right) \beta_{CD} \right) \\
& + \left(\frac{t_b}{r_b} - 0.0275 \right) \left(\left(\frac{W}{B_s} - 0.25 \right) \beta_{DE} \right) \\
& + \left(\frac{E_b}{\rho_b} - 1.82E^6 \right) \left(\left(\frac{t_b}{r_b} - 0.0275 \right) \left(\left(\frac{W}{B_s} - 0.25 \right) \beta_{ADE} \right) \right) \\
& + \left(\frac{E_s}{\rho_s} - 1.36E^6 \right) \left(\left(\frac{t_b}{r_b} - 0.0275 \right) \left(\left(\frac{W}{B_s} - 0.25 \right) \beta_{BDE} \right) \right)
\end{aligned}$$

Figure 49: Least squares regression general equation for the icosahedron model

Table 28: Least Squares Regression Estimates – Icosahedron Model Outputs

Least Squares Regression Estimates -Icosahedron			
Coefficient	Max Frame Stress	Max Skin Stress	Final W/B
β_0	1294694887	1392717264	1.050358468
β_A	18.71777355	-5.217387414	-1.08114E-10
β_B	-6.331392714	11.91944425	-5.81414E-11
β_C	-13153.1872	13196.10453	-9.98935E-07
β_D	14335566657	53616018562	0.45792722
β_E	-654652304.2	-1529662408	0.013771423
β_{AD}	87.66680832	-69.16238472	-2.08588E-09
β_{AE}	2.351367126	8.136964824	-4.61441E-11
β_{BD}	-152.162163	185.0910597	-2.62763E-09
β_{BE}	-14.15122939	-16.46715089	-2.63484E-11
β_{CD}	-557956.5037	575184.4978	6.66285E-06
β_{DE}	-1.47226E+11	-68903376796	-0.396552314
β_{ADE}	-816.5609657	616.9378339	1.51817E-09
β_{BDE}	161.8834764	-1116.930266	1.09624E-10

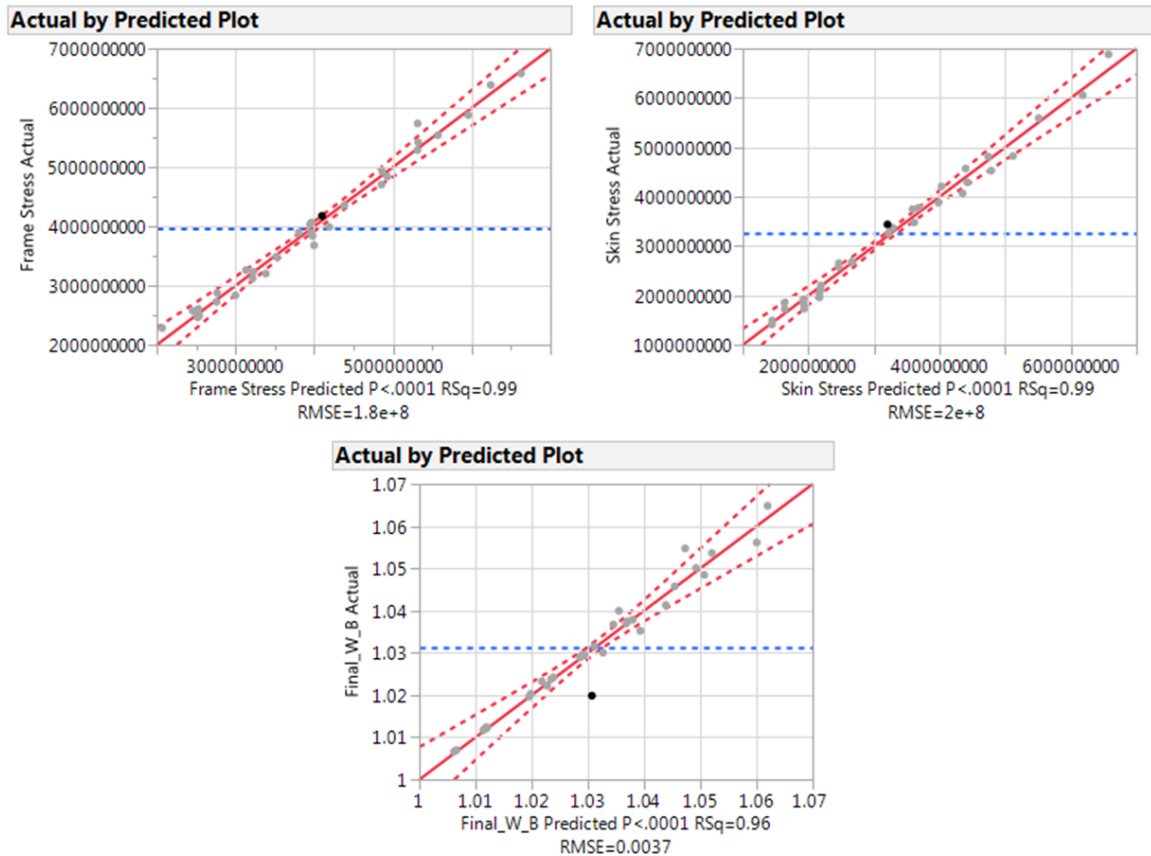


Figure 50: Least Squares Regression Fit for the Icosahedron Model Outputs

The graphs in Figure 50 are plotted with the actual design response data points on the vertical axis versus the estimated values generated using the regression equation in Figure 49, with the respective response set of β estimators in Table 28. How well the regression model fits the actual data can be observed by observing the fits root mean square error (RSME), and the R-square or R-square Adj. The RSME is effectively the averaged error between the fit and the actual data points for all the experiments conducted. Ideally, you want the RSME value to be small compared to the average response of the system that is being observed. If the regression fits RSME is similar to the average of all the responses then it can be concluded that the fit being used is not a good fit for the data set. For the icosahedron model the RSME values for all the

responses was compared to the average response of the data and is shown in the % RSME of Mean Response in Table 29. The RSME for max frame stress, max skin stress, and final W/B compared to the mean of the response was [4.56%, 6.26%, and 0.36%] respectively. This indicates that the regression fit has an average of [4.56%, 6.26%, and 0.36%] error when approximating the actual respective responses of the FEM. Typically, error values less than 10% are considered “good”. When viewing the R-square or R-square Adj value, values close to one tend to indicate that the regression fit is “good”. But, there are some pitfalls when observing the R-square or R-square Adj value. One reason that the value could be high is because of an over-fitted model. Over-fitted models are models that include too many factors and interactions to estimate the response compared to the number of experiments. For instance, if you include all of the factors and interactions to predict a response the R-square or R-square Adj value will always be one. For this research, since the RSME value is small compared to the average of the responses, the models fits will be considered “good”.

Table 29: Summary of Regression Fit Information – Icosahedron Model

Summary of Regression Fit - Icosahedron Model			
	Frame Stress	Skin Stress	Final_W_B
RSquare	0.987	0.988	0.964
RSquare Adj	0.978	0.979	0.939
Root Mean Square Error	1.8118E+08	2.0398E+08	0.004
Mean of Response	3.9676E+09	3.2588E+09	1.031
% RSME of Mean Response	4.566	6.259	0.362
Observations (or Sum Wgts)	33	33	33

Icosahedron Response Surfaces

It is now possible to produce surface plots with the first order regression models of the design space associated with the icosahedron model revolving around the DOE test points for the three outputs. The median surface plots for max frame and skin stress along with final W/B are shown in Figure 51, Figure 52, and Figure 53. In the figures, the black points at the corners of the surfaces represent the data points (FEA) obtained from the DOE, which the response surface is based on. The stress contours are plotted with respect to c-ratio and skin percentage to show the shape of the response surface that remains constant when the remaining factors are altered. When the material properties are varied, the response surface shifts up and down the vertical axis along the red arrows while maintaining its shape. The red arrows indicate the range of travel of the response surface when the factor levels of the non-plotted factors, frame and skin specific modulus, are moved from low to high.

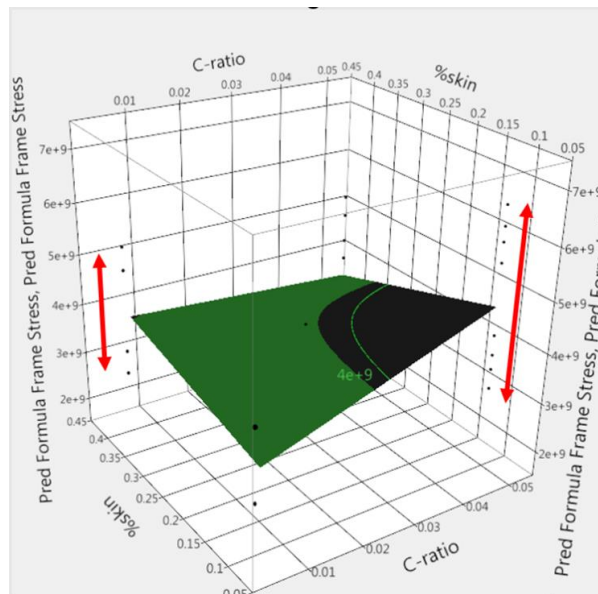


Figure 51: Icosahedron Max Frame Stress Response Surface

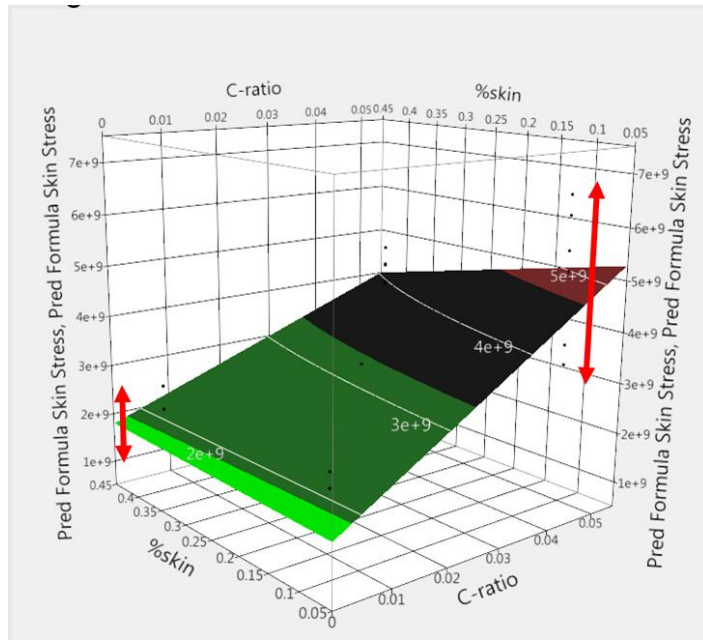


Figure 52: Icosahedron Max Skin Stress Response Surface

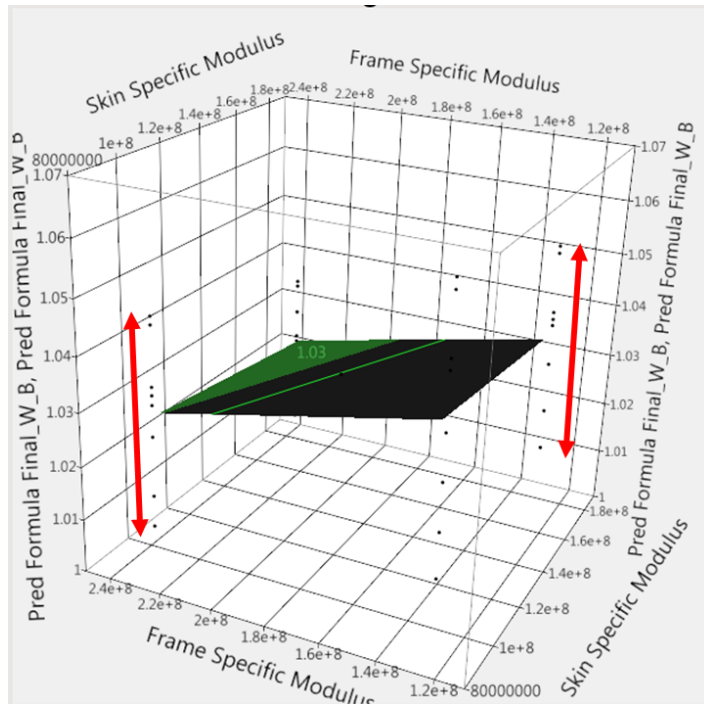


Figure 53: Icosahedron Final W/B Response Surface

At this point in the analysis it is now possible to develop the feasible design space for the icosahedron vehicle with respect to material failure. This process is performed by

taking the data from the stress response surfaces and converting it to indicate whether or not the structure has failed material wise. This is done by dividing the stress values for the frame and skin at each point by its materials yield strength value (σ_y). This produces the safety factor for the frame and skin. As long as the stress in the frame and skin respectively is lower than the respective materials yield value, then a safety factor greater than one will be produced. All designs with both the frame and skin safety factors equal to or above one will be considered feasible in terms of material failure. The above manipulation of the stress surfaces was performed for both the frame and skin and the safety factor surfaces are shown in Figure 54 and Figure 55 with the slicing grid pattern indicating where a SF of one lies. The next step in the analysis process will focus in on Figure 54 and Figure 55 to determine if and where the feasible design space lies for the icosahedron model.

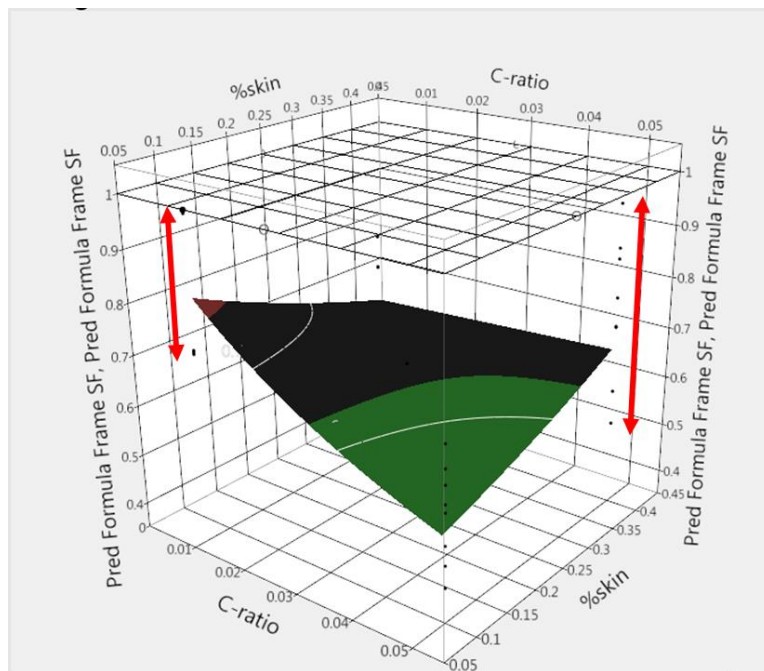


Figure 54: Icosahedron Frame SF Response Surface

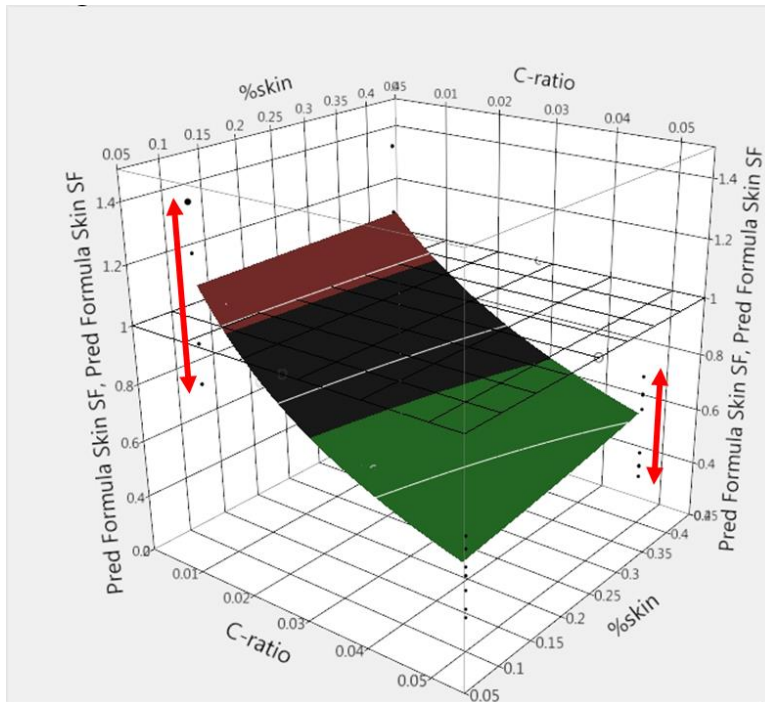


Figure 55: Icosahedron Skin SF Response Surface

Icosahedron VLTAV Structural Feasibility Assessment and Response

Discussion

Icosahedron Material Safety Factor Analysis

Starting with the SF response surfaces in Figure 54 and Figure 55, the possible feasible design space was investigated. With the requirement that both the frame and skin SF need to be equal to or greater than 1 to produce a feasible icosahedron structure material wise, both SF surfaces were observed simultaneously on a contour plot. A surface a contour plot showing both frame and skin SF contours with respect to c-ratio and skin percentage is shown in Figure 56. The material properties for this plot set to maximize the frame and skin SF's simultaneously. The material property values happen to be the high level setting for both frame and skin specific modulus. The exact factor settings for the contour plot can be observed in top portion of Figure 56.

It is observed from the contour plot in Figure 56 that the icosahedron model tested across the factor levels does not achieve a feasible design anywhere in the constructed design space and is limited by the frame safety factor. The shaded regions in Figure 56 indicate safety factors equal to and less than 1, with the blue denoting the frame safety factor region and the red denoting the skin safety factor region. The best case icosahedron within the limits of the test locations is located the bottom left corner of Figure 56. This point was one of the DOE test points and the FEA results are shown in Figure 57, Figure 58, and Figure 59. The input values for the best case icosahedron VLTAV are shown in Table 30.

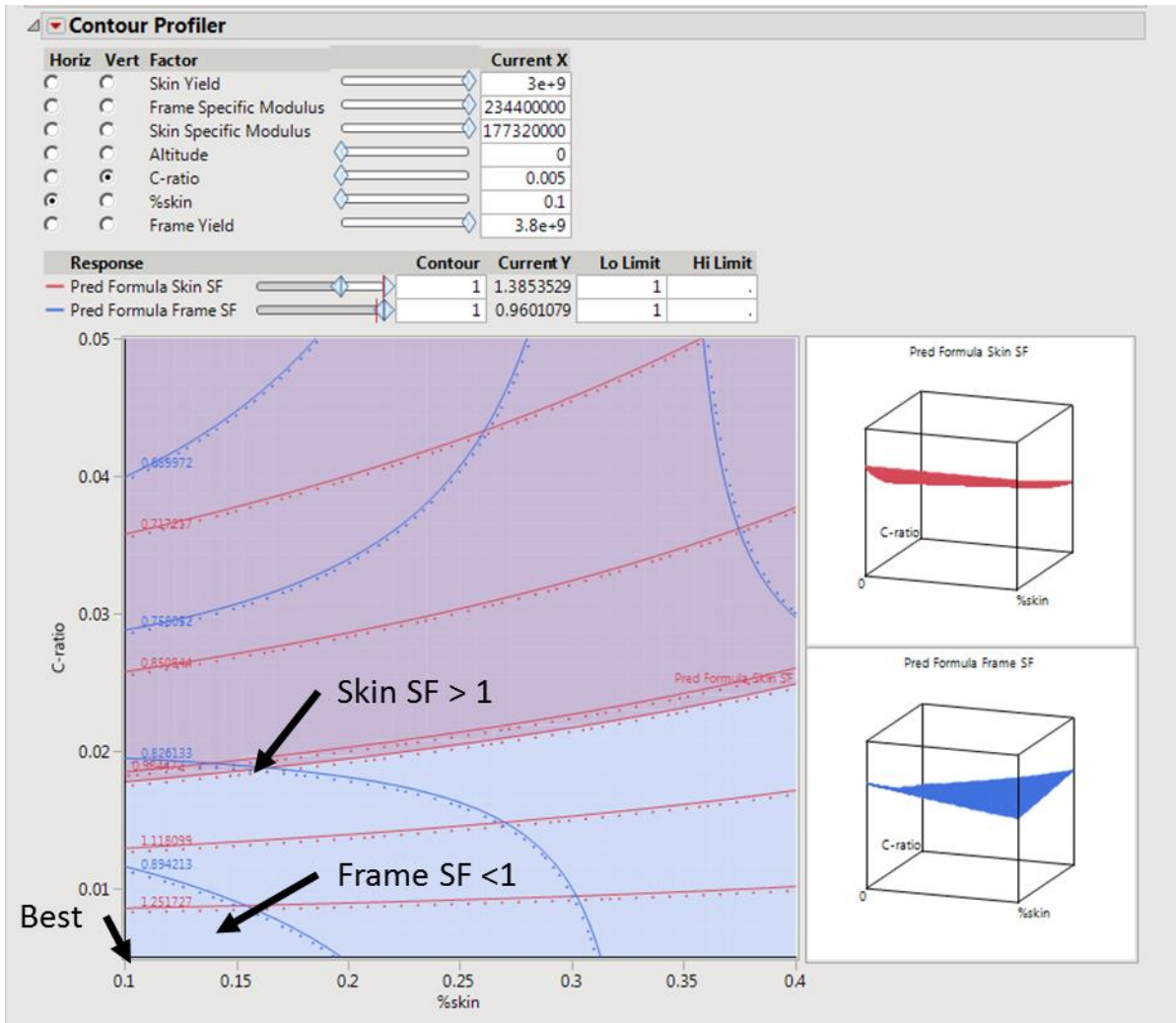


Figure 56: Icosahedron Contour Plot of Frame and Skin Safety Factor with respect to the input variables or factors.

Table 30: Icosahedron Input Parameters for Optimal Point

Icosahedron Properties		
Frame Specific Stiffness/Strength (m^2/s^2)	2.34E+08	3.04E+06
Skin Specific Stiffness/Strength (m^2/s^2)	1.77E+08	3.09E+06
Altitude (ft,m)	0	
C-ratio	0.005	
% Skin	10	

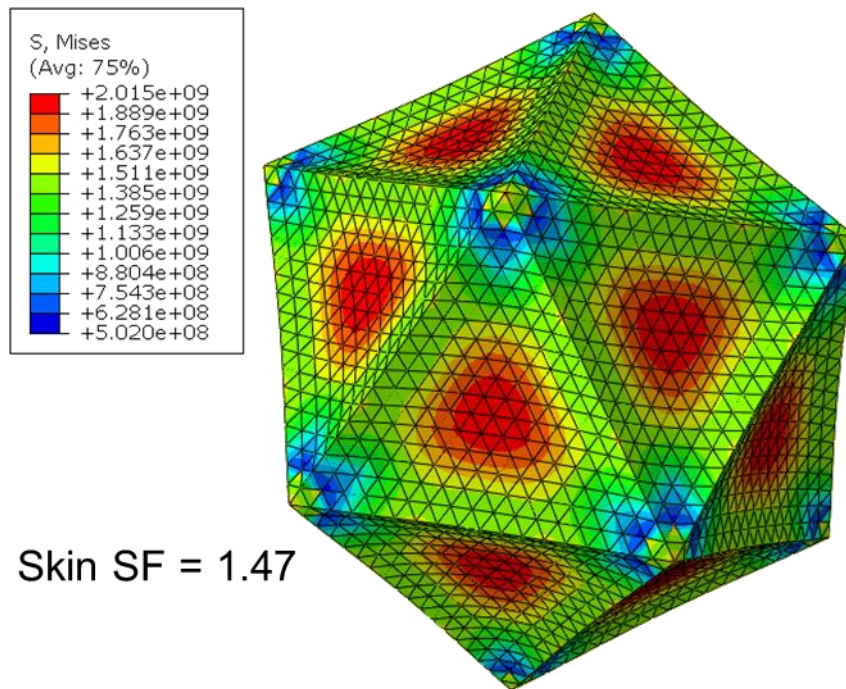


Figure 57: Icosahedron Skin Instance only FEA results for the optimum point

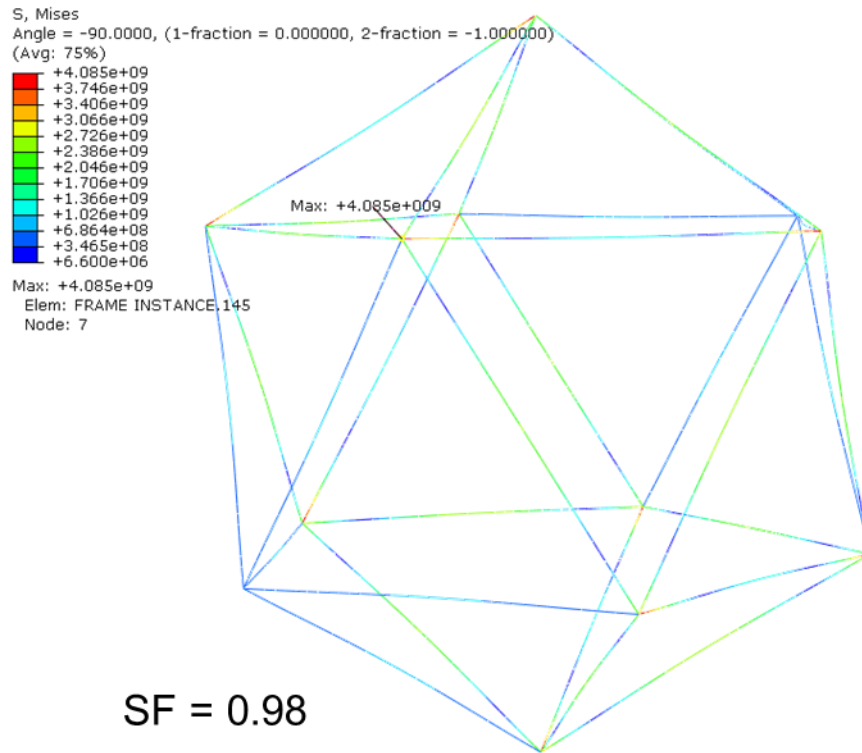


Figure 58: Icosahedron Frame Instance FEA results for the optimum point

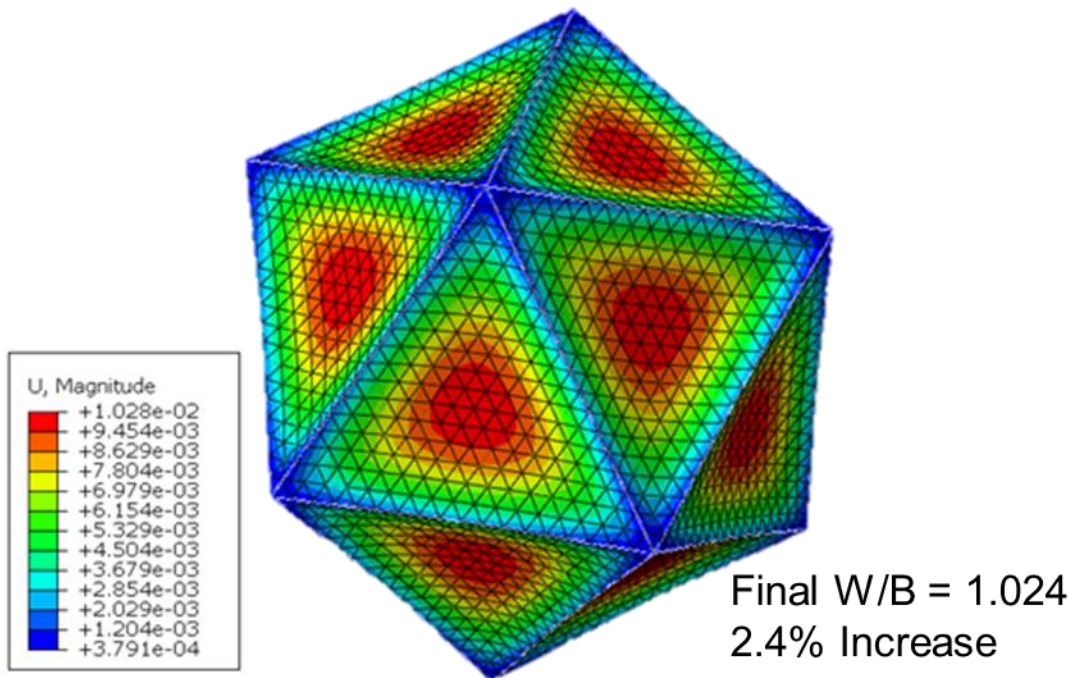


Figure 59: Icosahedron Displacement contour and resulting Final W/B.

The max stress in the frame, shown in Figure 58, of the icosahedron is located symmetrically at all of the vertices. This occurs because the frame is modeled as 2D line elements. This produces corners in the frame that would in reality not exist because the frame vertices would be filleted or curved in nature and not form a sharp corner. Therefore, it is expected that if 3D elements were used to create a fully 3 dimensional icosahedron frame and skin model that the max stress would occur at the vertices but the magnitude of the stress concentration would be less than what the current model predicts. Therefore, even though no accommodation was made, the max stress values in the frame would be consider to be an over estimate compared to a 3D model.

The maximum stress in the skin, shown in Figure 57, occurs at the center of the triangular faces when the $\frac{W}{B_s}$ is small, less than approximately 0.2 and when the $\frac{W}{B_s}$ is large, greater than approximately 0.3 the max stress moves to on top of the vertices. The max stress location on top of the vertices is what Rodriguez had observed when he evaluated the Metlen icosahedron. Rodriguez attributed the max stress to a singularity at the vertices for the skin. It is thought that when the $\frac{W}{B_s}$ term is small and the frame makes up the significant portion of the weight, the skin does not aid so much in stiffening the structure but distributes the load from the internal vacuum. This was observed when investigating the max stress values in the frame and skin while only varying $\frac{W}{B_s}$. When $\frac{W}{B_s}$ is large, the skin stress values are greater than the frame and as the $\frac{W}{B_s}$ term is reduced there is a point where the skin and frame max stress are effectively equal. If the $\frac{W}{B_s}$ is continued to be reduced, then the max stress in the frame becomes greater than the skin.

Depending on the materials selected for a design, it would be desired for the max stress to be in the frame and the skin to have a reduced load carrying role. The maximum deflection in the model, shown in Figure 59, was always observed at the center of all of the faces. Additionally, the W/B final response that was observed had a minimum increase from the original design W/B of 1 to 1.01 and a maximum increase of 1.06 looking at the entire data set from the DOE. This response agrees with the results obtained by Rodriguez in that the skin and frame deflection results in a small reduction in the internal volume which in turn increased the final W/B ratio of the design. If the icosahedron design space evaluated had any viable designs, they would have technically been negatively buoyant because of the volume loss due to the frame and skin deflection. However, if a viable design were found and the W/B final was observed to be the worst case of 1.06, that design would be redesigned and structurally analyzed starting with an initial W/B of at least 0.94 to account for the expected volume loss if a neutrally or slightly positively buoyant design was desired.

Icosahedron Geometric Instability Analysis

Since, a very small design window was found to almost satisfy the SF constraints for the icosahedron model within the DOE range, a buckling analysis was not performed on the “lowest stiffness” design. It was performed on the “highest stiffness” or best performing design within the design space because that is where the SF was the highest. This design was the point where frame and skin specific modulus were both at their high level and the remaining factors were all at their low level. Figure 60 shows the first buckling mode of the icosahedron frame with uniform pressure applied to the frame though the use of reference points as illustrated in the beginning of the chapter. The

critical buckling pressure for this mode was 966,486 Pa, which is 9.5 times greater than the applied pressure of 101,325 Pa. Therefore, there is no reason to believe that global buckling would occur in the structure before material failure would occur. Let it be noted that this design utilized beams with a c-ratio equal to 0.005 which exceeds the minimum value estimated for local buckling in chapter IV of 0.02. This does not mean that local buckling is guaranteed to occur because the approximation is based on a hollow cylinder with a simple support where the beams in the icosahedron have a differing BC. Nonetheless, it is important to note that it is a possibility. If this design were to be pursued then considering adding internal pressure to the beams or providing extra support by means of ring stiffeners would be advised.

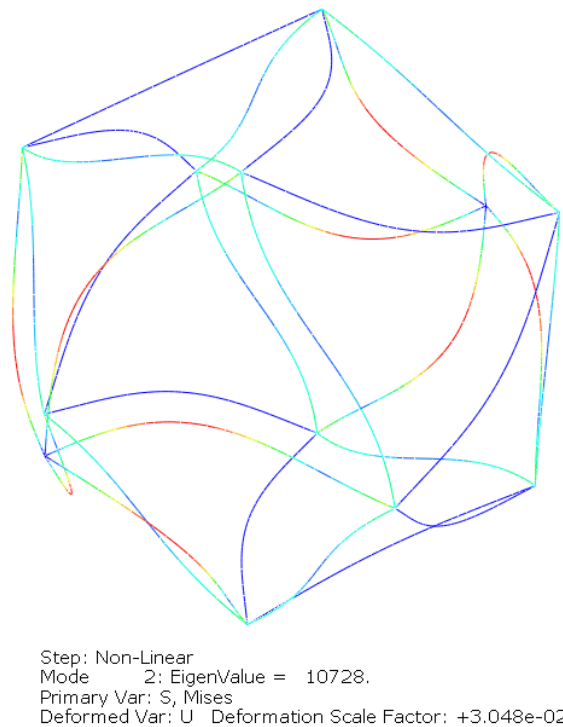


Figure 60: Icosahedron Critical Buckling Pressure at Optimal Design Point

Icosahedron Design Trades and Vehicle Sizing

Since no feasible design was found within the factor levels chosen for the DOE, a separate what-if analysis was performed to determine what potential factor levels would be necessary to potentially produce a feasible icosahedron design. By observing the regression fits beyond the current factor limits, a feasible icosahedron VLTAV would be potentially possible if the frames material properties were to increase, c-ratio were to decrease, or the skin percentage were to decrease. The fit equations were used to estimate what values of these parameters would be required to produce a feasible design by varying them one-by-one. This was performed, and the resulting values for frame specific modulus, c-ratio, and skin percentage were $2.4296E^8$, 0.0009, and 0.050 respectively to produce a frame $SF = 1$. These results show that either a 4% increase in frame specific modulus, a 100% reduction in c-ratio, or a 50% reduction in skin percentage from their respective limits of $2.34E^8$, 0.005, and 0.1 would produce a feasible icosahedron VLTAV. Let it be noted from the beam analysis performed in chapter IV, reducing the c-ratio can potentially have negative effects on the stability of the structure in terms of local buckling. Therefore, increasing the material properties or decreasing the skin percentage may be a more optimal choice. A contour plot with this expanded region is shown in Figure 61 where the white region is the region that would potentially produce a feasible icosahedron VLTAV.

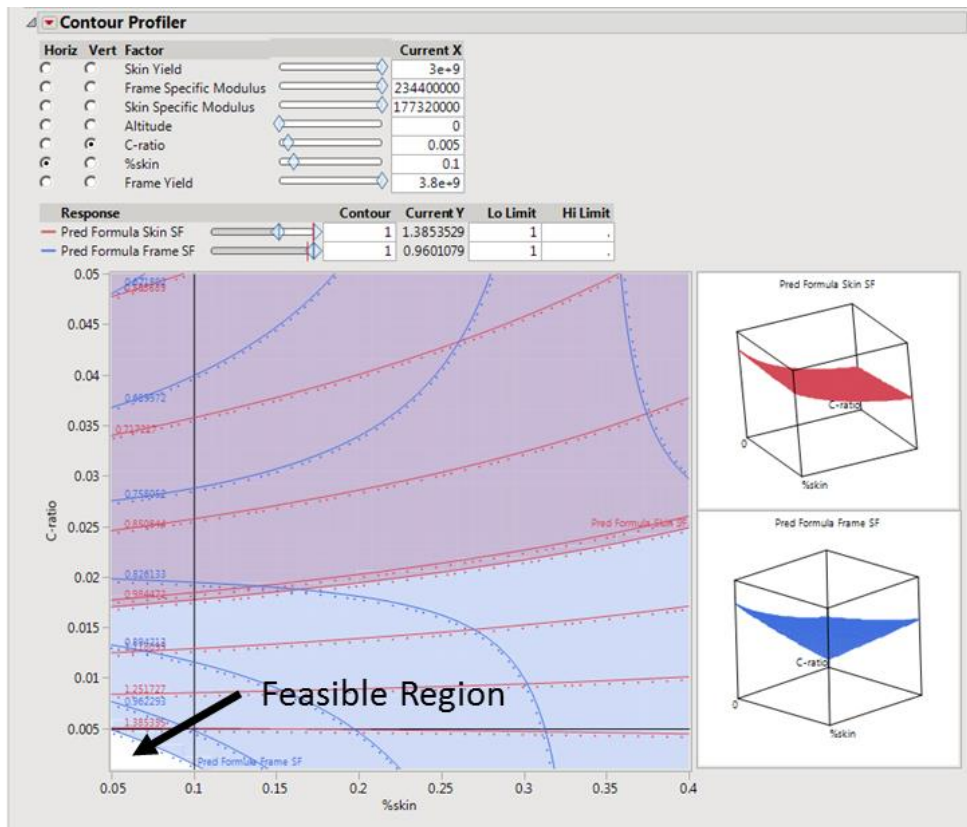


Figure 61: Icosahedron Contour Plot of Frame and Skin Safety Factor with expanded factor levels.

With a potentially feasible design space realized for the icosahedron it is now appropriate to apply the manufacturing constraints detailed earlier in the chapter. In order to realistically build a structure the dimensions of the structure need to be functional. The functional constraints that were determined through the materials research were that the minimum manufacturable membrane thickness was approximately 0.2mm and a minimum composite thickness was also 0.2 mm. Therefore, the skin and beam thickness for a feasibly manufacturable icosahedron VLTAV need to be equal to or greater than 0.2mm.

Since the DOE was composed of all of the invariant quantities that define the frame-skin finite analysis system, the results obtained from the DOE are all scale-invariant. This means that the structure dimensions can be scaled for any design points results with certainty that the results will remain constant. With the ability of scaling, the vehicle sizing equation can be recomposed so that all of the design parameters or factors are defined from the feasible region determined by the DOE and the vehicle radius solved for so that the manufacturing constraints of 0.2mm thicknesses are satisfied. This was performed for the icosahedron in the expanded potentially feasible zone and the results are shown in Figure 62. The line depicts the minimum structure size when the frame SF is constrained to equal 1 between the bounds of $\frac{W}{B_s} \in (0.009, 0.05)$ and $\frac{t_b}{r_b} \in (0.0009, 0.005)$. When $\frac{W}{B_s}$ is maximized, the structure minimum structure radius is 6m and when $\frac{t_b}{r_b}$ is maximized the minimum structure radius is 12m.

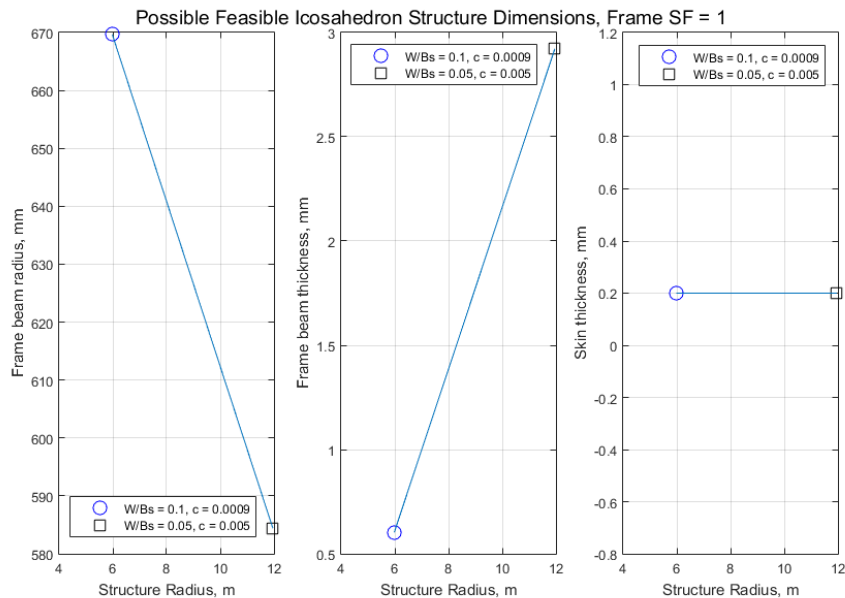


Figure 62: Possible Feasible Icosahedron Structure Dimensions for Frame SF = 1

All in all for the DOE investigation of the icosahedron VLTAV, it was determined which design parameters or invariants had a significant effect on the outputs. These invariants are $\frac{E_b}{\rho_b}$, $\frac{t_b}{r_b}$, $\frac{t_b W}{r_b B_s}$, $\frac{E_s}{\rho_s}$, and $\frac{E_s t_b}{\rho_s r_b}$. Within the range that the icosahedron vehicle was analyzed it showed that, with the materials and structure dimensionality chosen, an icosahedron VLTAV is not feasible. It also was shown that with some adjustments, a feasible vehicle could be designed using the regression equations developed as long as extrapolating the results beyond the tested range is appropriate. Utilizing the scaling-invariance, the minimum structure radius was determined that satisfied the manufacturing constraints of 0.2 mm skin and beam thicknesses.

Chapter V Summary

This chapter's objective was to perform the steps indicated in the methodology to create a structural design space bounded by present material and manufacturing limitations on the Metlen icosahedron VLTAV design. The chapter first developed the finite element model to produce the stress and displacement responses so that the maximum stresses for the skin and frame could be extracted as well as the final W/B. Next, a DA was performed on the finite element system input and out parameters to form the inputs into invariants, which are non-dimensional relational quantities of the original inputs. This allowed the original 10 model inputs to be reduced to five without eliminating any of the original 10 terms. Next, a 33 experiment DOE was performed to develop the data to determine which invariants from the DA, and their interactions had a significant effect on the structural response of the Metlen icosahedron design. The DOE

data was then used to create first order regression fits which were used to create first order response surfaces of the structural design space of the Metlen icosahedron within the limits of the levels prescribed. Through the evaluation of the design space, it was determined that utilizing present day materials did not produce any feasible designs with the corresponding limit chosen for altitude, c-ratio, and skin W/B. However, if the lower limits of c-ratio and skin W/B were relaxed further keeping the same material limits, it is predicted that a feasible design could exist.

VI. Hexakis Icosahedron DSE and Feasibility Assessment Case Study

Hexakis Icosahedron Selection

Stiffening of shells or membranes with an interior frame is not uncommon; however, the unique problem of managing large compressive stresses and being incredibly light weight is one that is rather new. An ideal structural shape to handle this loading scenario would be a sphere as indicated in chapter I. This has given rise to geodesic structures which use repeating geometric shapes, such as a triangle, connected to each other creating the shell of a “sphere”. These types of structures maximize load carrying capacity, while minimizing the amount of supporting structure. However when considering a vacuum lighter than air vehicle, Metlen determined that an icosahedron was the most ideal geodesic because all of the edges were the same length, and the faces were composed of a single unit equilateral triangle. These properties give rise to its symmetry classification of icosahedral symmetry. This symmetry appears to be the root of why the icosahedron design outperformed the more complex geodesics analyzed by Metlen. Additionally, the icosahedron along with similar polyhedron all can be thought of as geometric shapes that approximate a sphere with their segmented geometry while

keeping the faces planar. To have an idea of how closely the structures approximate a sphere, a parameter known as the isoperimetric quotient (IQ) is used [34]. An IQ of one yields a sphere; therefore any other convex solid has an IQ less than 1. With this, it is desired to choose a geometry that has a high IQ value. The equation for IQ is shown in equation 65, where V is volume and S is surface area.

$$IQ = 36\pi \frac{V^2}{S^3} \quad (65)$$

When considering a new frame design to evaluate, the necessary features are icosahedral symmetry, a single unit planar face, and a shape that approximates a sphere, ideally better than the icosahedron. Icosahedral symmetry involves 6 five-fold rotation axes passing through the vertices, 10 three-fold axes through each face, and 15 two-fold axes through the edges of an icosahedron [35]. An image of this is shown in Figure 63. There happens to be a group of polyhedron that have all of these features and that group is known as an isohedron. Within this group, there are seven shapes that have icosahedral symmetry and vary by their vertex locations, unit face shape, and number of faces. These solids are shown in Figure 64. As indicated above an ideal polyhedron would be one that has icosahedral symmetry, a single unit planar face and approximate a sphere the best. Out of these seven shapes, the 120 faced disdyakis triacontahedron or hexakis icosahedron falls out as the best. This shape is indicated by the one with the box around it in Figure 64. As a point of comparison, the IQ value of an icosahedron is approximately 0.83 and the hexakis icosahedron is approximately 0.95. The hexakis icosahedron will be the second structure considered for structural feasibility design space exploration.

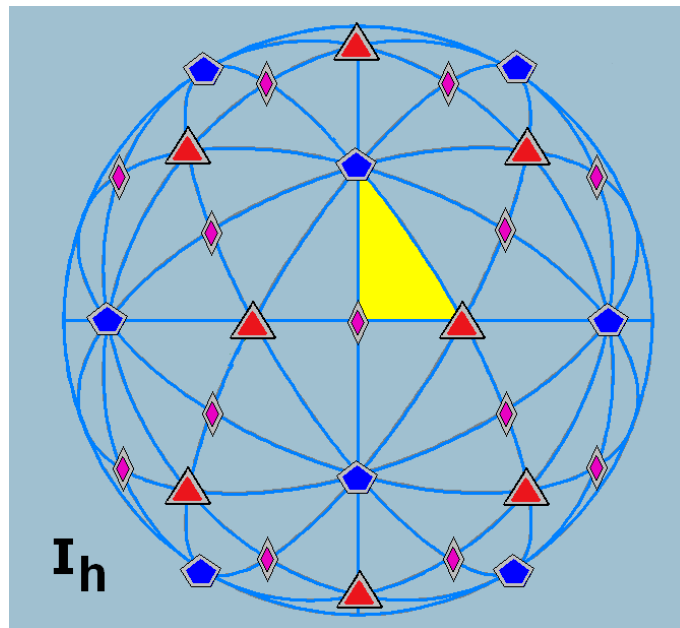


Figure 63: Icosahedral Symmetry

Platonic solids				
				
{5,3}	{3,5}			
Catalan solids				
				
V3.10.10	V4.6.10	V5.6.6	V3.4.5.4	V3.5.3.5

Figure 64: Full icosahedral symmetry isohedron shapes

Hexakis Icosahedron Finite Element Model Development

Hexakis Icosahedron Geometry Development

A hexakis icosahedron is a Catalan solid with 120 faces, 180 edges, and 62 vertices. The face configuration for this shape is V4.6.10, where there are 12 vertices with four lines intersecting, 20 vertices with six lines intersecting, and 30 vertices with ten lines intersecting. This polyhedron is composed of 120 identical scalene triangles. This shape is shown in Figure 65. The 12 vertices with four line intersections mark the vertices that represent an inscribed icosahedron.

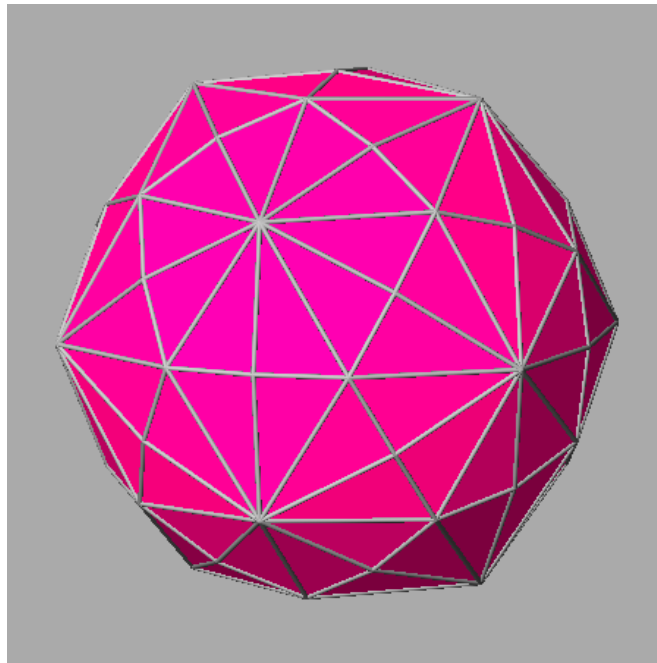


Figure 65: Hexakis Icosahedron

Similarly to the icosahedron, the vertex locations, surface area, and volume are necessary for modeling this structure. The 62 vertex locations of the hexakis icosahedron are determined by referencing Table 31. The following set of equations designating the C

values in Table 31 are shown in Table 32 based off an inscribed icosahedron with a unit edge length in Cartesian coordinates. Where, the inscribed icosahedrons vertices lie on the twelve vertices of the hexakis that have ten edges connecting at one point.

Table 31: Hexakis Icosahedron Vertex Locations

Hexakis Icosahedron Vertex Locations		
V0 = (0.0, 0.0, C8)	V20 = (-C3, 0.0, C6)	V41 = (C5, -C0, -C2)
V1 = (0.0, 0.0, -C8)	V21 = (-C3, 0.0, -C6)	V42 = (-C5, C0, C2)
V2 = (C8, 0.0, 0.0)	V22 = (C6, C3, 0.0)	V43 = (-C5, C0, -C2)
V3 = (-C8, 0.0, 0.0)	V23 = (C6, -C3, 0.0)	V44 = (-C5, -C0, C2)
V4 = (0.0, C8, 0.0)	V24 = (-C6, C3, 0.0)	V45 = (-C5, -C0, -C2)
V5 = (0.0, -C8, 0.0)	V25 = (-C6, -C3, 0.0)	V46 = (C2, C5, C0)
V6 = (0.0, C1, C7)	V26 = (0.0, C6, C3)	V47 = (C2, C5, -C0)
V7 = (0.0, C1, -C7)	V27 = (0.0, C6, -C3)	V48 = (C2, -C5, C0)
V8 = (0.0, -C1, C7)	V28 = (0.0, -C6, C3)	V49 = (C2, -C5, -C0)
V9 = (0.0, -C1, -C7)	V29 = (0.0, -C6, -C3)	V50 = (-C2, C5, C0)
V10 = (C7, 0.0, C1)	V30 = (C0, C2, C5)	V51 = (-C2, C5, -C0)
V11 = (C7, 0.0, -C1)	V31 = (C0, C2, -C5)	V52 = (-C2, -C5, C0)
V12 = (-C7, 0.0, C1)	V32 = (C0, -C2, C5)	V53 = (-C2, -C5, -C0)
V13 = (-C7, 0.0, -C1)	V33 = (C0, -C2, -C5)	V54 = (C4, C4, C4)
V14 = (C1, C7, 0.0)	V34 = (-C0, C2, C5)	V55 = (C4, C4, -C4)
V15 = (C1, -C7, 0.0)	V35 = (-C0, C2, -C5)	V56 = (C4, -C4, C4)
V16 = (-C1, C7, 0.0)	V36 = (-C0, -C2, C5)	V57 = (C4, -C4, -C4)
V17 = (-C1, -C7, 0.0)	V37 = (-C0, -C2, -C5)	V58 = (-C4, C4, C4)
V18 = (C3, 0.0, C6)	V38 = (C5, C0, C2)	V59 = (-C4, C4, -C4)
V19 = (C3, 0.0, -C6)	V39 = (C5, C0, -C2)	V60 = (-C4, -C4, C4)
	V40 = (C5, -C0, C2)	V61 = (-C4, -C4, -C4)

Table 32: Hexakis Icosahedron coordinate equations.

Hexakis Icosahedron Vertex coordinate location C equations
$C_0 = \frac{r_{icos}\sqrt{5/2(85 - 31\sqrt{5})}}{22}$
$C_1 = \frac{r_{icos}\sqrt{5/2(25 - 11\sqrt{5})}}{3}$
$C_2 = \frac{r_{icos}\sqrt{5(25 - 2\sqrt{5})}}{22}$
$C_3 = r_{icos}\sqrt{1/10(5 - \sqrt{5})}$
$C_4 = \frac{r_{icos}^5}{3\sqrt{(5 + 2\sqrt{5})}}$
$C_5 = \frac{r_{icos}\sqrt{5/2(65 + 19\sqrt{5})}}{22}$
$C_6 = r_{icos}\sqrt{1/10(5 + \sqrt{5})}$
$C_7 = \frac{r_{icos}\sqrt{5/2(5 - \sqrt{5})}}{3}$
$C_8 = \frac{r_{icos}\sqrt{5(25 - 2\sqrt{5})}}{11}$

From here the edge lengths of the unit scalene triangle that makes up the hexakis framework can be determined by using equations (66-68). l_{se} , l_{me} , l_{le} represent the short, medium, and long leg lengths of the triangle. With the edge lengths known, the surface area is computed using equation (69) and the number of triangles, shown in equations (69-70). Finally, the volume is readily computed using equation (71).

$$l_{se} = r_{icos} \frac{5}{11} \sqrt{49 - \frac{65\sqrt{5}}{3}} \quad (66)$$

$$l_{me} = r_{icos} \frac{1}{11} \sqrt{81 - 21\sqrt{5}} \quad (67)$$

$$l_{le} = r_{icos} 2 \sqrt{\frac{7}{3} - \sqrt{5}} \quad (68)$$

$$p_{ht} = \frac{l_{se} + l_{me} + l_{le}}{2} \quad (69)$$

$$A_{HI} = 120 \sqrt{p_{ht}(p_{ht} - l_{se})(p_{ht} - l_{me})(p_{ht} - l_{le})} \quad (70)$$

$$V_{HI} = \frac{r_{icos}^3 100}{3 \sqrt{53 + \frac{118}{\sqrt{5}}}} \quad (71)$$

Hexakis Icosahedron Sizing Equations

The sizing equation for the hexakis icosahedron is the same sizing equation developed for the icosahedron where the only difference are the equations to compute the beam radius and skin thickness. The equations for the beam radius and skin thickness are shown in equations 72 and 73. The beam thickness is computed the same way as the icosahedron with the c-ratio using equation 53.

$$r_{b_{hex}} = \sqrt{\frac{\frac{W}{B_f} \rho_a V_{HI}}{\left((\pi 60 (2c - c^2)) (l_{se} + l_{me} + l_{le}) \right) \rho_f}} \quad (72)$$

$$t_{s_{hex}} = \frac{\rho_a \frac{W}{B_s} V_{HI}}{A_{HI} \rho_s} \quad (73)$$

Hexakis Icosahedron Finite Element Models

The hexakis icosahedron finite element model was modeled using the same B32 beam elements for the frame and M3D3 membrane for the skin as in the icosahedron model, established in the previous case study. The boundary conditions and pressure loading were applied in the same fashion for the hexakis icosahedron model as in the icosahedron model and the vacuum finite element model is shown in Figure 66 with the converged mesh, boundary conditions, and loading shown. Figure 67 shows the finite element model developed to perform the frame buckling analysis in the feasibility section of the methodology. This model was developed using the same reference point technique developed for the icosahedron.

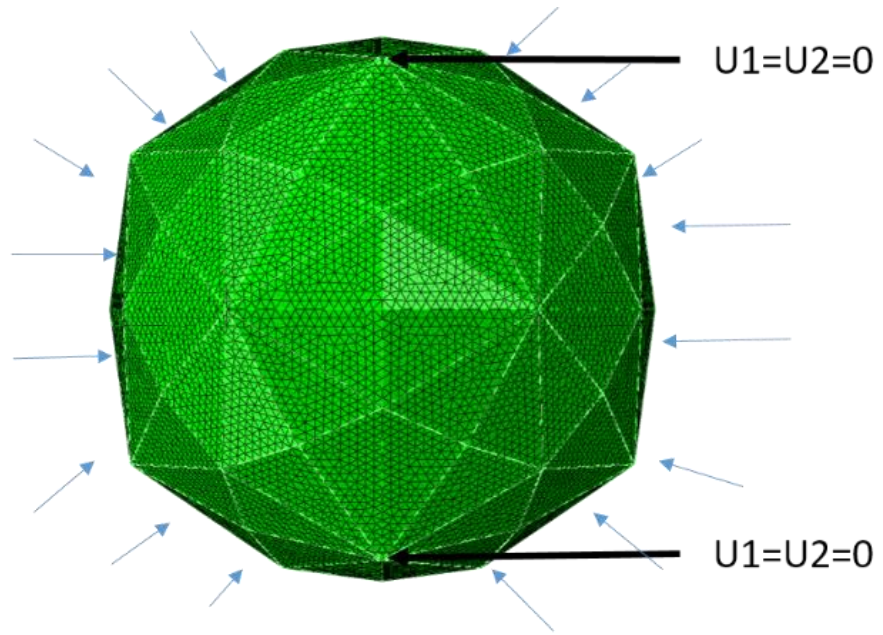


Figure 66. Boundary Conditions and Loads for the Hexakis Icosahedron VLTAV FE model.

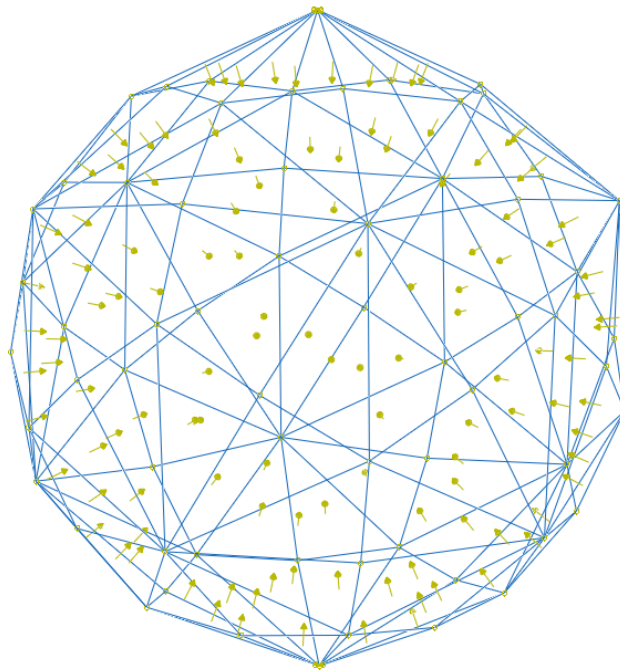


Figure 67: Hexakis Icosahedron Frame with Reference Point Loading

Hexakis Icosahedron FE Mesh Convergence Study

The hexakis icosahedron model developed was analyzed to determine mesh convergence. The model parameters for this investigation were the same as the icosahedron. The model properties for the convergence study are shown in Table 33.

Table 33: Hexakis Convergence Study Parameters

Hexakis Convergence Study Parameters		
Parameter		Units
W/Bf	0.9	
W/Bs	0.1	
ρ_a	1.225	kg/m ³
ρ_b	1250	kg/m ³
ρ_s	970	kg/m ³
c	0.005	
r_{icos}	0.1524	m
Eb	2.93E+11	Pa
Es	1.72E+11	Pa
P	101325	Pa

The seeding for the hexakis model was performed in a similar but different manner to the icosahedron. Since the edge lengths of the hexakis icosahedron are not all identical as they were for the icosahedron, the seeding was performed by choosing a global element size instead of number of elements per edge. The global element sizes for the convergence analysis were [0.1, 0.0167, 0.0091, 0.0063, 0.0048, 0.0038, 0.0032, and 0.0028]. The results of this convergence analysis are shown in Figure 68. The seed size that produced a converged solution was 0.0048 or approximately 18,000 elements. This seeding produced a frame stress, skin stress, and final W/B solution that was 2.7%, 2.5%, and 0.004% different than the solution with approximately 46,000 elements or 0.0028

seed size. This seeding also produced a CPU computation time of approximately 9 minutes, 55% less time than it took to solve the 46,000 element model.

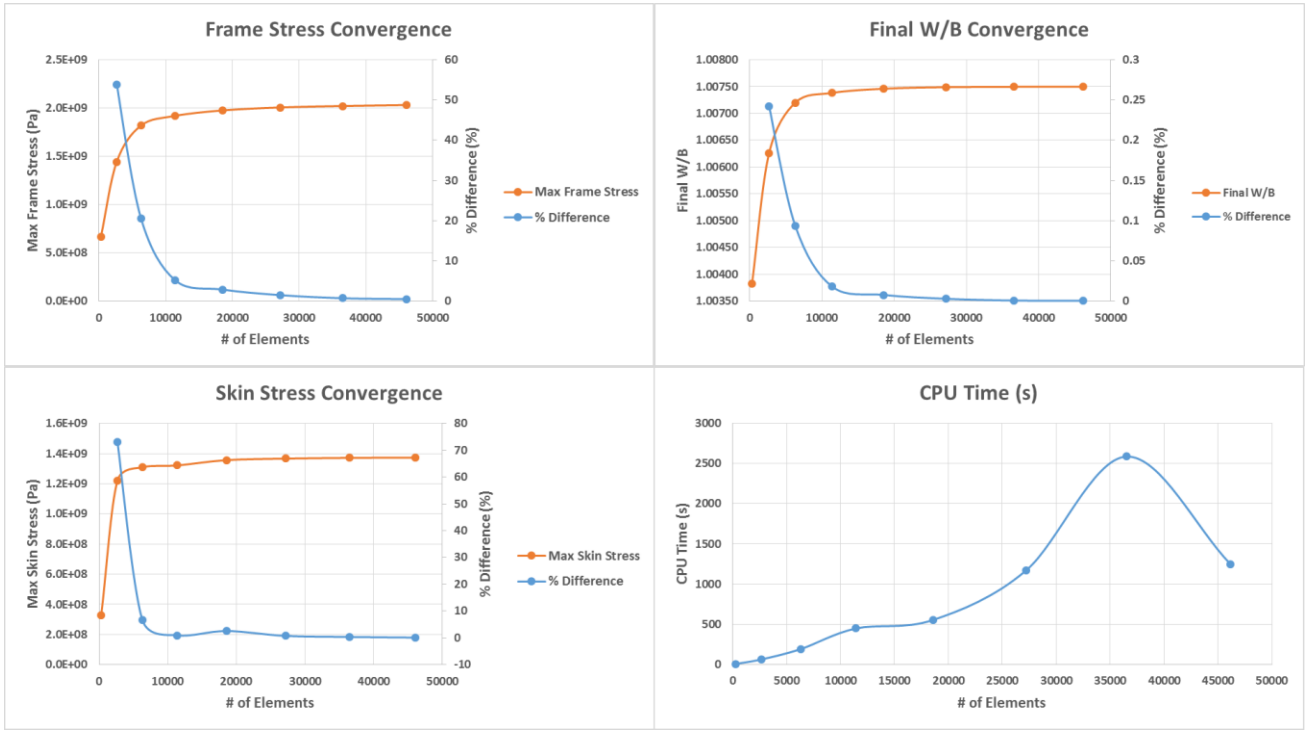


Figure 68: Hexakis Icosahedron Vacuum FE model mesh convergence study.

Additionally, these element seed sizes are particular to the scale of the vehicle. For instance, these sizes produced the number of elements and the convergence analysis for the six inch (0.1524 m) radius hexakis structure as shown in Figure 68. If the scale of the vehicle was smaller or larger, the global seed size numbers would have to be scaled respectively. The process of performing the seed size scaling is shown in equation (74).

$$s_{\#} = s_c \left(\frac{r_{icos}}{6} \right) \quad (74)$$

Where, $s_{\#}$ is the seed size, s_c is the converged seed size determined from the convergence analysis, r_{icos} is the hexakis radius, and the constant of six comes from the

fact that the s_c term was determined from analyzing a 6 inch (0.1524 m) radius hexakis icosahedron. Equation (74) ensures that no matter the structures radius, each model will have effectively the same converged discretization found in Figure 68.

Hexakis Icosahedron VLTAV FEA Dimensional Analysis

The input parameters for the hexakis icosahedron dimensional analysis are the same parameters developed for the icosahedron model. The parameters are identically the same because the designs are effectively the same with the only difference being the structure geometry.

Since the design parameters are the same for the hexakis icosahedron, the invariants will also be the same as for the icosahedron design. They are repeated here in equation (75) for convenience.

$$\Pi_i = \left(\frac{\sigma_{fmax}}{E_b} \right), \left(\frac{\sigma_{smax}}{E_b} \right), \left(\frac{u}{r_{icos}} \right), \left(\frac{W}{B_f} \right), \left(\frac{t_{bicos}}{r_{bicos}} \right), \left(\frac{W}{B_s} \right), \left(\frac{\rho_s}{\rho_b} \right), \left(\frac{E_s}{E_b} \right), \left(\frac{P}{E_b} \right) \quad (75)$$

In the same fashion as the icosahedron, a scale study was performed on the hexakis icosahedron design. The analysis also proved that only changing the vehicle radii has no effect on the stress and relative displacement results, as indicated by the near zero percent difference between all models when comparing them to the 3 inch (0.0762 m) model. The results are shown in Table 34.

Table 34: Hexakis Icosahedron Scale vs. FE Model Outputs and % Difference

Hexakis Icosahedron Radius (in)	Frame Stress (Pa)	% Difference (%)	Skin Stress (Pa)	% Difference (%)	Final W/B	% Difference (%)
3	1.915E+09	0.0000	1.320E+09	0.0000	1.0074	0.0000
6	1.915E+09	0.0099	1.319E+09	0.0107	1.0074	0.0016
12	1.915E+09	0.0032	1.319E+09	0.0051	1.0074	0.0038
24	1.915E+09	0.0010	1.319E+09	0.0054	1.0074	0.0019
48	1.915E+09	0.0016	1.319E+09	0.0059	1.0074	0.0016
96	1.915E+09	0.0089	1.319E+09	0.0064	1.0074	0.0016

DOE Analysis Results and Discussion for the Hexakis Icosahedron Vacuum Vehicle

The DOE for the hexakis icosahedron case study will use the same five steps outlined in the icosahedron study. In fact the only difference between the hexakis icosahedron DOE and the icosahedron DOE are the high levels for the c-ratio and skin percentage, and the structural response values of max frame and skin stress and final W/B. The DOE test matrix used to perform the hexakis FEAs followed the same arrangement as the icosahedron.

Determine Factors and Levels

The factor levels for the hexakis icosahedron analysis remained mainly the same as the levels defined in the icosahedron case study. The values that are different are the high levels for the c-ratio and skin percentage, which were made smaller than the icosahedron DOE. The reason for the more narrow range comes from the nature of the model and the ability to produce FE solutions within a “reasonable” amount of time. The factors and their levels to be investigated are shown in Table 35. The hexakis structure will look at the same outputs as in the icosahedron investigation pointed out in Table 19.

Table 35: Hexakis Icosahedron Factors

Hexakis Icosahedron Factorial Design Factors and Levels		
Factor	Level 1 (Low)	Level 2 (High)
<i>Frame Specific Modulus:</i> $\frac{E_b}{\rho_b}$ (m^2/s^2)	1.29E8	2.34E8
<i>Skin Specific Modulus:</i> $\frac{E_s}{\rho_s}$ (m^2/s^2)	9.52E7	1.77E8
<i>Altitude:</i> h (m)	0	4572
<i>Cratio:</i> $\frac{t_b}{r_b}$	0.005	0.025
<i>Skin Weight/Buoyancy:</i> $\frac{W}{B_s}$	0.1	0.2

Experiments and Results

The DOE test matrix for the hexakis structure was the same as for the icosahedron structure shown in Table 18. The DOE was automatically conducted utilizing the cyclic process identified in Figure 11 where it took approximately 20 hours to run the 33 FEA.

Table 36: Hexakis Icosahedron DOE Inputs and Results

Hexakis Icosahedron DOE Inputs and Results							
Frame specific stiffness	Skin specific stiffness	Altitude	C-ratio	%skin	Max Frame Stress	Max Skin Stress	Final W_B
1.289E+08	1.773E+08	0	0.025	0.2	2.084E+09	2.445E+09	1.0154
2.340E+08	9.524E+07	0	0.025	0.1	2.894E+09	1.180E+09	1.0087
1.289E+08	9.524E+07	15000	0.005	0.2	1.529E+09	8.755E+08	1.0123
1.289E+08	1.773E+08	15000	0.025	0.1	1.986E+09	3.006E+09	1.0150
1.289E+08	1.773E+08	0	0.005	0.1	1.290E+09	1.544E+09	1.0110
1.289E+08	9.524E+07	15000	0.025	0.2	2.317E+09	1.961E+09	1.0180
2.340E+08	1.773E+08	0	0.005	0.2	2.168E+09	1.002E+09	1.0074
2.340E+08	1.773E+08	15000	0.025	0.2	2.997E+09	2.237E+09	1.0096
1.289E+08	1.773E+08	15000	0.005	0.2	1.450E+09	1.342E+09	1.0115
2.340E+08	9.524E+07	15000	0.005	0.1	1.962E+09	1.003E+09	1.0065
1.289E+08	9.524E+07	15000	0.025	0.1	2.118E+09	1.988E+09	1.0161
2.340E+08	1.773E+08	0	0.005	0.1	1.915E+09	1.319E+09	1.0066
2.340E+08	9.524E+07	0	0.005	0.2	2.204E+09	7.653E+08	1.0076
1.289E+08	1.773E+08	15000	0.005	0.1	1.340E+09	1.460E+09	1.0109
2.340E+08	9.524E+07	0	0.005	0.1	1.883E+09	1.075E+09	1.0065
1.289E+08	9.524E+07	0	0.025	0.2	2.275E+09	1.700E+09	1.0169
2.340E+08	9.524E+07	15000	0.025	0.1	2.846E+09	1.454E+09	1.0091
2.340E+08	9.524E+07	0	0.025	0.2	3.213E+09	1.284E+09	1.0100
2.340E+08	9.524E+07	15000	0.005	0.2	2.266E+09	7.172E+08	1.0075
1.289E+08	1.773E+08	0	0.025	0.1	1.991E+09	2.566E+09	1.0145
2.340E+08	1.773E+08	15000	0.005	0.1	1.981E+09	1.237E+09	1.0066
2.340E+08	1.773E+08	15000	0.005	0.2	2.205E+09	9.886E+08	1.0073
1.289E+08	9.524E+07	0	0.005	0.1	1.297E+09	1.189E+09	1.0112
1.289E+08	1.773E+08	0	0.005	0.2	1.418E+09	1.365E+09	1.0117
2.340E+08	1.773E+08	15000	0.025	0.1	2.765E+09	2.294E+09	1.0088
1.289E+08	1.773E+08	15000	0.025	0.2	2.089E+09	2.701E+09	1.0161
2.340E+08	1.773E+08	0	0.025	0.1	2.833E+09	1.900E+09	1.0085
2.340E+08	9.524E+07	15000	0.025	0.2	3.144E+09	1.537E+09	1.0103
1.289E+08	9.524E+07	0	0.005	0.2	1.479E+09	9.189E+08	1.0125
1.289E+08	9.524E+07	0	0.025	0.1	2.094E+09	1.648E+09	1.0152
2.340E+08	1.773E+08	0	0.025	0.2	3.035E+09	1.942E+09	1.0094
1.289E+08	9.524E+07	15000	0.005	0.1	1.359E+09	1.119E+09	1.0111
1.883E+08	1.347E+08	7500	0.015	0.15	2.271E+09	1.466E+09	1.0103

Analysis of Variance

As with the icosahedron analysis, the same main effects $\left(\frac{E_b}{\rho_b}, \frac{E_s}{\rho_s}, h, \frac{t_{bicos}}{r_{bicos}} \text{ and } \frac{W}{B_s}\right)$ and interactions effects estimation was conducted to determine remove insignificant factors and/or interactions from the model so that an ANOVA can be conducted. Lenth's PSE will be used just as in the icosahedron analysis to produce a pseudo error for the initial determination of significant parameters for each response. The Pareto chart and half normal plot for the frame safety factor are shown in Figure 69, will be analyzed to determine which factors and interactions to keep in the model for the ANOVA. Charts showing the same information for the remaining responses are shown in .

Table 37: Initial Significant Factor Terms for the outputs of the hexakis icosahedron DOE.

Hexakis Icosahedron Significant Effects			
Max Frame Stress	Max Skin Stress	Final W/B	Combined
A	A	A	A
B	B	B	B
C	C	C	C
D	D	D	D
E	E	E	E
AB	AB	AB	AB
AC			AC
AD	AD	AD	AD
AE			AE
BD	BD	BD	BD
BE		BE	BE
CD	CD	CD	CD
	DE		DE
ACD			ACD
	ADE		ADE
	BDE		BDE
	CDE		CDE

The initial use of Lenth’s PSE allowed for 14 interactions indicated in Table 22 to be discarded. Table 37 shows the factors and interactions that were indicated to be significant for each respective response by inspecting their half normal and Pareto charts. Now that 14 interactions have been discarded, a natural ANOVA can be proceed with where the 14 discarded interactions make up the error term necessary to compute the ANOVA.

The ANOVA was computed using the combined significant terms between the 3 responses (max frame stress, max skin stress and final W/B), which are shown in the combined effects column of Table 37. The combined column was chosen so that all of the responses could be analyzed simultaneously as well as to see if any new terms out of the initially estimated significant terms using Lenth’s PSE became significant. Utilizing the

JMP software, the 14 insignificant interactions were removed from the analysis and the ANOVA was computed for the max frame stress, max skin stress, and final W/B with respect to the remaining 17 factors and interactions listed in the combined column of Table 37. The ANOVA data computed for the max frame stress response considering all 33 FEAs is shown in Table 38. Table 38 details the sum of squares (SS) values, the computed F ratio, and whether or not the effect is significant for each of the 17 factors and interactions included in the ANOVA. The individual sum of squares and F ratios were computed using the theory detailed in the ANOVA section of chapter III. With the F -ratios computed, the next step is to determine if the factors and interactions are significant with respect to their F values. As outlined in the ANOVA section of chapter III, the factor and interaction F ratio will be compared to a critical F value obtained from an F statistic table. The critical F ratio, $F_{\alpha, a-1, N-a}$, for this analysis was determined to be 4.17 by taking α to be 0.05, which is commonly chosen, $a = 2$ (2 levels), and $N = 33$ (total number of experiments). Equation (62) is then used to determine if the factor or interaction (Treatment) F -ratio is greater than the critical ratio. If the treatment F -ratio is greater than the critical ratio the factor or interaction (treatment) is determined to be significant. The resulting significant terms utilizing the error computed in the ANOVA for all of the responses is shown in Table 40.

Table 39 shows additional ANOVA information for each of the three responses, specifically SS_{Model} (SS_{Total}) and SS_E , which are used to compute the F ratios in Table 38.

Table 38: ANOVA Results for Hexakis Icosahedron Frame Safety Factor

Y	Source	DF	Sum of Squares	F Ratio	Prob > F	Significant
Frame Stress	Frame Specific Mod [A]	1	4.66E+18	8002.3807	<.0001	TRUE
Frame Stress	Skin Specific Mod [B]	1	5.59E+16	95.9534	<.0001	TRUE
Frame Stress	Altitude [C]	1	2.45E+15	4.2138	0.0593	TRUE
Frame Stress	C-ratio [D]	1	5.23E+18	8987.1437	<.0001	TRUE
Frame Stress	%skin [E]	1	3.46E+17	593.46	<.0001	TRUE
Frame Stress	Frame Specific Mod*Skin Specific Mod [AB]	1	2.90E+15	4.9831	0.0424	TRUE
Frame Stress	Frame Specific Mod*Altitude [AC]	1	1.74E+15	2.9945	0.1055	FALSE
Frame Stress	Frame Specific Mod*C-ratio [AD]	1	5.70E+16	97.8125	<.0001	TRUE
Frame Stress	Frame Specific Mod*%skin [AE]	1	3.05E+16	52.4343	<.0001	TRUE
Frame Stress	Skin Specific Mod*C-ratio [BD]	1	2.57E+16	44.1927	<.0001	TRUE
Frame Stress	Skin Specific Mod*%skin [BE]	1	1.24E+16	21.3041	0.0004	TRUE
Frame Stress	Altitude*C-ratio [CD]	1	1.12E+16	19.1897	0.0006	TRUE
Frame Stress	Altitude*%skin [CE]	1	4.62E+13	0.0793	0.7824	FALSE
Frame Stress	C-ratio*%skin [DE]	1	1.23E+14	0.2111	0.653	FALSE
Frame Stress	Frame Specific Mod*Altitude*C-ratio [ACD]	1	3.60E+15	6.1763	0.0262	TRUE
Frame Stress	Frame Specific Mod*C-ratio*%skin [ADE]	1	4.43E+13	0.0761	0.7867	FALSE
Frame Stress	Skin Specific Mod*C-ratio*%skin [BDE]	1	3.47E+14	0.5952	0.4533	FALSE
Frame Stress	Altitude*C-ratio*%skin [CDE]	1	3.95E+14	0.6788	0.4238	FALSE
(^ this term is part of a significant higher degree term						

With the F -ratios computed, the next step is to determine if the factors and interactions are significant with respect to their F values. As outlined in the ANOVA section of chapter III, the factor and interaction F ratio will be compared to a critical F value obtained from an F statistic table. The critical F ratio, $F_{\alpha, a-1, N-a}$, for this analysis was determined to be 4.17 by taking α to be 0.05, which is commonly chosen [14], $a = 2$ (2 levels), and $N = 33$ (total number of experiments). Equation (62) is then used to determine if the factor or interaction (Treatment) F -ratio is greater than the critical ratio. If the treatment F -ratio is greater than the critical ratio the factor or interaction (treatment) is determined to be significant. The resulting significant terms utilizing the error computed in the ANOVA for all of the responses is shown in Table 40.

Table 39: Model ANOVA values (SS_T and SS_E values) - Hexakis Icosahedron

Max Frame Stress Model ANOVA					
Source	DF	Sum of Squares	Mean Square	F Ratio	Prob > F
Model	18	1.04E+19	5.80E+17	995.8111	<.0001
Error	14	8.15E+15	5.82E+14		
C. Total	32	1.04E+19			
Max Skin Stress Model ANOVA					
Source	DF	Sum of Squares	Mean Square	F Ratio	Prob > F
Model	18	1.10E+19	6.13E+17	487.3817	<.0001
Error	14	1.76E+16	1.26E+15		
C. Total	32	1.10E+19			
Final W/B Model ANOVA					
Source	DF	Sum of Squares	Mean Square	F Ratio	Prob > F
Model	18	0.000360331	2.00184E-05	948.0419	<.0001
Error	14	2.96E-07	2.11E-08		
C. Total	32	0.000360627			

Table 40: Hexakis Icosahedron Significant Terms estimated using standard error

Hexakis Icosahedron Significant Effects			
Max Frame Stress	Max Skin Stress	Final W/B	Combined
A	A	A	A
B	B	B	B
C	C	C	C
D	D	D	D
E	E	E	E
AB	AB	AB	AB
AC		AC	AC
AD	AD	AD	AD
AE		AE	AE
BD	BD	BD	BD
BE		BE	BE
CD	CD	CD	CD
	DE	DE	DE
ACD		ACD	ACD
	ADE		ADE
	BDE		BDE
	CDE		CDE

Interaction plots can be created to visually observe the main effect and interaction effects, using the ANOVA data. A cube interaction plot and main effects with 2nd degree interactions chart for the max frame stress are shown in Figure 70 and Figure 71. The interaction plots for the other two outputs are shown in Appendix B.

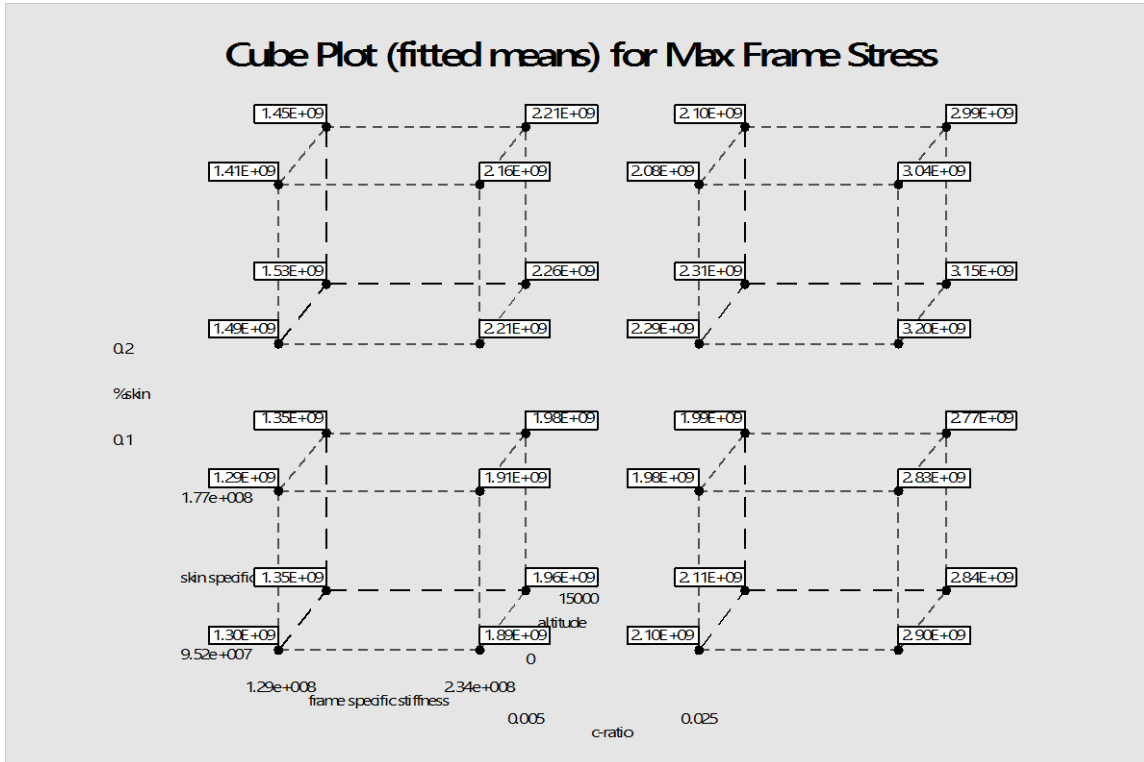


Figure 70: Cube Interaction Plot for the Max Frame Stress - Hexakis Icosahedron

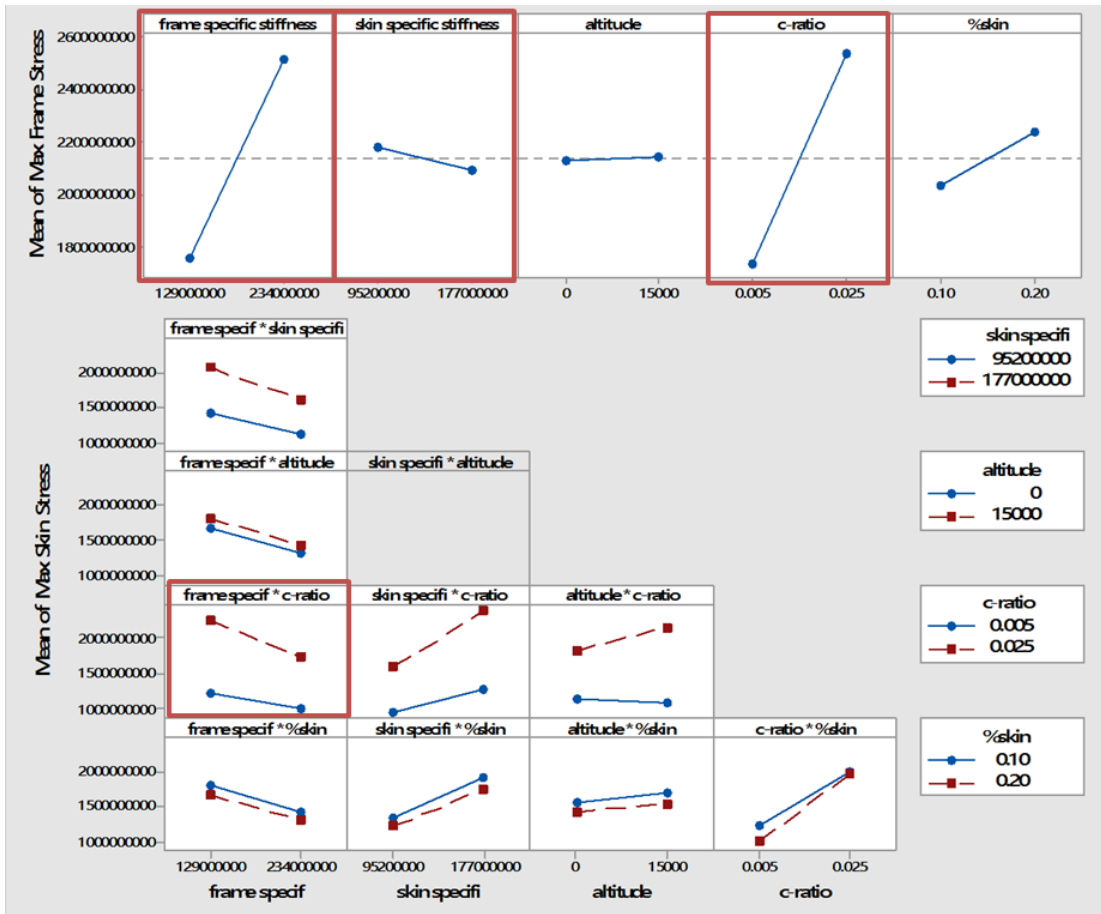


Figure 71: Main effects and 2nd degree interactions effects for Max Frame Stress - Hexakis Icosahedron

The data from the cube plot was reduced in the same fashion as in the icosahedron model, and which was used to produce the main effects with 2nd degree interactions plot in Figure 71. The effects were analyzed in the same fashion as the icosahedron and the dominating terms were extracted. The terms that are considerably dominate for the max frame stress are the frames material properties, $\frac{E_b}{\rho_b}$, the frames geometry, $\frac{t_b}{r_b}$, the combination of the frames geometry and the frames material properties, $\frac{t_b E_b}{r_b \rho_b}$, and the skins material properties, $\frac{E_s}{\rho_s}$. These effects and interactions are highlighted by the red boxes in Figure 71. The same observations were made for the max skin stress, and the

terms that are dominate are the frames geometry, $\frac{t_b}{r_b}$, the skins material properties, $\frac{E_s}{\rho_s}$, the frames material properties, $\frac{E_b}{\rho_b}$, the combination of frame geometry and the frames material properties, $\frac{E_b t_b}{\rho_b r_b}$, the combination of skin material properties and frame geometry, $\frac{E_s t_b}{\rho_s r_b}$ and the combination of altitude and frame geometry, $h \frac{t_b}{r_b}$. The final weight-to-buoyancy, had the combination of frame geometry and the frames material properties, $\frac{E_b t_b}{\rho_b r_b}$, the frames geometry, $\frac{t_b}{r_b}$, the skin percentage $\frac{W}{B_s}$, and the frames material properties, $\frac{E_b}{\rho_b}$, terms to be considerably dominate.

Curvature Assessment

In order to continue to the regression fitting, the curvature of the responses needs to be investigated. Curvature of a response is determined if the center point data is significantly difference from the mean of the response. Table 41 shows the mean of the response and the center point data in the first two rows. A percent difference between these rows was taken, and the results are show in the 3rd row of the table. It is shown that the error, for the frame stress, skin stress, and final W/B are approximately 6%, 5.5%, and .06% respectively. Since the percent difference is fairly small and comparatively equal to the % RSME of the mean response, indicates that the center point has no more error than any other point in the data set. From this, it will be concluded that curvature does not exist for the three observed outputs, and the existing DOE data can be used to perform the regression fits.

Table 41: Hexakis Icosahedron Curvature Analysis

Hexakis Icosahedron Curvature Study			
	Frame Stress	Skin Stress	Final_W_B
Mean of Response	2.142E+09	1.552E+09	1.011
Center Point Response	2.271E+09	1.466E+09	1.010
% Center Point Error	6.014	5.559	0.059
% RSME of Mean Response	1.126	2.284	0.014

Regression Fits and Fit Assessment

The reduced hexakis model containing only significant terms can be used to create a linear regression fit of the outputs. The least squares regression general equation for the icosahedron model is shown in Figure 72, where the β terms for each output parameter are defined in Table 42. The β terms are computed using the response data, y , and the corresponding inputs, X , provided by the DOE data, using equation (63) where only the 17 significant effects determined previously are considered. With the model now defined from the DOE data the fit of the model to the real data can be tested by evaluating the model at the DOE data points and comparing the results. The plots of the regression fits of the three outputs are shown in Figure 73 with 95% confidence intervals. Table 43 shows the fit statistics of all the outputs.

$$\begin{aligned}
y_{hexakis} = & \beta_0 + \beta_A \left(\frac{E_b}{\rho_b} \right) + \beta_B \left(\frac{E_s}{\rho_s} \right) + \beta_C (h) + \beta_D \left(\frac{t_b}{r_b} \right) + \beta_E \left(\frac{W}{B_s} \right) \\
& + \left(\frac{E_b}{\rho_b} - 1.82E^6 \right) \left(\left(\frac{E_s}{\rho_s} - 1.36E^6 \right) \beta_{AB} \right) + \left(\frac{E_b}{\rho_b} - 1.82E^6 \right) \left((h - 7500) \beta_{AC} \right) \\
& + \left(\frac{E_b}{\rho_b} - 1.82E^6 \right) \left(\left(\frac{t_b}{r_b} - 0.015 \right) \beta_{AD} \right) + \left(\frac{E_b}{\rho_b} - 1.82E^6 \right) \left(\left(\frac{W}{B_s} - 0.15 \right) \beta_{AE} \right) \\
& + \left(\frac{E_s}{\rho_s} - 1.36E^6 \right) \left(\left(\frac{t_b}{r_b} - 0.015 \right) \beta_{BD} \right) + \left(\frac{E_s}{\rho_s} - 1.36E^6 \right) \left(\left(\frac{W}{B_s} - 0.15 \right) \beta_{BE} \right) \\
& + (h - 7500) \left(\left(\frac{t_b}{r_b} - 0.015 \right) \beta_{CD} \right) + (h - 7500) \left(\left(\frac{W}{B_s} - 0.15 \right) \beta_{CE} \right) \\
& + \left(\frac{t_b}{r_b} - 0.015 \right) \left(\left(\frac{W}{B_s} - 0.15 \right) \beta_{DE} \right) \\
& + \left(\frac{E_b}{\rho_b} - 1.82E^6 \right) \left((h - 7500) \left(\left(\frac{t_b}{r_b} - 0.015 \right) \beta_{ACD} \right) \right) \\
& + \left(\frac{E_b}{\rho_b} - 1.82E^6 \right) \left(\left(\frac{t_b}{r_b} - 0.015 \right) \left(\left(\frac{W}{B_s} - 0.15 \right) \beta_{ADE} \right) \right) \\
& + \left(\frac{E_s}{\rho_s} - 1.36E^6 \right) \left(\left(\frac{t_b}{r_b} - 0.015 \right) \left(\left(\frac{W}{B_s} - 0.15 \right) \beta_{BDE} \right) \right) \\
& + (h - 7500) \left(\left(\frac{t_b}{r_b} - 0.015 \right) \left(\left(\frac{W}{B_s} - 0.15 \right) \beta_{CDE} \right) \right)
\end{aligned}$$

Figure 72: Least squares regression general equation for the hexakis icosahedron model

Table 42: Least Squares Regression Estimates – Hexakis Icosahedron Model Outputs

Least Squares Regression Estimates -Hexakis Icosahedron			
Coefficient	Max Frame Stress	Max Skin Stress	Final W/B
β_0	39160339.28	750720084.4	1.017266396
β_A	7.230111913	-3.491425483	-5.28168E-11
β_B	-1.018146071	6.798222539	-6.90319E-12
β_C	1167.563002	8650.858433	1.57543E-08
β_D	40440505573	43460560692	0.165287073
β_E	2078411065	-1376006389	0.010687032
β_{AB}	4.39718E-09	-1.6255E-08	7.39172E-20
β_{AC}	-1.86527E-05	-6.2422E-06	-1.30437E-16
β_{AD}	79.95339467	-146.8689993	-9.77339E-10
β_{AE}	11.70785755	2.624509503	-1.85585E-11
β_{BD}	-69.09747663	285.0661523	-3.4643E-10
β_{BE}	-9.595080905	-6.155697045	-6.40227E-11
β_{CD}	-249160.0907	1228102.275	2.11643E-06
β_{CE}	-3202.709333	-16854.98667	-1.22808E-08
β_{DE}	-3919497395	1.0917E+11	0.132397787
β_{ACD}	-0.002678809	-0.00067391	-2.05674E-14
β_{ADE}	-44.60878088	1093.212742	-1.40389E-09
β_{BDE}	-160.3756416	-1367.247656	-8.9037E-10
β_{CDE}	937196.8	-4696493.867	4.83691E-06

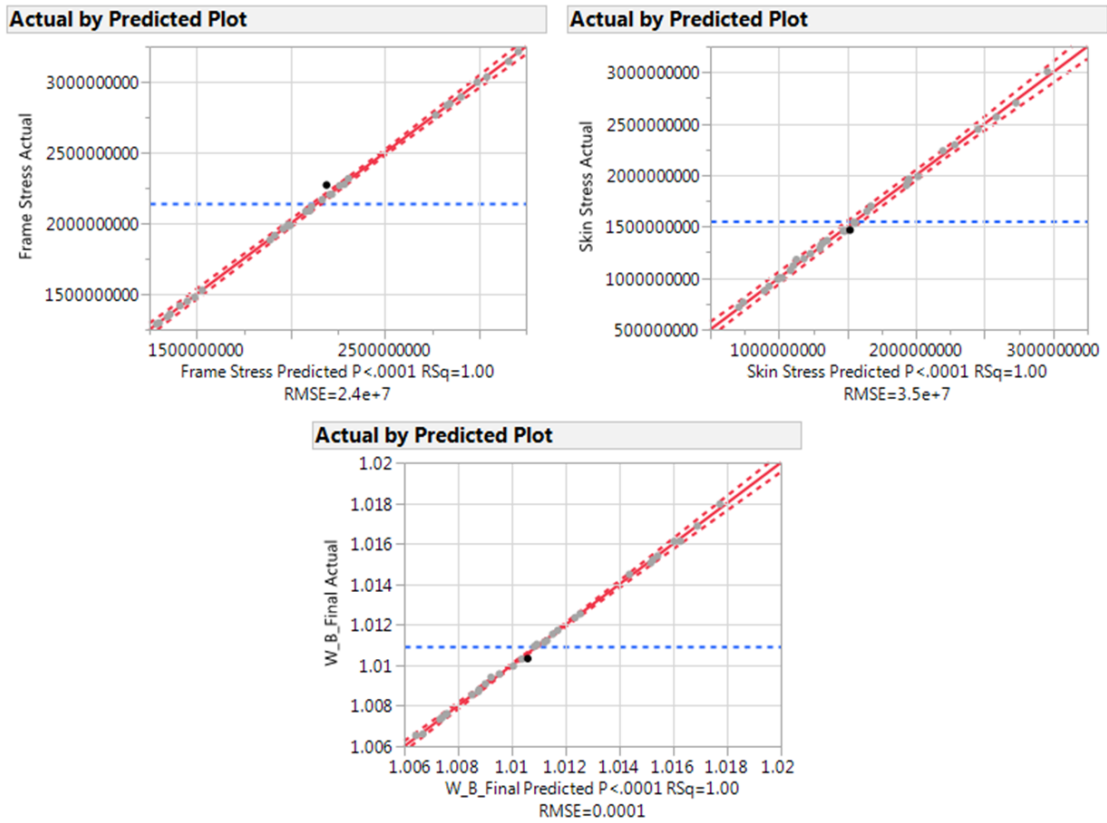


Figure 73: Least Squares Regression Fit for the Hexakis Icosahedron Model Outputs

The graphs in Figure 73 are plotted with the actual design response data point on the vertical axis versus the estimated value generated using the regression equation in Figure 72, with the respective response set of β estimators in Table 42. How well the regression model fits the actual data can be observed by observing the fits root mean square error (RSME), and the R-square or R-square Adj, shown in Table 43. The RSME for max frame stress, max skin stress, and final W/B compared to the mean of the response was [1.13%, 2.28%, and 0.014%] respectively. This indicates that the regression fit has an average of [1.13%, 2.28%, and 0.014%] error when approximating the actual respective responses of the FEM. For this research, the same justification given for the

icosahedron model applies to the hexakis analysis and the regression fits are determined to be “good”.

Table 43: Summary of Regression Fit Information – Hexakis Icosahedron Model

Summary of Regression Fit - Hexakis Icosahedron Model			
	Frame Stress	Skin Stress	Final_W_B
RSquare	0.999	0.998	0.999
RSquare Adj	0.998	0.996	0.998
Root Mean Square Error	2.413E+07	3.546E+07	0.000
Mean of Response	2.142E+09	1.552E+09	1.011
% RSME of Mean Response	1.126	2.284	0.014
Observations (or Sum Wgts)	33	33	33

Hexakis Icosahedron Response Surfaces

It is now possible to produce surface plots with the regression models of the design space associated with the hexakis icosahedron model revolving around the DOE test points for the three outputs. The median surface plots for max frame and skin stress along with final W/B are shown in Figure 74, Figure 75, and Figure 76. Like the icosahedron response surfaces, the stress contours are plotted with respect to c-ratio and skin percentage to show the shape of the response surface that remains constant when the remaining factors are altered. When the material properties are varied the response surface shifts up and down the vertical axis along the red arrows while maintaining its shape. The red arrows indicate the range of travel of the response surface when the factor levels of the non-plotted factors, frame and skin specific modulus, are moved from low to high.

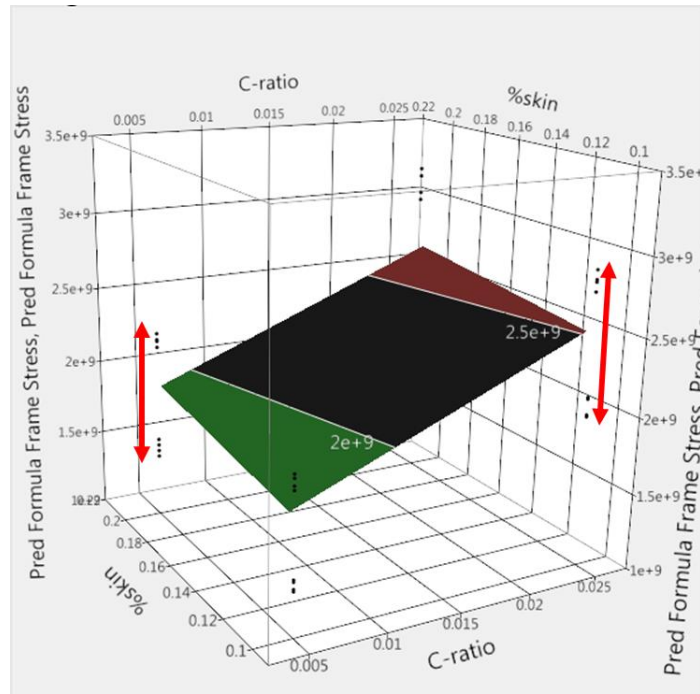


Figure 74: Hexakis Icosahedron Max Frame Stress Response Surface

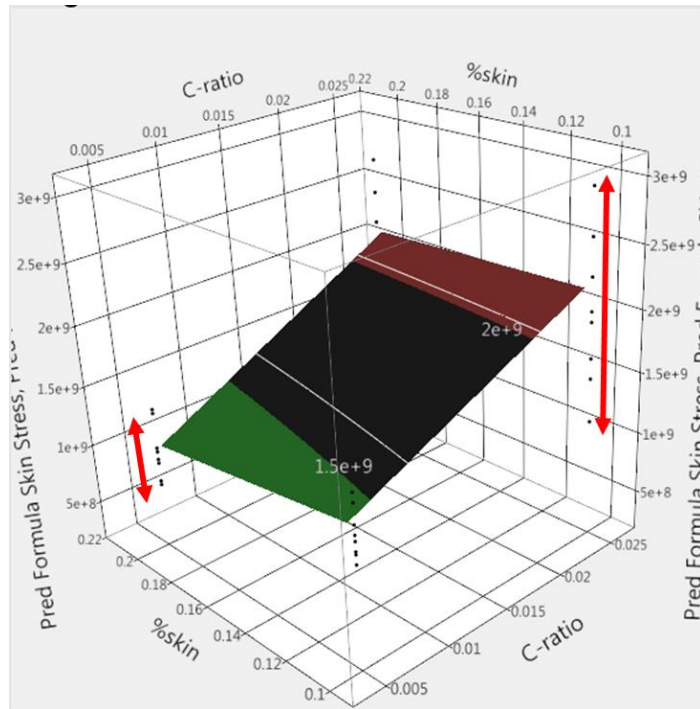


Figure 75: Hexakis Icosahedron Max Skin Stress Response Surface

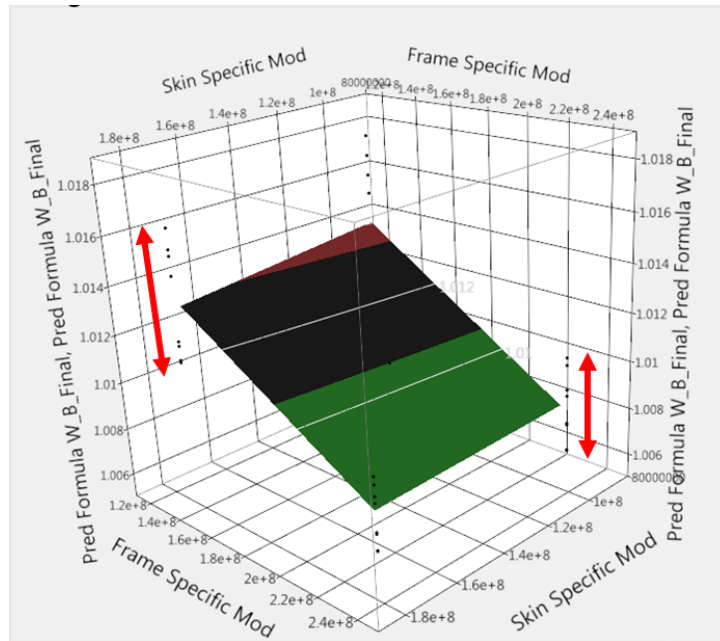


Figure 76: Hexakis Icosahedron Final W/B Response Surface

At this point in the analysis it is now possible to develop the feasible design space for the hexakis icosahedron vehicle with respect to material failure. This process is performed in the same fashion as the icosahedron where the frame and skin maximum stresses are divided by their materials yield strength, producing the safety factor for the frame and skin. As long as the stress in the frame and skin respectively is lower than the respective materials yield value, then a safety factor greater than one will be produced. All designs with both the frame and skin safety factors equal to or above one will be considered feasible in terms of material failure. The above manipulation of the stress surfaces was performed for both the frame and skin and the safety factor surfaces are shown in Figure 77 and Figure 78 with the slicing grid pattern indicating where a SF of one lies. The next step in the analysis process will focus in on Figure 77 and Figure 78 to determine if and where the feasible design space lies for the hexakis icosahedron model.

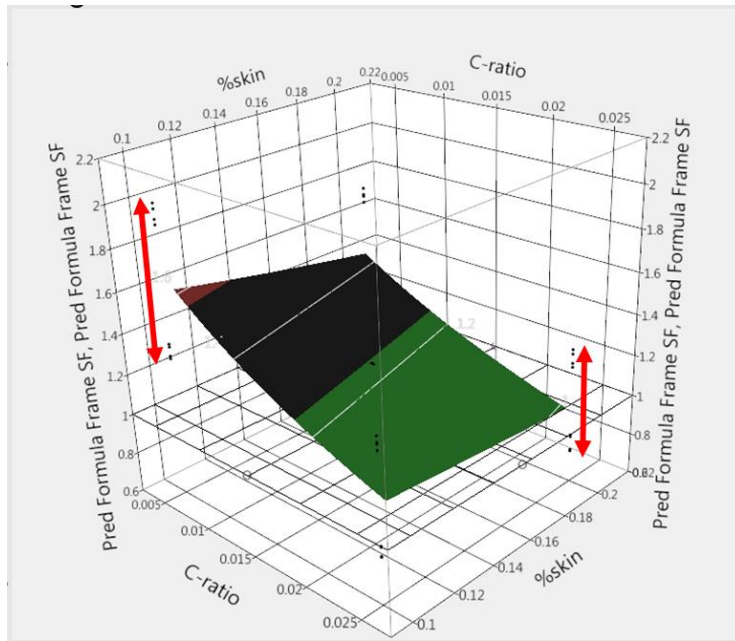


Figure 77: Hexakis Icosahedron Frame SF Response Surface

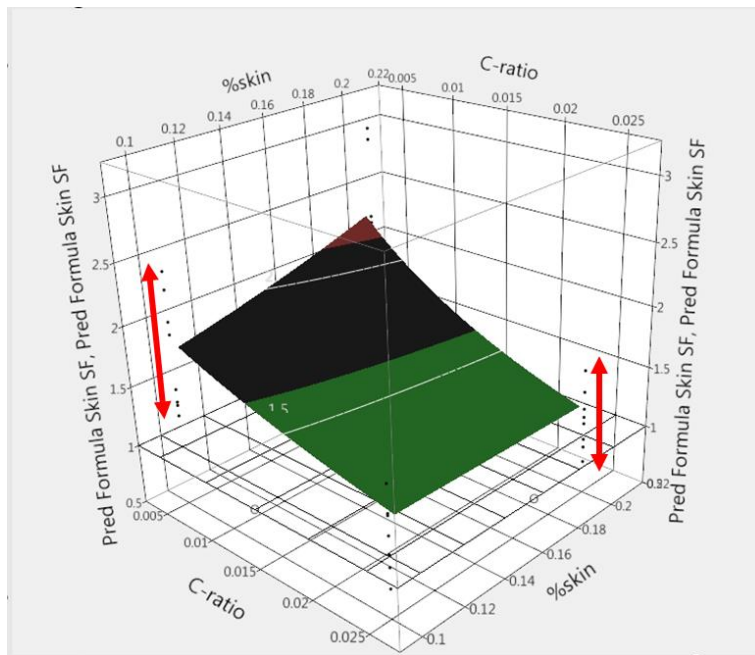


Figure 78: Hexakis Icosahedron Skin SF Response Surface

Hexakis Icosahedron VLTAV Structural Feasibility Assessment and Response

Discussion

Hexakis Icosahedron Material Safety Factor Assessment

At this point in the analysis it is now possible to develop the feasible design space for the hexakis icosahedron vehicle with respect to material failure. This process is performed by taking the data from the stress response surfaces and converting it to indicate whether or not the structure has failed material wise. This is done by dividing the stress values for the frame and skin at each point by its materials yield strength value. This produces the factor known as the safety factor. As long as the stress in the frame and skin respectively is lower than the respective materials yield value then a safety factor greater than unity will be produced. All designs with both the frame and skin safety factors equal to or above one will be considered feasible in terms of material failure. The above manipulation of the stress surfaces was performed for both the frame and skin and the safety factor surfaces are shown in Figure 77 and Figure 78 with the slicing grid pattern indicating where a SF of one lies. The next step in the analysis process will focus in on Figure 77 and Figure 78 to determine if and where the feasible design space lies for the hexakis icosahedron model.

The max frame and stress surfaces in Figure 74 and Figure 75 were converted to safety factor surfaces by dividing their values by the materials respective yield strength across the design points. The surfaces were observed by looking at their 2D contour with respect to c-ratio and $\frac{W}{B_s}$ at two levels. The levels were high material properties for both the skin and frame and low material properties for both the skin and frame. This will be

able to show the range of the potential design space by looking at the low and high ends of the responses. Beginning with the high level, where the material properties are as aggressive as possible for the structure, the feasible design space for the hexakis icosahedron fills the entire range of c-ratio and $\frac{W}{B_s}$ that was tested. The optimal solution lies in the bottom left corner of Figure 79 with a frame SF of 1.9 and skin SF of 2.3 and the “weakest” solution lies in the top right corner with a frame SF of 1.2 and skin SF of 1.54. The same procedure was performed with the material properties set to the low level where the hexakis structure has reached its limitations. The design space with the low material settings fills approximately half of the window with the full range of $\frac{W}{B_s}$ and with the c-ratio being limited by the frame SF. If it was desired to maximize $\frac{W}{B_s}$, then the c-ratio is forced to a maximum value of 0.012. If the desire was to maximize the c-ratio, it would only be able to go as high as 0.016 with a $\frac{W}{B_s}$ of 0.1 before the frame SF limit of one is reached. The region of feasible designs for the hexakis structure fills a significant portion of the entire design space that was created by the DOE. For comparison to the icosahedron model, the hexakis icosahedron stress and displacement contours for the icosahedron model identified in Table 30 is shown below, in Figure 81, Figure 82, and Figure 83.

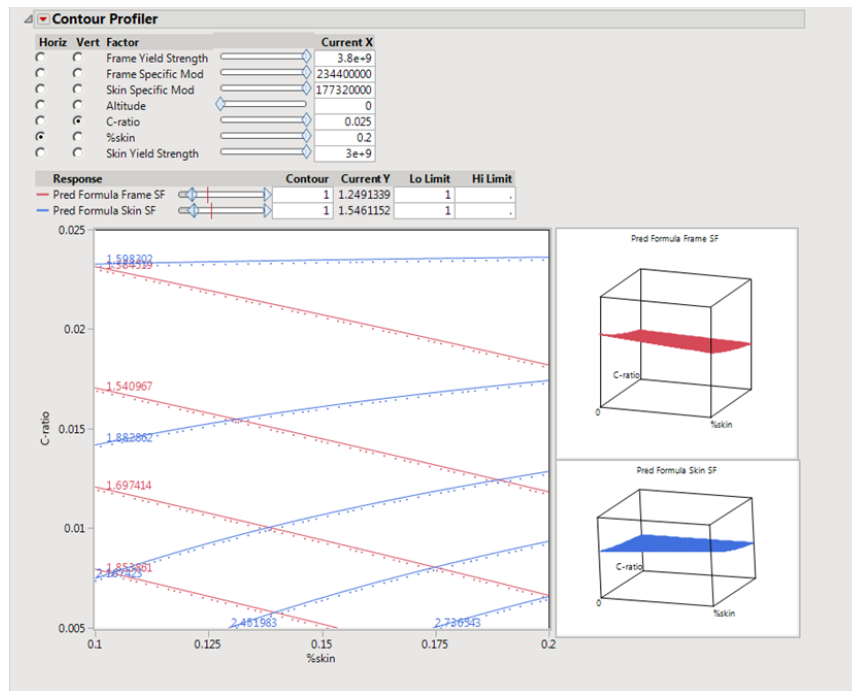


Figure 79: Hexakis Icosahedron Contour Plot of Frame and Skin Safety Factor with high level material properties.

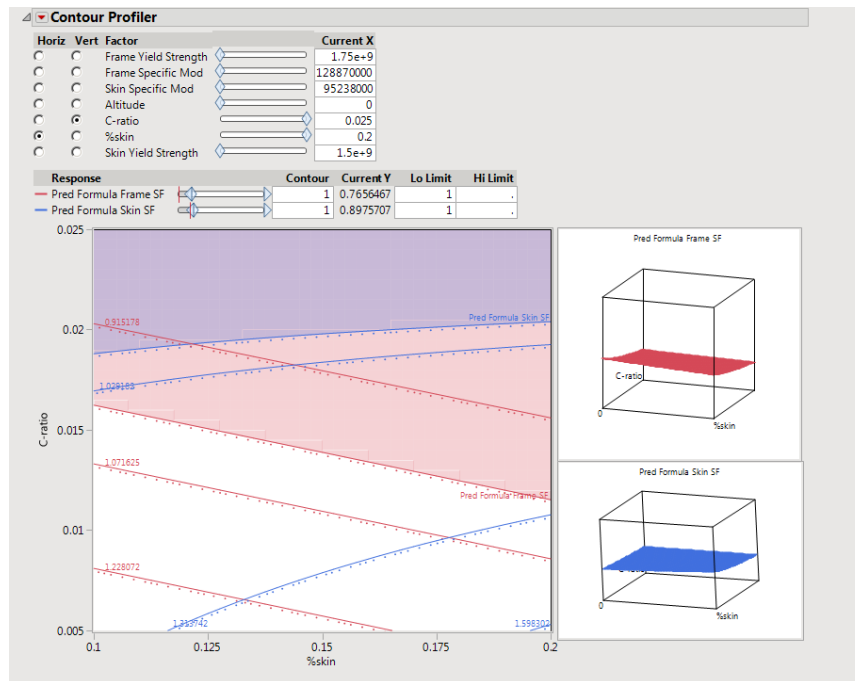


Figure 80: Hexakis Icosahedron Contour Plot of Frame and Skin Safety Factor low level material properties.

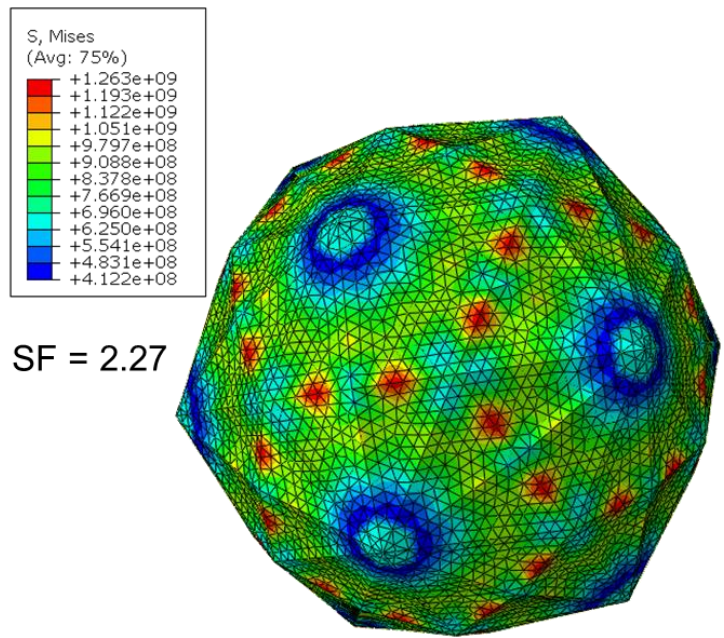


Figure 81: Hexakis Icosahedron Optimal Design Point Skin Stress Contour with SF

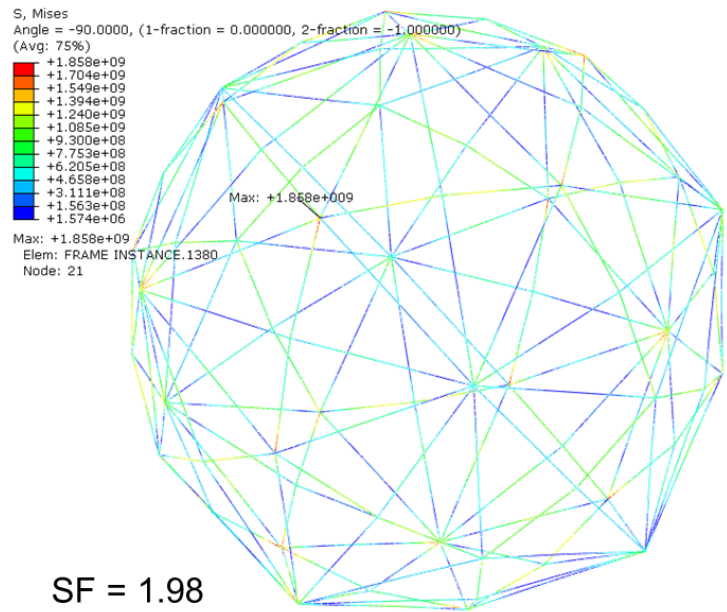


Figure 82: Hexakis Icosahedron Optimal Design Point Frame Stress Contour with SF

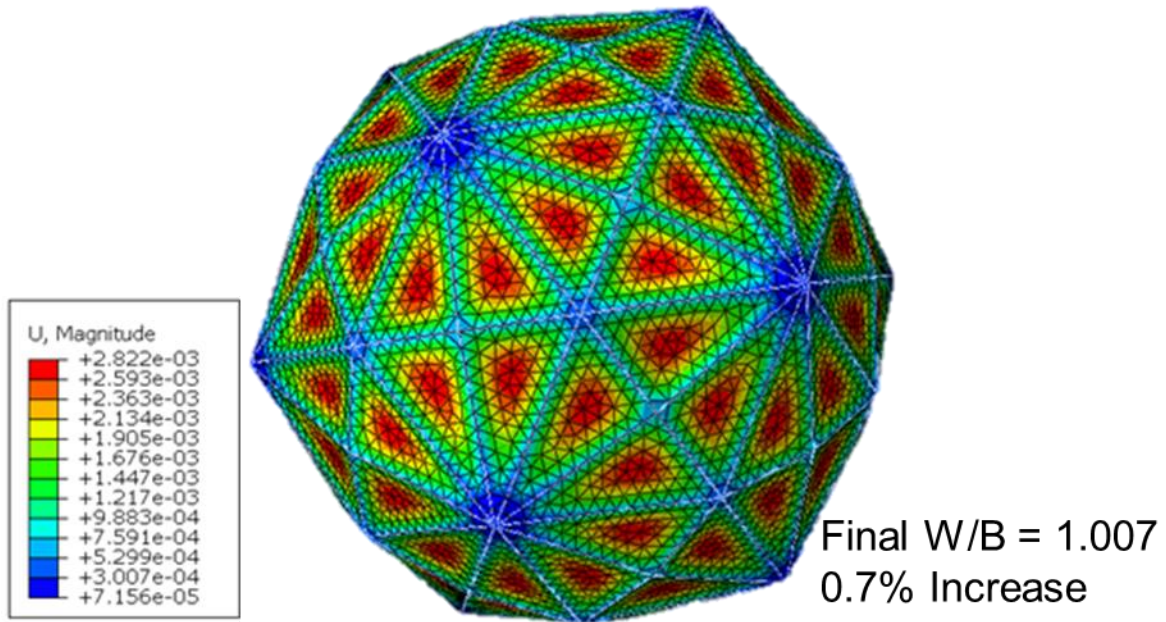


Figure 83: Hexakis Icosahedron Optimal Design Point Displacement Contour with Final W/B

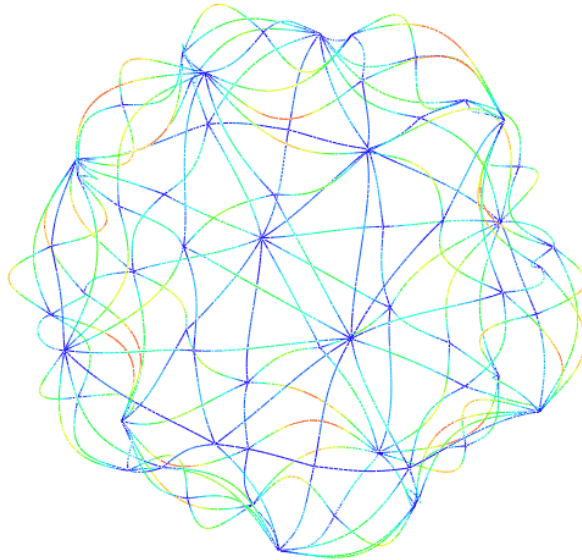
The max stress in the frame of the hexakis icosahedron, shown in Figure 82, is located symmetrically at all of the vertices where six beams meet, but it is noted the remaining vertices have similar stress values at their vertices. This occurs because the frame is modeled as 2D line elements. This produces corners in the frame that would in reality not exist because the frame vertices would be filleted or curved in nature and not form a sharp corner. Therefore, it is expected that if 3D elements were used to create a fully 3 dimensional icosahedron frame and skin model the max stress would occur at the vertices, but the magnitude of the stress concentration would be less than what the current model predicts. Therefore, even though no accommodation was made, the max stress values in the frame would be consider to be an over estimate compared to a 3D model.

The maximum stress in the skin, shown in Figure 81, occurs symmetrically along the top of the short beams. The maximum displacement in the model, shown in Figure 83, occurs in the membrane symmetrically at the center of all the triangular faces. Additionally, the W/B final response that was observed, had a minimum increase from the original design W/B of one to 1.006, and a maximum increase of 1.02 looking at the entire data set from the DOE. This response agrees with the results obtained by Rodriguez, in that the skin and frame deflection results in a small reduction the internal volume which in turn increased the final W/B ratio of the design. The reduction in the internal volume however for the hexakis structure is approximately three times less than what was observed in the icosahedron case study across the DOE analysis points. Since the design W/B was equal to one for the sizing equation, all the feasible designs for the hexakis icosahedron would technically be negatively buoyant because of the volume loss due to the frame and skin deflection. However, if a specific feasible design were desired to be investigated further, an additional FEA would have to be performed on the design with a design W/B equal to one minus the expected volume loss to obtain a neutrally buoyant vehicle or possibly slightly positively buoyant. For example, if the worst case scenario of final W/B observed of 1.02 for the hexakis structure were chosen to analyze further, the design W/B should be one minus 0.02 which would be equal to 0.98 design W/B so that the final W/B would be approximately one for neutral buoyancy.

Hexakis Icosahedron Geometric Instability Assessment

Since, there were feasible designs with the low level of material properties, the buckling analysis was performed at the design point of the top right corner of Figure 80.

This point has a SF less than one for both the frame and skin, but provides the most conservative buckling analysis. If the frame does not buckle at this design point, then it is assumed that none of the designs within the DOE range tested will buckle. Figure 84 shows the first buckling mode of the hexakis icosahedron frame with uniform pressure applied to the frame though the use of reference points as illustrated in the beginning of the chapter. The critical buckling pressure for this mode was 169,992 Pa, which is 1.67 times greater than the applied pressure of 101,325 Pa. Therefore, there is no reason to believe that global buckling would occur in the structure for any of the designs in the DOE range. This design point was tested with a c-ratio of 0.025. This is above the local buckling threshold of 0.02 that was established in chapter IV. Therefore, there is confidence that local buckling at this point would not occur before global buckling. But, let it be noted that other designs in this design space that are deemed feasible do have a c-ratio of less than 0.02 which exceeds the minimum value estimated for local buckling in chapter IV . This does not mean that local buckling is guaranteed to occur because the approximation is based on a hollow cylinder with a simple support where the beams in the hexakis icosahedron have a differing BC. Nonetheless it is important to note that, it is a possibility and that if this design were to be pursued then considering adding internal pressure to the beams or providing extra support by means of ring stiffeners would be advised just as in the case of the icosahedron.



Step: Nonlinear-Static, General-wStabi
Mode 2: EigenValue = 475.98
Primary Var: U, Magnitude
Deformed Var: U Deformation Scale Factor: +2.807e-02

Figure 84: Hexakis Icosahedron Critical Buckling Pressure at the most Sub-Optimal Point

Hexakis Icosahedron Vehicle Sizing

Using the same manufacturing constraint of 0.2mm skin and beam thickness established with the icosahedron analysis, the hexakis icosahedron vehicle sizing will be analyzed. This analysis will show what the smallest structure radius possible is that satisfies 0.2mm thickness constraint within the design space ranges shown for the high and low level contours in Figure 79 and Figure 80. The sizing for when the material is at the high level, is shown in Figure 85. In this figure, the dimensions for the beam thickness, radius, and skin thickness are shown. With the limit of 0.2mm skin and beam thickness, the sizing was optimized to create the smallest radius vehicle. It is shown that the skin thickness reaches this limit first and will determine the minimum radius of the vehicle design point. Since the skin thickness has no ties to the frame in terms of mass,

the only parameters that drive the skin thickness are the materials density, ρ_s the design altitude, ρ_a , and the skin percent $\frac{W}{B_s}$. The resulting minimum structure radius values for the hexakis icosahedron with high material level are 2.5m and 5.25m for 0.2 and 0.1 $\frac{W}{B_s}$ respectively, and is shown in the rightmost plot on Figure 85. The left and middle plots represent the beams radius and thickness respectively. The dark blue line and black represent lines of constant $\frac{t_b}{r_b}$ at 0.005 and 0.025 values respectively, which were the low and high levels used for DOE. The orange and light blue lines are lines of constant $\frac{W}{B_s}$ with values of 0.1 and 0.2 respectively. By connecting these lines, the bounding box for the feasible designs are created.

In a similar manner, the same analysis was performed for the low material level reflecting Figure 86. The big difference here is that the for each $\frac{W}{B_s}$ level as the c-ratio increased from 0.005, the value was eventually clipped before making it to the high level of that factor. This is because the design space, as pointed out in Figure 80 is not fully open. The designs become limited by the frame SF, and therefore so will the dimensions that will produce a feasibly manufacturable vehicle.

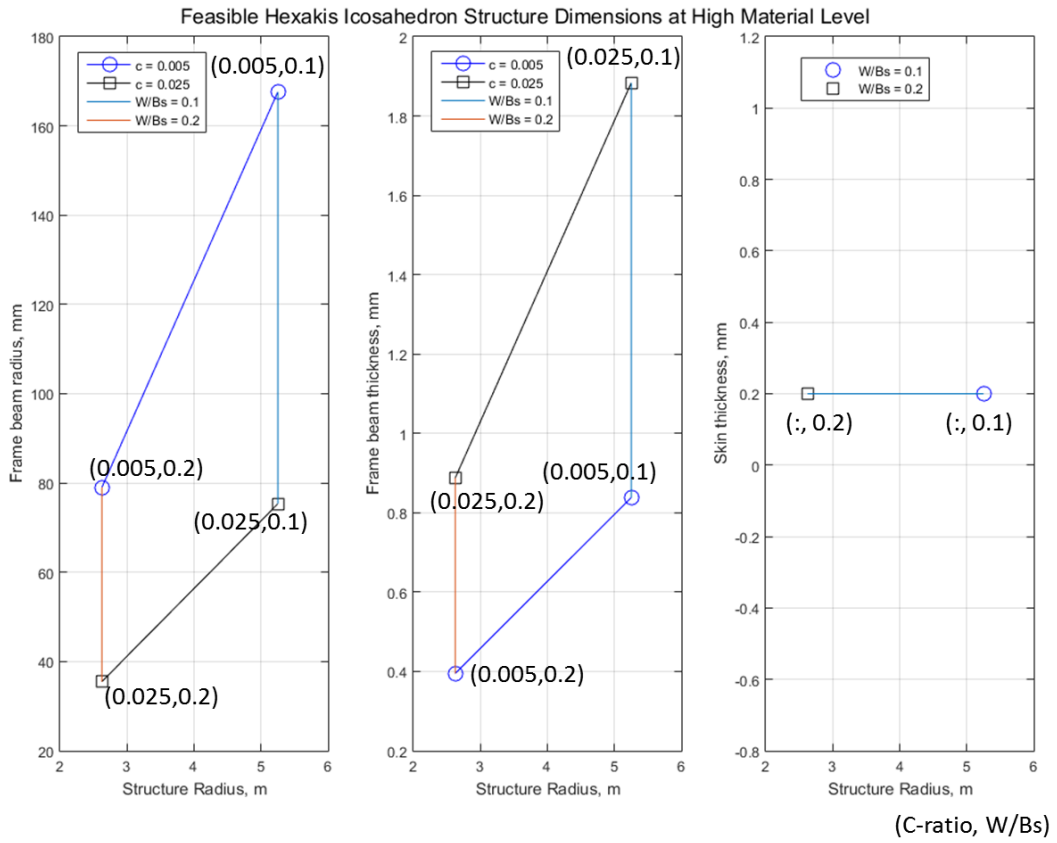


Figure 85: Feasible Hexakis Icosahedron Structure Dimensions for High Material Level

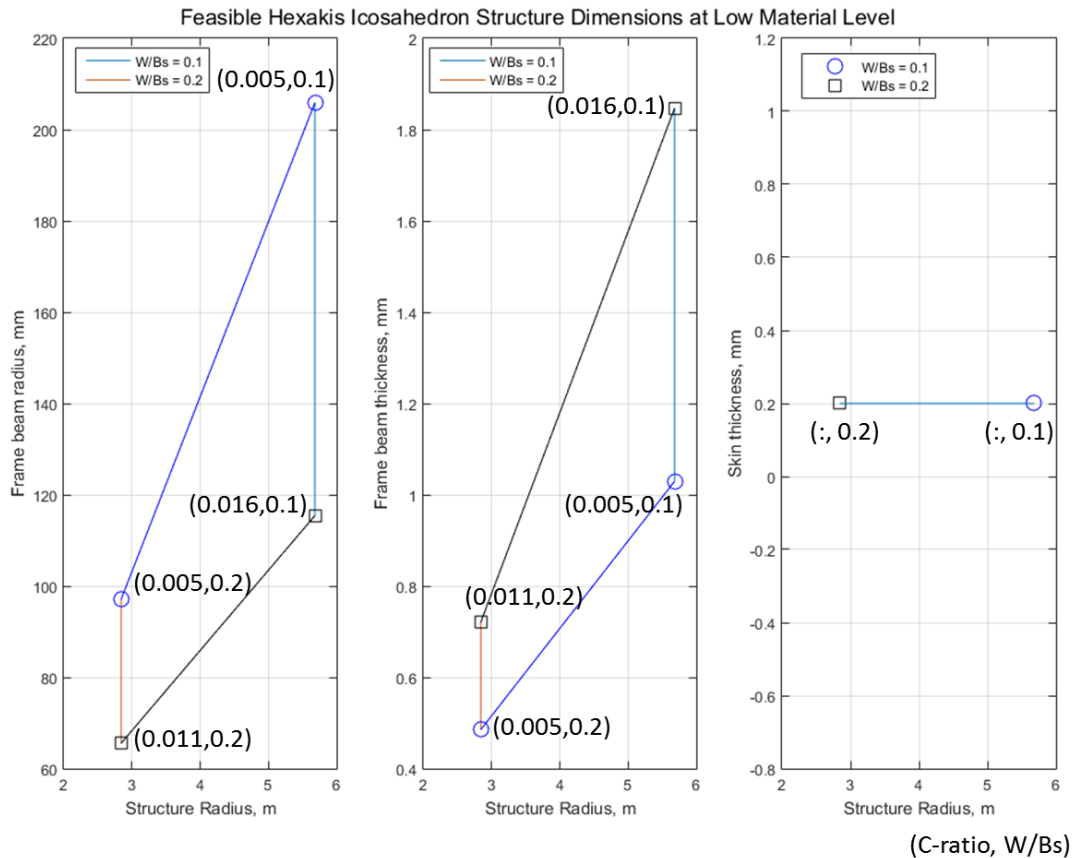


Figure 86: Feasible Hexakis Icosahedron Structure Dimensions for Low Material Level
Manufacturable Design with $W/B < 1$ and low material properties

Since the hexakis icosahedron had such a large feasible design space it was desired to perform a separate analysis at two design points to produce designs with W/B less than one using the low (conservative) material properties. It was desired to produce two designs, one with payload or float capacity maximized, and the other with the radius of the vehicle minimized. Both designs total W/B were decreased until the SF constraint was reached for either the frame or skin. The results of the two feasible vehicles that could potentially be built in the near future are shown in Figure 87. The design focusing on maximizing payload would have a vehicle radius of 7 m and could carry a payload of 260 kg or float to 2140 m. This vehicle was able to attain a final W/B of 0.8 limited by

the frames SF before the skin. The design focusing on minimized radius had a vehicle radius of 3.1 m and could carry a payload of 9 kg or float to 860 m. The second design's final W/B was 0.91.

Approximate Maximized Payload or Float Capacity

Hexakis Icosahedron Properties		
Frame Specific Stiffness/Strength	1.29E+08	1.80E+06
Skin Specific Stiffness/Strength	9.52E+07	1.43E+06
Altitude	0	
C-ratio	0.005	
%Skin	0.1	
Frame SF	1.019	
Skin SF	1.058	
Initial W/B	0.8	
Final W/B	0.8117	
Vehicle Radius (m)	7	
Beam Thickness (mm)	1.143	
Beam Radius (mm)	228.7	
Skin Thickness (mm)	0.2	
Payload (kg)	260.54	
Float Capacity (m)	2140	

Approximate Maximized Payload or Float Capacity with minimum vehicle radius

Hexakis Icosahedron Properties		
Frame Specific Stiffness/Strength	1.29E+08	1.80E+06
Skin Specific Stiffness/Strength	9.52E+07	1.43E+06
Altitude	0	
C-ratio	0.005	
%Skin	0.2	
Frame SF	1.054	
Skin SF	1.507	
Initial W/B	0.91	
Final W/B	0.923	
Vehicle Radius (m)	3.1	
Beam Thickness (mm)	0.501	
Beam Radius (mm)	101.1	
Skin Thickness (mm)	0.2	
Payload (kg)	9.06	
Float Capacity (m)	860	

Figure 87: Manufacturable Hexakis designs with W/B < 1 and low material properties.

Chapter VI Summary

This chapter's objective was to analyze the hexakis icosahedron VLTAV design with the methodology developed in chapter III. This design did have a fair amount of similarities to the icosahedron designs development. The only difference was the structures geometry. The icosahedron was made up of 12 vertices, 20 faces, and 30 edges, where the hexakis icosahedron was made up of 62 vertices, 120 faces, and 180 edges. The finite element modeling technique and general vehicle sizing equations were identical. This case study performed the same structural design space construction and analysis as the icosahedron design. Through evaluation of the design space, it was

observed that there exists a substantial amount of feasible design space utilizing present day materials and manufacturing limitations with the limits of altitude, c-ratio, and skin W/B selected. A vehicle sizing analysis was performed limiting the skin thickness to 0.2mm and the smallest diameter hexakis icosahedron vehicle that was structurally feasible was approximately five meters in diameter when the material properties were at the high level. A secondary analysis was performed limiting the material properties to the low level. Two designs were developed, where one targeted maximizing payload and the other minimizing vehicle radius. The large payload design could carry an estimated 260 kg or float to 2140 m with a vehicle radius of 7 m. The minimum radius design, achieved a radius of 3 m and could either carry a payload of 9 kg or float to 800 m.

VII. Summary and Conclusions

This research lays a foundation for a methodology to provide a broad scope early-stage investigation into the structural design space of a vehicle that is highly dependent on its structure. To determine if feasible designs may exist within user defined limitations or constraints. The methodology was applied to the previously studied Metlen icosahedron VLTAV and a similar frame and skin design, hexakis icosahedron, proposed by the author. The design space exploration process developed allowed both case studies to be investigated where all of their design parameters were allowed to vary so that the impact of each variable could be observed and quantified. Looking back, Metlen and Rodriguez would have benefitted greatly by analyzing the icosahedron design originally with the methodology proposed because it would have shown what input parameters could have possibly produced a viable vehicle.

The research began with an investigation into the brief history and previous technical work that has been performed with respect to VLTAV. It was shown that, to date, there have only been three documented VLTAV designs investigated: a thin-shelled sphere, sandwich sphere, and frame-skin polyhedron. The designs were either or both limited by current material properties or manufacturing limitations. This gave rise for the desire to develop a structural analysis design space exploration technique that could be applied to early-stage VLTAV designs with modern material and manufacturing constraints so that structural design feasibility could be observed early on in the design process. Being able to know where the functional design space of a vehicle lies before an in-depth, potentially costly, investigation occurs is ideal because then the design that is being pursued is already known to be feasible from an initial analysis point of view. This

research established the structural design space exploration methodology in chapter III. This technique utilized, a combination of finite elements, dimensional analysis, design of experiments, and response surface methodology to map the structural design space within material and manufacturing limitations could be observed for feasibility.

Chapter IV then performed experimental tests to investigate the validity of the technique developed and utilized to model the geometric frames. This was accomplished by devising an experiment to provide a similar loading scenario to the vacuum loading of uniform pressure without with skin. The loading was a single axis compression test to be performed on an additive manufactured 3D model. Constructing an experimental uniform compression test would have been ideal, but the ability to instrument and provide the loading scenario was deemed unnecessary and costly to validate the finite element model. The experiment devised, utilized a stereolithographic 3D printed and an MTS loading system to provide the compression, instrumentation, and data recording detailed. An additional modal analysis was performed to not only confirm the material properties of the printed test specimen, but to serve as an additional point of model validation along with the compression test. The experimental results produced great confidence that the technique devised to model these geometric frames was not only valid but accurate with respect to the frame. The combination of the frame and skin was not able to be experimented on and therefore is a point of error in the frame-skin finite element model. However, Rodriguez did show that a single triangular membrane segment, subject to a pressure loading, almost exactly predicted deflection theory for a membrane. Therefore, the skin deformation finite element results and modeling technique were determined to be satisfactory for an initial design space investigation. With a validated and robust finite

element modeling technique for a polyhedron framed structure, the research continued with the application of the proposed methodology on the Metlen icosahedron design and hexakis icosahedron design case studies in chapters V and VI.

Chapter V developed five unique invariant input parameters that first were determined to produce a scale-invariant model, and then used to construct and perform a structural response DOE on the design. The DOE showed that the dominating significant terms that effected the structural design space of the icosahedron design were, c-ratio and frame and skin specific moduli. The constructed safety factor response surfaces did show that for the set of constraints chosen, there existed no structurally feasible design space for the icosahedron design. If the design space could be extended past the region tested with the DOE, it was shown that a feasible design could be produced within material and manufacturing limitations. Additionally, the final W/B response observed showed a max W/B gain from the internal volume loss was 0.06 and the minimum was 0.01 which equates to 6% and 1% of the initial starting volume.

The same analysis was performed on the hexakis icosahedron case study in chapter VI. It showed the same set of finite element system input parameters as the icosahedron, and therefore the design had the same set of invariants and the result of scale-invariance. Utilizing the same DOE test matrix as the icosahedron, it was found that the same design parameters had the most significant effect on the structural response design space. The major difference between both case studies occurred when the feasible design space was investigated for the hexakis design. The feasible design space for the hexakis design, was almost the entire design space, only limited when the frame material properties were at their low level. This is a major difference compared to the icosahedron

design. The hexakis icosahedron yielded a SF of 1.98 and 2.23 respectively. The hexakis design was able to achieve a frame and skin SF that exceed the icosahedrons best case design by approximately 100% for both the frame and skin. Again, when the final W/B was observed, for the hexakis design, the max W/B gain from internal volume loss was 0.02 and the minimum was 0.006 which equates to 2% and 0.6% of the initial starting volume. This is a reduction of 300% comparing it to the icosahedron final W/B gains.

Major Contributions

The major findings determined by the author are given below:

- ***Structural Design Space Exploration Methodology***

The developed methodology was able to produce structural design spaces for the two frame-skin case studies so that conclusions could be drawn on whether structurally feasible designs exist within the constraints set. The methodology allowed for early stage investigation of structures that rely heavily on their structural response with respect to design constraints. The methodology can be extended to other VLTAV design or conceptual designs where the structures response determines its feasibility as long as the design can be phrased as a set of input parameters. The analysis will be able to show how the constraints limit a conceptual design with respect to its structural response and where, if a feasible region or points exist, a good starting functional design point or region lies to begin to perform next level analyses.

- ***Finite Element Polyhedron Frame Modeling***

The experimental tests performed on the 3D printed icosahedron, compared with an equivalent finite element model showed very good agreement (Figure 25). This

agreement allows for confidence in the finite element solutions for the more complex vacuum loading scenario, because the geometry of the model does not change, only the loading profile. Therefore, it is assumed that since there was good agreement in the simplified experimental loading case, that the results obtained from the vacuum loadings are valid. These results were in turn extended to the hexakis icosahedron model because the frame development and creation was similar to the icosahedron.

- ***Dimensional Analysis and DOE***

Performing a dimensional analysis on the system parameters before a DOE is constructed for a system where very little is known and many factors are initially present, allows for a potential to significantly reduce the system parameters. The dimensional analysis analyzed the system input parameters in terms of its dimensions or units. Then it created relational quantities or invariants out of the parameters, where the reduction in terms is at least equal to the number of dimensions defining the system parameters. The DA significantly reduced the number of experiments necessary to perform a DOE and characterize a system.

- ***Dimensional Analysis and Scale Invariance***

The frame-skin VLTA V structures as developed in this research constrained by W/B in their sizing were determined to be scale invariant with the invariant parameters computed by the dimensional analysis. Scale invariance with respect to a design, that is structurally oriented, is significant because it allows for the

finite element analysis of the structure to be performed at a single design point. The analysis results can be extended to other designs as long as the only difference between designs is scale. This proved to be particularly useful when applying the skin thickness manufacturing constraint of 0.2mm, because the structural response results for a smaller or larger scale design remains constant as long as only the dimensions of the design are scaled. This allows any design to be scaled to meet any dimension or manufacturing constraint as long as the invariant quantities defining the system are at the level desired by the researcher or manufacturer.

- ***Significant Design Parameters for a Frame-Skin VLTA Design***

The two case studies analyzed were both composed of a frame and skin structure, specifically with a polyhedron shaped frame. For both designs, beam thickness/beam radius ratio or c-ratio and frame and skin material properties were determined to have the most significant effect on the structural response of the vehicle. Before the analysis of the icosahedron took place, it was expected that the material properties would have a significant effect since they were the limiting factor for the designs investigated by both Metlen and Rodriguez. Rodriguez's research had indicated that lowering the c-ratio of the beam does increase its moment of inertia, and therefore its critical buckling load and stiffness. However, Rodriguez did not investigate the effect of changing the c-ratio $\left(\frac{t_b}{r_b}\right)$ with respect to the structures structural response. This research showed that the c-ratio for nearly all of the responses observed for both the case studies had the most significant effect on the response of the system. It is noted that the c-ratio cannot

be infinitely reduced so that the system performance infinitely increase, because there is a local buckling limit of a thin walled cylindrical rod where the walls of the cylinder will buckle far earlier than the entire cylinder itself. This is shown in in the beam profile study in chapter IV.

- ***Structural Feasibility of a Frame-Skin VLTA V Design Constrained by Modern Materials and Manufacturing Limitations***

Structural feasibility was observed for both the icosahedron and hexakis icosahedron designs with modern materials selected and manufacturing limitations. With the constraints developed in the research, it was observed that the icosahedron did not have any feasible design points. The hexakis icosahedron had a significant region of the constructed design space that was feasible. For the icosahedron, if the c-ratio or skin W/B were to be reduced below the limits used for the analysis, it is estimated that a feasible design could be developed. This is shown in Figure 61. Without the design space exploration of the icosahedron, it would have been quite a challenging endeavor for a designer to locate a design that could be feasible utilizing modern technology. For the hexakis icosahedron, the observed feasible design space was large and allows for a variety of parameter inputs to produce a feasible vehicle. For instance, if we select the low level of material properties as indicated in Figure 80, feasible designs exist for any skin W/B, but the design becomes limited by the c-ratio and frame SF where the max c-ranges from 0.016 and 0.012 as skin W/B varies from 0.1 to 0.2. The hexakis design was additionally analyzed for manufacturability as shown in Figure 85 and Figure 86 with the manufacturing limitation of skin thickness of 0.2mm produced

a minimum radius hexakis icosahedron structure of 2.5 m and a maximum radius structure of 5.75 m. A secondary analysis was performed limiting the material properties to the low level. Two designs were developed, where one targeted maximizing payload and the other minimizing vehicle radius. The large payload design could carry an estimated 260 kg or float to 2140 m with a vehicle radius of 7 m. The minimum radius design, achieved a radius of 3 m and could either carry a payload of 9 kg or float to 800 m.

A. Appendix A

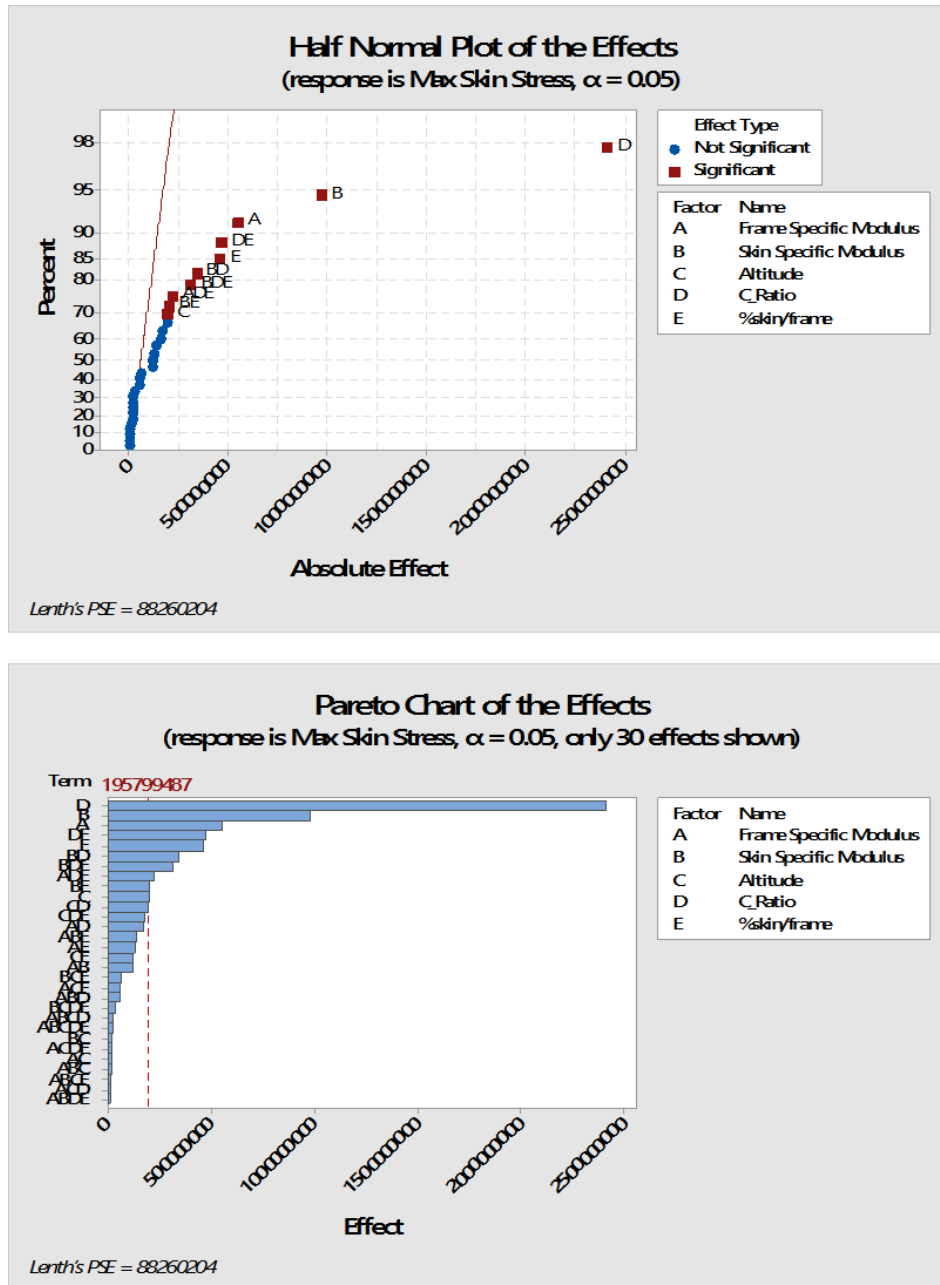


Figure 88: Half Normal Plot and Pareto Chart of the Effects with respect to Max Skin Stress (pseudo standard error term).

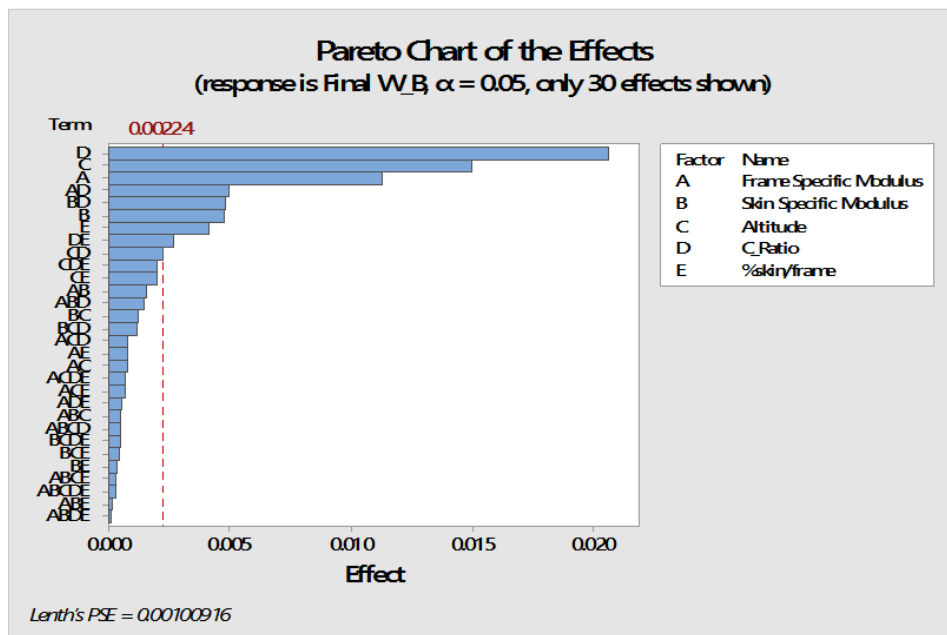
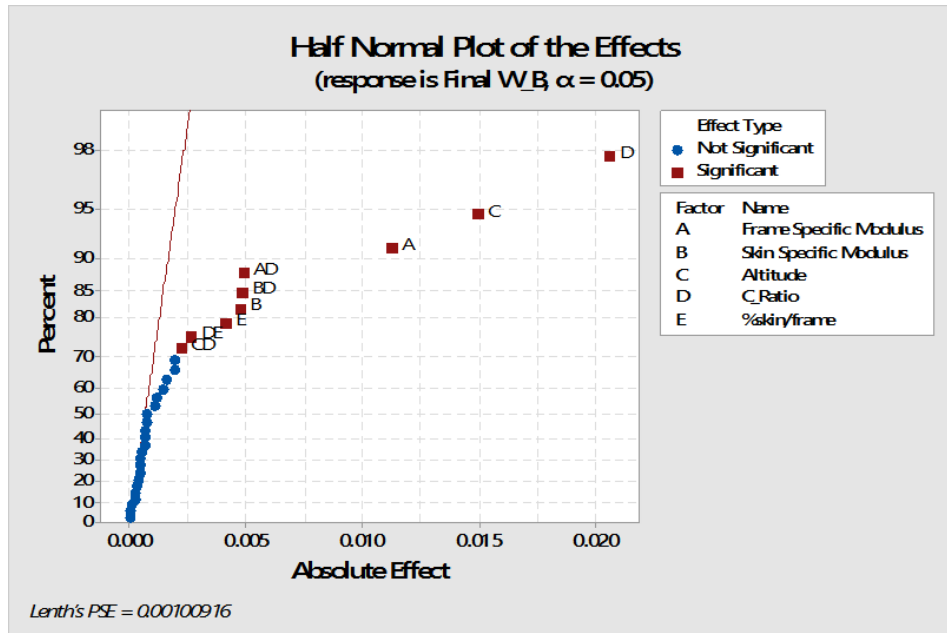


Figure 89: Half Normal Plot and Pareto Chart of the Effects with respect to Final W/B (pseudo standard error term).

Table 44: ANOVA Results for Max Skin Stress - Icosahedron

Y	Source	DF	Sum of Squares	F Ratio	Prob > F	Significant
Skin Stress	Frame Specific Modulus (A)	1	2.43E+18	58.3195	<.0001	TRUE
Skin Stress	Skin Specific Modulus (B)	1	7.66E+18	184.0502	<.0001	TRUE
Skin Stress	Altitude [C]	1	3.13E+17	7.5333	0.0129	TRUE
Skin Stress	C-ratio (D)	1	4.66E+19	1119.2326	<.0001	TRUE
Skin Stress	%skin [E]	1	1.68E+18	40.4893	<.0001	TRUE
Skin Stress	Frame Specific Modulus*C-ratio (AD)	1	2.16E+17	5.1856	0.0345	TRUE
Skin Stress	Frame Specific Modulus*%skin (AE)	1	1.33E+17	3.1901	0.0901	FALSE
Skin Stress	Skin Specific Modulus*C-ratio (BD)	1	9.35E+17	22.4667	0.0001	TRUE
Skin Stress	Skin Specific Modulus*%skin (BE)	1	3.29E+17	7.9036	0.0111	TRUE
Skin Stress	Altitude*C-ratio (CD)	1	3.01E+17	7.2456	0.0144	TRUE
Skin Stress	C-ratio*%skin (DE)	1	1.73E+18	41.5906	<.0001	TRUE
Skin Stress	Frame Specific Modulus*C-ratio*%skin (ADE)	1	3.86E+17	9.2839	0.0066	TRUE
Skin Stress	Skin Specific Modulus*C-ratio*%skin (BDE)	1	7.66E+17	18.4079	0.0004	TRUE

(^ a higher order term containing this term is significant)

Table 45: ANOVA Results for Final W/B - Icosahedron

Y	Source	DF	Sum of Squares	F Ratio	Prob > F	Significant
Final_W_B	Frame Specific Modulus (A)	1	0.001041962	74.887	<.0001	TRUE
Final_W_B	Skin Specific Modulus (B)	1	0.00018221	13.0956	0.0018	TRUE
Final_W_B	Altitude [C]	1	0.00179617	129.0927	<.0001	TRUE
Final_W_B	C-ratio (D)	1	0.003397042	244.1493	<.0001	TRUE
Final_W_B	%skin [E]	1	0.000136547	9.8138	0.0055	TRUE
Final_W_B	Frame Specific Modulus*C-ratio (AD)	1	0.000196253	14.1049	0.0013	TRUE
Final_W_B	Frame Specific Modulus*%skin (AE)	1	4.27E-06	0.3068	0.5861	FALSE
Final_W_B	Skin Specific Modulus*C-ratio (BD)	1	0.000188398	13.5403	0.0016	TRUE
Final_W_B	Skin Specific Modulus*%skin (BE)	1	8.42E-07	0.0605	0.8083	FALSE
Final_W_B	Altitude*C-ratio (CD)	1	4.04537E-05	2.9075	0.1045	FALSE
Final_W_B	C-ratio*%skin (DE)	1	5.73181E-05	4.1195	0.0566	TRUE
Final_W_B	Frame Specific Modulus*C-ratio*%skin (ADE)	1	2.34E-06	0.1681	0.6864	FALSE
Final_W_B	Skin Specific Modulus*C-ratio*%skin (BDE)	1	7.38E-09	0.0005	0.9819	FALSE

(^ a higher order term containing this term is significant)

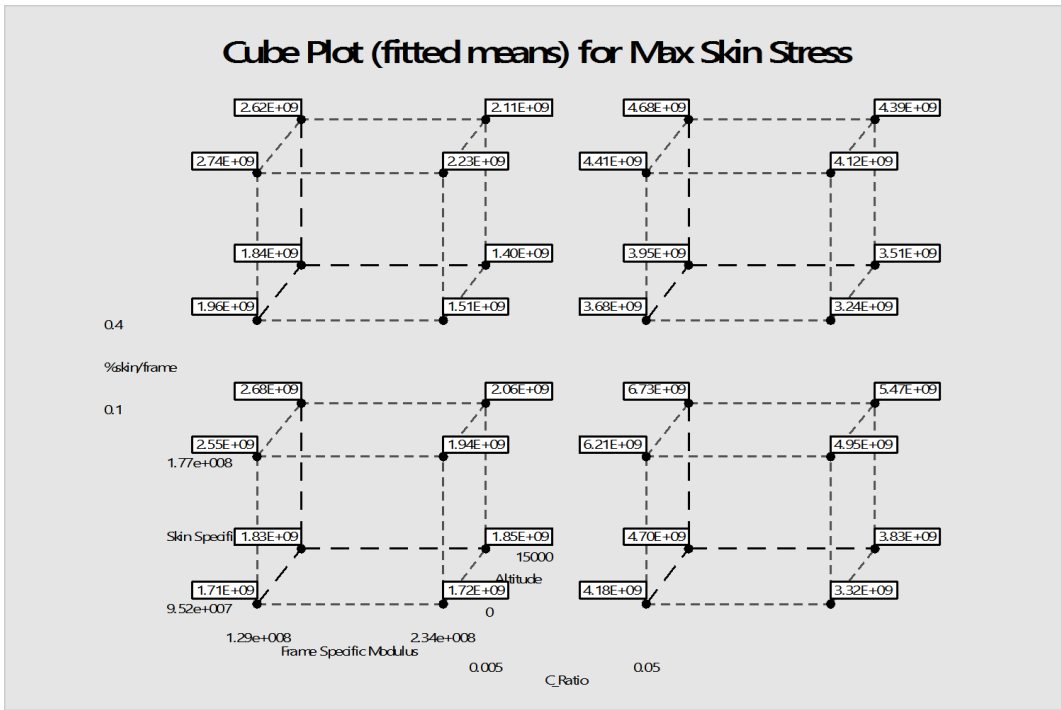


Figure 90: Cube Interaction Plot for Max Skin Stress – Icosahedron

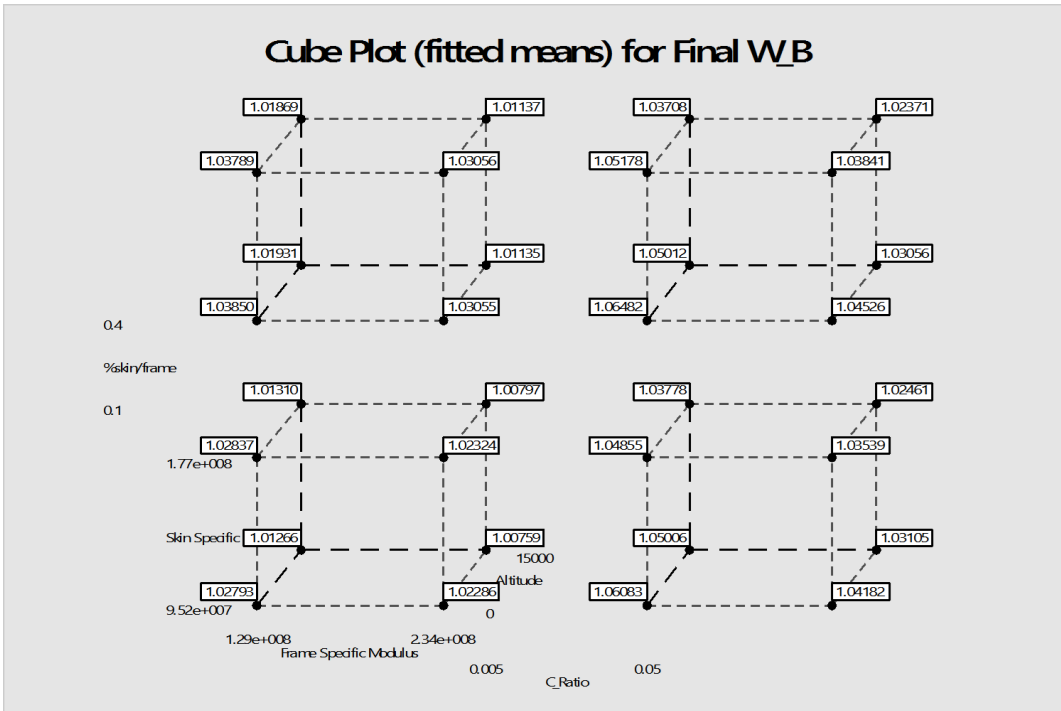


Figure 91: Cube Interaction Plot for Final W/B – Icosahedron

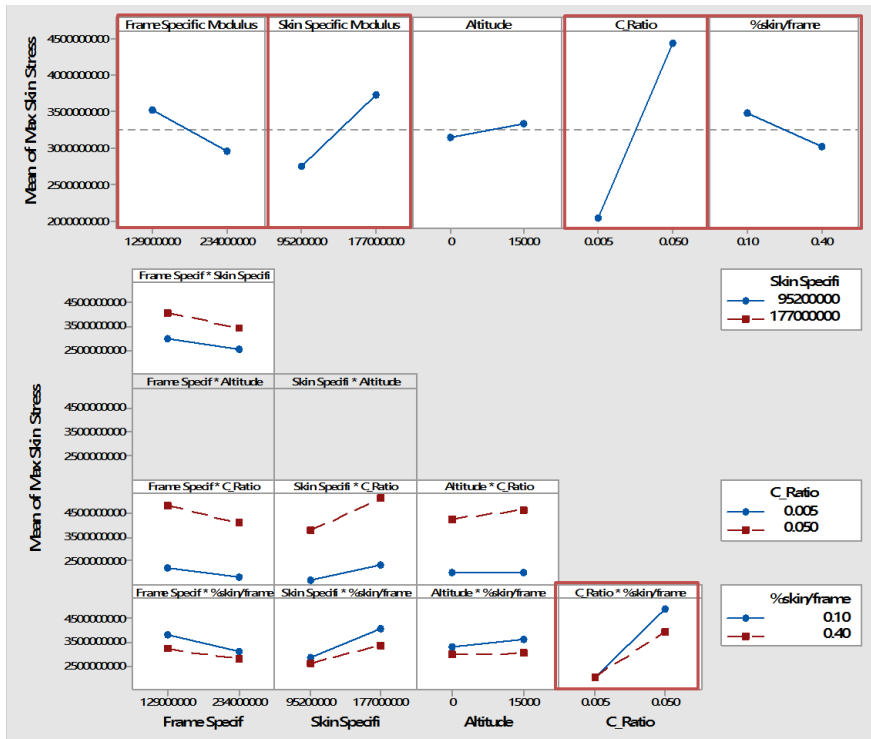


Figure 92: Main effects and 2nd degree interactions effects for Max Skin Stress – Icosahedron

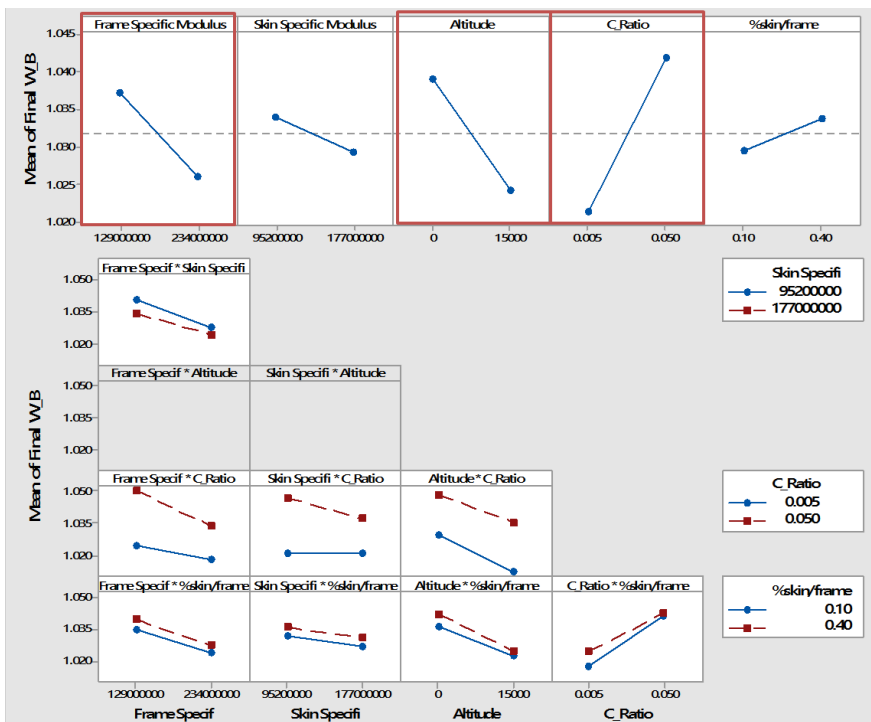


Figure 93: Main effects and 2nd degree interactions effects for Final W/B – Icosahedron

B. Appendix B

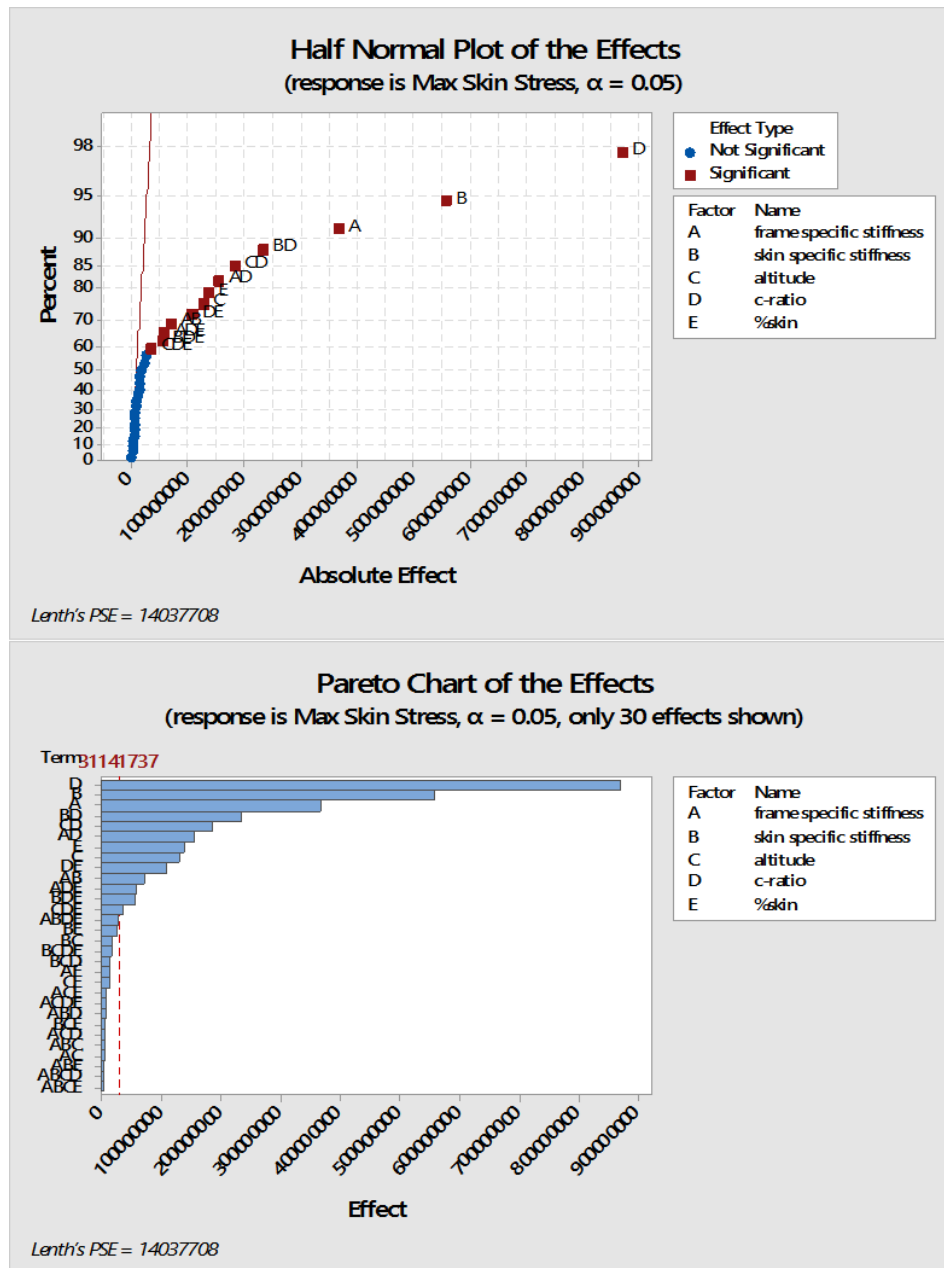


Figure 94: Half Normal Plot and Pareto Chart of the Effects with respect to Max Skin Stress (Hexakis).

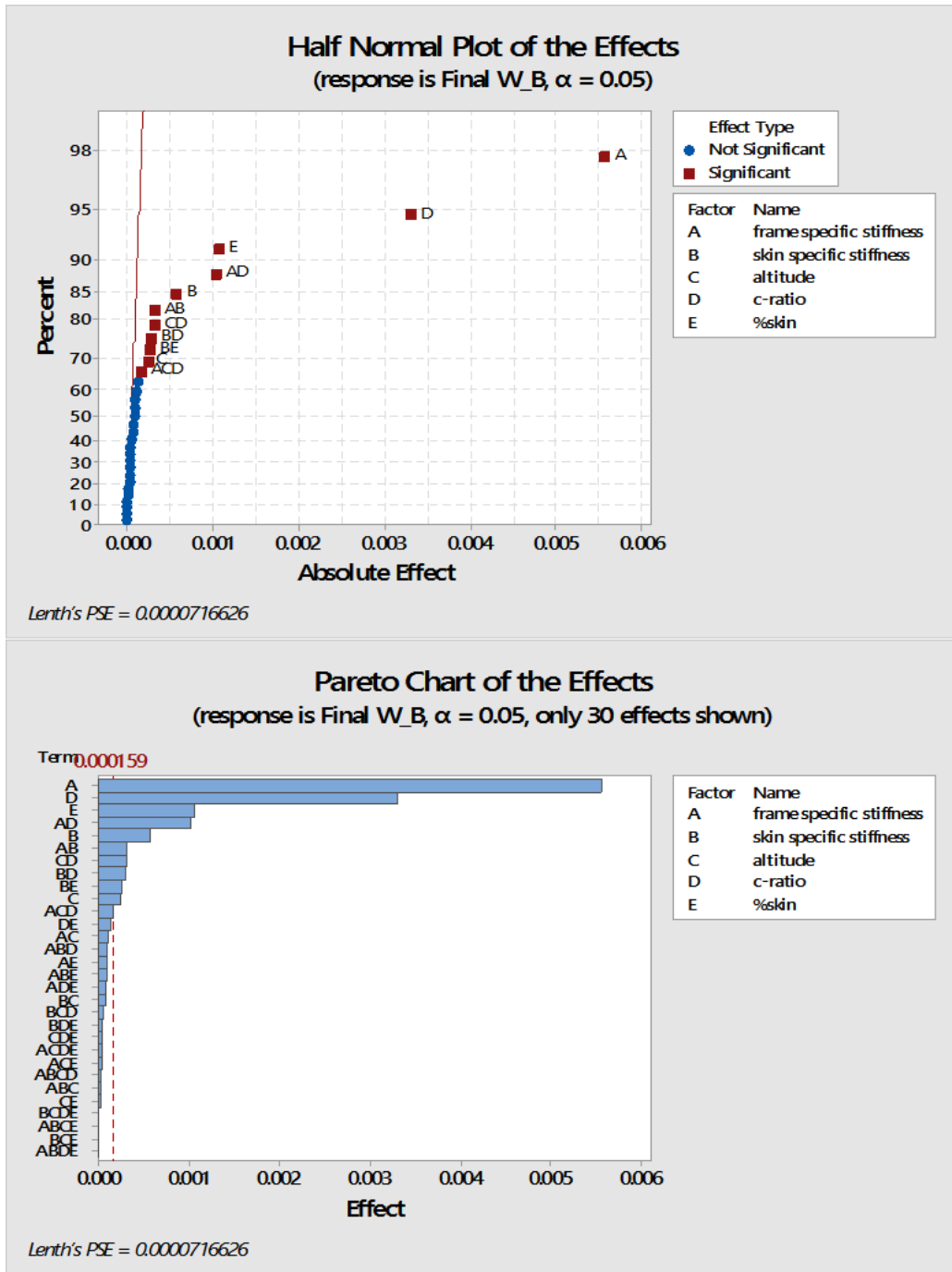


Figure 95: Half Normal Plot and Pareto Chart of the Effects with respect to Final W/B (Hexakis).

Table 46: ANOVA Results for Max Skin Stress - Hexakis

Y	Source	DF	Sum of Squares	F Ratio	Prob > F	Significant
Skin Stress	Frame Specific Mod [A]	1	1.09E+18	864.2644	<.0001	TRUE
Skin Stress	Skin Specific Mod [B]	1	2.49E+18	1981.2668	<.0001	TRUE
Skin Stress	Altitude [C]	1	1.35E+17	107.1376	<.0001	TRUE
Skin Stress	C-ratio [D]	1	6.04E+18	4807.1878	<.0001	TRUE
Skin Stress	%skin [E]	1	1.51E+17	120.4707	<.0001	TRUE
Skin Stress	Frame Specific Mod*Skin Specific Mod [AB]	1	3.97E+16	31.5381	<.0001	TRUE
Skin Stress	Frame Specific Mod*Altitude [AC]	1	1.95E+14	0.1553	0.6994	FALSE
Skin Stress	Frame Specific Mod*C-ratio [AD]	1	1.92E+17	152.8596	<.0001	TRUE
Skin Stress	Frame Specific Mod*%skin [AE]	1	1.53E+15	1.2203	0.2879	FALSE
Skin Stress	Skin Specific Mod*C-ratio [BD]	1	4.38E+17	348.3607	<.0001	TRUE
Skin Stress	Skin Specific Mod*%skin [BE]	1	5.11E+15	4.061	0.0635	FALSE
Skin Stress	Altitude*C-ratio [CD]	1	2.71E+17	215.9199	<.0001	TRUE
Skin Stress	Altitude*%skin [CE]	1	1.28E+15	1.0168	0.3304	FALSE
Skin Stress	C-ratio*%skin [DE]	1	9.53E+16	75.8306	<.0001	TRUE
Skin Stress	Frame Specific Mod*Altitude*C-ratio [ACD]	1	2.28E+14	0.181	0.677	FALSE
Skin Stress	Frame Specific Mod*C-ratio*%skin [ADE]	1	2.66E+16	21.173	0.0004	TRUE
Skin Stress	Skin Specific Mod*C-ratio*%skin [BDE]	1	2.52E+16	20.0342	0.0005	TRUE
Skin Stress	Altitude*C-ratio*%skin [CDE]	1	9.93E+15	7.8944	0.0139	TRUE
(^ this term is part of a significant higher degree term)						

Table 47: ANOVA Results for Final W/B - Hexakis

Y	Source	DF	Sum of Squares	F Ratio	Prob > F	Significant
W_B_Final	Frame Specific Mod [A]	1	0.000248673	11776.7639	<.0001	TRUE
W_B_Final	Skin Specific Mod [B]	1	2.57E-06	121.6444	<.0001	TRUE
W_B_Final	Altitude [C]	1	4.47E-07	21.1573	0.0004	TRUE
W_B_Final	C-ratio [D]	1	0.000087422	4140.1756	<.0001	TRUE
W_B_Final	%skin [E]	1	9.14E-06	432.7083	<.0001	TRUE
W_B_Final	Frame Specific Mod*Skin Specific Mod [AB]	1	8.20E-07	38.8324	<.0001	TRUE
W_B_Final	Frame Specific Mod*Altitude [AC]	1	8.53E-08	4.0383	0.0642	FALSE
W_B_Final	Frame Specific Mod*C-ratio [AD]	1	8.51E-06	403.0543	<.0001	TRUE
W_B_Final	Frame Specific Mod*%skin [AE]	1	7.67E-08	3.6333	0.0774	FALSE
W_B_Final	Skin Specific Mod*C-ratio [BD]	1	6.47E-07	30.6344	<.0001	TRUE
W_B_Final	Skin Specific Mod*%skin [BE]	1	5.52E-07	26.1569	0.0002	TRUE
W_B_Final	Altitude*C-ratio [CD]	1	8.06E-07	38.1831	<.0001	TRUE
W_B_Final	Altitude*%skin [CE]	1	6.79E-10	0.0321	0.8603	FALSE
W_B_Final	C-ratio*%skin [DE]	1	1.40E-07	6.6411	0.0219	TRUE
W_B_Final	Frame Specific Mod*Altitude*C-ratio [ACD]	1	2.12E-07	10.0405	0.0068	TRUE
W_B_Final	Frame Specific Mod*C-ratio*%skin [ADE]	1	4.39E-08	2.0791	0.1713	FALSE
W_B_Final	Skin Specific Mod*C-ratio*%skin [BDE]	1	1.07E-08	0.5059	0.4886	FALSE
W_B_Final	Altitude*C-ratio*%skin [CDE]	1	1.05E-08	0.4986	0.4917	FALSE
(^ this term is part of a significant higher degree term)						

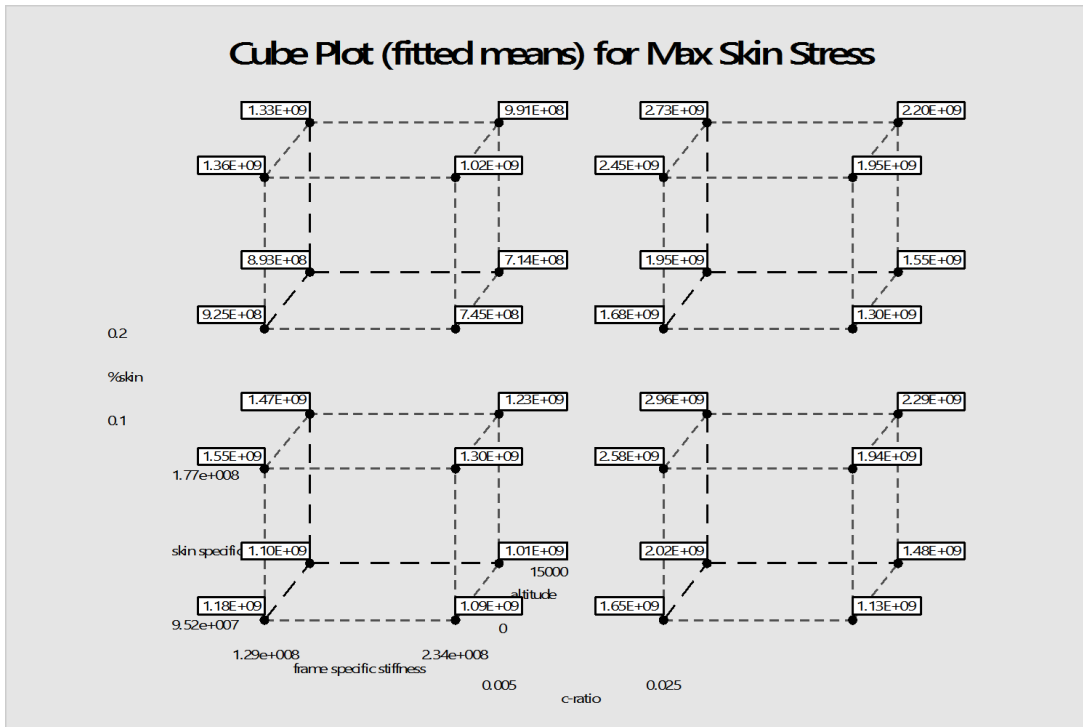


Figure 96: Cube Interaction Plot for Max Skin Stress – Hexakis

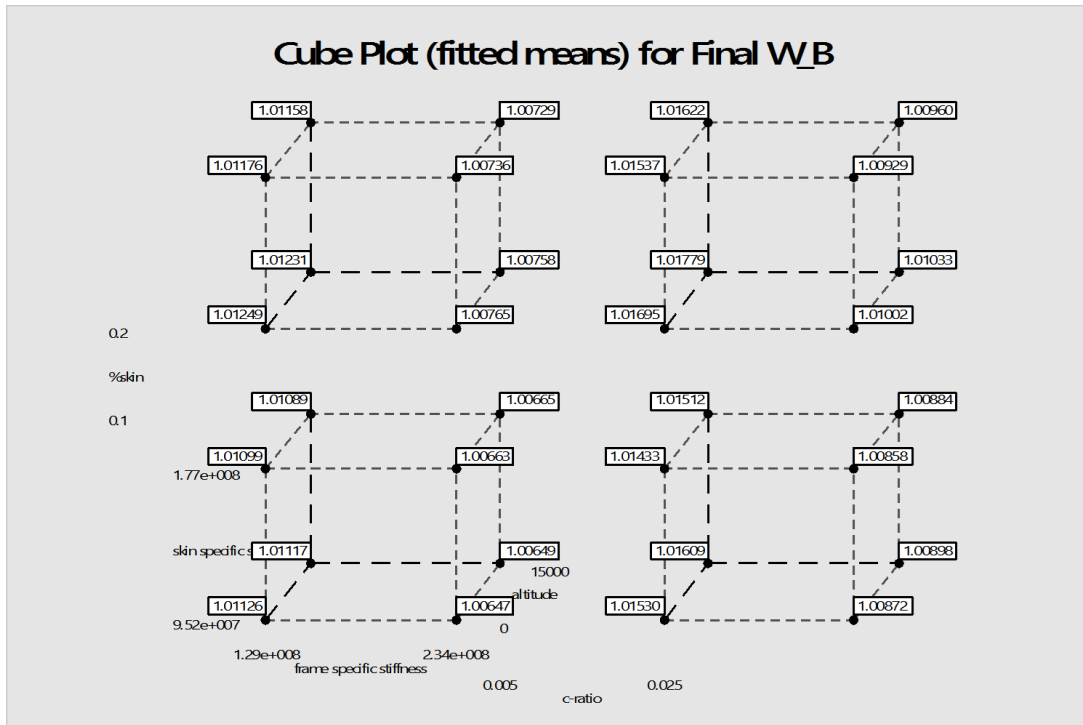


Figure 97: Cube Interaction Plot for Final W/B – Hexakis

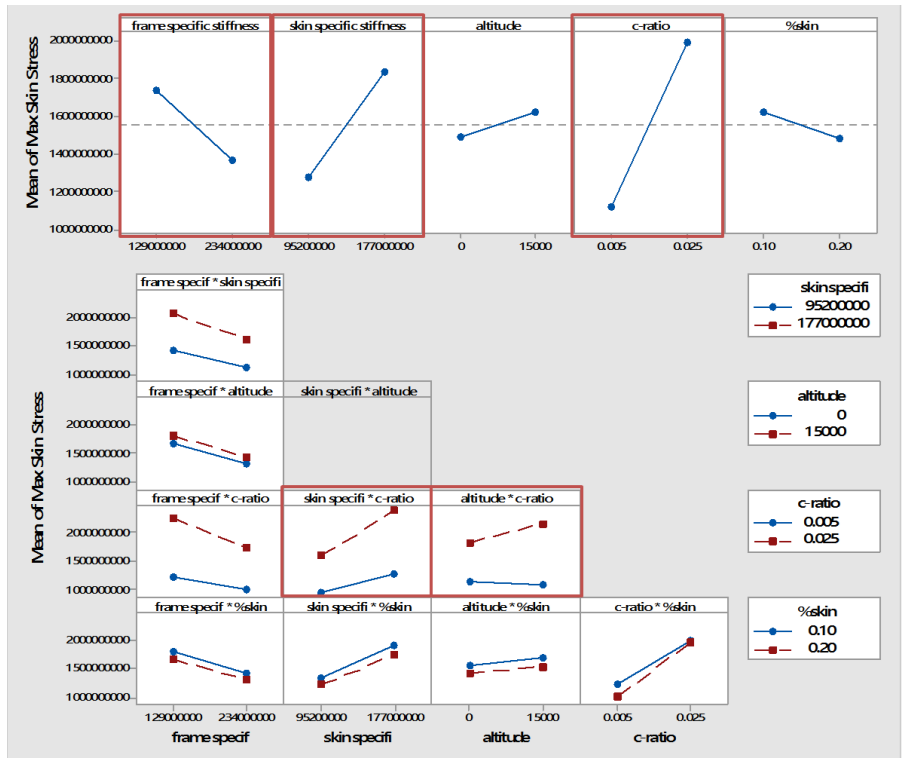


Figure 98: Main effects and 2nd degree interactions effects for Max Skin Stress – Hexakis

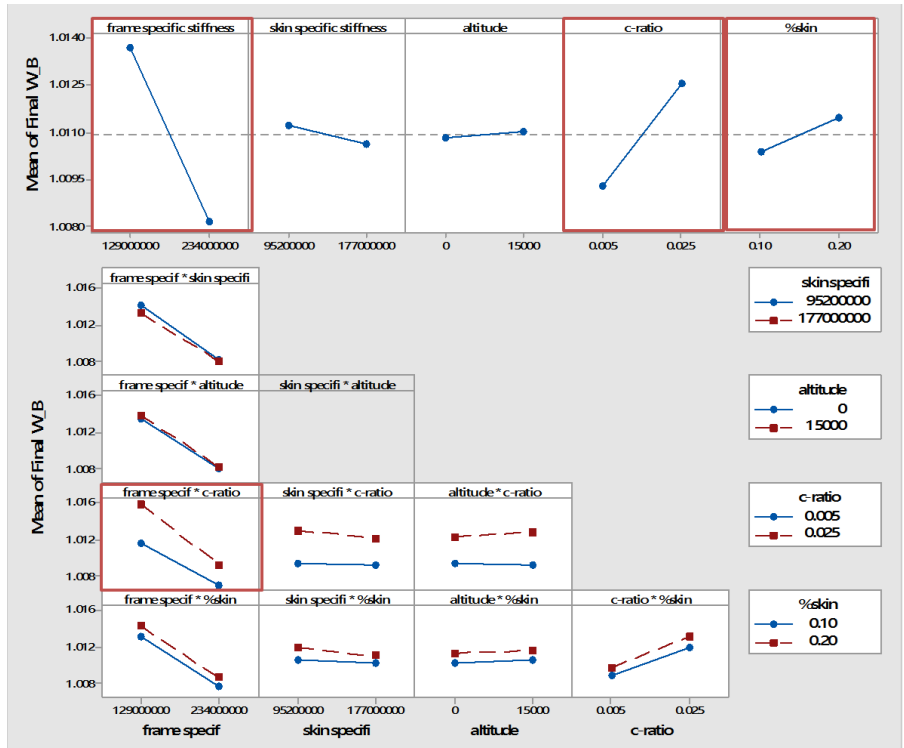


Figure 99: Main effects and 2nd degree interactions effects for Final W/B – Hexakis

References

- [1] T. T. Metlen, "DESIGN OF A LIGHTER THAN AIR VEHICLE THAT ACHIEVES POSITIVE BUOYANCY IN AIR USING A VACUUM," Air Force Institute of Technology, WPAFB , 2012.
- [2] S. Piazza, "Why the world is running out of helium," *The Independent*, 02 September 2014. [Online]. Available: <http://www.independent.co.uk/news/science/why-the-world-is-running-out-of-helium-2059357.html>. [Accessed 15 July 2014].
- [3] F. Lana-Terzi, "The Aerial Ship," *The Aeronautical Society of Great Britian*, 1910.
- [4] A. V. G. Andrey M. Akhmeteli, "Layered Shell Vacuum Balloons". United States of America Patent 11/127,613, 12 May 2005.
- [5] R. Adorno-Rodriguez, "Nonlinear Structural Analysis of an Icosahedron and its Application to Lighter than Air Vehicles Under a Vacuum," Air Force Institute of Technology, WPAFB, 2014.
- [6] e. a. X. Wang, "Ultrastrong, Stiff and Multifunctional Carbon Nanotube Composites," *Materials Research Letters*, pp. 1-7, 22 March 2012.
- [7] N. H. L. I. M. Ward, "Ultra High Modulus Polyethylene Composites," *Pure & Applied Chemistry* , vol. 57, no. 11, pp. 1641-1649, 1985.
- [8] D. R. R. a. J. W. Halliday, *Fundamentals of Physics*, John Wiley and Sons, 2004.
- [9] C. Gillispie, *The Montgolfier Brothers, and the Invention of Aviation*, Princeton University Press, 1983.
- [10] G. K. a. J. Gillett, *Airship Technology*, London: Cambridge University Press, 2012.
- [11] D. Grossman, "Airships: The Hindenburg and other Zeppelins," 2008. [Online]. Available: <http://www.airships.net>. [Accessed 15 July 2014].
- [12] D. S. SIMULIA, "Abaqus/CAE Users Manual," SIMULIA, 2010. [Online]. Available:

- <http://web.eng.gla.ac.uk/v6.10/books/usi/default.htm?startat=pt05.html>. [Accessed 04 Oct 2014].
- [13] Aerospace Students, "Dimensional Analysis," 2016. [Online]. Available: <http://aerostudents.com/files/aerodynamicsA/dimensionalAnalysis.pdf>. [Accessed 10 2 2016].
- [14] D. C. Montgomery, *Design and Analysis of Experiments*, Wiley, 2012.
- [15] S. M. Andre Khuri, "Response Surface Methodology," *WIREs Computational Statistics*, vol. 2, no. March/April, pp. 128-149, 2010.
- [16] J. R. Kathleen M. Carley Natalia Y. Kamneva, "Response Surface Methodology," Carnegie Mellon University, Pittsburgh, 2004.
- [17] Stratasys, "Objet Eden500V," [Online]. Available: <http://www.stratasys.com/3d-printers/design-series/precision/objet-eden500v>. [Accessed 15 July 2014].
- [18] P. A. Lagace, "Bifurcation Buckling," MIT, 2002.
- [19] P. A. Lagace, "The Column and Buckling," MIT, 2009.
- [20] L. H. Donnell, "The New Theory for the Buckling of Thin Cyinders Under Axial Compression and Bending," American Society of Mechanical Engineers, Akron, 1934.
- [21] MTS, "661.19 Force Transducer," MTS, 1996. [Online]. Available: https://www.mts.com/ucm/groups/public/documents/library/dev_003709.pdf. [Accessed 04 Oct 2015].
- [22] M. Barclift and C. Williams, "Examining Variability in the Mechanical Properties of Parts Manufactured via Polyjet Direct 3D Printing," in *International Solid Freeform Fabrication Symposium*, Austin, 2012.
- [23] M. AlGhofaily, "Finite Element Analysis and Experimentation of an Icosahedron Frame under Compression," Air Force Institute of Technology, WPAFB, 2015.
- [24] K. G. McConnell, "The Elusive Free-Free Boundary Condition," Iowa State University of Science and Technology, Ames .
- [25] e. a. S. Bellucci, "CNT Composites for Aerospace Applications," *Journal of Experimental Nanospace*, vol. 1, pp. 129-133, 2006.

- [26] e. a. Shaokai Wang, "Carbon Fiber/Carbon Nanotube Buckypaper Interly Hybrid Composites: Manufacturing Process and Tensile Properties," *Advanced Engineering Materials*, pp. 1-12, 2015.
- [27] e. a. Wang, "Carbon Fiber/Carbon Nanotube Buckypaper Interply Hybrid Composites: Manufacturing Process and Tensile Properties," *Advanced Engineering Materials*, vol. 10, no. 1002, 2015.
- [28] e. X. Wang, "Ultrastrong, Stiff, and Multifunctional Carbon Nanotubes Composites," *Materials Research Letters*, pp. 19-25, 2013.
- [29] e. a. J. W. Zhang, "MECHANICAL PROPERTIES OF HYBRID OF CARBON NANOTUBE AND CARON FIBER REINFORCED EPOXY COMPOSITES," in *18TH INTERNATIONAL CONFERENCE ON COMPOSITE MATERIALS*, Changsha.
- [30] K. McDaniels, "High Strength-to-Weight Ratio Non-Woven Technical Fabrics for Aerospace Applications," Cubic Tech Corp, Mesa, 2009.
- [31] G. Khoury, *Airship Technology*, Cambridge: Cambridge Univerisy Press, 2012.
- [32] S. P. H. A. K. Gupta, "Analysis of Mechanical Properties of Carbon Nanotube Reinforced Polymer Composites Using Continuum Mechanics Approach," *Procedia Materials Science*, vol. 6, pp. 18-25, 2014.
- [33] V. K. Srivastava, "Enhancement of Elastic Modulus of Epoxy Resin with Caron Nanotubes," *World Journal of Nano Science and Engineering*, 2011.
- [34] P. Aravind, "How Spherical are the Archimedean Solids and Their Duals," *College Mathematics*, pp. 98-107, 2011.
- [35] NLV, "Virology: Virus Structure," 2002. [Online]. Available: <http://www.nlv.ch/Virologytutorials/Structure.htm>. [Accessed 15 July 2014].
- [36] A. Windle, "Carbon Nanotube Fibres: Science and Technology Transfer," Cambridge.
- [37] M. J. Wenninger, *Dual Models*, Cambridge University Press, 2003.

- [38] E. W. Weisstein, "Rhombic Triacontahedron," [Online]. Available: <http://mathworld.wolfram.com/RhombicTriacontahedron.html>. [Accessed 10 June 2014].
- [39] E. W. Weisstein, "Disdyakis Triacontahedron," [Online]. Available: <http://mathworld.wolfram.com/DisdyakisTriacontahedron.html>. [Accessed 10 June 2014].
- [40] K. P. W.K. Tredway, "Carbon Fiber Reinforced Glass Matrix Composites for Structural Space Based Applications," Department of the Navy Office of Naval Research, Arlington, 1989.
- [41] Vectran, "Tensile Properties," [Online]. Available: <http://www.vectranfiber.com/BrochureProductInformation/TensileProperties.aspx>. [Accessed 11 June 2014].
- [42] P. J. P. P. V. I. Weingarten, "Buckling of Thin-Walled Circular Cylinders," National Aeronautics and Space Administration, Washington D.C., 1965.
- [43] K. Urner, "Geodesic Domes," [Online]. Available: <http://www.cjfeanley.com/fuller-faq-4.html>. [Accessed 10 June 2014].
- [44] M. D. Taczak, "A Brief Review of Nanomaterials for Aerospace Applications: Carbon Nanotube-Reinforced Polymer Composites," The MITRE Corporation , McLean, 2016.
- [45] P. SLYSH, "The Isogrid," [Online]. Available: <http://isogrid-sst.com/machine%20design.htm>. [Accessed 10 June 2014].
- [46] C.-Y. L. Shih-Chuan Her, "Dynamic Behavior of Nanocomposites Reinforced with Multi-Walled Carbon Nanotubes (MWCNTs)," *Materials*, pp. 2274-2284, 2013.
- [47] P. M. D. Sheet. [Online]. Available: http://usglobalimages.stratasys.com/Main/Secure/Material%20Specs%20MS/PolyJet-Material-Specs/PolyJet_Materials_Data_Sheet.pdf?v=635376606224140355. [Accessed 04 June 2014].
- [48] C. W. Samar Malek, "Structural Implications of using Cairo Tiling and Hexagons in Gridshells," in *Shell and Spatial Structures (IASS) Symposium 2013*, Poland, 2013.

- [49] J. C. a. J. Salsburg, "Geodesic Math," [Online]. Available: <http://mr-fusion.hellblazer.com/pdfs/geodesicmath.pdf>. [Accessed 15 July 2014].
- [50] M. C. W. R. Andrews, "Carbon Nanotube Polymer Composites," *Current Opinion in Solid State and Materials Science* , vol. 8, pp. 21-3, 2004.
- [51] M. A. A. Philip M. Cunniff, "High Performance "M5"Fiber for Ballistics/Structural Composites," U.S. Army Soldier and Biological Chemical Command , Natick .
- [52] S. Pahari, "Robotic Rigid Vacuum Airship for Exploration of Mars," Politecnico di Milano, Milano, 2008.
- [53] J. H. Noggle, "Symmetry Operations," *Physical Chemistry*, p. 840, 1996.
- [54] S. Z.-R. N. Nouri, "Mechanical Property Evaluation of Carbon Nanotube Sheets," *Scientifica Iranica* , vol. 17, no. 2, pp. 90-101, 2010.
- [55] J. Melton, "Airships 101: Rediscovering the Potential of Lighter-Than-Air (LTA)," 2011. [Online]. Available: <http://event.arc.nasa.gov/airships/sites/default/files/pdf/Dr.JohnMelton.pdf>. [Accessed 10 July 2014].
- [56] T. A. Mariano, "A Design of Experiment Using Finite Element Analysis to Predict the Stress in an Involute Spline Interface," Rensselaer Polytechnic Institue, Hartford, 2012.
- [57] M. K. J. P. D. F. Lokendra Pal, "A Simple Method for Calculation of the Permeability Coefficient of Prorous Media," *Tappi Journal*, pp. 10-16, 2006.
- [58] T. T. Lan, "Space Frame Structures," in *Handbook of Structural Engineering* , Boca Raton, CRC Press , 2005, pp. 1-50.
- [59] M. Kubik, "Structural Analysis of Geodesic Domes," Durham University School of Engineering, 2009.
- [60] A. W. Krysztof Koziol, "Controlled Continuous Spinning of Fibres of Single Wall Carbon Nanotubes," in *Guadalupe Workshop*, Houston , 2011.
- [61] M. Krenzke, "The Inelastic Buckling Strength of Near-Perfect Deep Spherical Shells With Ideal Boundaries," US Navy, 1963.

- [62] S. Kidane, "BUCKLING ANALYSIS OF GRID STIFFENED COMPOSITE STRUCTURES," Louisiana State University , 2002.
- [63] X. Hung, "Fabrication and Properties of Carbon Fibers," *Materials* , pp. 1-35, 16 December 2009.
- [64] X. S. T. C. Huisheng Peng, "Polymer Composites with Carbon Nanotubes in Aligment," in *Carbon Nanotubes - Polymer Nanocomposites* , Rijeka, InTech, 2011, pp. 231-250.
- [65] R. W. Gray, "Rhombic Triacotahedron," 5 August 2007. [Online]. Available: <http://www.rwgrayprojects.com/rbfnote/polyhed/PolyhedraData/RhombicTriacotahedron/RhombicTriacotahedron.pdf>. [Accessed 10 June 2014].
- [66] J. H. Giffard, "Century of Flight," [Online]. Available: <http://www.century-of-flight.net/Aviation%20history/to%20reality/Jules%20Henri%20Gi>. [Accessed 10 July 2014].
- [67] R. O. P. Frederick Rosalino da Silva, "Joints covers Bamboo and membrane; Design, Manufacturing and Assembly," in *10th World Bamboo Congress*, Korea, 2015.
- [68] W. W. Fok, "Systematic Narcissism," in *New Constellations/New Ecologies* , San Francisco , 2013.
- [69] C. Duty, "Additive Manufacturing," Oak Ridge National Laboratory, Oak Ridge, 2013.
- [70] A. A. N. Derek J. Edinger, "Selection of I-220H Beryllium for the NIRCam Optical Bench," Lockheed Martin Advanced Technology Center, Palo Alto.
- [71] G. Y. Dean Harman, "Molecular Motion of Gases: Effusion and Diffusion," Thinkwell Corp.
- [72] T. Davis, "Geodesic Domes," 15 September 2004. [Online]. Available: <http://mathcircle.berkeley.edu/BMC6/ps0405/geodesic.pdf>. [Accessed 15 July 2014].
- [73] C. S. M. G. D. Cadogan, "DEVELOPMENT AND EVALUATION OF THE MARS PATHFINDER INFLATABLE AIRBAG LANDING SYSTEM," in *49th International Astronautical Congress*, Melbourne, 1998.

- [74] J. D. Clinton, "Topology/Geometry of Geodesics," SNEC, 2003.
- [75] J. Clinton, "Geodesic Math".
- [76] N. Cheung, "Chemical Vapor Deposition," U.C. Berkeley, 2010. [Online]. Available: http://www-inst.eecs.berkeley.edu/~ee143/fa10/lectures/Lec_13.pdf. [Accessed 15 July 2014].
- [77] D. L. Chandler, "New ultrastiff, ultralight material developed," 19 June 2014. [Online]. Available: <http://newsoffice.mit.edu/2014/new-ultrastiff-ultralight-material-developed-0619>. [Accessed 10 July 2014].
- [78] H. Becker, "STRENGTH OF STIFFENED CURVED PLATES AND SHELLS," *Handbook of Structural Stability*, 1958.
- [79] P. Beccarelli, "The Design, Analysis and Construction of Tensile Fabric Structures," in *Biaxial Testing for Fabrics and Foils*, Springer International Publishing, 2015, pp. 9-33.
- [80] A. Bagger, "Plate shell structures of glass," DTU Civil Engineering, Lyngby, 2010.
- [81] K. E. Arden, "Euler Buckling," Newport News Shipbuilding, Newport News.
- [82] Aeros, "Aeros," 2012. [Online]. Available: <http://www.aeroscraft.com/#/aeroscraft/4567337667>. [Accessed 10 July 2014].
- [83] W. A. Ackel, "Geodesics are Built by Subdividing Regular Solids," 2001. [Online]. Available: <http://home.comcast.net/~wackel/Geometry,GeoSubdivision.html>. [Accessed 15 July 2014].
- [84] J. Aanhaanen, "The stability of a glass faceted shell structure," Delft University of Technology, 2008.
- [85] U.S. Government Printing Office, "U.S. Standard Atmosphere 1976," Washington, 1976.
- [86] Omega, "The Strain Gauge," [Online]. Available: <http://www.omega.com/literature/transactions/volume3/strain.html>. [Accessed 10 July 2014].

- [87] Georgia Tech, "Strain Measurement," 2000. [Online]. Available: <http://soliton.ae.gatech.edu/people/jcraig/classes/ae3145/Lab2/strain.pdf>. [Accessed 10 July 2014].
- [88] Automation Creations Inc., "Matweb: the Manual Materials Information Resource," 1996-2014. [Online]. Available: www.matweb.com. [Accessed 10 July 2014].
- [89] TWI, "Laser Metal Deposition," [Online]. Available: <http://www.twi-global.com/technologies/welding-surface-engineering-and-material-processing/additive-manufacturing/laser-metal-deposition/>. [Accessed 15 July 2014].
- [90] McDonnell Douglas Astronautics Company, "Isogrid Design Handbook," NASA Marshall Space Flight Center, Huntington Beach, 1973.
- [91] Thre3D, "How Ultrasonic Additive Manufacturing Works," [Online]. Available: <https://thre3d.com/how-it-works/sheet-lamination/ultrasonic-additive-manufacturing-uam>. [Accessed 15 July 2014].
- [92] Sensors and Actuators, "How Laser Triangulation Sensor works," [Online]. Available: <http://sensors-actuators-info.blogspot.com/2009/08/laser-triangulation-sensor.html>. [Accessed 10 July 2014].
- [93] RDP Group, "How it Works - LVDT," 09 06 2006. [Online]. Available: <http://www.rdpe.com/displacement/lvdt/lvdt-principles.htm>. [Accessed 15 July 2014].
- [94] "High Strength High Modulus Fibers," 2000. [Online]. Available: <http://gertrude-old.case.edu/276/materials/21.htm>. [Accessed 10 June 2014].
- [95] Vectran, "General Considerations for the Processing of Vectran Yarns," Kuraray America Inc., Fort Mill, 2011.
- [96] Arcam, "EMB Electron Beam Melting," [Online]. Available: <http://www.arcam.com/technology/electron-beam-melting/>. [Accessed 15 July 2014].
- [97] NASA, "Designing a High Altitude Balloon," [Online]. Available: <http://www.grc.nasa.gov/WWW/k->

- 12/Numbers/Math/Mathematical_Thinking/designing_a_high_altitude.htm.
[Accessed 10 July 2014].
- [98] Mecmesin, "Compression Testing - Theory, Applications and Systems," [Online]. Available: <http://www.azom.com/article.aspx?ArticleID=5550>. [Accessed 10 July 2014].
- [99] Instron, "Compression Test," [Online]. Available: http://www.instron.us/wa/applications/test_types/compression.aspx. [Accessed 10 July 2014].
- [100] Department of Defense: United States of America, "Composite Materials Handbook," *MIL-HDBK-17-2F*, 2002.
- [101] Different Spaces, "Characteristics and properties of Geodesic Domes," [Online]. Available: <https://sites.google.com/site/dsdomes/conceptos>. [Accessed 10 June 2014].
- [102] Orbital Vector, "Advanced Airships," 02 11 2010. [Online]. Available: <http://orbitalvector.com/Aircraft/Airships/ADVANCED%20AIRSHIPS.htm>. [Accessed 10 June 2014].
- [103] American Precision Prototyping, "Additive vs Subtractive Manufacturing: Which is Right for You?," 9 6 2014. [Online]. Available: <http://www.approto.com/Media-Center/Additive-vs-Subtractive-Manufacturing--Which-is-Ri.aspx>. [Accessed 15 July 2014].
- [104] N. K. J. R. Kathleen Carley, "Response Surface Methodology," Carnegie Mellon University, Pittsburgh, 2004.
- [105] A. Sonin, *The Physical Basis of Dimensional Analysis*, Cambridge: MIT, 2001.
- [106] PCB Piezotronics, Inc., *Modally Tuned Impulse Hammer w/force sensor and tips*, Depew: PCB Piezotronics Inc., 2010.
- [107] X. e. a. Wang, "Ultrastrong, Stiff and Multifunctional Carbon Nanotube Composites," *Materials Research Letters*, vol. 1, no. 1, pp. 19-25, 2013.
- [108] e. R. Guzman de Villoria, "Aligned Carbon Nanotube Reinforcement of Aerospace Carbon Fiber Composites: Substructural Strength Evaluatino for

Aerospace Applications," in *AIAA/ASME/ASCE/ASC Structures, Structural Dynamics and Materials Conference*, Honolulu, 2012.

- [109] e. a. Nanda Gopal Sahoo, "Polymer Nanocomposites Based on Functional Carbon Nanotubes," *Progress in Polymer Science*, vol. 35, pp. 837-867, 2010.
- [110] e. a. Qunfeng Cheng, "High Mechanical Performance Composite Conductor: Multi-Walled Carbon Nanotube Sheet/Bismaleimide Nanocomposites," *Advanced Functional Materials*, vol. 19, pp. 3219-3225, 2009.
- [111] e. Weijun Wang, "Carbon Nanotube Enhanced Composite Materials," Zyvex Performance Materials, Columbus.
- [112] e. a. Nicolas Baral, "High Modulus Carbon Fibre Composites: Correlation Between Transverse Tensile and Mode I Interlaminar Fracture Properties," *Materials Letters*, vol. 62, no. 6-7, pp. 1096-1099, March 2006.
- [113] A. Deza, "Isoperimetric Problem for Polyhedra," [Online]. Available: http://www.cas.mcmaster.ca/~deza/CG_Domes.pdf. [Accessed 4 10 2014].
- [114] e. a. D. Qian, "Load transfer and deformation mechanisms in carbon nanotube-polystyrene composites," *Applied Physics Letters*, 2000.
- [115] I. W. Frank, "Mechanical Properties of Suspended Graphene Sheets," *Journal of Vacuum Science & Technology B*, vol. 25, no. 6, pp. 2558-2561, 2007.
- [116] J. M. F. d. Paia, "Comparision of Tensile Strength of Different Carbon Fabric Reinforced Epoxy Composites," *Materials Research*, vol. 9, no. 1, pp. 83-89, 2006.
- [117] T. G. Carne, "Support Conditions for Experimental Modal Analysis," *Sound and Vibrations*, pp. 10-15, June 2017.
- [118] K. Ozawa, "Mechanical Properties of Tri-Axially Braided Carbon Fiber Composite," Oak Ridge National Laboratory, Oak Ridge.
- [119] Y. Huang, "Mechanical properties of Zylon/epoxy composite," Van der Waal-Zeeman Institute, Valckenierstraat 65.
- [120] K. Koziol, "High-Performance Carbon Nanotube Fiber," *Science*, pp. 1892-1895, 10 January 2008.

- [121] K. Song, "Structural Polymer-Based Carbon Nanotube Composite Fibers: Understanding the Processing-Structure-Performance Relationship," *Materials*, pp. 1-35, 20 June 2013.
- [122] Z. Spitalsky, "Carbon Nanotube-Polymer Composites: Chemistry, Processing, Mechanical and Electrical Properties," *Progres in Polmer Science*, vol. 35, pp. 357-401, 2010.
- [123] J. N. Coleman, "Improving the Mechanical Properties of Single-Walled Carbon Nanotube Sheets by Intercalation of Polmeric Adhesives," *Applied Physics Letters*, vol. 82, no. 11, pp. 1682-1684, 2003.

REPORT DOCUMENTATION PAGE			<i>Form Approved</i> OMB No. 0704-0188		
The public reporting burden for this collection of information is estimated to average 1 hour per response, including the time for reviewing instructions, searching existing data sources, gathering and maintaining the data needed, and completing and reviewing the collection of information. Send comments regarding this burden estimate or any other aspect of this collection of information, including suggestions for reducing this burden to Department of Defense, Washington Headquarters Services, Directorate for Information Operations and Reports (0704-0188), 1215 Jefferson Davis Highway, Suite 1204, Arlington, VA 22202-4302. Respondents should be aware that notwithstanding any other provision of law, no person shall be subject to any penalty for failing to comply with a collection of information if it does not display a currently valid OMB control number. PLEASE DO NOT RETURN YOUR FORM TO THE ABOVE ADDRESS.					
1. REPORT DATE (DD-MM-YYYY) 14-03-2016		2. REPORT TYPE Dissertation		3. DATES COVERED (From — To) Dec 2012-Mar 2016	
4. TITLE AND SUBTITLE Conceptual Design, Structural Analysis, and Design Space Exploration of a Vacuum Lighter than Air Vehicle			5a. CONTRACT NUMBER		
			5b. GRANT NUMBER		
			5c. PROGRAM ELEMENT NUMBER		
6. AUTHOR(S) Cranston, Brian C, Civ			5d. PROJECT NUMBER		
			5e. TASK NUMBER		
			5f. WORK UNIT NUMBER		
7. PERFORMING ORGANIZATION NAME(S) AND ADDRESS(ES) Air Force Institute of Technology Graduate School of 2950 Hobson Way WPAFB OH 45433-7765			8. PERFORMING ORGANIZATION REPORT NUMBER AFIT-ENY-DS-16-M-202		
9. SPONSORING / MONITORING AGENCY NAME(S) AND ADDRESS(ES) Air Force Office of Scientific Research 875 North Randolph Street, Suite 325, Room 3112, Arlington, VA., 22203-1768 Mr. James Fillerup James.fillerup@us.af.mil			10. SPONSOR/MONITOR'S ACRONYM(S) AFOSR		
			11. SPONSOR/MONITOR'S REPORT NUMBER(S)		
12. DISTRIBUTION / AVAILABILITY STATEMENT DISTRIBUTION STATEMENT A. APPROVED FOR PUBLIC RELEASE; DISTRIBUTION UNLIMITED					
13. SUPPLEMENTARY NOTES This work is declared a work of the U.S. Government and is not subject to copyright protection in the United States					
14. ABSTRACT The research detailed in this study investigates an internal vacuum as well as its optimal structural design, utilizing currently available materials, as an alternative to traditional gases to create and sustain buoyancy in lighter than air vehicles. To date, the consideration of a vacuum lighter than air vehicle has been limited to three sources of literature, the earliest of which dates back to 1663. This study will initially summarize and review this literature. We will then combine finite element analysis, dimensional analysis, design of experiments, and response surface methodology studies to explore the feasibility, and the functional design of a vacuum lighter than air vehicle constrained by modern technology and materials. The process developed herein allows a designer to perform a broad scope initial structural response design space investigation based on user defined constraints to determine if and where structurally feasible regions or points lie. This research then specifically analyzes two cylindrical pultruded rod geometric frame designs with membrane skins stretched over the top vacuum lighter than air vehicle designs. The first being an icosahedron frame and skin structure proposed by Metlen at the Air Force Institute of Technology.					
15. SUBJECT TERMS Lighter than air vehicle, vacuum, design of experiments, finite elements					
16. SECURITY CLASSIFICATION OF:			17. LIMITATION OF ABSTRACT	18. NUMBER OF PAGES	19a. NAME OF RESPONSIBLE PERSON
a. REPORT	b. ABSTRACT	c. THIS PAGE			UU
U	U	U			19b. TELEPHONE NUMBER (Include Area Code) (937) 785-3636 x4599 anthony.palazotto@afit.edu

Standard Form 298 (Rev. 8-98)

Prescribed by ANSI Std. Z39.18